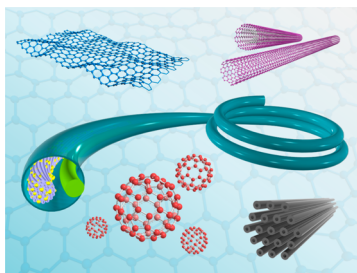


## Recent Advancement of Nanostructured Carbon for Energy Applications

Zhibin Yang, Jing Ren, Zhitao Zhang, Xuli Chen, Guozhen Guan, Longbin Qiu, Ye Zhang, and Huisheng Peng\*

State Key Laboratory of Molecular Engineering of Polymers, Collaborative Innovation Center of Polymers and Polymer Composite Materials, Department of Macromolecular Science and Laboratory of Advanced Materials, Fudan University, Shanghai 200438, China



### CONTENTS

|   |   |
|---|---|
| 1. Introduction                                 | A |
| 2. Carbon Nanomaterials in Different Dimensions | B |
| 2.1. Fullerene                                  | B |
| 2.1.1. Structure                                | B |
| 2.1.2. Synthesis                                | B |
| 2.1.3. Property                                 | B |
| 2.2. Carbon Nanotube                            | B |
| 2.2.1. Structure                                | B |
| 2.2.2. Synthesis                                | B |
| 2.2.3. Property                                 | B |
| 2.2.4. Preparation of Carbon Nanotube Fibers    | B |
| 2.3. Graphene                                   | C |
| 2.3.1. Structure                                | C |
| 2.3.2. Synthesis                                | C |
| 2.3.3. Property                                 | C |
| 2.3.4. Preparation of Graphene Fibers           | C |
| 2.4. Mesoporous Carbon                          | D |
| 2.4.1. Structure                                | E |
| 2.4.2. Synthesis                                | E |
| 2.4.3. Property                                 | E |
| 2.5. Summary                                    | F |
| 3. Application in Energy Conversion             | G |
| 3.1. Transparent Conducting Electrode           | G |
| 3.1.1. Carbon Nanotube                          | H |
| 3.1.2. Graphene                                 | H |
| 3.2. Polymer Solar Cells                        | I |
| 3.2.1. Conducting Electrode                     | J |
| 3.2.2. Hole/Electron Transport Layer            | J |
| 3.3. Dye-Sensitized Solar Cells                 | L |
| 3.3.1. Counter Electrodes                       | N |
| 3.3.2. Working Electrodes                       | N |
| 3.3.3. Electrolyte                              | P |
| 3.4. Carbon Nanomaterial-Silicon Solar Cells    | Q |
| 3.4.1. Carbon Nanotube                          | S |
| 3.4.2. Graphene                                 | S |
| 3.5. Perovskite Solar Cells                     | T |
| 3.6. Fiber-Shaped Solar Cells                   | V |

|  |    |
|--|----|
| 3.7. Summary   | X  |
| 4. Application in Energy Storage                       | Y  |
| 4.1. Lithium Ion Battery                               | Y  |
| 4.1.1. Carbon Nanotube                                 | Y  |
| 4.1.2. Graphene  | AC |
| 4.1.3. Mesoporous Carbon                               | AG |
| 4.1.4. Fiber-Shaped Lithium Ion Batteries              | AH |
| 4.1.5. Nanostructured Carbon for Post Li-Ion Batteries | AJ |
| 4.2. Electrochemical Capacitor                         | AJ |
| 4.2.1. Carbon Nanotube                                 | AK |
| 4.2.2. Graphene  | AO |
| 4.2.3. Mesoporous Carbon                               | AU |
| 4.2.4. Fiber-Shaped Electrochemical Capacitors         | AW |
| 4.3. Summary   | AY |
| 5. Integrated Energy Conversion and Storage Devices    | AY |
| 5.1. Planar Structure                                  | AY |
| 5.2. Fiber Shape                                       | AZ |
| 6. Summary and Perspective                             | BA |
| Author Information                                     | BB |
| Corresponding Author                                   | BB |
| Notes  | BB |
| Biographies  | BB |
| Acknowledgments  | BC |
| References   | BC |

### 1. INTRODUCTION

Wood fuel was the main energy source before the 18th century, and then coal started to dominate the energy component since the invention of steam engine in the industrial revolution. By the 1970s, electrical energy replaced coal with the appearance of the steam engine, and fossil oil became the main energy source in the world. Obviously, carbon materials always play a significant role at the energy field in human history. However, the use of carbon-material-based energy will cause the release of a lot of carbon dioxide, which results in an undesired greenhouse effect. In addition, carbon materials such as coal and fossil oil are nonrenewable. Will carbon materials quit the stage of energy history?

The answer is “no”. During the past half century, renewable and green energy technologies (i.e., solar cells, fuel cells, and lithium ion batteries, LIBs) have been developed with the use

Received: October 28, 2014

of carbon nanomaterials including fullerene, carbon nanotube (CNT), graphene, and porous carbon due to their remarkable mechanical, electrical, catalytic, optical, and thermal properties.<sup>1–3</sup> More specifically, fullerene derivatives are still the best electron acceptor in polymer solar cells (PSCs); CNT and graphene are promising candidates of the next-generation of transparent conductive films in solar cells, and they also exhibit high electrochemical performances in LIBs and supercapacitors. Porous carbon has also been broadly used as catalyst supports and filters in many energy devices. Therefore, carbon materials continue to play a critical role in the energy field.

In fact, there already exist some review articles that focus on different aspects on the application of carbon nanomaterials for energy in early years.<sup>3–6</sup> Here we present a comprehensive review on the advancement of carbon nanomaterials for energy applications in recent years. The synthesis and properties of four widely explored carbon nanomaterials, i.e., fullerene, CNTs, graphene, and porous carbon, are systematically described. Their promising applications in both energy conversion and storage including solar cells, LIBs, and supercapacitors as well as their integrations are then carefully investigated with an emphasis on the flexible devices, particularly, the recent emergence of lightweight and wearable fiber-shaped devices. The remaining challenges and main developing directions are finally highlighted.

## 2. CARBON NANOMATERIALS IN DIFFERENT DIMENSIONS

Carbon plays a key role in the earth's civilizations. It can form strong bonds in different forms. Diamond and graphite are the typical allotropes of carbon at nature. C–C sp<sup>3</sup> hybridization makes diamond the hardest natural material, while graphite is a solid lubricant due to the loose interlamellar coupling among sheets. In the last three decades, a lot of new carbon nanomaterials were discovered, including fullerene, CNT, graphene, mesoporous carbon, and so on. These carbon nanomaterials exhibit promising applications in the field of energy.

### 2.1. Fullerene

Buckminsterfullerene (C<sub>60</sub>) was the first discovered fullerene molecule and the family's namesake. It was named for in homage to Buckminster Fuller. The structure, where it formed the core of a "bucky onion", was independently identified by different researchers in the early 1980s. The discovery of fullerenes greatly expanded the number of known carbon allotropes, which were mainly limited to graphite and diamond. The unique physical and chemical properties of these new forms of carbon inspired many scientists to predict their technological applications. C<sub>60</sub> carbon clusters are good electron acceptors,<sup>7</sup> and PSCs based on conjugated polymer and fullerene offer high opportunities as renewable energy sources.<sup>8</sup> It has been further shown that C<sub>60</sub> and derivatives undergo a variety of chemical reactions to produce functional materials for efficient photoelectric devices.<sup>9</sup>

**2.1.1. Structure.** A typical fullerene molecule has a cage-like fused-ring structure (truncated icosahedron) which bears a strong resemblance to a soccer ball.<sup>10</sup> C<sub>60</sub> is made of 20 carbon hexagons and 12 carbon pentagons with a bond along each polygon edge (Figure 1). The bond between two hexagons can be considered "double bond" and is shorter than the bond between a hexagon and a pentagon. The van der Waals diameter of a C<sub>60</sub> molecule is about 1.01 nm, while nucleus to

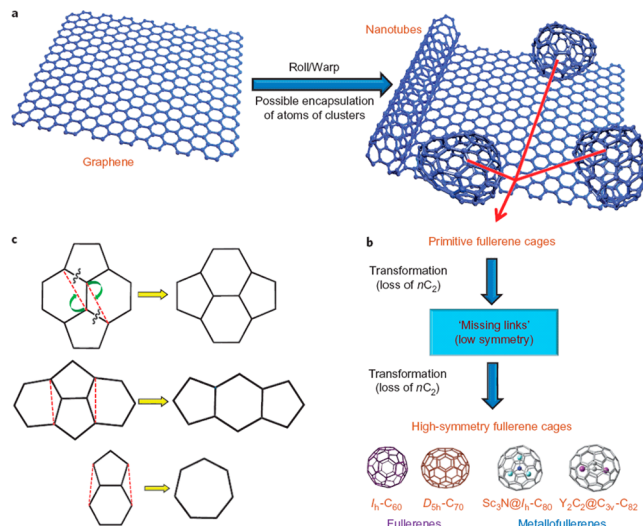


**Figure 1.** (a) Schematic illustration of fullerene and CNT from graphene. (b) fullerenes and metallofullerenes. (c) Carbon hexagons, pentagons and heptagons. Reproduced with permission from ref 10. Copyright Macmillan Publishers (2013).

nucleus diameter is about 0.71 nm.<sup>7</sup> Another fairly common fullerene is C<sub>70</sub>, while fullerenes with 72, 76, 84, and even up to 100 carbon atoms are also able to be obtained. The structure of a fullerene is a mathematical polyhedron with pentagonal and hexagonal faces. Fullerenes are similar in structure to graphite, which is composed of a sheet of linked hexagonal rings, but they contain pentagonal (or sometimes heptagonal) rings that prevent the sheet from being planar.

However, finding applications for these peculiar structures has been difficult because no one knows exactly how they are formed. The first and oldest is the "bottom-up" theory, where carbon cages are built atom-by-atom. The second, more recent, theory takes a "top-down" approach, suggesting that fullerenes form when much larger structures break into constituent parts. After several years of debate with how the top-down theory might work, researchers have discovered that asymmetrical fullerenes formed from larger structures appear to settle into stable fullerenes.<sup>11</sup>

**2.1.2. Synthesis.** Fullerenes occur only in small amounts naturally, so a lot of efforts are made to synthesize them on a large scale.<sup>12</sup> Generally, they are synthesized by applying a large current between two graphite electrodes in an inert atmosphere. The resulting carbon plasma arc between the electrodes cools into a sooty residue from which many fullerenes can be isolated. The vaporization of graphite rods and catalytic chemical vapor deposition (CVD) from carbon sources are also used to synthesize fullerenes.<sup>13</sup>

**2.1.3. Property.** C<sub>60</sub> is extremely stable at both high temperatures and pressures. Fullerenes are insoluble in water and sparingly soluble in aromatic solvents such as toluene. The chemical reactivity of C<sub>60</sub> is typical of an electron deficient olefin,<sup>14</sup> and it can react with nucleophiles. The vast majority of reactants attack the 6, 6 ring junctions which possess higher electron densities. Atomic doping converted C<sub>60</sub> to C<sub>59</sub>NH<sub>5</sub>, which paved a road to the use of C<sub>60</sub> in the storage device for hydrogen.<sup>15</sup>

The buckminsterfullerene C<sub>60</sub> is an electron acceptor, which can be electrochemically reduced up to 6 electrons. Due to this spherical-conjugated system, it shows an exceptional energy level structure. The molecular orbital spin–spin coupling

constant is significantly higher than the benzene, even higher than graphene.<sup>16</sup> Hence, the difference of molecular energy levels between singlet and triplet states is as low as 0.15 eV. As a result, the electron intersystem crossing from singlet to triplet states is abnormally fast ( $\tau_{ISC} = 650$  ps) with a high efficiency up to 96%. For photoinduced electron-transfer reactions (i.e., photodoping), it has been blended into electron-donating matrices with hole conducting properties.<sup>17</sup> Soluble derivatives of C<sub>60</sub>, such as 1-(3-methoxycarbonyl) propyl-1-phenyl[6,6]C<sub>61</sub> (PCBM), have been widely used for PSCs.<sup>7,18,19</sup>

What makes fullerenes special is the combination of several interesting properties, particularly in terms of electron-acceptor capability, both in the solid state and in solution.<sup>20</sup> For instance, the formation of charge-transfer salts with a number of donor groups or doping with metals has led to ferromagnetic or superconducting materials. Furthermore, an entirely new discipline, commonly called “fullerene chemistry”, has emerged in the past few years. Fullerenes and metallofullerenes are also involved in various biomedical applications.<sup>21–23</sup> The medical promise of metallofullerenes stems from the metal atoms caged within them. Because the metal atoms are trapped in a cage of carbon, they do not react with the outside world, making their side effects low in both number and intensity.<sup>24</sup> A lot of studies are underway to further explore their excellent chemical and physical properties.<sup>86,87</sup>

## 2.2. Carbon Nanotube

CNT is a representative one-dimension structure allotrope of carbon. Since the discovery in 1991,<sup>25</sup> CNT has been a superstar in nanomaterials by attracting a great deal of interest in both academy and industry due to its remarkable properties and potential applications in a wide variety of fields. According to the searching result from Web of Science, more than 37 000 papers and 2000 patents have been published related to CNTs.

**2.2.1. Structure.** CNT can be considered as a hollow cylinder of carbon by scrolling single or multilayered graphene<sup>26</sup> (Figure 2a). A single-walled CNT (SWCNT) can be considered as a single molecule and shows a great deal of diversity in structure including diameter, length, and chirality.

The diameter and chirality of a SWCNT can be decided by its  $(n, m)$  indices that depict the vector  $c_h = na_1 + ma_2$  which connects crystallographically equivalent sites in a two-dimensional graphene sheet (Figure 2b,  $a_1$  and  $a_2$  are unit vectors of the graphene layer, and  $n$  and  $m$  are integers).<sup>27</sup> The diameter and chirality are then calculated by the following equation.<sup>3</sup>

$$D = a(n^2 + nm + m^2)^{1/2}/\pi \quad (2.1)$$

$$\theta = \tan^{-1}[3^{1/2}m/(m + 2n)] \quad (2.2)$$

The CNT presents an armchair and zigzag type when  $n = m$  and  $m = 0$ , respectively. The others belong to a chiral type. The electrical properties of CNTs depend on their diameters and chiralities, which are both functions of  $(n, m)$ .<sup>27</sup> According to the chirality, CNTs may be classified as semiconductive and metallic, which follow a general rule: if  $(n - m)$  is a multiple of 3, they exhibit a metallic behavior, and if not, they show a semiconducting behavior.<sup>28</sup> In the case of multiwalled CNTs (MWCNTs), as the distance between two walls is a constant of 0.34 nm, the chirality of each wall is different. Therefore, they are metallic.

**2.2.2. Synthesis.** There are three main methods to synthesize CNTs, i.e., arc-discharge deposition, laser ablation, and CVD. The CNTs were first discovered during character-

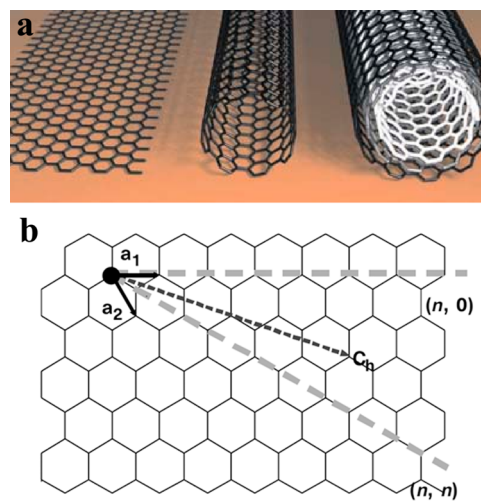


**Figure 2.** (a) Illustration of the form of a graphene sheet (left), SWCNT (middle), and MWCNT with three shells (right). Reproduced with permission from ref 26. Copyright Springer (2005). (b) Schematic of a two-dimensional graphene sheet illustrating lattice vectors  $a_1$  and  $a_2$  and the roll-up vector  $c_h = na_1 + ma_2$ . The  $(n, 0)$  zigzag and  $(n, n)$  armchair tubes are indicated with dashed lines. Reproduced with permission from ref 27. Copyright Macmillan Publishers Ltd. (2005).

izing the product of fullerene synthesized by arc discharge deposition.<sup>25</sup> Later, the SWCNTs were synthesized by codeposition of metal Co and carbon.<sup>29,30</sup> In 1995, Smalley et al. discovered a new method to synthesize CNTs by heating the graphic carbon with laser ablation instead of arc discharge.<sup>31</sup> Arc discharge and laser ablation are both operated at relatively high temperatures which result in a high cost.

Instead of solid carbon, carbon sources in a gas format can be used to make CNTs by a CVD process at a much lower temperature range of 500–1200 °C. The often used carbon sources include CO, methanol, ethanol, and hydrocarbons.<sup>32–35</sup> This method is more consistent with the conventional semiconductor industry. In a CVD process, one can control the diameter, wall number, and length of CNTs by varying the structure and composition of catalysts. In 2004, Hata et al. successfully elongated the lifetime of catalyst and synthesized millimeter-long SWCNT arrays by adding ppm content of water during the CVD synthesis.<sup>35</sup> The outer diameters of CNTs are mainly determined by the sizes of catalyst particles. Yamada et al. selectively synthesized double-walled CNT (DWCNT) arrays by changing the catalyst thickness.<sup>36</sup> For more details on synthesis, the readers may refer to more specific reviews.<sup>37,38</sup>

**2.2.3. Property.** Due to their unique structures, CNTs have been widely investigated for combined excellent mechanical, electronic and thermal properties. Theoretical and experimental results indicate that the CNT exhibits high Young's modulus, tensile strength, and electrical conductivity. Yu et al. measured the Young's modulus at a range of 320 to 1470 GPa by atomic force microscopy.<sup>39</sup> Demczyk et al. measured a Young's modulus of 0.9 TPa and tensile strength of 150 GPa.<sup>40</sup> The electrical conductivities of CNTs reached  $10^7$  S/m, and current densities on the level of  $10^6$  A cm<sup>-2</sup> had been achieved.<sup>41</sup> CNTs also exhibit excellent thermal and catalytic properties. Pop et al. measured a thermal conductivity of almost 3500 W/m K at room temperature for a SWCNT with a diameter of 1.7 nm and developed a model to predict the thermal conductivity as a

function of diameter and temperature.<sup>42</sup> Similarly, Kim et al. measured a thermal conductivity above 3000 W/m K at room temperature for MWCNTs using a microfabricated suspended device.<sup>43</sup> CNTs showed a high catalytic activity in oxygen reduction reaction.<sup>44</sup> They were comparable to the conventional platinum in the reduction of triiodide, a key reaction of the dye-sensitized solar cells (DSSCs).<sup>45</sup> The excellent physical and chemical properties of CNTs make them promising as high-performance fillers in polymers.<sup>46</sup>

**2.2.4. Preparation of Carbon Nanotube Fibers.** The synthesized CNT powders are generally polydispersed in both length and diameter. In particular, the CNTs are highly entangled with each other. This random organization of CNTs has largely decreased the mechanical and electronic properties of the resulting bulk materials and limited their applications in many fields including energy. To this end, a lot of efforts are made to prepare aligned CNT materials including arrays, films, and fibers. In particular, aligned CNT fibers have recently attracted increasing attentions for their application in flexible energy conversion and storage devices. Several general and effective methods are successfully developed to prepare CNT fiber materials aiming at excellent mechanical and electronic properties.

**2.2.4.1. Wet Spinning to Prepare the Carbon Nanotube Fiber.** Wet spinning is a traditional method for preparing polymer fibers. This process requires a polymer solvent as spinning dope. Wet spinning gets its name from the wet bath where the spinneret is submerged and the fiber coagulates. However, the intrinsic chemical inertness as well as the strong interaction of CNTs limits their solubility in aqueous, organic, or acid media. Therefore, surfactants or chemical treatments are necessary to increase the compatibility with solvent.

Figure 3 illustrates the wet spinning and collecting process for a CNT fiber. CNT powders are first dispersed in a solvent

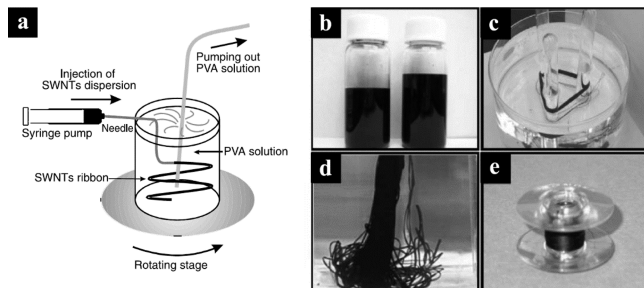


**Figure 3.** (a) Schematic of the experimental setup used to extrude SWCNT ribbon. (b) CNTs used for wet spinning. Reproduced with permission from ref 47. Copyright The American Association for the Advancement of Science (2000). (c–e) CNT fibers containing PVA fabricated by the wet spinning method. Reproduced with permission from ref 48. Copyright Royal Society of Chemistry (2004).

with the aid of surfactants, and the resulting suspension is extruded into a poly(vinyl alcohol) solution to form the desired fiber. The as-spun fibers contained poly(vinyl alcohol) that can be removed after a washing treatment.<sup>47</sup> The CNT fiber showed excellent mechanical properties with elastic modulus to be ten times higher than a Bucky paper. The tensile strength and electrical conductivity achieve 150 MPa and 1000 S/m, respectively.

After optimization of the fabrication and without removing poly(vinyl alcohol), Dalton et al. made a supertough CNT fiber with a tensile strength up to 1.8 GPa.<sup>48</sup> The poly(vinyl

alcohol)-containing CNT fibers could be further woven into flexible supercapacitors. However, due to the existence of surfactants and polymers that decrease the electronic properties of CNTs such as conductivities, the electrochemical performance needs to be improved. The related application detail and following improvement will be discussed later

Based on the fact that SWCNTs could be dissolved in sulfuric acid fumes and formed a liquid-crystalline phase to enable a high alignment, an encouraging breakthrough was made by Ericson et al. in 2004. Macroscopically continuous, neat SWCNT fibers were successfully spun from a suspension of SWCNTs in superacids.<sup>49</sup> Polarized Raman spectroscopy and X-ray diffraction (XRD) characterization confirmed the alignment of SWCNTs within the fiber. The neat SWCNT fibers possess excellent mechanical properties, with a Young's modulus of 120 GPa and a tensile strength of 116 MPa. Compared with the SWCNT/PVA composite fibers, the bare CNT fibers displayed a poor toughness; however, the CNT fibers demonstrated high electrical conductivities up to  $5 \times 10^5$  S/m and thermal conductivities of 21 W/m K due to the absence of impurities, which is promising for use in electronic textiles, a mainstream direction in wearable electronics, to be discussed later. To further improve the spinning processability of SWCNT solutions, chlorosulfonic acid was utilized to enhance the solubility in the liquid phase. By controlling the liquid-crystalline phase behavior of SWCNTs in superacids, Davis et al. had prepared bare SWCNT fibers and films in a process similar to those used in the commercial spinning of high-performance aramidic fibers out of strong acids.<sup>50</sup> The high concentrated CNT solutions favored the formation of liquid-crystal domains, and thus CNTs can be readily assembled into macroscopic fibers or sheets with controlled morphologies. Mechanical and electrical tests indicated that the obtained single-walled CNT fibers had a strength within 50–150 MPa and an electrical conductivity up to 8300 S cm<sup>-1</sup>.

These achievements encouraged the engineering of macroscopic single-walled CNT fibers through a superacid route, but it is not effective for multiwalled CNTs. To this end, Zhang et al. further developed a coagulation process in which MWCNT fibers were spun from a liquid-crystalline ethylene glycol dispersion with ethylene glycol as a dispersant.<sup>51</sup> This process was also applicable for nitrogen-doped MWCNTs. The modulus of N-doped MWCNT fibers was  $142 \pm 70$  GPa with a strength of  $0.17 \pm 0.07$  GPa. The electrical conductivities of MWCNT and N-MWCNT fibers were  $8 \times 10^3$  and  $3 \times 10^4$  S/m, respectively, relatively lower than the SWCNT fiber. Further optimization of the spinning process is imperative to improve the mechanical and electrical properties of multiwalled CNT fibers.

A great deal of attention was paid to optimizing the spinning process to further improve the mechanical and electrical properties of MWCNT fibers.<sup>52</sup> By using longer MWCNTs with a length of about 5  $\mu$ m and chlorosulfonic acid as the solvent, Behabtu et al.<sup>52</sup> report high-performance fibers that combined an average tensile strength of  $1.0 \pm 0.2$  GPa and an average electrical conductivity of  $(2.9 \pm 0.3) \times 10^6$  S/m as well as high stiffness and thermal conductivity. These fibers consisted of large production of CNTs with low cost and were produced by high-throughput wet spinning (Figure 4). It was found that in the wet spinning process, technique optimization and process control play a more important role in the resulting performance of CNT fiber while the CNT

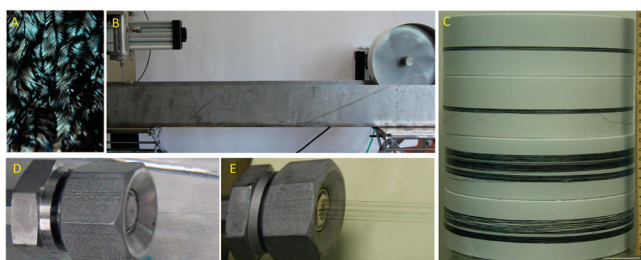


**Figure 4.** (a) Optical micrograph of a briefringent fiber. (b) Experimental equipment for wet spinning. (c) Winding drums with collected fibers. (d, e) Side views of a single- and 19-filament spinning, respectively. Reproduced with permission from ref 52. Copyright The American Association for the Advancement of Science (2013).

characters including length, diameters, and wall numbers, notwithstanding some exceptions, are not dominant.

**2.2.4.2. Dry-Drawing from Spinnable Carbon Nanotube Array.** Dry-drawing CNTs from spinnable arrays into fibers represents another promising method.<sup>53,54</sup> Similar to the wet spinning method, the synthesis of CNTs and preparation of fibers include two separated steps. A superaligned CNT array that consists of both narrowly dispersed wall number and diameter for the CNT is first synthesized by CVD. Aligned CNTs are then assembled into continuous fibers by a dry-drawing and twisting process. Specifically, aligned CNT sheets are pulled out of the array and have been then made into flexible fibers by two typical methods. One, an aligned CNT sheet is directly twisted into a fiber (Figure 5a).<sup>54</sup> Two, the

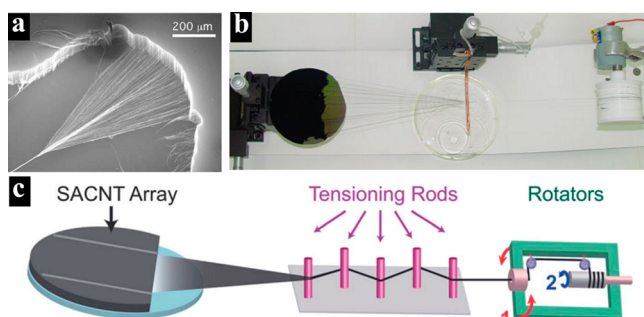


**Figure 5.** CNT fibers fabricated from aligned spinnable CNT arrays by (a) simple twisting. Reproduced with permission from ref 54. Copyright The American Association for the Advancement of Science (2004). (b) Solvent treatment. Reproduced with permission from ref 55. Copyright John Wiley and Sons (2006). (c) Tensioning and twisting. Reproduced with permission from ref 57. Copyright Royal Society of Chemistry (2004).

aligned CNT sheet passes through a volatile solvent and shrinks into a dense fiber after evaporation of solvent (Figure 5b).<sup>55</sup> However, both methods are not ideal, e.g., there remain many voids in the fiber during a twisting process, while the surface structure is irregular and rough after a shrinking treatment. Recently, the two methods were integrated into one by adding the volatile solvent in the region of the triangle sheet and then twisting the fiber for a densification.<sup>56</sup> This combined method may be also developed to incorporate a second phase to make CNT composite or hybrid fibers by replacing the pure solvent with a functional material solution. In addition, applying a tensile stress during twisting, by drawing fiber through a zigzag path where tensions are exerted between the pillars, the resulting CNT fibers are improved in alignment and increased in

mechanical strength (Figure 5c).<sup>57</sup> However, the tensioning zone may introduce an extra tension force, which was unfavorable for preparing ultrathin fibers that were prone to break under the tension during the twisting process.

**2.2.4.3. Direct Synthesis of Carbon Nanotube Fibers.** To sustain the superior mechanical and electrical properties of individual CNTs, it is required that individual CNTs are grown as long as possible and interaction forces among CNTs are designed as strong as possible. Longer CNTs reduce the number of CNT ends and CNT junctions in a fiber, yielding both higher strengths and electrical and thermal conductivities. An ideal model lies in that all individual CNTs with the same length are penetrated from one end to the other end. There has been a great effort devoted to fabricate long CNTs in the past decade. Zheng et al. synthesized 4-cm-long SWCNTs under an ambient condition.<sup>58</sup> Recently, by optimizing the growing parameters and applying a “furnace-moving” method, Zhang et al. synthesized 55 cm-long CNTs with integral structures.<sup>59</sup> The tensile strength of such long CNTs was up to 120 GPa and the breaking strain was up to 15%, both approximating their theoretical values. However, the yield of long CNTs and the array density are relatively low, and both of them need to be increased for a large-scale application.

**2.2.4.4. Spinning from Carbon Nanotube Aerogels.** In the effort to synthesize structure-controllable CNTs, an encouraging breakthrough was made to produce macroscopic SWCNT strands with thicknesses of tens to hundreds of micrometers and lengths of several centimeters through a vertically floating CVD method.<sup>60</sup> Metallic behavior was discovered with a conductivity of around  $5 \times 10^5$  S/m at a temperature range of 90–300 K.

Adopting a similar method, Li et al. prepared continuous CNT fibers by mechanically drawing CNT aerogel from the gaseous reaction zone and then directly winding it onto a roller.<sup>61</sup> This method relied on assembling CNTs in the gas flow via van der Waal's interactions. Ethanol or acetone vapor is usually employed as the carbon source. The maximal electrical conductivity of as-synthesized CNT fibers reached  $8.3 \times 10^5$  S/m, but the tensile strength was typically lower than 1 GPa. Recently, Li et al. advanced this approach by using a mixture of ethanol and acetone vapors as the carbon source to make continuous CNT fibers with a multilayered structure.<sup>62</sup> The continuous CNT fiber can be as long as several kilometers with conductivity of  $5000$  S cm<sup>-1</sup>. Besides, this process is favorable for MWCNTs with large diameters while a few wall numbers, so the MWCNTs collapsed into a dog-bond structure under the stress. The increased friction force among the collapsed MWCNTs was further found to strengthen the fibers.<sup>63,64</sup>

### 2.3. Graphene

Graphene was discovered by Novoselov and Geim with a micromechanical exfoliation method in 2004.<sup>65</sup> It had attracted increasing attention from both academy and industry since then.<sup>1,5,6,66–68</sup>

**2.3.1. Structure.** Graphene, a single layer of carbon atoms bonded together in a honeycomb crystal lattice, is the fundamental structure in the carbon world. As shown in Figure 6, graphene is the mother of all graphitic forms. They can be made into 0D fullerenes, rolled into 1D nanotubes and stacked into 3D graphite.<sup>66</sup>

**2.3.2. Synthesis.** Graphene had been first obtained by repeatedly striping graphite crystal until a monatomic sheet was maintained.<sup>65</sup> A lot of new approaches are then developed

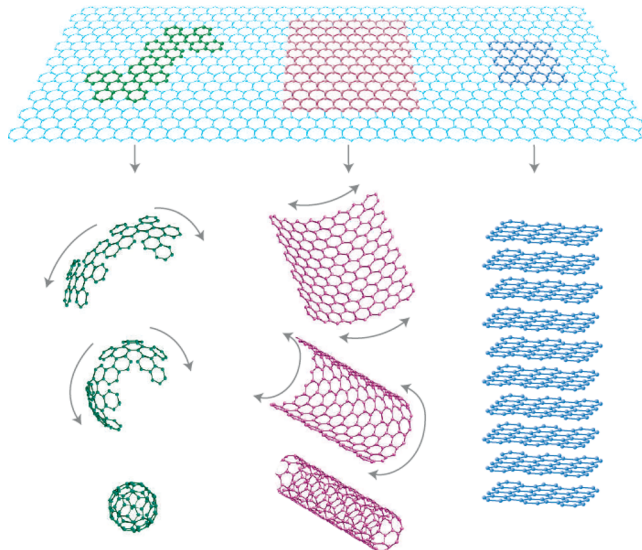


**Figure 6.** Graphene is the mother of all graphitic forms including 0D fullerene, 1D SWCNT, and 3D graphite. Reproduced with permission from ref 66. Copyright Macmillan Publishers Ltd. (2007).

mainly through chemical reactions. One, it is epitaxially grown on electrically insulating surfaces such as SiC.<sup>69,70</sup> Two, hydrocarbons are used to synthesize graphene on metal substrates like Ni and Cu. Few-layer graphene sheets were formed on Ni substrates,<sup>71,72</sup> while single-layer graphene sheets had been produced on Cu substrates.<sup>73,74</sup> Third, graphene oxide sheets were prepared by exfoliation of graphite under acid oxidation, followed by reduction.<sup>75</sup> Although a great quantity of graphene can be obtained to meet large-scale applications, the quality is relatively lower due to the damage of graphene during the oxidation and reduction. Finally, graphene nanoribbon may be also synthesized by unzipping the CNTs.<sup>76</sup>

**2.3.3. Property.** Similar to CNTs, graphene has been widely explored for distinguished mechanical, electronic, and thermal properties. The tensile strength and Young's modulus are as high as 125 and  $\sim$ 1100 GPa, respectively, enabling potential applications for ultrastrong materials and composite materials.<sup>77</sup> The electrical conductivity and charge mobility achieve  $1 \times 10^8$  S/m and  $2 \times 10^5$  cm<sup>2</sup>/(V s), respectively, so they can be widely used for various electronic devices.<sup>78</sup> The high specific surface area (e.g., 2630 m<sup>2</sup>/g) is particularly useful for energy storage materials including lithium ion batteries and supercapacitors.<sup>79</sup> A high thermal conductivity of  $\sim$ 5000 W/mK is also necessary for a good stability in the use of both energy conversion and storage.<sup>80</sup>

**2.3.4. Preparation of Graphene Fibers.** A wet spinning method is generally used to prepare graphene fibers based on graphene oxide (GO) dispersions. GO lyotropic nematic liquid crystals are first injected into a coagulation bath to form continuous fibers.<sup>81</sup> More aligned fibers can be prepared by use of a drawing tension during the collecting process. The diameters of GO fibers depend on the concentration of graphene oxide solution, injecting speed, collecting speed, and diameter of syringe needle. Subsequent chemical reduction of GO fibers in HI solution or hydrazine hydrate produces the desired graphene fibers. After reduction, the interlayer distances are decreased to 0.37 nm, close to that in graphite (0.34 nm). These graphene fibers exhibit a tensile strength of 250 MPa and electrical conductivity of  $\sim 2 \times 10^4$  S/m.

However, the surface morphologies of graphene fibers were not smooth and displayed a noncircular cross section (Figure 7). The cross-sectional shape of wet-spun fibers is closely

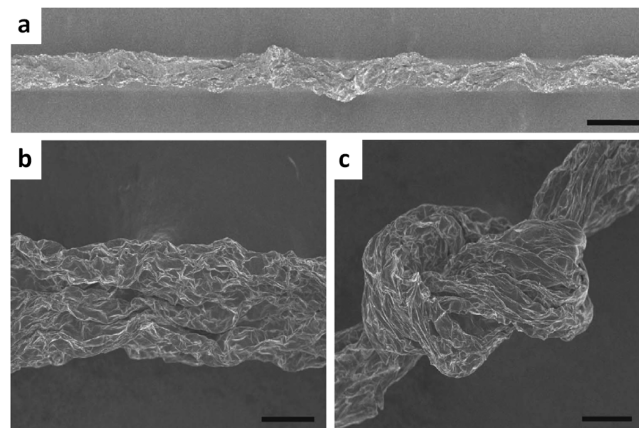


**Figure 7.** SEM images of graphene fibers. Scale bars, 50  $\mu$ m. Reproduced with permission from ref 81. Copyright Macmillan Publishers Ltd. (2011).

associated with the choice of coagulation conditions, so this problem could be solved by selecting an appropriate solvent for GO dispersion and matching coagulation bath.<sup>60</sup> It is also effective to make graphene fibers with a circular cross section by coating a GO film, followed by a scrolling process.<sup>82</sup> Compared with the wet spinning, this scrolling method exhibits several advantages. For instance, the toughness has been found to be much increased with a smooth surface and high ductility. The scrolling process was carried out in a dry state and could be used to easily prepare multifunctional GO nanocomposite fibers.

Graphene fibers can be also prepared by baking a GO aqueous suspension in a glass tube. The aqueous GO suspension is injected into the glass pipeline and then sealed at the two ends, followed by a baking process. The pipe geometry determines the fiber shape. The as-prepared graphene fiber typically showed a porous network structure, which allowed for the effective incorporation of guest components for composite fibers.<sup>83</sup>

Besides modified Hummer's methods, there are also other approaches to make graphene at a large scale based on the solution process, e.g., graphene nanoribbons obtained by unzipping CNTs. Carretero et al. present a scalable method for fabricating long and narrow graphene nanoribbons that can be assembled into aligned continuous fibers with excellent electronic and mechanical properties. They are achieved by chemically unzipping an aligned MWCNT sheet, followed by a thermal reduction of the oxidized GO. Polarized infrared spectra verified a high degree of alignment in the graphene nanoribbon before and after the reduction.<sup>84</sup>

#### 2.4. Mesoporous Carbon

Mesopores are identified as a narrow pore size range of 2–50 nm. Mesoporous materials were first reported in 1992, when the researchers from Mobil discovered a novel family of M41S.<sup>85</sup> Significant interests have been attracted to these novel nanostructured carbon materials since then due to a high surface area, tunable pore size, diversified pore shape, and controllable pore dispersibility. In 1999, a highly ordered mesoporous carbon (OMC) was reported by Ryoo et al.

through a negative replication of mesoporous silica.<sup>86</sup> The highly ordered and tunable mesoporous structure and high specific surface area make it a good candidate for various applications such as electrochemical sensors, catalyst supports, adsorbents and fuel cells. Further efforts on functionalizing the OMC by introducing the other components to create carbon-based composites are made to improve the material performance in application.

**2.4.1. Structure.** OMC is generally produced by a template method, and a wide variety of shapes and morphologies including single crystals,<sup>87</sup> monoliths,<sup>88</sup> fibers,<sup>88</sup> nanospheres,<sup>89</sup> vesicles,<sup>90</sup> and films<sup>91</sup> are available. The OMC is also well recognized by a long-range structural order made of mesoporous channels that may be arranged in hexagonal, cubic, lamellar, or wormlike mesostructures, enabling high specific surface areas.<sup>92</sup>

The first OMC synthesized by Ryoo et al., denoted as CMK-1, is a reversal of the MCM-48 silica template with an  $Ia3d$  symmetry.<sup>86</sup> It exhibits a porous structure consisting of two disconnected interwoven three-dimensional pores (Figure 8).

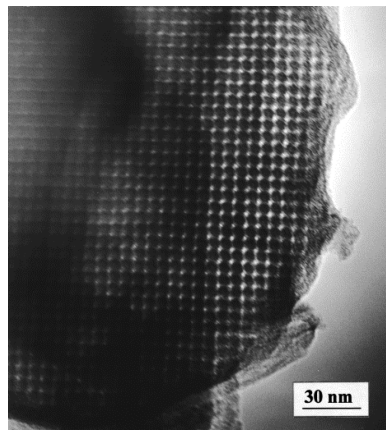


**Figure 8.** Transmission electron microscopy image of the ordered mesoporous carbon, CMK-1, synthesized by using a mesoporous silica molecular sieve MCM-48 as the template. Reproduced with permission from ref 86. Copyright American Chemical Society (1999).

CMK-1 displays a high nitrogen Brunauer–Emmett–Teller (BET) specific surface area ( $1500\text{--}1800\text{ m}^2/\text{g}$ ) and a large total pore volume ( $0.9\text{--}1.2\text{ cm}^3/\text{g}$ ) with a uniform pore size of appropriately 3 nm.<sup>86,93</sup> The adsorption capacity and specific surface area of CMK-1 are even larger than those of the MCM-48, indicating that the OMC is not a simply negative replica from the silica template. A structure transformation should occur during the removing process of silica framework.<sup>92</sup>

The ordered structures can be easily controlled by varying the mesoporous silica templates. For one example, the  $Ia3d$  symmetric MCM-48 and FDU-5 silica templates resulted in  $I41a$  symmetric carbon and cubic  $Ia3d$  symmetric carbon, respectively. For another example, SBA-15 templates with  $Pm3n$  and  $p6mm$  structures produced CMK-2 carbon with a cubic  $Pm3n$  symmetry and CMK-3 and CMK-5 carbon with a 2D hexagonal  $p6mm$  symmetry, respectively.<sup>94</sup> The different types of mesoporous structures are key to the application of the OMC.

**2.4.2. Synthesis.** Both hard and soft templates can be used to synthesize the OMC materials. The cubic mesoporous silica MCM-48 was first used by Ryoo et al.<sup>86</sup> as the hard template to synthesize the OMC. Briefly, a carbon source solution was

impregnated into the mesoporous silica template, followed by heating to a temperature of around  $800\text{ }^\circ\text{C}$  for carbonization. The hydrofluoric acid or sodium hydroxide solution was finally used to remove the silica to obtain the desired OMC. Besides MCM-48, many other mesoporous silicas such as SBA series,<sup>95,96</sup> M41S family,<sup>97</sup> MSU-H<sup>98</sup> and hexagonal mesoporous silicas<sup>99</sup> are also developed as hard templates. Recently colloid silica particles and silica gels were explored as hard templates,<sup>100</sup> but they need time-consuming steps with a low efficiency during the preparation. Furfuryl alcohol, sucrose, naphthalene, mesophase pitch, acetylene, polyacrylonitrile and phenolic resin are generally used as carbon sources. A carbonization of mesoporous phenyl-bridged organosilica/surfactant materials may also produce carbon nanomaterials without the use of extra carbon precursors.<sup>101</sup>

A soft template is developed through a self-assembly process with amphiphilic surfactant block copolymers as both templates and carbon precursors.<sup>102–104</sup> First, phenolic resin and block copolymer surfactant are assembled into three-dimensional ordered mesostructures. Second, the surfactant is removed to synthesize mesoporous polymer materials. Third, the carbonization of polymers leads to the formation of the mesoporous carbon. The synthesis by soft templates is basically derived from the hydrogen-bonding interactions between templates and precursors, which proves an efficient route to synthesize OMC materials.<sup>105</sup> Compared with the hard templates above, a soft template is also low-cost, convenient, and suitable for a large-scale production; the as-synthesized carbon nanomaterials can be more accurately tuned and are mechanically stable due to the continuous framework structure. However, the soft templates typically showed a minimal pore size of 3 nm, so they were also combined with the other templates such as AAO,<sup>106</sup> silica inverse opal,<sup>107</sup> inorganic nanofibers,<sup>108</sup> and bioceramics<sup>25</sup> to produce various hierarchical structures. What's more, a lot of interests are recently attracted to make functionalized and modified OMC materials, i.e., graphitized OMC,<sup>109</sup> N-doped OMC,<sup>110</sup> and BN-doped OMC,<sup>111</sup> which have been described by the other review.<sup>112</sup>

**2.4.3. Property.** OMC is a promising candidate for energy storage due to a 3D interconnected mesoporous structure. Compared with the conventional activated carbon, OMC displays higher surface areas up to  $2910\text{ m}^2/\text{g}$  with tunable pore sizes<sup>113</sup> and better mass transfer efficiencies. The soft template provides an effective platform to introduce guest molecules in the pore and/or incorporate other moieties in the pore wall. Some reports also suggested that the electron transfer resistance of the OMC was lower than that of the CNT,<sup>91</sup> so the OMC can serve as a good electron pathway between the electrode and electrolyte. However, it would be complicated in the practical applications and may be affected by many parameters, e.g., properties of electrolytes and sizes of solvent molecules, which will be discussed later.

## 2.5. Summary

The evolution of carbon materials has grown from simply carbonizing cellulosic biomass or utilizing coal precursors to synthesizing precisely controlled nanomaterials with tunable dimensions, pore structures and sizes, and further to doping other elements or forming hybrids. A lot of novel properties have been discovered from new structures to doped elements. However, the preparations of high-quality carbon nanomaterials still require exhausting and expensive synthetic steps, making them far from ready for commercialization although the

synthesis at a lab scale is well developed. The future study of carbon nanomaterials requires the development of more efficient and environmentally nontoxic methods with lower costs.

### 3. APPLICATION IN ENERGY CONVERSION

The development of renewable and clean energy represents a mainstream direction to solve the global energy crisis in the world. The use of solar energy has been widely recognized as a general and efficient solution. Solar cell technologies that convert solar energy into electric energy are mostly explored with the potential to be safe, green, and low-cost. However, silicon-based solar cells that currently dominate the commercial market need strict and complex fabrications with high costs. Alternately, increasing interests are attracted to develop new types of solar cells such as DSSCs, PSCs, and schottky solar cells (SSCs) that may be fabricated by low-cost solution processes. Carbon nanomaterials including fullerene, CNT, and graphene have been widely studied as promising active and electrode materials in these new types of solar cells. For instance, fullerene and its derivatives are electron acceptors in PSCs, while CNT and graphene demonstrate high performances as counter electrode materials in DSSCs and hole transfer layers in SSCs.

#### 3.1. Transparent Conducting Electrode

Unlike traditional silicon-based solar cells, new types of solar cells require at least one transparent electrode with high electrical conductivity. Transparent conducting (TC) electrodes such as indium tin oxide (ITO) and fluorine-doped tin oxide (FTO) have been commonly used as the transparent substrates in DSSCs and PSCs. However, both ITO and FTO need complex fabrications and are fragile and expensive, which limit a large-scale application in the future.<sup>114,115</sup> In particular, they cannot satisfy the requirements of flexible devices that are highly desired in the next-generation electronics. To this end, the above carbon nanomaterials can be made flexible and exhibit high optical transmittances, electrical conductivities, and mechanical strength. Therefore, they have been widely studied as TC electrodes to replace traditional ones.<sup>2,116,117</sup>

**3.1.1. Carbon Nanotube.** CNTs have been widely studied for transparent conductive electrodes (Table 1).<sup>2</sup> There are two main structures for CNT-based flexible transparent electrodes, i.e., networked CNT buckypapers and aligned CNT films. Buckypapers are generally prepared by filtrating CNT dispersions with filtering membranes,<sup>118</sup> and they exhibit

electrical conductivities at the order of  $10^5$  S/m.<sup>119</sup> They are affected by several factors including defects, lengths, and graphitization degrees of CNTs and thicknesses and porosities of CNT films. For instance, the conductivities can be enhanced by increasing the thickness and decreasing the porosity of the CNT film. However, the optical transparencies would be decreased, which may limit their applications for transparent electrodes. Therefore, a balance among several parameters has to be considered on the basis of specific systems.

To prepare CNT buckypapers, they are first dispersed in solvents mainly including *N*-methylpyrrolidone (NMP), *N,N*-dimethylformamide (DMF), and 3-aminopropyltriethoxysilanized  $\gamma$ -butyrolactone.<sup>120–124</sup> Some surfactants such as sodium dodecyl sulfate (SDS), sodianum dodecyl benzenesulfonate (SDBS), and water-soluble perylene derivatives are also widely used to improve the dispersion of CNTs in water.<sup>125</sup> However, the as-prepared buckypapers are typically brittle. To this end, CNTs can be further functionalized and then chemically cross-linked through nitrene reactions;<sup>126</sup> polymers may be also infiltrated into the pores of CNT buckypapers to increase their flexibility and mechanical strengths. Poly(vinyl alcohol) (PVA), poly(vinylpyrrolidone), and polystyrene are widely introduced to both SWCNT and MWCNT buckypapers and served as binding agents. The Young's modulus, tensile strength, and toughness had been all improved.<sup>127–130</sup> However, the electrical properties are decreased with the introduction and increase of polymers. Therefore, an optimal polymer content has been explored to reach excellent comprehensive mechanical and electrical properties, e.g., polymer weight percentage of 30% for oxidized CNT/PVA composites.<sup>129</sup> For the convenience in handling the CNT buckypapers for flexible electronic devices, the CNT dispersions are often deposited onto flexible polymer substrates such as poly(ethylene terephthalate) (PET), poly(methyl-methacrylate) (PMMA), and poly(dimethylsiloxane) (PDMS) through a vacuum filtration or transfer-printing process.<sup>131</sup>

Beyond the vacuum-assisted filtration method, spray coating, dip coating, and spin coating are also used to prepare thin CNT films.<sup>132–135</sup> For instance, CNT dispersions (often called inks) are spray-coated onto the desired substrates that generally need to be heated to aid drying of solvents. To improve the uniformity of the resulting CNT film, a modified ultrasonic spraying process had been developed to prevent agglomeration of CNTs.<sup>133</sup> The prepared CNT film exhibited a conductivity of  $150 \Omega/\square$  with an optical transmittance of 78%, compared with  $4500 \Omega/\square$  at a similar transmittance without sonication.

Through a PEDOT passivation and  $\text{SOCl}_2$  doping, the resulting thin SWCNT films showed a higher surface smoothness and lower sheet resistance,<sup>136</sup> e.g., sheet resistance and transparency of  $160 \Omega/\square$  and 87%, respectively. The decreased sheet resistance after  $\text{SOCl}_2$  treatment was produced by a *p*-type doping of the pristine SWCNTs.<sup>137</sup> Acid treatment represents another effective method to decrease the sheet resistance by combining doping and removing the residual surfactant, e.g.,  $40 \Omega/\square$  with transmittance of 70% (550 nm) and  $70 \Omega/\square$  with transmittance of 80% (550 nm).<sup>119,138</sup> Besides, conductive metal nanomaterials such as gold nanoparticles can be also incorporated to improve the conductivities of CNT buckypapers even at low contents.<sup>139</sup>

Aligned CNT films have recently attracted increasing attention as the excellent electrical and mechanical properties of individual CNTs are effectively extended from the nanoscale to macroscopic level through the aligned structure (Figure

Table 1. Comparison of Sheet Resistance of CNT-Based Transparent Electrodes

| material (method)                          | sheet resistance ( $\Omega \square^{-1}$ ) | transmittance    | ref |
|--|--|------------------|-----|
| ITO  | 8  | 90%              |     |
| CNTs-PEDOT                                 | 160  | 87% (30–1000 nm) | 136 |
| single-walled CNTs buckypaper (filtration) | 40   | 70% (550 nm)     | 119 |
| single-walled CNTs buckypaper (filtration) | 70   | 80% (550 nm)     | 119 |
| CNT film on PET (filtration)               | 200  | 80% (550 nm)     | 131 |
| CNT film (ultrasonic spray coating)        | 150  | 78%              | 133 |
| CNT-gold nanoparticles                     |  |                  | 139 |

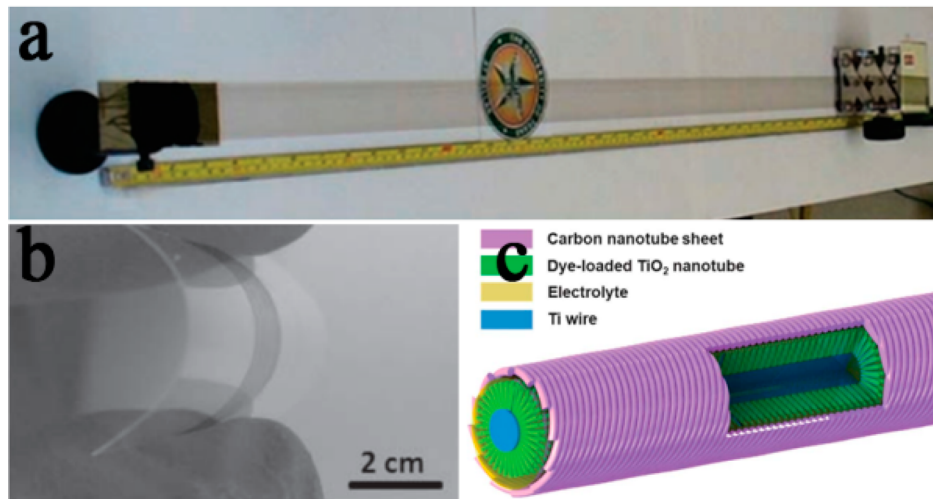


**Figure 9.** (a) Photograph of a CNT sheet drawn from spinnable CNT array. Reproduced with permission from ref 140. Copyright AAAS (2005). (b) Photograph of flexible CNT sheet on PET film. Reproduced with permission from ref 141. Copyright John Wiley and Sons (2011). (c) Schematic illustration to the structure of the fiber-shaped DSSC using CNT sheet as transparent electrode. Reproduced with permission from ref 145. Copyright Royal Society of Chemistry (2013).

9).<sup>140–145</sup> The aligned CNT sheets can be directly drawn from spinnable CNT arrays synthesized by CVD with conductivities of  $10^4$ – $10^5$  S/m along the CNT-aligned direction. A layer of CNT sheet with thickness of 20 nm was highly transparent with transmittance of 90%.<sup>141</sup> Paving such aligned CNT sheets onto prestretched PDMS substrates may further produce stretchable electrodes for various elastic devices.<sup>146</sup>

In summary, to obtain a high-performance transparent conductive electrode from CNTs, there remains a dilemma in selecting CNTs. Shorter CNTs can be more uniformly dispersed but result in high contact resistances among them in the resulting electrode. In contrast, longer CNTs decrease their contact resistances but are more difficult to be dispersed. Some chemical modifications are therefore made for CNTs to improve their dispersions in solvent. However, the electrical conductivities of the modified CNTs have been largely decreased. Under this situation, DWCNTs are proposed to prepare transparent conducting electrodes because the outer walls can be modified to improve their dispersion while the inner tubes provide effective pathways for charges. The MWCNT-based films generally show higher sheet resistances under the same transmittance due to much lower optical transparencies even individual MWCNTs exhibit higher electrical conductivities.

**3.1.2. Graphene.** Graphene, with a high crystal structure and atomic thickness, exhibits high electrical conductivity and transmittance (e.g., 97.7% for a single-layer graphene sheet).<sup>147</sup> Although graphene was discovered just ten years ago, many methods have been developed to prepare graphene-based transparent electrodes. After a solution process by reducing graphene oxide (GO) sheets, large-area ultrathin graphene films with a sheet resistance of  $2000 \Omega/\square$  and transmittance of 85% had been achieved.<sup>148</sup> A CVD method can greatly enhance the intrinsic quality of graphene and thus improve the conductivity to  $770 \Omega/\square$  and transmittance to 90%.<sup>71,149</sup> The prepared thin, transparent graphene films can be easily transferred to both glass and flexible polymer substrates (Figures 10a,b).<sup>148</sup> They can be also prepared on stretchable PDMS for elastic electrodes.<sup>150</sup>

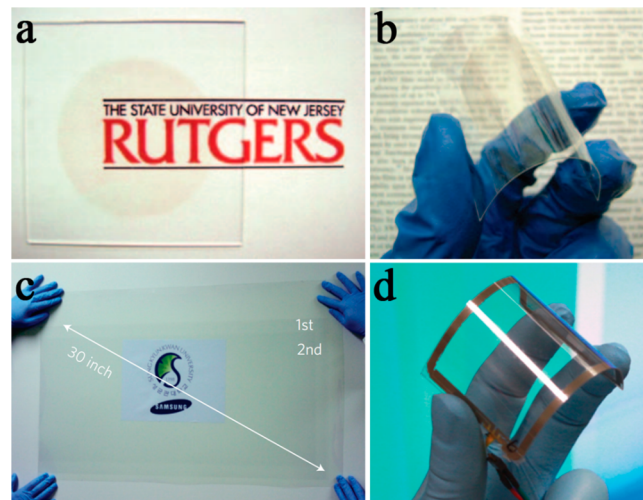


**Figure 10.** Photographs of solution-processed flexible and transparent GO films. (a) On glass. (b) On flexible substrate. Reproduced with permission from ref 148. Copyright Macmillan Publishers Ltd. (2008). (c) A large-area graphene film on a 35-in. PET sheet. (d) A graphene/PET touch panel. Reproduced with permission from ref 73. Copyright Macmillan Publishers Ltd. (2010).

A lot of efforts have been made to tune and improve the electronic performance of the graphene-based electrodes. There are two general methods to enhance their electrical conductivities, i.e., synthesis of large-area graphene sheets by CVD and doping with the other component to increase the charge carrier number.<sup>71,113,149,151</sup> The CVD and doping methods can be also combined to reach even higher conductivities.<sup>73,152</sup> Bare monolayer graphene films were first synthesized on flexible copper substrates through CVD and then chemically p-doped, and the resulting modified graphene films exhibited a sheet resistance of  $125 \Omega/\square$  and transmittance of 97.4%. A doped four-layer film through a layer-by-layer stacking decreased the sheet resistance to  $30 \Omega/\square$  with a comparative transmittance of 90% (Figures 11c,d).

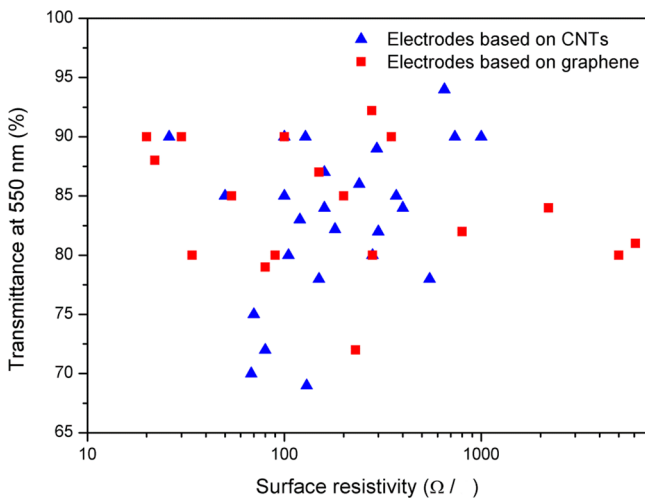


**Figure 11.** Relationship between optical transmittance and surface resistivity.

To summarize, high-performance CNT- and graphene-based transparent conductive electrodes have been achieved in recent years. As demonstrated in Figure 11, these electrodes generally exhibit low sheet resistances of 60–200  $\Omega/\square$  and high transmittances of 80%–90%, which already can be used for many applications such as touch screens for cell phones or televisions. However, they still cannot satisfy the solar cells that require lower resistances and higher transmittances in use.

### 3.2. Polymer Solar Cells

A delocalized  $\pi$  electron system has been widely studied to absorb sunlight to create and transport photogenerated charge carriers. The organic photovoltaic (OPV) devices based on the conjugated organic materials with a donor–acceptor bilayer planar structure was first realized until 1979 with a power conversion efficiency (PCE) of around 1%. A breakthrough was made by using  $C_{60}$  fullerene and its derivatives (such as [6,6]-phenyl- $C_{61}$ -butyric acid methyl ester<sup>153</sup>) to replace the n-type molecules in OPV devices. After the photoinduced phenomenon of conjugated polymer and  $C_{60}$  was discovered by Sariciftci in 1992,<sup>154</sup> the first bilayer planar PSC was realized in 1993.<sup>155</sup>

However, the bilayer junction structure shows a severe limitation of low surface area at the donor–acceptor interface, thus requiring a long carrier lifetime to ensure that the electrons and holes reach their respective electrodes. This problem may be solved by designing a bulk heterojunction structure where donor and acceptor materials are mixed as the active layer. This concept was first demonstrated by Hiramoto et al. through a coevaporation of donor and acceptor materials under high-vacuum conditions.<sup>156</sup> The first efficient bulk heterojunction PSCs were independently realized by Heeger and Friend in polymer–fullerene and polymer–polymer blends in 1995, respectively.<sup>157,158</sup> Polymer–fullerene systems currently dominate the field of high-efficiency PSCs, and the maximal PCE currently reaches 10.6%.<sup>157</sup>

The working mechanism of the PSC involves the photoexcitation of the donor polymer by the absorption of photons to generate excitons. The electron–hole pair, the exciton, diffuses to the donor–acceptor interface where exciton dissociation occurs via an electron-transfer process. The fully separated free charge carriers transport to the respective electrodes in the opposite direction with the aid of the internal

electric field, which in turn generates the photocurrent and photovoltage.<sup>159</sup> Compared with a bilayer structure, the heterojunction structure with a higher interface between the donor and acceptor enhance the charge separation and transport, resulting in a high PCE. The energy diagram of a polymer–fullerene-based PSC is illustrated in Figure 12.<sup>160</sup>

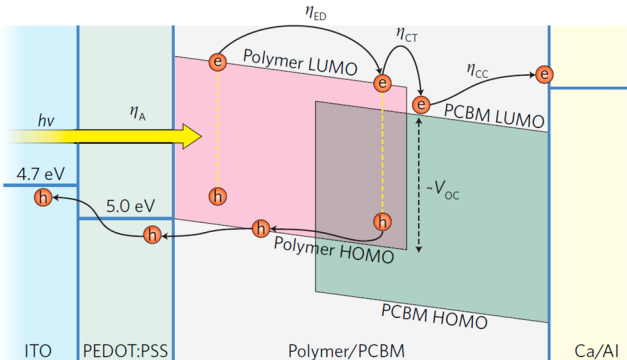


**Figure 12.** Working mechanism of a PSC. Reproduced with permission from ref 160. Copyright Macmillan Publishers (2012).

PSCs are typically fabricated by solution processes with several promising advantages compared with the silicon-based technologies, e.g., abundant in photoactive materials with low costs. PSCs are also thin, flexible, and lightweight. There are already many review articles summarizing the materials, fabrications, properties and applications of PSCs, so the use of carbon nanostructured materials for efficient PSCs that have been extensively investigated in recent years is emphasized here. These carbon nanomaterials including fullerene, CNT, and graphene can be either coated into films to replace conventional electrode materials such as ITO or incorporated into active layers to improve charge separation and transport. Therefore, they may be divided into three classifications as transfer layers, additives of the donor–acceptor layer and transparent conductive electrode during use.

**3.2.1. Conducting Electrode.** Transparent electrodes such as ITO are generally used for efficient PSCs, but they are expensive and fragile, so it is important to replace ITO with new materials particularly for flexible photovoltaic devices. A wide variety of routes have been developed to prepare transparent and flexible electrodes based on carbon nanomaterials including solution casting, layer-by-layer assembly, swelling, spin coating, spray coating, and dry transferring.

The sheet resistances of the CNT-based transparent electrodes are compared in Table 2. SWCNT electrodes for hole collection showed even higher photovoltaic performances than ITO in PSCs.<sup>161</sup> However, there remains a common and critical challenge for the use of carbon nanomaterials as electrodes, i.e., it is difficult to simultaneously achieve high

**Table 2. Sheet Resistance of Transparent Conductive Electrodes Based on Cnts**

| material                               | sheet resistance ( $\Omega \square^{-1}$ ) | transmittance     | ref |
|--|--|-------------------|-----|
| purified SWCNT                         | 282  | 80% (250–850 nm)  | 161 |
| HNO <sub>3</sub> treatment of CNT film | 86   | 70% (550 nm)      | 164 |
| GO/CNT film                            | 20   | 95% (400–1000 nm) | 165 |
| CNT/polyaniline                        | 300  | 80–90% (550 nm)   | 166 |

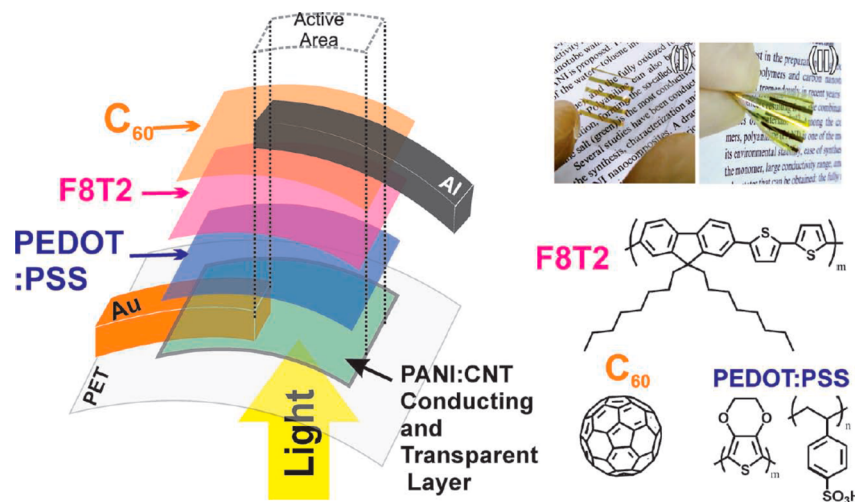


**Figure 13.** Structure of the PSC based on a PET/PANI:CNT film and organic layers. Reproduced with permission from ref 166. Copyright John Wiley and Sons (2012).

optical transmittance and electrical conductivity. In other words, the increase in transmittance will lead to a decrease in conductivity, and vice versa. Therefore, a balance between the transmittance and conductivity has been widely investigated for CNT electrodes.<sup>162–164</sup>

The sheet resistance of the CNT films can be decreased by acid treating. Feng et al. found that the HNO<sub>3</sub> treatment reduced the resistance dramatically while slightly sacrificing the transmittance.<sup>164</sup> Kim mixed SWCNTs and GO with a mass ratio of 1/0.2 to significantly improve the  $J_{SC}$  of the resulting PSCs due to the reduced vertical resistance and improved hole extraction from the polymer.<sup>165</sup> Rodrigo et al. synthesized transparent CNT electrodes by incorporation of PANI for high performance PSCs (Figure 13).<sup>166</sup>

For both randomly dispersed CNT buckypapers and aligned CNT sheets, they share a porous structure among CNTs, which is unfavorable for hole collection. Graphene film can overcome this problem due to the two-dimensional continuous structure. The graphene-based electrodes also exhibited much higher flexibility than ITO-coated electrodes on polymer substrates. The widely studied graphene-based transparent electrodes are compared at Table 3.

OPVs can be easily fabricated from highly reduced GO anodes through a solution process.<sup>167</sup> The work functions of such solution-processable graphene/CNT hybrid electrodes can be further tuned from 5.1 to 3.4 eV, depending on the

doping alkali carbonate salt. The graphene-based electrode with a lower work function as the cathode in inverted-architecture PSC displayed a high capability in collecting electrons.<sup>168</sup> The laminated graphene electrode synthesized by CVD was used to replace the top metal electrode in fabricating a semitransparent inverted PSC.<sup>169</sup> Through a modified roll-to-roll production method to transfer the graphene film to form a multilayered structure as a single layer of graphene does not have sufficiently high sheet conductivity, Lee et al. found that the resulting PSC with ten graphene layers exhibited the best performance.

Similarly, ultraviolet-ozone treated gold-modified multilayered graphene films had been also widely explored as transparent anodes.<sup>170</sup> The gold layer was used to further improve the interfacial contact to enhance fill factor and PCE. Graphene-based films could be also used as bottom transparent electrodes.<sup>171</sup>

Although a continuous graphene film exhibits a high optical transmittance, the conductivity is relatively lower compared with ITO. A lot of efforts are then made to decrease the sheet resistances of graphene electrodes. Individual graphene films were first treated by HNO<sub>3</sub> solution and then stacked into multilayered electrodes (Figure 14).<sup>172</sup> A modified graphene/tetracyanoquinodimethane/graphene multilayered film was also found to show a low sheet resistance.<sup>173</sup>

Theoretically, highly doped graphene films may show both higher transparency and conductance than ITO.<sup>73</sup> A single-layered graphene film displayed much increased conductance by chemical doping,<sup>174</sup> e.g., the conductivity was increased by above 400% after doped with Au nanoparticles and PEDOT:PSS. As an application demonstration, single-layered graphene sheets had been further used as counter electrodes for fiber-shaped PSCs,<sup>175</sup> and the PCE reached 2.53% under standard illumination. The PCE was further improved to 4.36% with assistance of a diffusive reflector.

For the conducting electrodes based on carbon nanomaterials, they are still incomparable with the ITO glass in the overall performance. A lot of efforts are made to enhance them through optimization in structure, functionalization on the surface, and compositing with metals. On the other hand, carbon nanomaterial-based electrodes have already served as back electrodes for PSCs without the requirement in high transparency.

**Table 3. Sheet Resistance of Transparent Conductive Electrodes Based on Graphene**

| material                                | sheet resistance ( $\Omega \square^{-1}$ ) | transmittance     | ref |
|---|--|-------------------|-----|
| Top laminated graphene film             | 100  | 80% (400–1000 nm) | 167 |
| RGO-SWCNT film                          | 331  | 65.5% (550 nm)    | 168 |
| Graphene film                           | 230  | 72% (400–1000 nm) | 169 |
| Graphene-Au film                        | 2–3 k $\Omega \square^{-1}$                | unavailable       | 170 |
| Acid-doped graphene film                | 80   | 90% (550 nm)      | 171 |
| HNO <sub>3</sub> -treated graphene film | 30   | 90% (400–1000 nm) | 172 |
| Stacked graphene/TCNQ film              | 182  | 88% (550 nm)      | 173 |

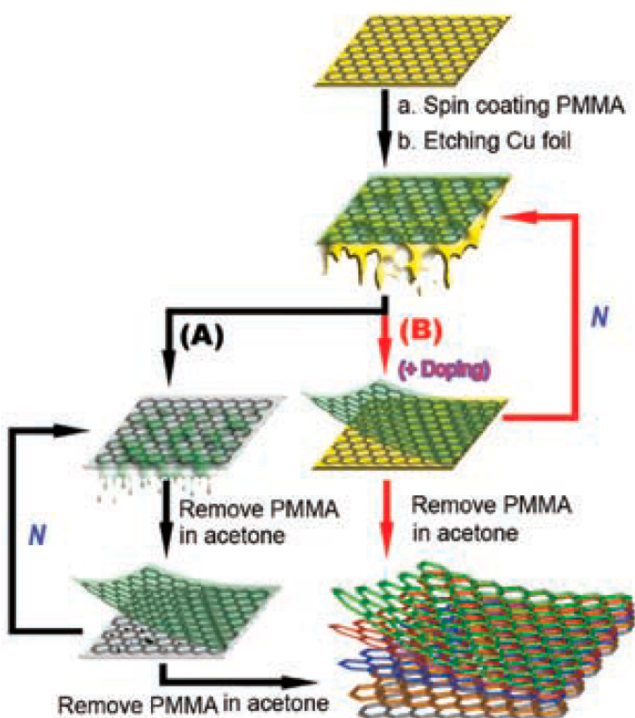


**Figure 14.** Schematic illustration of preparing multilayer graphene film by normal wet transfer (A) and direct coupling layer-by-layer assembly (B) ( $N = 0, 1, 2, 3, \dots$ ). Reproduced with permission from ref 172. Copyright John Wiley and Sons (2011).

**3.2.2. Hole/Electron Transport Layer.** SWCNT films were used as hole transfer layers to achieve high photovoltaic performances.<sup>176</sup> The SWCNT network had been compared for PCEs at different locations in PSCs. When the SWCNT layer was deposited between the active material and PEDOT:PSS layer, the PSC exhibited the highest PCE of 4.9%. The SWCNTs can mostly enhance hole transports by providing conducting pathways to the electrode.<sup>177</sup>

CNTs had been also directly added to the active layer to form networks to create effective hole conduction pathways with high PCEs up to 10%.<sup>178</sup> The design of nanostructured donor-phase components was also found to increase hole transports.<sup>179</sup> For instance, a core–shell CNT-polythiophene nanowire network was synthesized by electrochemically depositing polythiophene around the interconnected metallic CNTs. Figure 15a showed a typical SEM image of the metallic CNT nanowires, and the coaxial CNT-polythiophene nanowire network had been produced after deposition of polythiophene on the surfaces of CNTs (Figure 15b). PCBM can be spin-casted to infiltrate the open space of the core–shell network to form effective heterojunction structures for an efficient PSC (Figure 15c). When the SWCNTs were added to both active and hole transport layers to enhance the exciton dissociation and hole transfer, the PCE was further increased by 26%.<sup>180</sup>

A graphene film can also be used as the hole transfer layer to replace PEDOT:PSS in the PSC.<sup>181–184</sup> However, the GO film that serves as the hole transfer layer suffers from a low electrical conductivity, resulting in a high series resistance. In order to enhance the charge carrier transport, butylamine-modified GO sheets was found to reduce the recombination effect in the active layer,<sup>185</sup> and a PCE of 3.55% was achieved for the plasmonic PSC by incorporating Au-GO sheets into the PEDOT:PSS buffer layer.<sup>186</sup> The utilization of the GO sheet

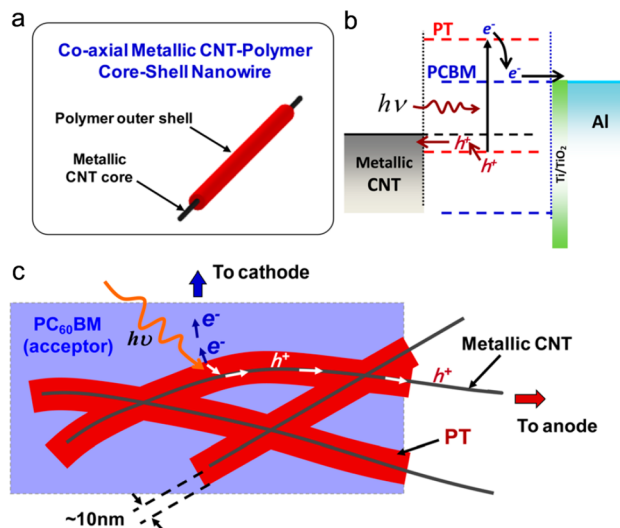


**Figure 15.** (a) Schematic illustration to a single coaxial CNT (core)-polythiophene (shell) nanowire. (b) Energy band diagram of the photovoltaic device showing the energy levels of the composing materials and transporting directions of charge carriers. (c) Schematic illustration of the physical steps in the CNT-polythiophene nanowire/PCBM heterojunction: (i) light absorption by polythiophene, (ii) exciton dissociation at polythiophene-PCBM interface, (iii) free electron diffusion in PCBM, (iv) hole diffusion through thin polythiophene shell, and (v) efficient hole transport toward the anode via the metallic CNT network. Reproduced with permission from ref 179. Copyright AIP Publishing LLC (2011).

prohibited the aggregation of Au nanoparticles and introduced the plasmonic effect without dramatically sacrificing the electrical properties.

To minimize the contact resistances and improve conductivities of the hole transfer layers for low series resistances, sulfated GO was introduced as a hole transfer layer to produce a PCE of 4.37%.<sup>187</sup> The strong acidic  $-\text{SO}_3\text{H}$  groups in the carbon basal plane of GO sheet and  $-\text{COOH}$  groups at edges enhanced the doping effect of the donor polymer (Figure 16). Recently, GO nanoribbons were discovered to possess a proper energy level alignment, high solubility, and good film-forming property, which enable a promising material for hole extraction.<sup>188</sup> Generally, such GO nanoribbons were synthesized by unzipping SWCNTs using  $\text{KMnO}_4$  as the oxidant in a concentrated  $\text{H}_2\text{SO}_4$ .

In addition, the carbon nanomaterials are also used as electron transport layer in the PSCs. The incorporation of CNTs into the active layer favors the exciton dissociation and charge transfer. It was found that photogenerated excitons on SWCNTs were dissociated at the interfaces of PCBM and P3HT.<sup>189</sup> Functionalized MWCNTs could serve as efficient compatibilizers and charge transport assisters for the photoactive layer.<sup>190,191</sup> For instance, N-doped MWCNTs were added to the polythieno[3,4-*b*]thiophene/benzodithiophene/PC<sub>71</sub>BM layer to produce a high PCE of 8.6% as they acted as both extra exciton dissociation centers and efficient charge transport channels (Figure 17).<sup>192</sup> However, if the MWCNTs were grafted with PCBM in the photoactive layer, the interaction between P3HT and PCBM-grafted MWCNT had been decreased, thus also reducing the efficiencies as hole transporters.<sup>193</sup> Note that SWCNTs can be also directly used as acceptors in PSCs, but it was theoretically predicted that they were less efficient in the charge generation for the widely

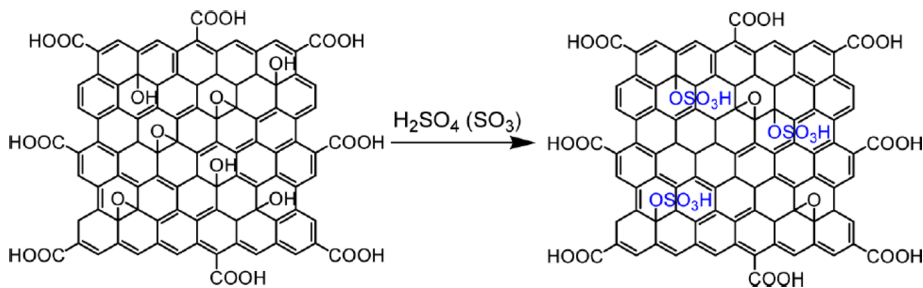


**Figure 16.** Synthetic route to GO-OSO<sub>3</sub>H. Reproduced with permission from ref 187. Copyright American Chemical Society (2013).

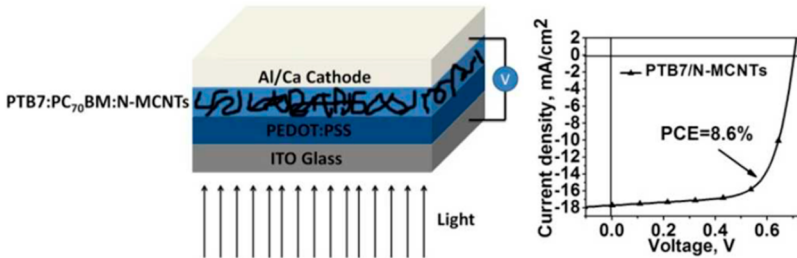


**Figure 17.** Schematic illustration to the structure and *J*–*V* characteristics of the PSC. Reproduced with permission from ref 192. Copyright American Chemical Society (2013).

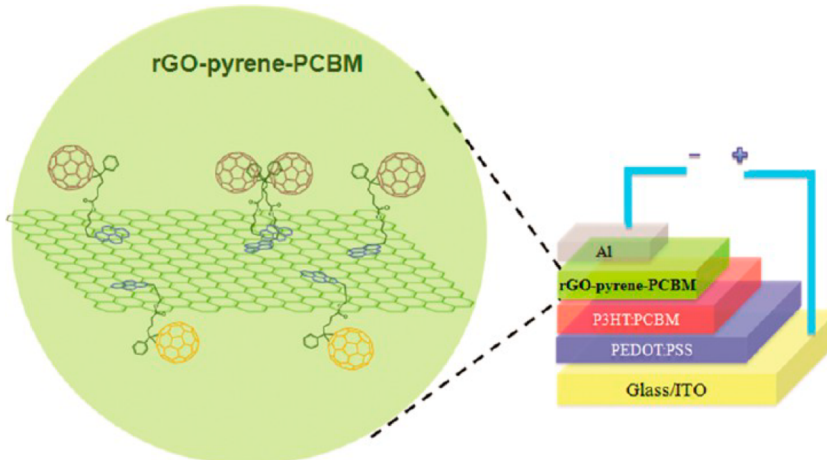


**Figure 18.** Schematic illustration to the PSC with the incorporation of rGO-pyrene-PCBM electron transfer layer. Reproduced with permission from ref 196. Copyright American Chemical Society (2013).

explored P3HT, particularly, when the SWCNTs were metallic.<sup>194</sup>

GO has been also extensively introduced to enhance the photovoltaic performance of the PSC, and it can function as both electron and hole transfer layers.<sup>195</sup> For instance, the PSC based on the ITO/GO/P3HT:PCBM/GOCs/Al structure exhibited a PCE of 3.67%. Here the bare GO served for hole extraction while the cesium-neutralized GO worked for electron extraction. Of course, graphene can be incorporated into PSCs for higher PCEs. The attachment of PCBM onto reduced GO sheets by noncovalent interactions was used as an electron extraction layer to improve the PCE to 3.89% (Figure 18).<sup>196</sup>

Besides, CNT and graphene can also be used as acceptor material in the PSCs. For example, a PSC using SWCNTs as an acceptor material was demonstrated by blending poly(3-octylthiophene) (P3OT) with 1 wt % of SWCNTs, and both  $V_{OC}$  and  $J_{SC}$  had been increased.<sup>197,198</sup> This enhancement can be ascribed to the introduction of internal polymer/nanotube

junctions within the polymer matrix. These junctions allowed excitons to be efficiently dissociated and also created continuous pathways for electron transport to the charge-collecting electrode. Later, the same lab demonstrated that an annealing treatment enhanced the film uniformity for higher PCEs.<sup>199</sup> A modification by combining the CNT into a polarized polybithiophene layer also provided the PSC with an increased PCE of 1.5%.<sup>200</sup> For the above PSC based on SWCNT and P3HT or P3OT, the P3HT was found to show a slightly higher  $J_{SC}$  while lower  $V_{OC}$  than P3OT.<sup>201</sup> A lot of efforts are also made to understand the mechanism and underlying rule in the CNT/P3HT solar cell.<sup>202–212</sup> A general and effective route to increase the PCE is to enhance the hole mobility of P3HT by increasing its nanocrystal ordering (Figure 19).<sup>203</sup>

Graphene had been also widely studied as a promising electron-accepting material in the PSC where either P3OT or P3HT could be used as the donor.<sup>204–206</sup> Figure 20 represents

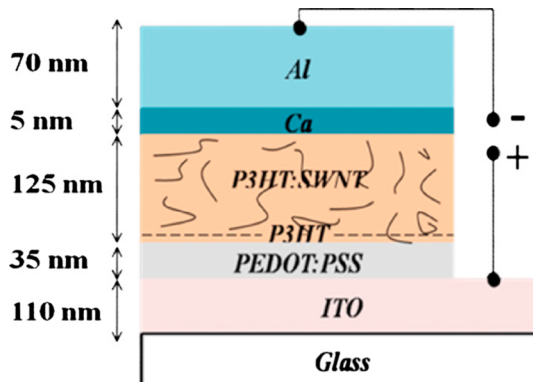


**Figure 19.** Structure of a PSC. The P3HT layer below the dotted line was mostly dissolved upon the coat of the active layer. Reproduced with permission from ref 203. Copyright AIP Publishing LLC (2010).

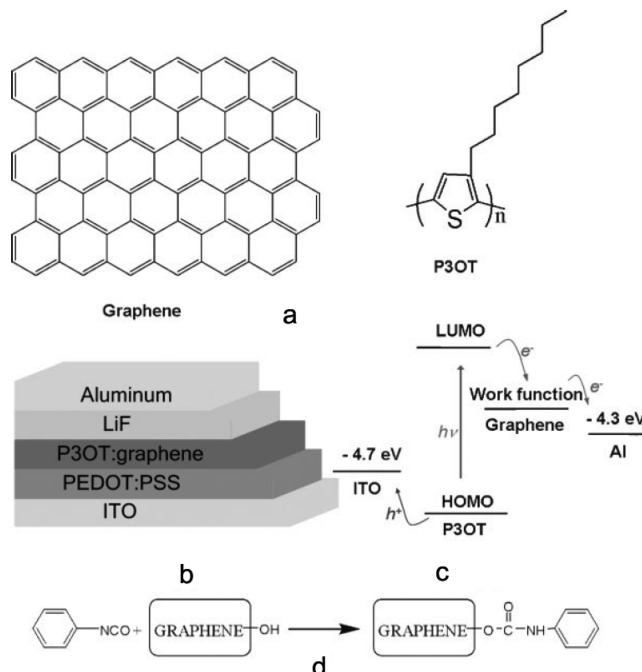


**Figure 20.** (a) Idealized chemical structures of graphene and P3OT. (b) Schematic illustration to the PSC with the P3OT/graphene thin film as the active layer. The structure was composed of ITO/PEDOT:PSS (40 nm)/P3OT:graphene (100 nm)/LiF (1 nm)/Al (70 nm) from the bottom to the top. (c) Energy level diagram of the PSC. (d) Schematic illustration to the reaction of phenyl isocyanate with GO to form isocyanatederivatized GO. Reproduced with permission from ref 204. Copyright John Wiley and Sons (2008).

the structure of a typical PSC with a P3OT/graphene thin film as the active layer.<sup>204</sup> Although a high PCE was produced by the generally used organic solvent-based process, the use of organic solvents was not favorable for the environment, which may limit the practical application of the PSC. Some attempts were then made to fabricate the PSC through an aqueous solution process, but the PCE was still too low, e.g., 0.027%, and more efforts are required to further enhance the PCE to a competitive level.<sup>207</sup>

In summary, the carbon nanomaterials like CNT and graphene can be used as both hole and electron transport layers in the PSCs due to high hole and electron mobility. However, they are relatively less used in the PSCs due to a low

selectivity in carrier transport as they exhibit a high carrier mobility for both holes and electrons, which will cause the carrier recombination during the photoelectric conversion process. It is important but remains challenging to explore their excellent electronic properties in this direction.

### 3.3. Dye-Sensitized Solar Cells

DSSCs have attracted continuous and increasing interests in both academy and industry after they were discovered by Grätzel and co-workers in 1991. They are widely recognized for many advantages including ease of fabrication, low cost, and high performance at low light intensity. The PCE of DSSC has been improved to approximately 15% in past two decades with a competitive power to the traditional Si-based technology. A typical working mechanism of DSSC is summarized in Figure 21.<sup>141</sup> Upon illumination, electrons are generated from a dye

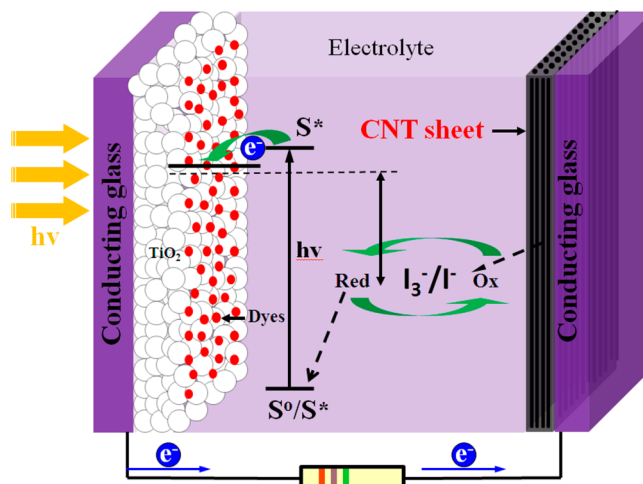


**Figure 21.** Schematic illustration of a DSSC. Reproduced with permission from ref 141. Copyright John Wiley and Sons (2011).

molecule after absorbing photons immediately, followed by being injected into the conduction band of n-type semiconductor (e.g., titanium dioxide and zinc oxide), flowing along the external circuit and being collected by the counter electrode (e.g., platinum) where  $I_3^-$  ions are reduced to  $I^-$  ions. The dye molecules are recovered to the ground state after accepting electrons from  $I^-$  ions that are reverted to  $I_3^-$  ions at the same time to complete a cycle.

**3.3.1. Counter Electrodes.** The counter electrode bears the responsibility for transporting electrons derived from the photoanode to the electrolyte where  $I_3^-$  ions are reduced to  $I^-$  ions. Traditionally, a counter electrode was prepared by depositing a thin platinum layer (thickness of 2–3 nm) on FTO glass.<sup>1,2,213</sup> Platinum has been generally used for the reduction of  $I_3^-$  ion in the  $I^-/I_3^-$  redox electrolyte system due to its remarkable electrocatalytic activity. Previously, main efforts were made to develop various methods such as thermal decomposition, electrodeposition, sputtering, and vapor deposition to prepare the platinum counter electrode.<sup>213</sup> However, as a noble metal, platinum exhibits obvious disadvantages including limited supply, high cost, and instability during use.<sup>1</sup> Alternately, based on high catalytic activities, carbon nanomaterials including carbon black, activated carbon, CNT, and graphene have been extensively studied as promising candidates as counter electrode materials to replace the conventional platinum.

Earlier, Grätzel and coauthors investigated the photovoltaic performance of carbon black counter electrodes that were prepared through a doctor-blading method.<sup>214</sup> The charge-transport resistances ( $R_{CT}$ ) of the counter electrodes could be decreased to  $0.74 \Omega \text{ cm}^2$  at a thickness of  $22.5 \mu\text{m}$  for the carbon layer, and it was even smaller than the heat-deposited platinum electrode. The resulting DSSC showed  $V_{OC}$ ,  $J_{SC}$ , and FF of  $0.79 \text{ V}$ ,  $16.8 \text{ mA/cm}^2$ , and  $0.685$ , respectively, which produced a PCE of  $9.1\%$ . Late, conducting PEDOT:PSS with high optical transmittance and catalytic activity was incorporated into carbon black to produce a composite counter electrode that enabled a PCE of  $7.01\%$ .<sup>215</sup> A promising advantage of carbon black is that it has been already produced at a large scale with low cost at industry, though the PCE is relatively lower than that based on the platinum.

Activated carbon with a higher surface area also showed a superior catalytic activity in the reduction of  $\text{I}_3^-$ ,<sup>215,216</sup> and the  $\text{I}_3^-$  can infiltrate into the internal space of activated carbon for a better catalysis. As a result, a high PCE had been achieved. Based on this strategy, it is expected that the use of nanostructured carbon materials may further improve the photovoltaic performance of the DSSC.

CNTs have been long studied as counter electrode materials in the DSSC.<sup>217–233</sup> Among them, MWCNTs are most explored to be made into electrodes by various routes such as spin coating,<sup>217</sup> spray coating,<sup>218,219</sup> electrophoretic deposition,<sup>220,221</sup> gel coating,<sup>222</sup> dry spinning,<sup>45,223,224</sup> and CVD.<sup>225</sup> For instance, Ramasamy et al. prepared MWCNT counter electrodes by a spray coating method (Figure 22a,b) and the

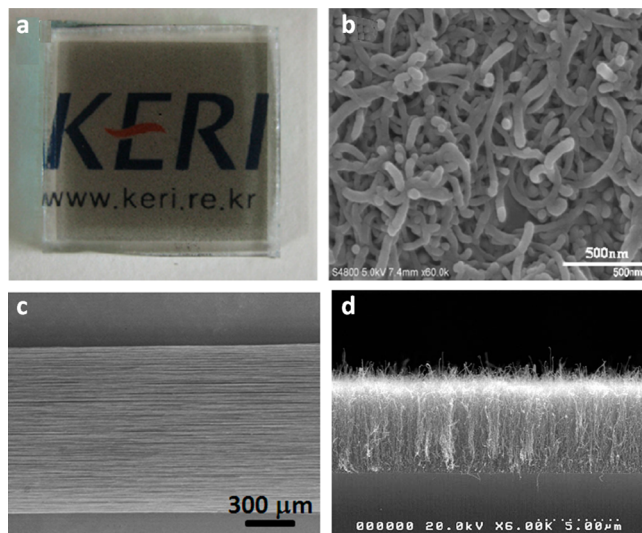


**Figure 22.** (a,b) Photograph and SEM image of MWCNT electrode with spray time of 100s, respectively. Reproduced with permission from ref 203. Copyright Elsevier (2008). (c) SEM image of an aligned MWCNT sheet electrode. Reproduced with permission from ref 223. Copyright John Wiley and Sons (2011). (d) Cross-sectional SEM image of a CNT array on soda lime glass. Reproduced with permission from ref 225. Copyright Elsevier (2010).

resulting DSSC displayed a maximal PCE of  $7.59\%$ .<sup>219</sup> However, for the previously studied MWCNT counter electrodes, the MWCNTs appeared in a network structure. As a result, the generated charges have to transport among a lot of boundaries in MWCNT networks, and the PCE was lower than the conventional platinum.

To this end, we have recently developed aligned MWCNT materials as a new family of electrodes. When the MWCNT sheet that had been dry-drawn from a spinnable MWCNT array and aligned along the drawing direction was used as a counter electrode (Figure 22c),<sup>223</sup> the derived DSSC showed a PCE of  $4.18\%$ , about  $80\%$  of the platinum counter electrode. The relative lower PCE was explained by the fact that the charges still had to transport among aligned MWCNTs from the top to the bottom in the sheet as they were parallel in the film. As an effective solution, penetrated and aligned MWCNT electrodes were obtained by rolling MWCNT arrays down to form thin films.<sup>226</sup> When they were used as counter electrodes, the resulting DSSCs typically showed  $V_{OC}$  of  $0.726 \text{ V}$ ,  $J_{SC}$  of  $17.35 \text{ mA/cm}^2$ , and FF of  $0.67$  with PCE of  $8.46\%$ . In contrast, the DSSC based on the platinum counter electrode exhibited  $V_{OC}$  of  $0.735 \text{ V}$ ,  $J_{SC}$  of  $16.66 \text{ mA/cm}^2$ , and FF of  $0.60$ , and a relatively lower PCE of  $7.32\%$  was therefore produced. The obvious improvement in the photovoltaic performance was derived from the much lower electrical resistances of individual MWCNTs than the contact resistances among MWCNTs. For the perpendicularly aligned MWCNT counter electrode, the charges transported along their axial directions. Besides, aligned MWCNT arrays had been directly grown on the conducting glass for counter electrodes to decrease the contact resistance between the MWCNT layer and conducting substrate (Figure 22d), so a higher PCE of  $10.04\%$  was observed.<sup>225</sup> Similarly, SWCNTs have been also explored as counter electrodes in DSSCs,<sup>226</sup> and the control on their structures is key to their performances. CNTs had been also widely doped with a second element such as nitrogen to enhance catalytic activity. Perpendicularly aligned nitrogen-doped MWCNT counter electrodes provided the resulting DSSCs with higher PCEs.<sup>224</sup>

Besides bare CNT materials, increasing interests have been attracted to prepare CNT-based composite or hybrid materials for effective counter electrodes.<sup>228–235</sup> For instance, CNT were mixed with a wide variety of inorganic and organic moieties such as graphene,<sup>234</sup> P3HT,<sup>235</sup> PEDOT:PSS,<sup>233</sup> TiN,<sup>229</sup> polypyrrole,<sup>232</sup> cobalt sulfide,<sup>231</sup> and tungsten sulfide<sup>228</sup> to form high-quality composite or hybrid materials. Both high electrical conductivity and electrocatalytic activity had been achieved after thermal hydrolysis of  $\text{TiOSO}_4$  on CNTs and subsequent nitridation in an ammonia atmosphere.<sup>229</sup> The resulting DSSC derived from the TiN/CNT hybrid counter electrode showed a PCE of  $5.41\%$ .

After discovery in 2004, graphene has been also widely studied for the counter electrode in DSSC. Although the graphene materials share high surface areas, the large-sized graphene sheets did not demonstrate expected high catalytic activities as counter electrodes because their edges and defects were much more effective in catalyzing the redox reaction of the  $\text{I}^-/\text{I}_3^-$  redox couple,<sup>242</sup> while much less percentages of edges were available in the large graphene sheets. As a result, the resulting DSSC fabricated from a graphene counter electrode produced a low PCE of  $3.63\%$ , much lower than the platinum-based DSSC (Figures 23a,b).<sup>236</sup>

To improve the performance, a wide variety of graphene composite and hybrid materials have been developed for counter electrodes such as PANI/graphene composite,<sup>237</sup> platinum nanoparticles/graphene hybrid,<sup>238</sup> metal nitride/graphene hybrid,<sup>239</sup> graphene/PEDOT-PSS composite,<sup>240</sup> and  $\text{MoS}_2$ -graphene nanosheet hybrid.<sup>241</sup> For instance, a PANI/graphene composite had been synthesized by *in situ* polymerization of aniline monomer in a graphene dispersion

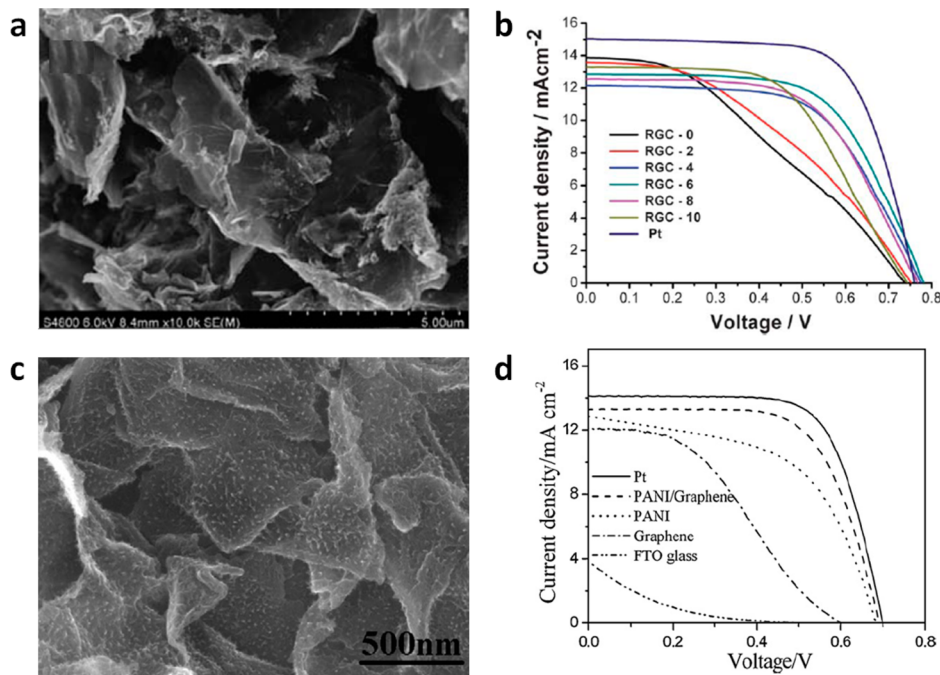


**Figure 23.** (a) SEM image of graphene nanosheets. (b)  $J$ - $V$  curves of DSSCs with graphene, graphene/CNT composites and platinum as counter electrodes measured under AM1.5 illumination. Reproduced with permission from ref 236. Copyright Royal Society of Chemistry (2011). (c) SEM image of polyaniline/graphene hybrid after polymerization for 24 h. (d)  $J$ - $V$  curves of DSSCs with different counter electrodes. Reproduced with permission from ref 237. Copyright Elsevier (2012).

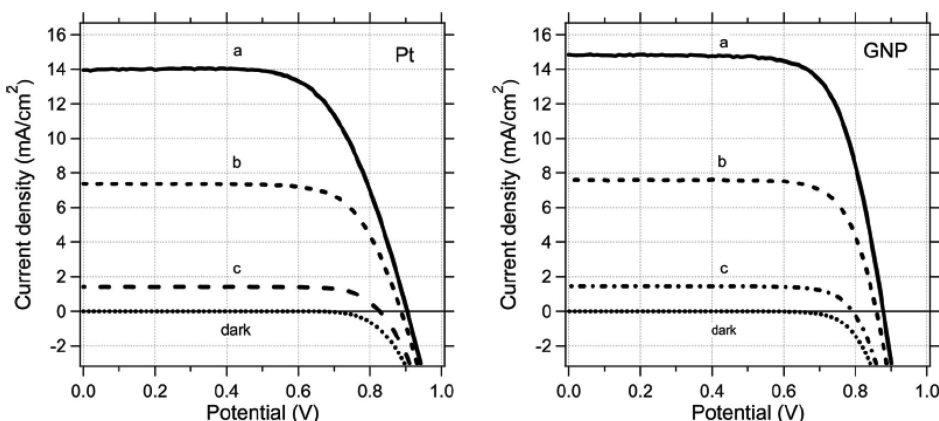


**Figure 24.**  $J$ - $V$  curves of the DSSC with Y-123 sensitized  $\text{TiO}_2$  photoanode and acetonitrile solution of  $\text{Co}(\text{bpy})_3^{3+/2+}$ . Left chart: DSSC with Pt-FTO counter electrode. Right chart: DSSC with GNP-FTO counter electrode (G66). The illumination intensities are 1 sun (curves a), 0.51 sun (curves b), 0.095 sun (curves c), and 0 (curves dark). Reproduced with permission from ref 243. Copyright American Chemical Society (2011).

(Figure 23c),<sup>237</sup> and the introduction of PANI had not only increased the catalytic activity but electrical conductivity. When it was used for the counter electrode, the DSSC exhibited a PCE of 6.09%, just a little lower than that of the DSSC from the platinum counter electrode (Figure 23d).

Although the graphene shows a relatively low electrocatalytic activity for the  $\text{I}^-/\text{I}^{3-}$  redox reaction, it can effectively catalyze the  $\text{Co}(\text{bipyridine})_3^{3+}/\text{Co}(\text{bipyridine})_3^{2+}$  redox couple with the donor-bridge-acceptor sensitizer.<sup>242,243</sup> Therefore, based on the graphene nanoplatelets as the counter electrode while the  $\text{Co}(\text{bipyridine})_3^{3+}/\text{Co}(\text{bipyridine})_3^{2+}$  redox couple in the electrolyte, the resulting DSSC showed a comparable photovoltaic performance to the platinum counter electrode (Figure 24).<sup>243</sup>

To summarize, carbon materials including CNT, graphene, activated carbon and carbon black can serve as good counter

electrode materials for DSSCs and display comparable performances to the conventional platinum after optimization. The key point lies in the design of the inner structure in the carbon electrode because the surface area and electron transport pathways largely affect the electron transport.

**3.3.2. Working Electrodes.** The working electrodes are generally composed of a layer of dye-adsorbed titanium dioxide ( $\text{TiO}_2$ ) nanocrystalline nanoparticles on transparent conductive glasses. They play a critical role for the conversion from photons to electrons and collection and diffusion of electrons in the DSSC. Upon illumination, electrons are generated from a dye molecule after absorbing photons immediately, followed by being injected into the conduction band of n-type  $\text{TiO}_2$  and diffused and collected in the transparent conductive electrode.<sup>213</sup> Herein, it is key to accelerate the diffusion process to compete with the charge recombination process. An effective

strategy is to incorporate functional nanomaterials with high conductivities to improve the separation and diffusion of the photoinduced charge.<sup>1,2</sup>

CNTs have been widely studied to modify the working electrodes to improve the photovoltaic performance of DSSCs.<sup>244–251</sup> For instance, SWCNTs were used as conducting scaffolds in the TiO<sub>2</sub> film to improve the photoinduced charge separation and transport of carriers to the collecting electrode surface (Figure 25).<sup>250</sup> The resulting DSSC showed a much

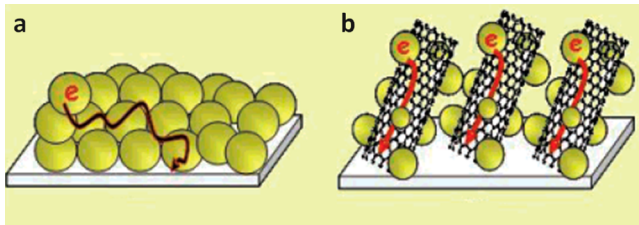


**Figure 25.** Charge transport in photoanodes with (a) and without (b) SWCNTs in the TiO<sub>2</sub> nanocrystalline films. Reproduced with permission from ref 250. Copyright American Chemical Society (2007).

improved  $J_{SC}$  compared with the one without SWCNTs in the working electrode, but the  $V_{OC}$  was decreased due to the increased Fermi level of the modified working electrode after incorporation of SWCNTs. Alternately, TiO<sub>2</sub>/MWCNT hybrid nanofiber film was prepared via a facile electrospinning method, and both  $V_{OC}$  and  $J_{SC}$  had been enhanced with the PCE being increased by 26% even at a low MWCNT load of 0.3 wt % in the working electrode.<sup>247</sup> Note that the PCE would be decreased with the further increase in the MWCNT content as the MWCNTs started to aggregate, inducing the decrease in the Fermi level of the composite working electrode.

Although the DSSCs based on the TiO<sub>2</sub>/CNT electrode showed high PCEs, the stability was relatively low as there were not effective interactions and connections between TiO<sub>2</sub> and one-dimensional CNT, which lead to the formation of transport barriers and occurrence of charge recombination. To this end, the two-dimensional graphene had been widely studied to replace the CNT for efficient hybrid working electrodes in the DSSCs.<sup>252–255</sup> In this case, TiO<sub>2</sub> particles can be well anchored on the graphene sheet, so the photoinduced electrons can be efficiently captured and transported by the graphene (Figure 26).<sup>253</sup> As a result, the  $J_{SC}$  was increased by

45% without sacrificing the  $V_{OC}$ ; the PCE was increased by 39% compared with the pristine TiO<sub>2</sub> working electrode.

Currently, there are much fewer studies on incorporating carbon nanomaterials into the working electrode as the mesoporous TiO<sub>2</sub> electrodes are already highly effective as working electrodes in DSSCs. On the other hand, although the introduction of carbon nanomaterials into the TiO<sub>2</sub> working electrode can promote the electron transport and collection, it also causes some loss in transparency.

**3.3.3. Electrolyte.** Electrolyte is one of the indispensable parts and also plays a critical role in the performance of the DSSC. The electrolyte is responsible for the dye regeneration during the photoelectric conversion process.<sup>256</sup> An effective electrolyte is expected to exhibit high electrical conductivity, high thermal stability, and low vapor pressure.<sup>263–266</sup>

Although liquid electrolytes such as I<sup>-</sup>/I<sub>3</sub><sup>-</sup> redox couple in acetonitrile have still been mostly used in the DSSC due to a high conductivity and diffusion coefficient,<sup>257,258</sup> the high flowability and low vapor pressure that may cause severe problems including leakage, thermal instability, and sealant corrosion have pushed scientists to discover new electrolytes with better performances.<sup>259,260</sup> A lot of effort has been then made to develop quasi-solid-state or solid-state electrolytes. For instance, ionic liquid electrolytes, a kind of quasi-solid-state electrolytes, have attracted increasing interests with combined high thermal stability, high ionic conductivity, negligible vapor pressure, and broad electrochemical potential window.<sup>259,261</sup> However, the PCEs of the DSSCs based on ionic liquid electrolytes are generally lower than the ones based on liquid electrolytes, which is mainly derived from the relative low speed for ion diffusions in the ionic liquid electrolyte.

Importantly, carbon nanomaterials are found to be able to improve ion diffusions in the ionic liquid electrolyte.<sup>2,261–278</sup> For instance, modified ionic liquid electrolytes had been prepared by incorporating graphene, SWCNT or a graphene/SWCNT mixture into 1-methyl-3-propylimidazolium iodide (PMII) ionic liquid.<sup>265</sup> When they were used to fabricate DSSCs, the PCEs were enhanced to 2.10%, 1.43% and 2.50% after the introduction of graphene, SWCNT and their mixture. For the pure PMII, the resulting DSSC displayed a very low PCE of 0.16%. This significant improvement was explained by the fact that the carbon nanomaterials simultaneously served as both charge transporter in the ionic liquid and catalyst for the electrochemical reduction of I<sub>3</sub><sup>-</sup>. Later, Yan and co-workers had further developed acid-oxidized MWCNT-based ionic liquid

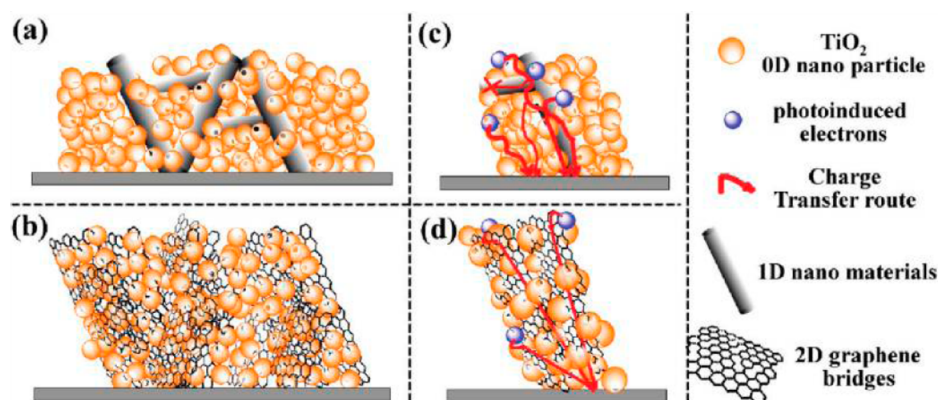


**Figure 26.** Schematic illustration to hybrid electrodes composed of TiO<sub>2</sub> particles and (a, c) 1D and (b, d) 2D nanomaterials. Reproduced with permission from ref 253. Copyright American Chemical Society (2010).

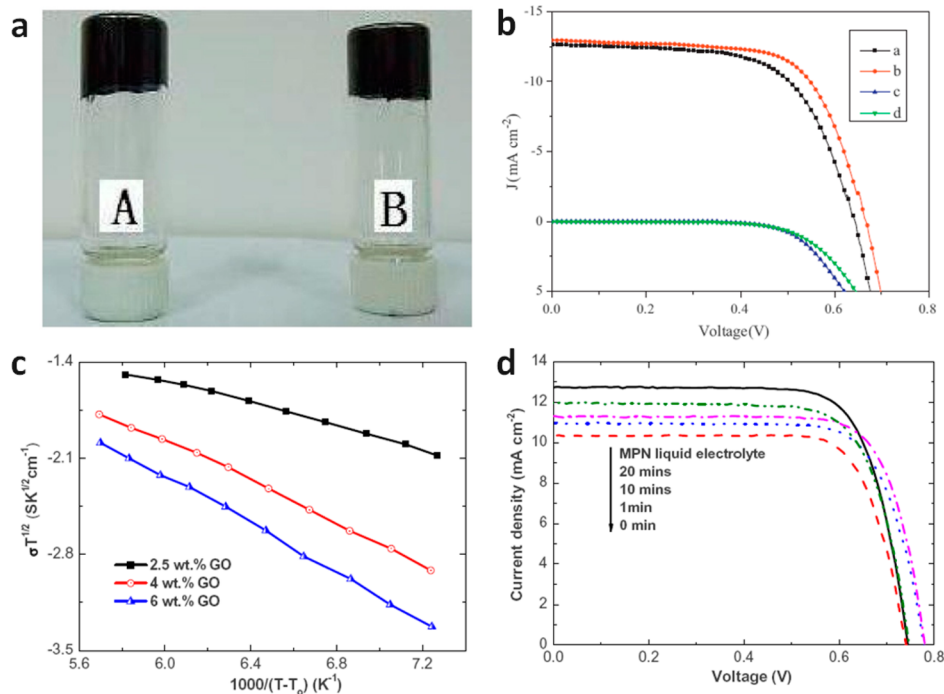


**Figure 27.** (a) Photograph of the MWCNT/ionic liquid gels based on (A) 1 wt % raw MWCNTs and (B) 2 wt % acid-oxidized MWCNTs. (b)  $J$ – $V$  curves of the raw MWCNT/ionic liquid DSSC (curves a and c) and the acid-oxidized MWCNT/ionic liquid DSSC (curves b and d) measured in dark (curves c and d) and under simulated AM 1.5 illumination at  $100 \text{ mW cm}^{-2}$  (curves a and b). Reproduced with permission from ref 264. Copyright Elsevier (2012). (c) Temperature dependence of ionic conductivities of GO-MPN gels containing 2.5 wt % GO-MPN with GO ultrasonicated from 0 to 20 min. (d)  $J$ – $V$  curves of DSSCs with 2.5 wt % GO-MPN gels. The GO sheets were ultrasonicated from 0 to 20 min. Reproduced with permission from ref 262. Copyright Elsevier (2013).

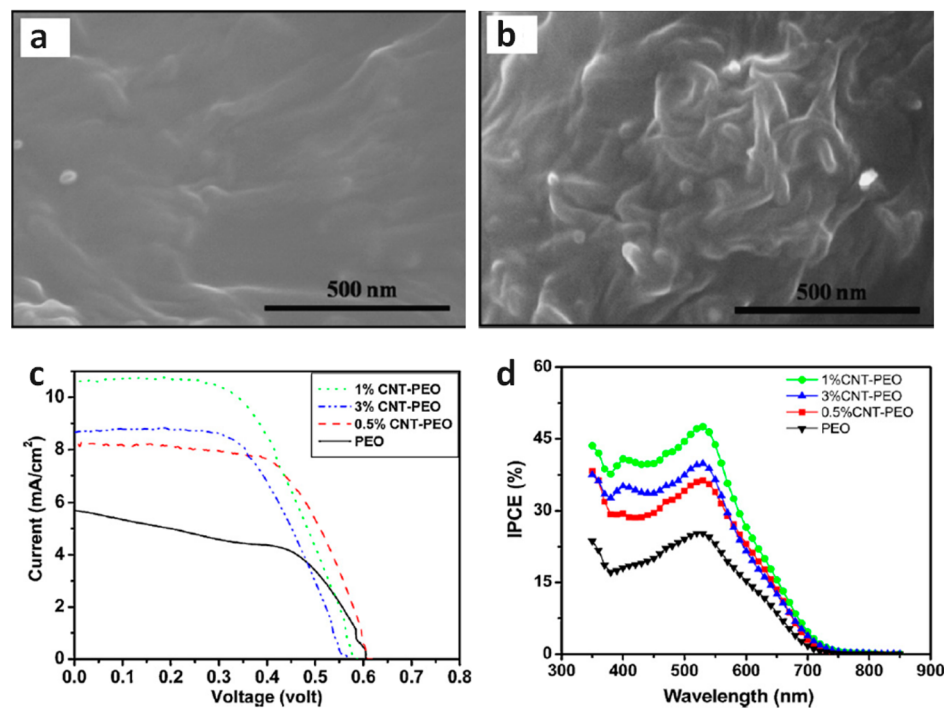


**Figure 28.** (a,b) SEM images of PEO and CNT/PEO composite (1 wt % for CNT) electrolytes, respectively. (c, d)  $J$ – $V$  and IPCE curves of DSSCs with PEO, CNT/PEO (0.5 wt % for CNT), CNT/PEO (1 wt % for CNT) and CNT/PEO (3% for CNT) electrolytes measured under AM1.5 illumination, respectively. Reproduced with permission from ref 269. Copyright Elsevier (2010).

electrolytes where the acid-oxidized MWCNTs showed a much better miscibility with the ionic liquid than the pristine MWCNTs, which was found to enhance the formation of

gels (Figure 27a).<sup>264</sup> The resulting DSSC yielded a PCE of 5.74% (Figure 27b). Alternately, Ouyang and co-workers introduced GO as the gelator to prepare a quasi-solid-state

electrolyte with a high ionic conductivity (Figure 27c).<sup>262</sup> The highest PCE reached 6.70% (Figure 27d), a little lower than 7.18% for the DSSC based on the liquid electrolyte.

Carbon nanomaterials had been also used in the solid-state electrolytes.<sup>269,270</sup> For instance, a solid-state electrolyte was developed by incorporating CNTs into poly(ethylene oxide) (PEO) to realize much improved roughness, amorphicity and ionic conductivity (Figure 28a,b).<sup>269</sup> When the modified solid-state electrolyte was used for the DSSC, a PCE of 3.5% was achieved (Figure 28c). The incident photon-to-electron conversion efficiency (IPCE) curve of the DSSC based on the solid-state electrolyte had further verified the enhanced photovoltaic performance. This improvement may be ascribed to the increased ionic conductivity in the composite electrolyte and interfacial contacts between electrode and electrolyte (Figure 28d). In summary, CNTs represent a good additive for quasi-solid-state or solid-state electrolytes in DSSCs by enhancing their conductivities.

### 3.4. Carbon Nanomaterial-Silicon Solar Cells

Carbon nanomaterials such as CNT and graphene are mainly used to promote charge separation and transport rather than generating excitons upon absorption of light in both DSSCs and PSCs. Recently, a new type of carbon nanomaterial-silicon solar cells has been developed to take advantage of the excellent electronic property of CNT and graphene during the photogeneration process.<sup>271–280</sup>

**3.4.1. Carbon Nanotube.** For the application in PSCs, the CNTs are mainly used as transparent electrodes for charge collection or as nanoscale fillers for charge transport. For the application in DSSCs, the CNTs have been mainly used as counter electrodes for charge collection and transport or as fillers in the photoanode to enhance charge transports.<sup>1,2</sup> Obviously, the CNT does not participate the exciton generation process. In 2007, Wu and co-workers fabricate thin-film solar cells with DWCNTs serving as both photogeneration sites and a charge collection and transport layer (Figure 29a).<sup>271</sup> More specifically, this hybrid solar cell showed a p–n heterojunction consisting of a DWCNT layer p-type emitter material and an n-type silicon (n-Si) wafer. Upon illumination, excitons were generated from the n-type silicon and diffused to the space-charge region where they were separated into free charge carriers under the action of the built-in potential formed by Fermi level equilibration at the junction (Figure 29b,c).<sup>272</sup>

Previously, DWCNTs were deposited on the n-silicon substrates via a H<sub>2</sub>O expansion, followed by an aqueous transport of the as-grown film synthesized by CVD, and a relatively low PCE of 1.3% was obtained as the FF was less than 0.19 due to a high series resistance.<sup>271</sup> Later, the series resistance was decreased by a photolithography etching technology with a much increased FF of 0.53.<sup>272</sup> As a result, a higher PCE of 7.3% had been produced.

In order to further improve the performance of the CNT/Si solar cell, Cao and co-workers had replaced the DWCNTs with SWCNTs that showed higher optical transmittances.<sup>274</sup> In addition, the SWCNT/Si solar cells could be inserted into a dilute HNO<sub>3</sub> solution for doping (Figure 30a) to largely reduce the series resistance for higher FF values. After the acid treatment, the  $J_{SC}$  and FF were increased from 27.4 mA/cm<sup>2</sup> and 0.47 to 36.3 mA/cm<sup>2</sup> and 0.72, respectively. The PCE jumped to 13.8% (Figure 30b). Recently, Cao and co-workers had further optimized the SWCNT/Si solar cell by spin-coating

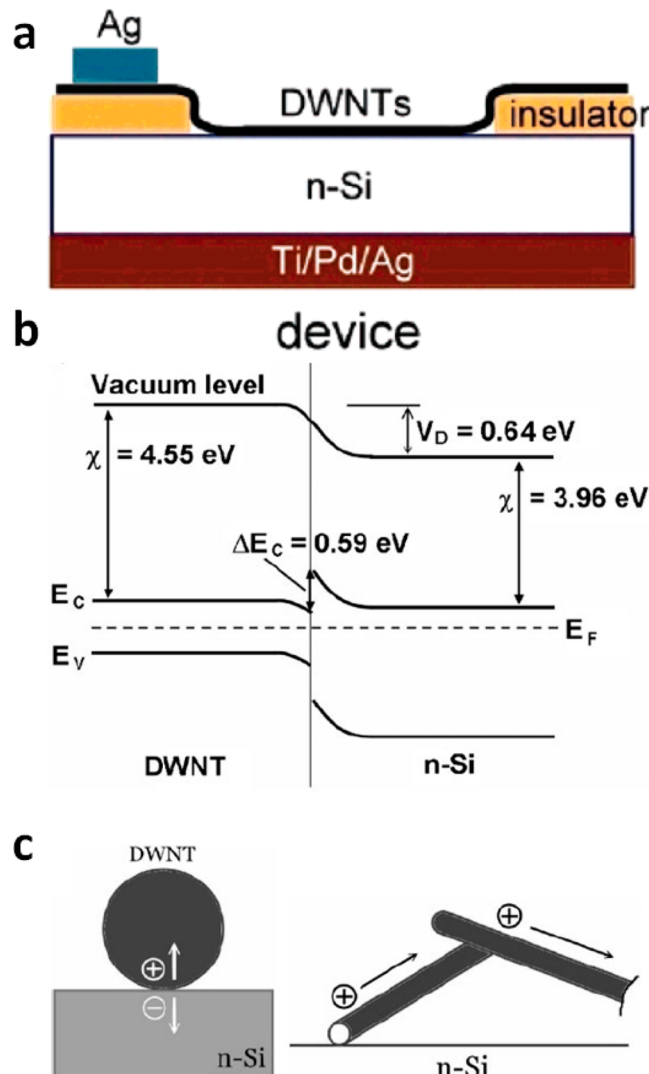


**Figure 29.** (a) Schematic illustration to the DWCNT/Si solar cell. Reproduced with permission from ref 271. Copyright American Chemical Society (2007). (b) Energy band diagram of the DWCNT/Si solar cell. (c) Schematic illustration of the charge separation occurring at the interface between a DWCNT and Si substrate and charge transport through a percolated DWCNT network. Reproduced with permission from ref 272. Copyright John Wiley and Sons (2008).

a TiO<sub>2</sub> layer (50–80 nm) on the SWCNT film to decrease the light reflection from the surface of the solar cell, followed by doping with HNO<sub>3</sub>/H<sub>2</sub>O<sub>2</sub> for higher electrical conductivity and contact (Figure 30c).<sup>277</sup> The resulting solar cell exhibited  $J_{SC}$  of 32 mA/cm<sup>2</sup>,  $V_{OC}$  of 0.61 V, and FF of 0.77, which produced an even higher PCE of 15.1%.

Besides, superaligned DWCNT sheets that showed a high transmittance of above 88% in the visible and infrared spectral range (Figure 31a) were also developed as window electrodes for the hybrid solar cell (Figure 31b,c). It was found that the resulting device exhibited a higher PCE of 10.8% than that based on a randomly dispersed DWCNT window electrode.<sup>279</sup> The superaligned structure promoted the charge transport and collection efficiency.

In summary, the unique high electron mobility, high transparency, and appropriate work function of CNTs make the CNT-silicon hybrid solar cells available. Two main directions are recognized to further enhance the performance

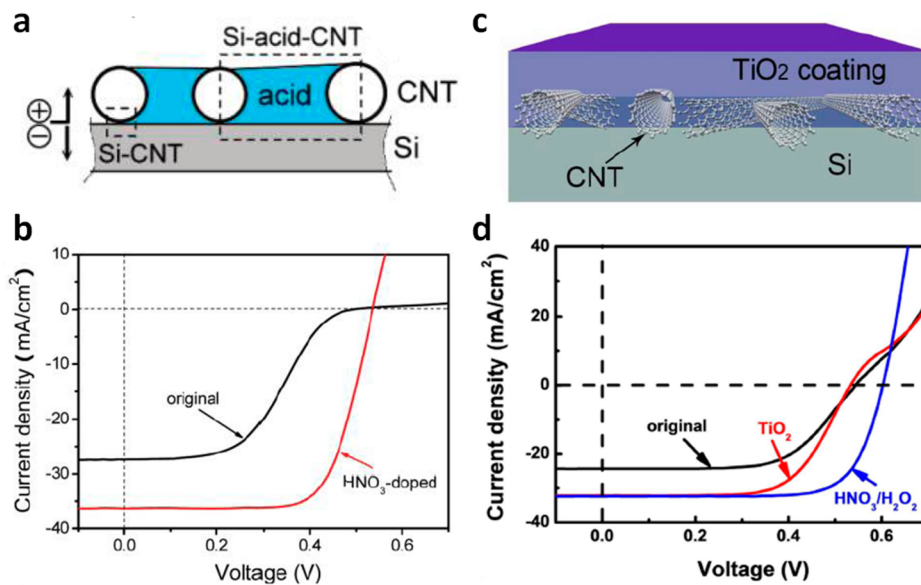


**Figure 30.** (a) Schematic illustration to the SWCNT/Si solar cell based on a SWCNT network coated on an n-type Si wafer and infiltration of nitric acid into the network to form Si-acid-CNT photoelectrochemical units in addition to Si-CNT heterojunctions at the interface. (b)  $J$ – $V$  characteristics of the SWCNT/Si solar cell before (black curve) and after (red curve) infiltration of dilute  $\text{HNO}_3$ . Reproduced with permission from ref 274. Copyright American Chemical Society (2011). (c) Schematic illustration to the SWCNT/Si solar cell consisting of a Si substrate, a CNT film and a  $\text{TiO}_2$  layer. (d)  $J$ – $V$  characteristics of the SWCNT/Si solar cell without coating, with coat of a  $\text{TiO}_2$  antireflection layer, and after  $\text{HNO}_3/\text{H}_2\text{O}_2$  treatment, respectively. Reproduced with permission from ref 277. Copyright Macmillan Publishers Ltd. (2012).

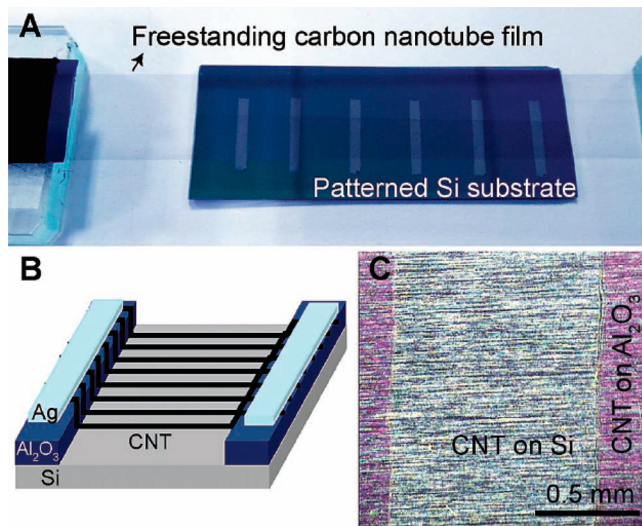


**Figure 31.** Preparation (top), scheme (left bottom), and photograph (right bottom) of the aligned DWCNT-Si solar cell. Reproduced with permission from ref 279. Copyright John Wiley and Sons (2013).

of the hybrid solar cell in the future development, i.e., high transparency along with low sheet resistance of the CNT and alignment of the energy level with a surface passivation.

**3.4.2. Graphene.** Different from the CNT/Si solar cells with a heterojunction, the graphene/Si solar cells are derived from a Schottky junction, which is formed between a metal (graphene) and a semiconductor (n-type silicon). Upon the illumination, excitons are mainly generated from the n-type silicon wafer and diffused to the base region where they are separated into free charge carriers by the built-in potential between the graphene and silicon.

A typical single-layered graphene/Si Schottky junction solar cell is shown in Figure 32ax.<sup>276</sup> The graphene sheet was grown

on a copper foil by CVD, and the bis (trifluoromethanesulfonyl)-amide (TFSA) doped graphene was also introduced for the graphene/Si solar cells because the TFSA doping can reduce the resistance of graphene sheet and increase its work function without changing its optical properties. As a result, the pristine graphene/Si solar cell showed a low PCE of 1.9%, whereas the TFSA-doped graphene/Si solar cell yielded a much higher PCE of 8.6% (Figure 32b). Cao and co-workers had further improved the PCE to 14.5% by adding an antireflection  $\text{TiO}_2$  layer through a simple spin-coating method (Figures 32c,d).<sup>280</sup> The  $\text{TiO}_2$  antireflection layer promoted the light absorption by Si and lead to a much higher IPCE of 80–90% across the visible and near-infrared range (400–1000 nm) than the bare graphene/Si cell (IPCE of ~60%).

Compared with CNT films, graphene films may exhibit high optical transmittances and better connections with the Si substrate. Therefore, the graphene-Si hybrid solar cells are expected to show high photovoltaic performances than CNT-silicon solar cells. This conclusion may be supported after high-quality graphene films are realized which will be a focus in the future development of this direction.

### 3.5. Perovskite Solar Cells

Recently, organic–inorganic halide perovskite solar cells become a superstar of the photovoltaic field for their dramatically increased power conversion efficiencies from 3.9% to 20.1% in less than five years.<sup>281</sup> In the research progress, carbon nanomaterials exhibit unique applications by improving stability and simplifying fabrications.

Generally, perovskite solar cells suffer from their instability in the existence of moisture, so a lot of methods have been developed to improve the moisture resistance.<sup>282</sup> Among them, carbon materials showed promising applications. For one instance, a carbon black/graphite hybrid was used as a back electrode to produce a power conversion efficiency of 12.8% with stable performance for over 1000 h (Figure 33a). The

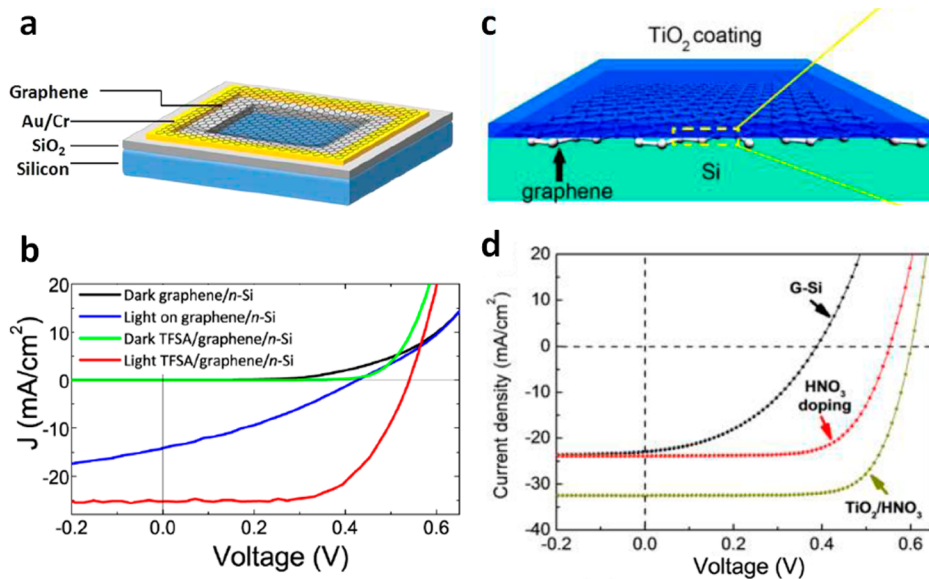


**Figure 32.** (a) Schematic illustration to a graphene-Si solar cell. (b)  $J$ - $V$  characteristics of the graphene/Si and doped-graphene/Si solar cells measured in dark and under AM1.5 illumination. Reproduced with permission from ref 276. Copyright American Chemical Society (2012). (c) Schematic illustration of a graphene-Si solar cell consisting of a Si substrate, a CNT film and a TiO<sub>2</sub> layer. (d)  $J$ - $V$  characteristics (AM1.5 illumination) of a graphene-Si solar cell recorded in original state (without coating), with a TiO<sub>2</sub> antireflection layer and after HNO<sub>3</sub>/H<sub>2</sub>O<sub>2</sub> treatment, respectively. Reproduced with permission from ref 280. Copyright American Chemical Society (2013).

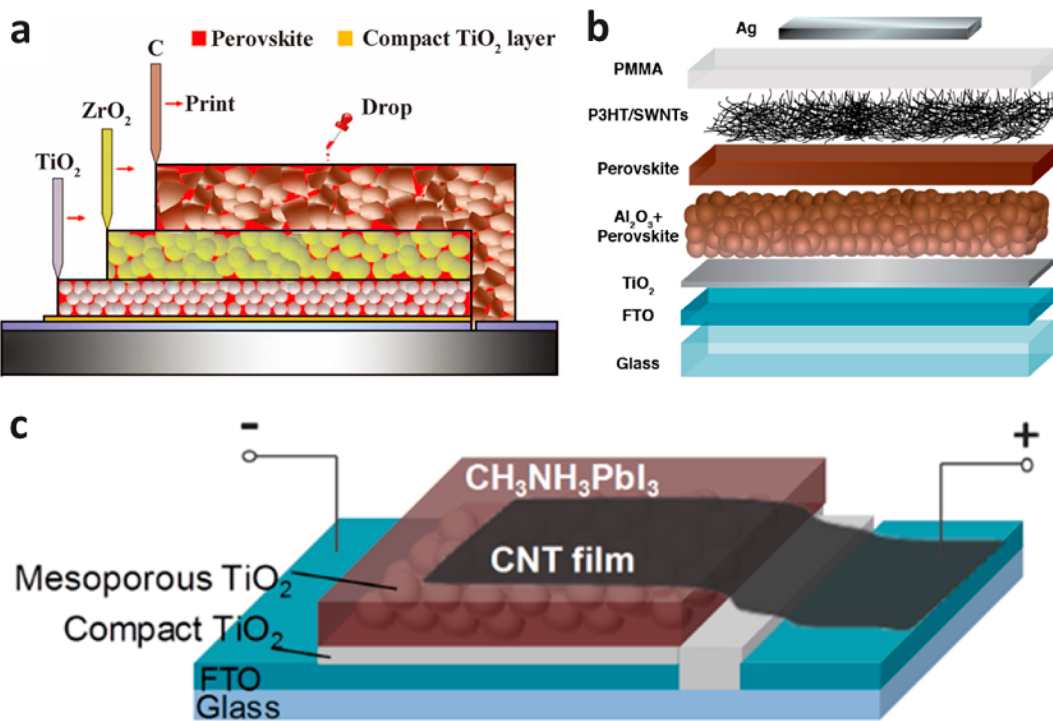


**Figure 33.** (a) Perovskite solar cell with a carbon black/graphite back electrode. Reproduced with permission from ref 282a. Copyright the American Association for the Advancement of Science (2014). (b) Perovskite solar cell with P3HT/SWCNT composite as hole transport materials. Reproduced with permission from ref 282b. Copyright American Chemical Society (2014). (c) Perovskite solar cell with a freestanding CNT film as back electrode. Reproduced with permission from ref 283. Copyright American Chemical Society (2014).

high stability may be explained by the fact that the hydrophobic carbon black/graphite electrode prevented the moisture from contacting the perovskite. For another instance, a polymer-functionalized SWCNTs embedded in an insulating polymer had been also incorporated as hole transport materials to enhance the moisture stability (Figure 33b).<sup>282b</sup> Besides high power conversion efficiencies up to 15.3%, the perovskite solar

cell can well maintain the high performance even after running in water for 60 s. Freestanding CNT films could also serve as both hole transport layer and back electrode for hole extraction and collection (Figure 33c).<sup>283</sup>

The perovskite solar cells are still running at the initial stage, and a lot of efforts are required to explore carbon nanomaterials to enhance their performances in the near future. In particular,

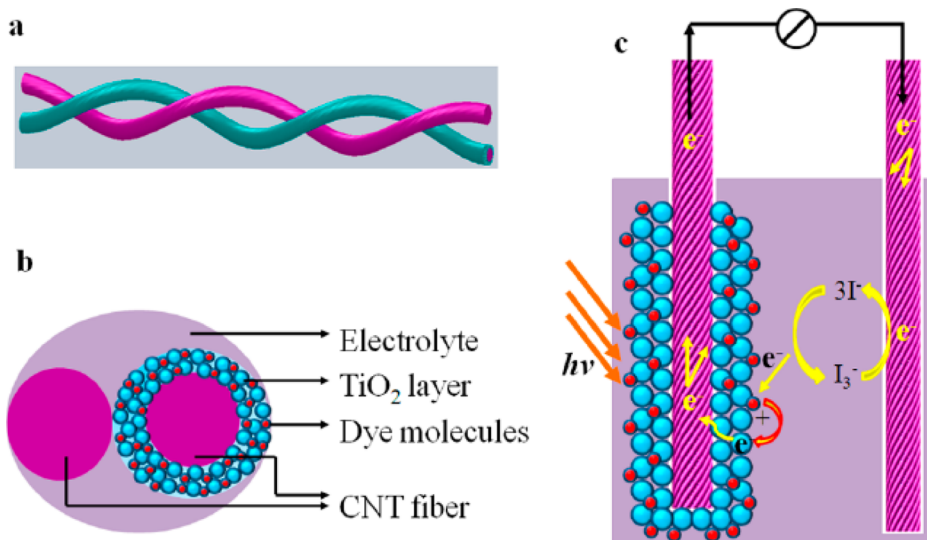


**Figure 34.** Schematic illustration to a fiber-shaped DSSC fabricated from two CNT fibers. (a) Two CNT fibers twined into a DSSC. (b) Top view of the fiber-shaped DSSC. (c) Working mechanism. Reproduced with permission from ref 209. Copyright American Chemical Society (2012).

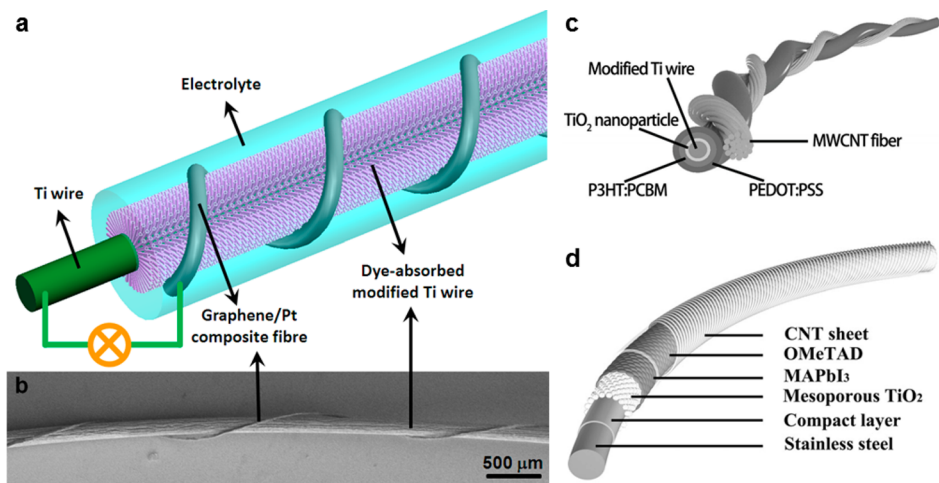


**Figure 35.** (a, b) Schematic illustration and SEM image of a fiber-shaped DSSC prepared by using a graphene/Pt hybrid fiber as the counter electrode and a Ti wire impregnated with  $\text{TiO}_2$  nanotubes as the working electrode. Reproduced with permission from ref 285. Copyright John Wiley and Sons (2013). (c) Schematic illustration of a fiber-shaped PSC. Reproduced with permission from ref 286b. Copyright John Wiley and Sons (2014). (d) Schematic illustration of a fiber-shaped perovskite solar cell. Reproduced with permission from ref 286c. Copyright John Wiley and Sons (2014).

the use of them in back electrodes, hole transport layers, and stability improvements are promising as they well meet the roll-to-roll solution fabrication that is recognized as a general process to scale up the next-generation solar cell.

### 3.6. Fiber-Shaped Solar Cells

With the advancement of the microelectronic technology, electronic devices are simultaneously required to be lightweight, small, and flexible, while the conventional silicon-based and organic planar solar cells cannot fully meet the requirements. As a result, fiber-shaped miniature solar cells that are thin, flexible, and lightweight have attracted increasing attentions, particularly in the portable and wearable electronics. To achieve highly efficient fiber-shaped solar cells, it is critical to make high-performance fiber electrodes with combined high electrical conductivity, tensile strength, catalytic activity, and flexibility. However, the widely used, conventional metal wire, modified polymer fiber, and carbon fiber fail to satisfy all of them.

Fortunately, carbon nanomaterials such as CNT and graphene can be assembled into micrometer-sized fibers with remarkable electronic and mechanical properties discussed above. Highly aligned CNT fibers had been dry-spun from spinnable CNT arrays, and the aligned structure of CNTs provided the fibers with high electrical conductivities of  $10^4$ – $10^6$  S/m and tensile strengths of  $10^2$ – $10^3$  MPa as well as high catalytic activity and flexibility. When they were used as counter electrodes to fabricate fiber-shaped DSSCs, high PCEs over 7% had been achieved.<sup>208–212,284</sup> Figure 34 represents a typical twisted fiber-shaped DSSC where an aligned CNT fiber coated with  $\text{TiO}_2$  nanoparticles served as a working electrode while a bare aligned CNT fiber acted as the counter electrode.<sup>209</sup> Although the first report displayed a relatively low PCE of 2.60%, a modification on the fiber electrode and electrolyte can greatly enhance the PCE. For instance, when an organic thiolate/disulfide redox couple with low absorption in the visible region was used as the electrolyte and a Ti wire

perpendicularly grown with aligned  $\text{TiO}_2$  nanotubes on the surface as the working electrode, a much higher PCE of 7.33% had been achieved.<sup>212</sup> Note that the use of a flexible aligned CNT fiber as the counter electrode was critical for the high PCE as it could be closely and stably wound onto the Ti wire for rapid charge separation and transport.

Graphene can be also assembled into micrometer-sized fibers with combined remarkable electronic and mechanical properties through a wet-spinning process. For instance, high tensile strengths of  $10^2\text{--}10^3$  MPa and electrical conductivities of  $10^4\text{--}10^5$  S/m were obtained for the graphene fiber.<sup>285</sup> The graphene fibers could be further electrodeposited with a second phase including metal and conducting polymer for enhanced electronic and catalytic properties. When platinum nanoparticles were deposited onto the graphene fiber as a counter electrode and a Ti wire impregnated with perpendicularly aligned  $\text{TiO}_2$  nanotubes functioned as the working electrode (Figure 35a,b), the resulting twisted fiber-shaped DSSC showed a certified PCE of 8.45%.<sup>285</sup> Compared with a very low PCE in the DSSC based on the bare graphene fiber, the largely increased PCE is derived from the strong interactions between graphene sheet and platinum nanoparticles, which has therefore mostly combined the high conductivity and electrocatalytic activity.

Fiber-shaped DSSCs generally require the use of liquid electrolytes that can not effectively display the advantages of the fiber structure and may also cause some safety problems. Therefore, it is necessary to develop all-solid-state fiber-shaped solar cells aiming at practical applications. To this end, PSCs may provide an effective and promising platform as no liquid materials are required.<sup>286</sup> Figure 35c schematically shows the structure of a typical fiber-shaped PSC.<sup>286a</sup> A Ti wire with titanium dioxide nanotube arrays was used as a cathode after sequentially depositing titanium dioxide nanoparticles, P3HT:PCBM active layer and PEDOT:PSS hole layer, and an aligned MWCNT fiber was then twisted onto the modified Ti wire as the anode. This fiber-shaped PSCs exhibited a power conversion efficiency of 1.78% and is much lower than the fiber-shaped DSSCs. A lot of attentions are currently paid to enhancing the photovoltaic performances of fiber-shaped PSCs by incorporating new materials and optimizing device structures.

As previously discussed, perovskite solar cells have been widely explored with high power conversion efficiencies also in an all-solid-state structure. An attempt was recently made to fabricate fiber-shaped perovskite solar cells with a coaxial architecture that demonstrated a maximal power conversion efficiency of 3.3% (Figure 35d).<sup>286b</sup> A stainless steel wire was used as the cathode; compact titanium dioxide nanoparticle,  $\text{CH}_3\text{NH}_3\text{PbI}_3$  and spiro-OMeTAD layers were then sequentially dip-coated onto the steel wire as the hole blocking, light-absorbing and hole-transporting layers, respectively; and an aligned MWCNT sheet was finally wrapped around the modified steel wire as the anode. For the fiber-shaped perovskite solar cell, the interface in the curved structure plays a critical role and needs optimizations to further increase the photovoltaic performance.

Compared with the conventional planar structure, the fiber-shaped solar cells are particularly promising for wearable electronic devices. They are often stretched besides being bent during the various body movement in use, and the thin fiber-shaped solar cells easily break under stretching. To this end, increasing interests are attracted to realize stretchable fiber-

shaped solar cells including both DSSCs and PSCs. Figure 36 represents a stretchable fiber-shaped DSSC.<sup>286c</sup> Typically, an

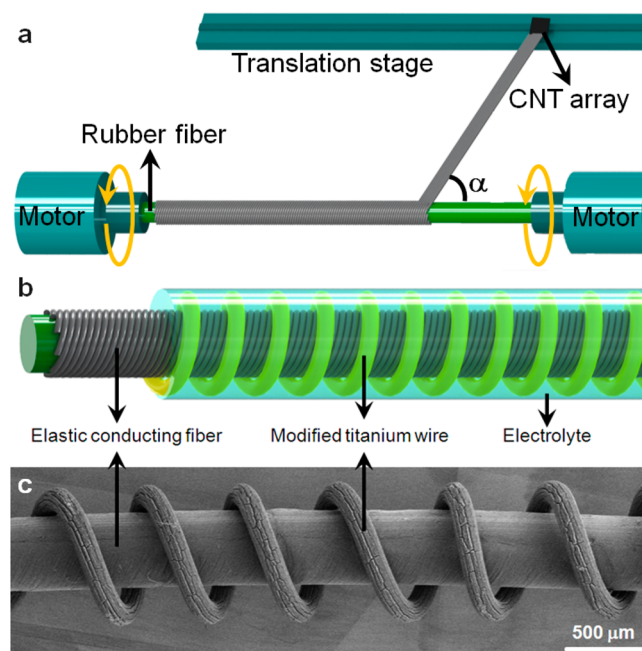


**Figure 36.** (a) Schematic illustration to the rotation-translation method for preparing the elastic conducting fiber. (b,c) Schematic illustration and SEM image of a stretchable fiber-shaped DSSC. Reproduced with permission from ref 286a. Copyright John Wiley and Sons (2014).

elastic conducting fibers, e.g., a coaxial fiber by winding aligned CNT sheets on a rubber fiber, was used as a counter electrode (Figure 36a), and a spring-like Ti wire with perpendicularly aligned  $\text{TiO}_2$  nanotubes served as the working electrode (Figure 36b,c). This stretchable DSSC demonstrated a high PCE of 7.13% that could be well maintained after stretching with a strain of 30% for 20 cycles.

The other functionalities had been also incorporated into the fiber-shaped solar cells to further enhance the application scope.<sup>287</sup> For instance, a magnetically responsive fiber-shaped DSSC was achieved by introducing superparamagnetic metal oxide nanoparticles into the aligned CNT fiber counter electrode.<sup>284</sup> Such a fiber-shaped DSSC can be remotely controlled to be attached onto or detached from the substrate by magnetic fields, which may provide it with some new applications unavailable for the conventional solar cells. It can be stabilized to power an electronic device by the magnetic field and removed without use. Due to the high surface area of aligned CNTs, the metal oxide nanoparticles had been uniformly attached onto and interacted with CNTs to enable a high stability for the DSSC during use. In addition, the DSSC also exhibited a high PCE of 8.03%. By incorporation of self-healing polymer fibers as substrates, an interesting kind of fiber-shaped DSSCs that can be self-healed after breaking has been recently discovered.<sup>287a</sup> This self-healable property is necessary for the fiber-shaped solar cells as they are thin and easily cut by the external object during the operation. If one fiber breaks, the whole woven photovoltaic textile may fail to work with a short lifetime. Under this situation, the self-healable fiber-shaped solar cell can repair itself to maintain a stable performance in a long period. Note that, compared with the conventional planar

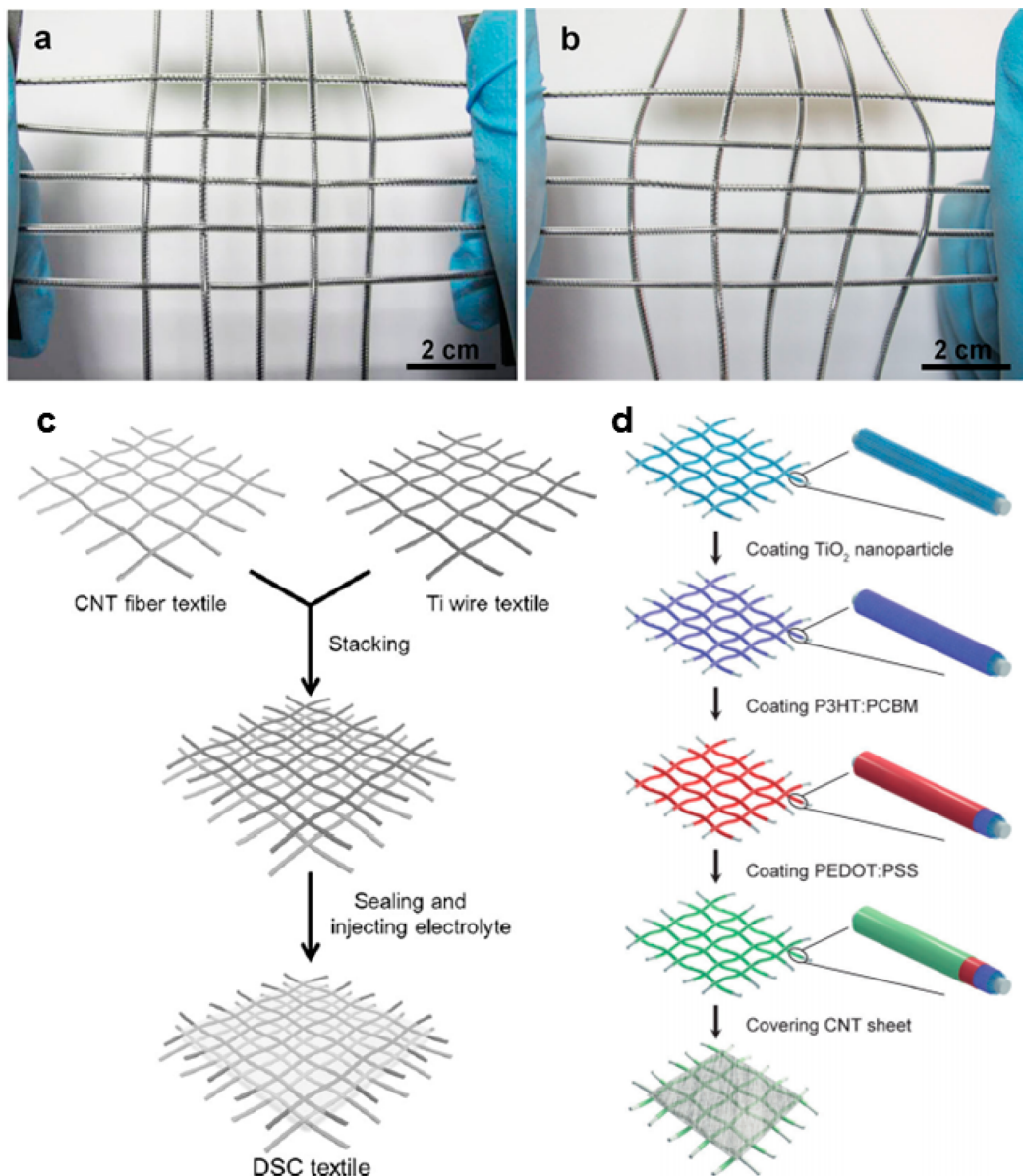


**Figure 37.** (a, b) A DSSC textile before and after stretching. Reproduced with permission from ref 286a. Copyright John Wiley and Sons (2014). (c) Schematic illustration to fabricate a DSSC textile. Reproduced with permission from ref 287b. Copyright John Wiley and Sons (2014). (d) Schematic illustration to fabricate a PSC textile. Reproduced with permission from ref 287c. Copyright John Wiley and Sons (2014).

solar cell, the fiber shape also enables some unique advantages besides lightweight, weaveable, and integratable, e.g., the PCE is independent of the angle of incident light.

Fiber-shaped solar cells are extensively proposed to power various electronic devices by formation of textiles through the well-developed weaving technology. However, it remains challenging to maintain high photovoltaic performances in the resulting solar cell textiles due to the difficulty in connecting many fiber electrodes and the production of short circuits during fabrication and use. For instance, ten fiber-shaped DSSCs were woven into a powering textile (Figure 37a,b), and the power conversion efficiency of the solar cell textile was decreased by 30–40% compared to the calculated value from building fiber-shaped solar cells.<sup>286c</sup> Alternately, a solar cell textile may be also fabricated by first weaving electrically conducting fibers into textile electrodes, and two textile electrodes can be then stacked into a textile-like solar cell. Figure 37c represents a typical structure of a DSSC textile in

developing this strategy with a metal textile as the working electrode and an MWCNT fiber-based textile as the counter electrode with the photoactive materials sandwiched between them.<sup>287b</sup> Similarly, Figure 37d demonstrates the fabrication of a PSC textile from two textile electrodes.<sup>287c</sup> Both DSSC and PSC textiles were flexible and efficient and had been explored to power microelectronic devices.

### 3.7. Summary

Carbon nanomaterials, especially CNT and graphene, have exhibited many promising applications in the energy harvesting due to the combined high carrier mobility, transparency, catalytic activity, specific surface area and tunable work functions. The preparation of carbon nanomaterials for transparent conductive electrodes represents a widely explored and important direction. The development of carbon nanostructured electrodes aiming at both high conductivity and specific surface area represents another promising direction to

push the next-generation solar cell ahead. In addition, carbon nanomaterials can also be used as additives for promoting the carrier transfer. In summary, the exceptional properties of carbon nanomaterials offer many opportunities to improve the energy harvesting efficiency.

#### 4. APPLICATION IN ENERGY STORAGE

Energy storage has been well recognized as one of the most important challenges in this century. The increasing emerging ecological problem badly requires the development of low-cost and environmentally friend energy storage systems with high efficiencies. For instance, the rapid advancement in portable electronics and electric vehicles has stimulated the discovery of new energy storage devices toward both high power density and energy density. LIBs and supercapacitors represent two mostly explored energy storage systems, where the energy storage and output are realized by charge and discharge to store electricity through electrochemical processes. During the charging process, an external voltage is applied between two electrodes to promote the movements of electrons and reactions at the electrodes; during the discharging process, the electrochemical reactions occur at the electrodes, generating electrons to flow through the external circuit with the produced electrical current to power the connected device. An electrochemical energy storage device is typically composed of anode, cathode, separator, and electrolyte. The improvement in the energy storage mostly depends on the advancement of new materials used in the electrodes. Carbon materials have been playing a significant role in the development of electrochemical energy storage systems. Activated carbon has been long used for the electrochemical energy storage as it is commercially available and cheap. Recently, carbon nanomaterials including CNT, graphene and OMC have attracted increasing interests due to more excellent mechanical, electronic and catalytic properties compared with the active carbon. The use of these three carbon nanomaterials in LIBs and supercapacitors are summarized below.

##### 4.1. Lithium Ion Battery

Lithium is the lightest metal in the elemental table with a specific gravity of 0.53 g/cm<sup>3</sup>. It is also the most powerful reducing element, thus leading to a high voltage and capability of delivering high energy density. The theoretical electrochemical capacity of Li to Li<sup>+</sup> is 3860 mAh/g.<sup>288</sup> In the 1970s, Li started to be used as negative electrode materials to assemble primary Li batteries, and the resulting batteries enabled the realization of cellular telephones and lap-top computers. However, the formation of dendritic metallic lithium during the charging process brought severe safety problems as well as high cost and short lifetime, plaguing the further application in modern electric vehicles and devices. In the 1990s, following the discovery of LiCoO<sub>2</sub> as a positive electrode, the commercialization of the lithium-ion battery by SONY provided huge room for safe and efficient energy storage.<sup>289</sup> Compared with the traditional secondary batteries such as lead–acid or nickel–cadmium batteries, the new rechargeable lithium-ion batteries exhibited superior performance including long cycle life, high specific energy, and no memory effect. In the LIB system, the metallic lithium is replaced by a carbon host structure that can reversibly absorb and release lithium ions at low electrochemical potentials. Therefore, lithium ions shuttle between an insertion cathode (e.g., LiCoO<sub>2</sub>) and an insertion anode (e.g., carbon), presenting only a slight decrease

of energy density compared with parent Li metal batteries; a great improvement in cycle life and safety had been also realized.<sup>288</sup>

Carbon is known to be intercalated into lithium by a chemical route.<sup>290,291</sup> For typical carbon materials such as graphite, the basic building unit is a planar sheet of carbon atoms arranged in a hexagonal format. Lithium intercalates into the carbon layer to form Li<sub>x</sub>C alloy, delivering a theoretical specific capacity of 372 mAh/g (LiC<sub>6</sub>) and a potential plateau lower than 0.5 V vs Li<sup>+</sup>/Li<sub>6</sub>. The practical performance of carbonaceous materials strongly depends on their crystallinity, microstructure and morphology.<sup>292,293</sup> Lithium ion batteries based on CNT, graphene, and OMC are compared in Figure 38 and further detailed below.

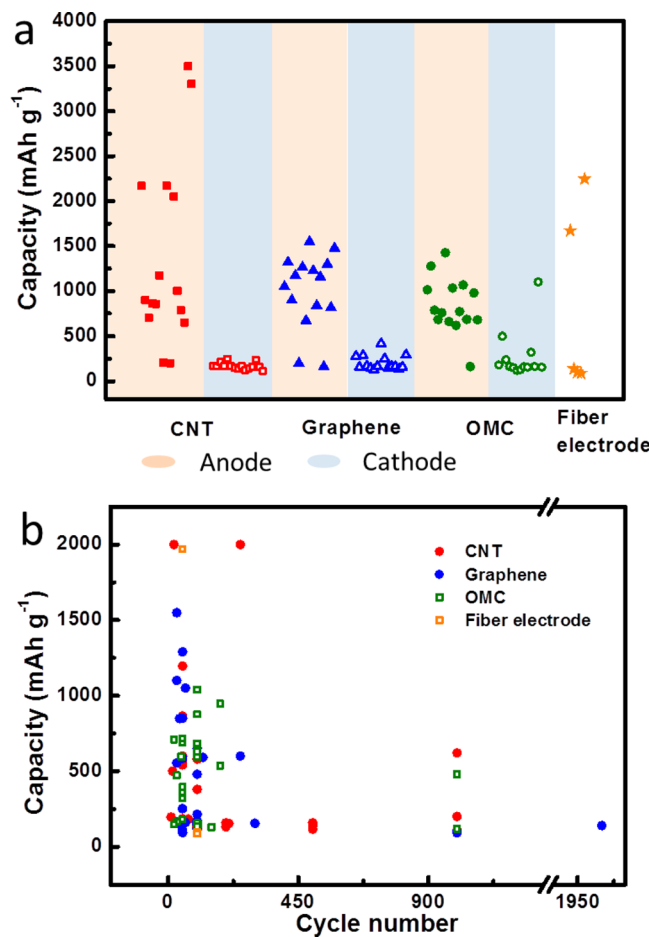


**Figure 38.** Performance overview of the lithium ion batteries based on CNT, graphene, OMC, as well as their derived fiber-shaped devices. (a) The capacity distribution. (b) The long-life stability.

**4.1.1. Carbon Nanotube.** CNTs, compared with the other LIB materials like graphite and nanoparticles, reveal a great benefit of one-dimensional nanomaterials: (1) the higher specific surface area provides a higher electrode/electrolyte contact, (2) the higher electrical conductivity leads to an enhanced ion transportation, and (3) the unique hollow structure and multilayered wall in the case of MWCNTs enable more connection sites. Li ion intercalation will occur at the outside walls or within the inner core through the open ends, as well as between the multilayers through the wall-defects or the open ends of MWCNTs. It is calculated that a reversible

capacity of 1.116 A/g of SWCNTs could be attained due to the more efficient integration from LiC<sub>2</sub> alloy rather than the LiC<sub>6</sub> alloy of traditional carbon materials.<sup>294,295</sup> Overall, pristine CNTs could be directly assembled into freestanding LIB electrodes without extra binder or current collector, revealing a reversible potential plateau lower than 0.5 V vs Li<sup>+</sup>/Li. The more common application is to use CNTs to modify the traditional electrode materials by serving as conductive additives, current collectors, or electrode skeletons. Furthermore, the moldability allows CNTs to be fabricated into a variety of shapes, controlled into desired alignments, or spun into yarns, which is particularly promising for the rapidly developed fiber-shaped energy storage devices in recent years.

**4.1.1.1. Pristine CNT Electrodes.** Both SWCNTs and MWCNTs can be used as the anode by simply depositing them onto a current collector from a uniform suspension or being grown onto a catalyst premodified current collector. In fact, the CNT paper obtained by a filtration method can be further used as a freestanding electrode itself without extra binder or current collector due to the  $\pi-\pi$  interactions within the tangled nanotubes, increasing both effective capacity and specific energy density of the overall battery. The lightweight and flexible CNT paper with a three-dimensional porous network also showed a high conductivity, electrochemical stability, and mechanical strength. When aligned CNT materials such as vertically aligned arrays had been introduced, the aligned CNTs provided more effective pathways that allowed the ions and electrons to transport along the CNTs directly to the current collector or into the electrolyte compared with the networked structure. Therefore, open ends and lateral defects on the walls of CNTs would make the intercalation and deintercalation process easier for lithium ions, resulting in a higher capacity and rate performance.

The impact of CNT structure on the electrochemical performance of the resulting LIBs has been widely studied and summarized below. (1) Chirality. Obviously, the electrochemical performances are different between metallic and semiconducting CNTs. A higher electrical conductivity favors the transport of both electrons and ions among the electrolyte, electrode, and current collector. It was reported that metallic SWCNTs performed a lithium ion storage capacity to be five times higher than semiconducting SWCNTs.<sup>296</sup> (2) Diameter. To certain degree, there existed a linear dependence between the diameter of the CNT and the capacity, and the lithium ion absorption energy and binding energy of CNTs were also dependent on the CNT diameter, so a larger diameter is favorable for a better electrochemical performance.<sup>297</sup> When the lithium ion was intercalated with SWCNTs, a larger curvature of the nanotubes would enhance the ion condensation inside the core and further enhance the interactions between the ion and CNT.<sup>298</sup> For the MWCNTs, the tension from the multilayered structure would be also influenced by the curvature of the nanotubes, so larger MWCNTs increased the lithium capacity performance.<sup>299,300</sup> (3) Length. Shorter CNTs provide more efficient pathways for the entrance of lithium ions, particularly, when the both ends are opened. Therefore, a lot of methods were explored to obtain short CNTs such as chemical etching, ball milling,<sup>301</sup> and frozen cutting<sup>302</sup> besides decreasing the synthetic time. For instance, a vertically aligned and penetrated MWCNT/epoxy resin film has been prepared through a slicing technology with both ends of MWCNTs being cut opened, and it exhibited a low resistivity of 10<sup>-4</sup> Ω cm in the vertical direction of the

composite film, enabling a high electrochemical performance in the LIB.<sup>303</sup> (4) Defects. As previously mentioned, the lithium ion intercalation occurs within the MWCNT layers through the lattice defects of side walls and open ends, so the introduction of defects in the walls of short SWCNTs displayed a high specific capacity of 1000 mAh/g, approaching the theoretical value of 1116 mAh/g calculated by a LiC<sub>2</sub> stoichiometry.<sup>294,295</sup> It was also found that, after etching by nitric acid and sulfuric acid, numerous defects were created on the surfaces of MWCNTs to enhance the reversible capacity from the untreated 351 to 681 mAh/g.<sup>304</sup> Of course, the purification of CNTs also plays a critical role on their electrochemical performance besides their structures as their conductivities would be generally decreased at lower purifications. A purified SWCNT paper reached a conductivity of 5 × 10<sup>5</sup> S/m and showed a reversible capacity of 450 mAh/g rather than 50 mAh/g for a raw SWCNT sample under the same condition.<sup>288</sup>

Both MWCNT and SWCNT suffer from a large first cycle insertion loss owing to the formation of solid–electrolyte interface (SEI) layer at around 0.9 V, resulting in a significant irreversible capacity loss in the first cycle. This problem is related to the interaction between the porous scaffold and electrolyte in a solvent decomposition process.<sup>305</sup> It was revealed that during the lithiation process for SWCNTs in half-cells, only the insertion under 0.25 V vs Li/Li<sup>+</sup> experienced a reversible delithiation (Figure 39). A longer alkyl-chained cosolvent, e.g., propylene carbonate and vinylene carbonate,<sup>306</sup> or a change in solvent composition could be helpful to induce

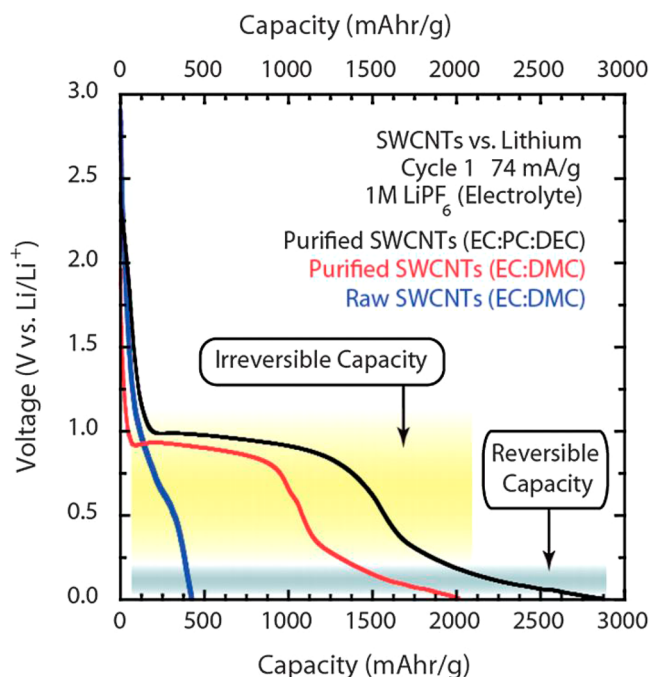


**Figure 39.** Galvanostatic cycling of SWCNT paper electrodes vs lithium metal for the first cycle of insertion. A comparison of raw SWCNTs (blue curve) and purified SWCNTs (red curve) using EC:DMC (1:2 v/v) illustrates the significantly higher reversible capacity after purification. The modification of electrolyte for purified SWCNTs using EC:PC:DEC (1:1:2 v/v) further enhanced the reversible capacity (black curve). The regions of the electrochemical cycling data attributed to reversible and irreversible capacities are marked by gray and yellow shaded regions, respectively. Reproduced with permission from ref 305. Copyright Elsevier (2008).

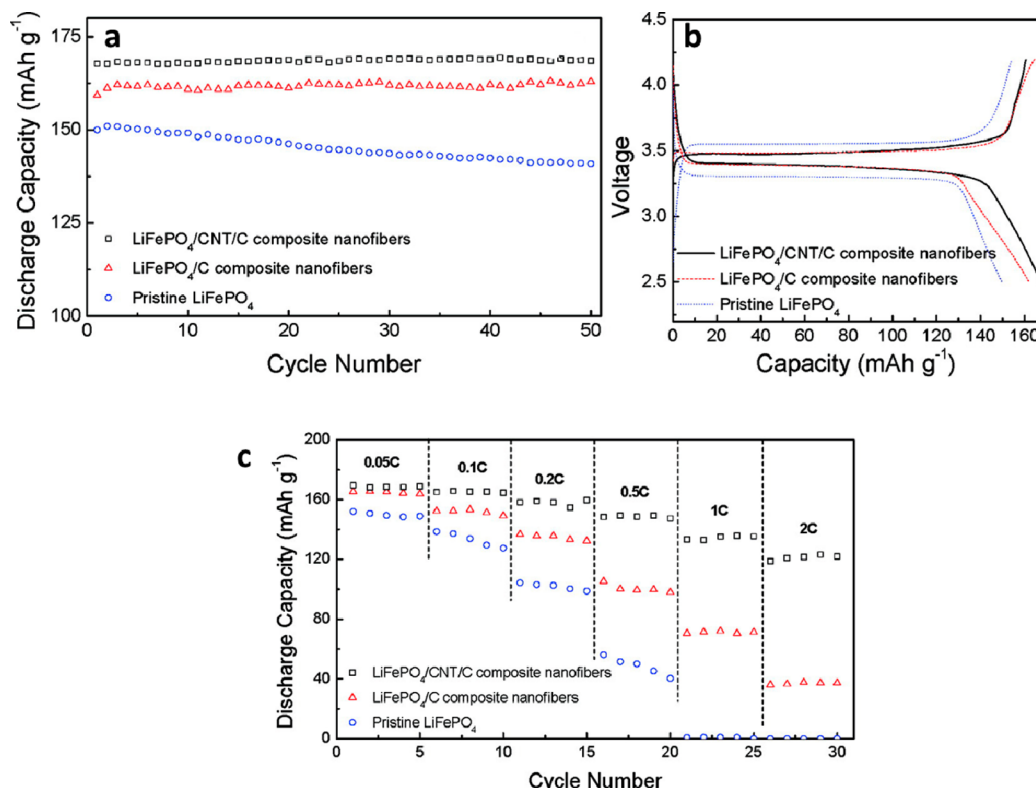


**Figure 40.** (a) Cycling performance, (b) initial voltage vs capacity curves, and (c) rate capabilities of pristine LiFePO<sub>4</sub> powder, LiFePO<sub>4</sub>/C composite nanofibers, and LiFePO<sub>4</sub>/CNT/C composite nanofibers, respectively. The charge–discharge rate used at (a) and (b) was 0.05 C. Reproduced with permission from ref 314. Copyright American Chemical Society (2008).

the reversible capacity.<sup>305,307–309</sup> Another attempt to improve the performance for CNTs is to make an elemental doping, and some anomalous-shaped CNT with more electro-active sites had been synthesized such as bamboo-shaped CNTs and CNTs with a quadrangular cross section. Heteroatoms on carbon surfaces dramatically enhanced specific capacitances by pseudocapacitive effects. Yun and co-workers found that N-doped and micropore-containing MWCNTs prepared by carbonization of nitrogen-enriched, polymer-coated MWCNTs produced a specific capacitance of 190.8 F/g, much higher than 48.4 F/g of pristine MWCNTs.<sup>310</sup> However, more efforts are still required to understand the formation of SEI layer and the exact effect of extra elements for the CNT electrode.

**4.1.1.2. CNTs as Conductive Additives.** Conductive additive is an important part of the LIB and facilitates the transport for both lithium ions and electrons. In recent years, nanosized active electrode materials with large surface areas and numerous active sites are attracting more applications. However, the commonly studied cathode active materials (e.g., LiFePO<sub>4</sub>, LiCoO<sub>2</sub>, LiNiO<sub>2</sub>, LiMn<sub>2</sub>O<sub>4</sub>, and alloys of the same species) are semiconductors or insulators with low electrical conductivities, while the corresponding anode active materials (e.g., alloys of Si and SnSb, Li<sub>4</sub>Ti<sub>5</sub>O<sub>12</sub>, graphite, and hard carbon spheres) are relatively easier to collapse during lithiation/delithiation processes. The conductive additives are required not only for good ionic and electrical conductivities, but also a capability to absorb and retain the electrolyte and hold the active material to restrict their volumetric changes.

CNTs had been widely added to the electrode as active materials and binders by physical blending. Compared with the conventional conductive carbon additives such as carbon black, acetylene black, super P, and graphite, the CNTs exhibited a

higher aspect ratio of length to diameter (>100) and lower weight load with a comparable conductivity for the whole electrode. Purified CNTs can achieve a high electrical conductivity of  $5 \times 10^5$  S/m at room temperature and provide one-dimensional rapid pathways with a flexible three-dimensional network structure. As a result, they could reach the same electrochemical performance by 1 order of magnitude lower than the conventional carbon additives in content. In addition, the CNTs show high thermal conductivities that are helpful to realize safer batteries. Wang and co-workers had compared CNTs with acetylene black and vapor-grown carbon fibers as conductive additions in the LiCoO<sub>2</sub> cathode.<sup>311</sup> The CNT-based cathode showed a higher capacity and better cyclic performance at a current density range of 0.01, 1, and 2 to 3 C. Li and co-workers discovered that CNTs exhibited higher electrochemical performance than Super P because CNTs were aggregated from resilient conductive bridges among the active particles, and these inner connections did not break even when the hybrid broke during the lithiation and delithiation process.<sup>312</sup> The same conclusions were made for CNTs by comparing them with acetylene black, vapor-grown carbon fibers and flake natural graphite as the anode.<sup>313</sup>

Recently, CNTs were further mixed with the other materials as multicomponent conductive additives to take advantages of two or more components and obtain a more adaptive structure. It is well-known that the particulate carbon tends to aggregate and lacks of connections with each other, while one-dimensional CNTs easily form a three-dimensional network. Therefore, when CNT and acetylene black were mixed as conductive additives, high rate capacity and cyclic life of the LiCoO<sub>2</sub> hybrid cathode had been both effectively achieved.<sup>307</sup> Here the particulate carbon served as an intermediary between

the active material and CNT network to increase the contact between  $\text{LiCoO}_2$  with conductive additives. This strategy represents a general and effective route to combine conductive carbon materials with different morphologies to realize synergistic effects. Two-dimensional carbon flakes and three-dimensional carbon fiber networks had been also mixed as additives.<sup>307</sup> The former component increased the conductivity within the active particle and electrolyte while the later component enhanced the retention of electrolyte, thus leading to an improved rate capacity of the hybrid electrode.

To summarize, cheap carbon powders were first used as conductive additives of LIBs among the carbon materials, and they still represent the main product that is available at the current market. To further enhance the electrochemical performance, a lot of efforts were later made to explore carbon nanomaterials including CNTs with an emphasis on the mixture of them with carbon powders, fibers, and films. A synergistic effect had been widely investigated to achieve much improved electrochemical properties. With the advancement in nanoscience and nanotechnology, the other carbon nanomaterials such as graphene and mesoporous carbon open a new avenue and will be discussed later.

**4.1.1.3. Carbon Nanotube-Based Cathodes.** Besides being simply blended with the electrode material, the CNTs may exhibit much more profound advantages by chemically bonding with active cathode materials. They could not only serve as the skeleton to attach the active cathode material but provide large specific surface area, fast transport pathways, and high mechanical strength and flexibility. When active materials are attached along the CNT bundles, each bundle or even each CNT acts as a current collector. On one hand, CNTs can be added to the precursor during the early synthetic process of the active material, so the CNTs will be penetrated through the active material to form a better inner connection. Here the CNTs are typically pretreated and modified with functional groups such as  $-\text{COOH}$ ,  $-\text{NH}_3$ , or  $-\text{OH}$  to favor the chemical connection between the CNT and active material. On the other hand, the CNTs may be grown within the active material to reach effective contacts at nanoscale.

Toprakci and co-workers demonstrated a CNT-loaded electrospun  $\text{LiFePO}_4$ /carbon hybrid nanofiber as the stable and binder-free cathode.<sup>314</sup> The CNTs that were pretreated with functional  $-\text{SOCl}_2$  groups had been first added to the  $\text{LiFePO}_4$  precursor and polyacrylonitrile as an electrospinning media and carbon source in *N,N*-dimethylformamide solution. The above mixture was electrospun to form hybrid nanofibers and then heated to obtain  $\text{LiFePO}_4/\text{CNT}/\text{C}$  nanofibers as freestanding electrodes. Compared with bare  $\text{LiFePO}_4$  and  $\text{LiFePO}_4/\text{C}$  hybrid without the use of CNTs, an obvious increase was found for the conductivity, cyclic performance, and rate performance (Figure 40). The functionalized CNTs increased the electrochemical performance of the  $\text{LiFePO}_4$  cathode by forming conducting bridges among  $\text{LiFePO}_4$  particles and enhancing the electron transport.

Based on the same strategy, some more complex structures had been designed for high performances. For instance, a porous  $\text{LiFePO}_4/\text{CNT}$  hybrid material was further synthesized by an *in situ* sol–gel process.<sup>315</sup> The CNTs were penetrated through and among the pores of  $\text{LiFePO}_4$  particles, and the formed hierarchical architecture greatly enhanced the electrochemical performance. The mechanism was explored by studying the reaction kinetics during the electrochemical process, and an obvious decrease in both R1 ( $-222 \text{ Ohm}$  of

the hybrid vs  $-420 \text{ ohm}$  of the pristine) and R2 ( $-56 \text{ ohm}$  of the hybrid vs  $-505 \text{ ohm}$  of the pristine) components was found. Here R1 corresponds to the SEI film, while R2 reflects the electronic and ionic resistance between the electrode and electrolyte. The lithium ion diffusion coefficients of bare  $\text{LiFePO}_4$  and  $\text{LiFePO}_4/\text{CNT}$  hybrid were further calculated to be around  $4.9 \times 10^{-15}$  and  $6.3 \times 10^{-13} \text{ cm}^2/\text{s}$ , respectively. Therefore, the diffusion of lithium ions, the rate-limiting step, was drastically promoted in the  $\text{LiFePO}_4/\text{CNT}$  hybrid. The decreased charge transfer resistance and increased lithium-ion diffusion agreed with the high specific capacity and rate performance.

A coaxial  $\text{MnO}_2/\text{CNT}$  array electrode was also prepared through the *in situ* growth of CNTs within the active cathode material.<sup>316</sup> Specifically,  $\text{MnO}_2$  nanotubes were first synthesized and then grown with CNTs by a CVD method. The  $\text{MnO}_2/\text{CNT}$  nanotube array maintained the highly aligned structure during the synthesis and was attached onto an Au current collector from one side (Figure 41). The coaxial structure

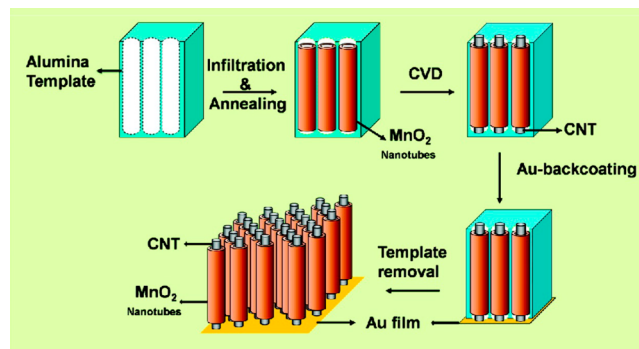


**Figure 41.** Schematic diagram showing the fabrication of  $\text{MnO}_2/\text{CNT}$  hybrid coaxial nanotube arrays inside AAO template using a combination of simple vacuum infiltration and CVD techniques. A thin layer of gold (100 nm) was sputter-coated to act as a current collector for the electrode. Reproduced with permission from ref 316. Copyright American Chemical Society (2009).

favored close and stable contacts between  $\text{MnO}_2$  and CNT and had effectively taken their advantages as the electrode. The highly conductive CNT core could not only offer a rapid electronic transport to the  $\text{MnO}_2$  shell but acted as an efficient buffer to alleviate the volume expansion of the  $\text{MnO}_2$  component. In addition, the CNTs also provided additional sites for lithium storage, leading to an enhanced reversible capacity by an order compared to the bare  $\text{MnO}_2$  nanotubes.

**4.1.1.4. Carbon-Nanotube-Based Anodes.** The difference between CNT-based hybrid cathodes and anodes is that the CNTs themselves have a capacity as the anode material. For the widely explored CNT networks without modifications, they typically display a specific capacity of approximately 100 mAh/g. Similar to the cathode, the CNTs also maintain high electronic and mechanical properties in the anode. The structure, composition, and functionalization play critical roles on the electrochemical performance. Figure 42 showed the design of core–sheath MWCNT/TiO<sub>2</sub> nanocables that were synthesized by controlled hydrolysis of tetrabutyl titanate in the presence of MWCNTs for the anode.<sup>317</sup> A totally reversible capacity of appropriately 406 mAh/g was obtained at a current density of 0.05 A/g compared with 74 mAh/g for the bare MWCNT without TiO<sub>2</sub>; the coaxial hybrid nanocables enabled a capacity of 244 mAh/g even at a high current density of 3 A/

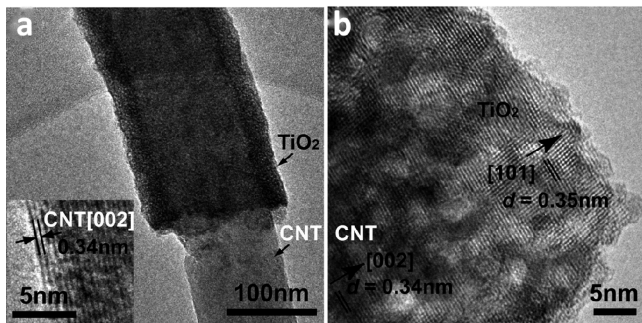


**Figure 42.** (a and b) TEM images of a coaxial CNT/TiO<sub>2</sub> nanocable and TiO<sub>2</sub> sheath, respectively. Reproduced with permission from ref 317. Copyright American Chemical Society (2010).

g, whereas the CNT-free TiO<sub>2</sub> nearly showed no capacity under the same condition. When the MWCNTs were further treated by acids, the capacities had been maintained by 90% when the current densities were increased from 0.8 to 5 A/g. An excellent cyclic performance with almost no capacity loss was also obtained after over 100 cycles at a current density of 1 A/g. The MWCNT core provided sufficient electrons for the TiO<sub>2</sub> sheath, while the TiO<sub>2</sub> sheath offered a high capacity ability, thus resulting in a rapid, high, and stable lithium storage.

When the active material was attached onto individual CNTs, the loaded active materials could be accurately controlled. For instance, MWCNTs had been deposited with a thin layer of SnO<sub>2</sub> to synthesize SnO<sub>2</sub>/CNTs composite fibers by a thioglycolic acid-assisted wet method,<sup>318</sup> the thickness of the active material in the sheath may be tuned by varying the pH value of the solution and hydrolysis time during synthesis. It was found that the formation of thinner SnO<sub>2</sub> layer increased both charge capacities and durability against decay. This phenomenon was ascribed to the good dispersion of SnO<sub>2</sub> nanoparticle on the surfaces of MWCNTs, which was beneficial to the utilization of SnO<sub>2</sub> and the release of the stress caused by the volume change during the lithiation/delithiation process.

Another anode active material, silicon, has been widely explored due to the high theoretical capacity (4200 mAh/g) and abundant source. However, the bulk Si electrode suffers from a huge volume change of 400% during lithiation/delithiation processes, leading to an intolerable capacity loss. CNTs are therefore introduced to the silicon to accommodate the volume change. For instance, a cage-like CNT/Si hybrid where the silicon particles were wrapped by a cage composed of CNT network had been designed to stabilize the silicon.<sup>319</sup> A flexible and efficient three-dimensional aligned CNT/Si hybrid electrode had been also produced by depositing silicon onto an aligned CNT sheet, followed by a perpendicular growth of an aligned CNT array on the Si which had been decorated with a catalyst of Fe (1.2 nm)/Al<sub>2</sub>O<sub>3</sub> (3 nm).<sup>320–322</sup> The silicon was sandwiched between the aligned CNT sheet and array, and the aligned CNT materials provided the composite with a high electrical conductivity and effective buffer layers. A specific capacity of 2562 mAh/g was achieved at a current density of 1 A/g with 93% retention after 100 cycles, and it reached 1055 mAh/g after 1000 cycles at 5 A/g. Based on the same strategy, an aligned CNT/silicon hybrid fiber electrode was also developed by depositing silicon onto the outer surfaces of individual MWCNTs of a highly aligned sheet, followed by rolling into a hybrid yarn.<sup>320</sup> This fiber anode showed a much higher specific capacity of around 1500 mAh/g

at a current density of 2 A/g compared with the other fiber-shaped electrodes. In almost all studies, the CNTs mainly play roles of conductive additions, volume changing buffers, and skeletons for flexible and freestanding electrodes.

**4.1.2. Graphene.** Although graphite has been used as the most common anode material due to high reversibility and long cycling life in lithium storage, the theoretical specific lithium insertion capacity is relatively low, i.e., 372 mAh/g, as one Li ion interacts with six carbon atoms. For a single-layered structure, graphene can store Li ions on both sides, so theoretically it may provide a specific capacity two times that of graphite; it may enable even a higher capacity in practical applications due to much larger specific surface areas of graphene materials. In addition, the graphene sheet can serve as two-dimensional substrates for the growth of various active anode or cathode materials for lithium storage.<sup>65,323–326</sup>

**4.1.2.1. Anode.** As an anode material, the theoretical maximal capacity of graphene was calculated to be 740 mAh/g by forming Li<sub>2</sub>C<sub>6</sub> during lithium storage.<sup>327</sup> If the graphene sheets were small enough with a diameter of 0.7 nm, Li<sub>4</sub>C<sub>6</sub> can be formed to enable a capacity of 1488 mAh/g.<sup>325,328</sup> In real applications, the capacitors were relative lower but much higher than the theoretical value of graphite. A specific capacity of 540 mAh/g was produced for the graphene anode in 2008;<sup>329</sup> a higher specific capacity of above 1600 mAh/g was achieved at 0.1 C (1C = 0.744 A/g) during the first cycle, and a rechargeable specific capacity of 887 mAh/g was obtained at 0.1 C.<sup>330</sup> The irreversible capacity was often observed for LIBs based on graphene anodes due to the formation of SEI on the electrode surface.<sup>325,330,331</sup> The capacities turned out to be stable in the following cycles after the first cycle and displayed high rate performance and cyclic reversibility.

Nitrogen and/or boron doping can further improve the Li storage properties of graphene.<sup>332–334</sup> Ajayan and co-workers synthesized nitrogen-doped graphene on a Cu current collector through a CVD method in NH<sub>3</sub> gas,<sup>332</sup> and the reversible discharge capacity had been improved by one time compared with the pristine graphene. Cheng and co-workers had further prepared N- and B-doped graphene after a heating treatment of pristine graphene in NH<sub>3</sub>/Ar at 600 °C and BC<sub>13</sub>/Ar at 800 °C, respectively.<sup>333</sup> The doped graphene exhibited a high reversible capacity of above 1040 mAh/g at 0.05 A/g. In addition, the N- and B-doped graphene exhibited a good high-rate capability with 199 and 235 mAh/g at 25 A/g, respectively. In other words, they showed both high power and energy capacities. The remarkable Li storage performance of doped graphene was ascribed to the large number of surface defects induced by N- or B-doping to enable improved electrical conductivity, increased intersheet distance and better electrode/electrolyte wettability. Recently, however, a theoretical study also suggested that not all the nitrogen doping can improve the Li storage capacity of graphene. Instead, only N-decorated single and double vacancy defects, especially the pyridinic N<sub>2</sub>V<sub>2</sub> defect in graphene could greatly improve the reversible Li storage capacity.<sup>334</sup> It was predicted that the reversible Li storage capacity of N-doped graphene would be 1039 mAh/g that was close to the experimental result of 1040 mAh/g.<sup>333</sup>

Graphene had been also mixed with the other carbon nanomaterials such as fullerene, CNTs, and porous carbon materials to improve the Li storage performance.<sup>329,335–337</sup> As mentioned above, the Li intercalation capacity of graphene can reach 540 mAh/g. After formation of hybrid materials with CNT or fullerene by mixing GO with acid treated-CNTs or

fullerene followed by reduction, the capacities had been accordingly improved to 730 or 784 mAh/g, and they turned out to be 480 or 600 mAh/g after 20 cycles, respectively.<sup>329</sup> It was found that the reversible capacities of the hybrids were greatly affected by the distance between two neighboring graphene layers, and the distance further depended on the interaction between graphene and CNT or fullerene. For multilayered graphene/CNT hybrids synthesized by an *in situ* growth, the lengths of used CNTs played a critical role on the electrochemical performance.<sup>335</sup> The shortest CNTs exhibited a capacity of 573 mAh/g at 0.074 A/g, and it was maintained at 518 mAh/g after 30 cycles.<sup>329,335</sup> Note that a more homogeneous and stable structure had been produced for the hybrid by the *in situ* growth. As expected, the graphene/CNT ratio was also a key to the electrochemical performance of the hybrid.<sup>337</sup> For the graphene/CNTs hybrid film, the optimal ratio occurred at 1/2 with the highest Li storage capacity of 375 mAh/g at 0.1 A/g; the capacitor could be maintained above 330 mAh/g after 100 cycles. To summarize, the size, structure, and proportion of the carbon nanomaterial hybrid are important for their electrochemical performances, and their impacts may depend on different systems.

Similar to the CNT, graphene had been also widely incorporated into silicon to decrease or even prevent its volume change.<sup>338–347</sup> Silicon nanoparticles could be easily deposited onto graphene sheets by mixing a silicon nanoparticle suspension and GO suspension, followed by filtration to form a composite film.<sup>339</sup> The resulting composite film was self-supported and exhibited a Li storage capacity of >2200 mAh/g after 50 cycles and >1500 mAh/g after 200 cycles. The thickness of the composite film was expected to be critical to the electrochemical property based on the fact that Li ions were diffused through the bulk film. To further improve the uniformity of the dispersion of Si nanoparticles on graphene, Guo and co-workers figured out a self-assembly approach based on the interaction between negatively charged GO and positively charged poly(diallyldimethylammonium chloride)-modified Si nanoparticles, followed by thermal reduction.<sup>342</sup> The solution process has now been developed as a general and effective strategy in the preparation of silicon with graphene.

The graphene/silicon hybrids had been also prepared by mechanically blending graphene with Si aggregates together.<sup>341</sup> Here graphene sheets were first synthesized by expanding graphite after being rapidly heated to high temperatures. The resulting hybrids were homogeneous and exhibited not only excellent cycling performance but also high Li storage capacity of 2753 mAh/g. Similarly, the graphene/Si composite could be synthesized by bending graphene and silicon nanomaterial through an *in situ* vapor deposition (Figure 43), and the same high Li storage capacity of >2000 mAh/g at 0.14 A/g was achieved.<sup>343</sup>

Silicon nanowires had been also extensively investigated for LIBs due to the unique one dimension for high specific surface areas. Generally, silicon nanowires were first synthesized via a CVD vapor–liquid–solid growth method and were then mixed with GO aqueous solution, followed by a vacuum filtration to form a hybrid film.<sup>347</sup> The GO/silicon hybrid film was thermally reduced to obtain the desired graphene/silicon film that exhibited a specific capacity of ~3350 mAh/g at 0.84 A/g. The high capacity had been well maintained after over 20 cycles. The high electrochemical performances of these flexible binder-free graphene/silicon nanowire electrodes should be ascribed to the fact that graphene accommodated the volume

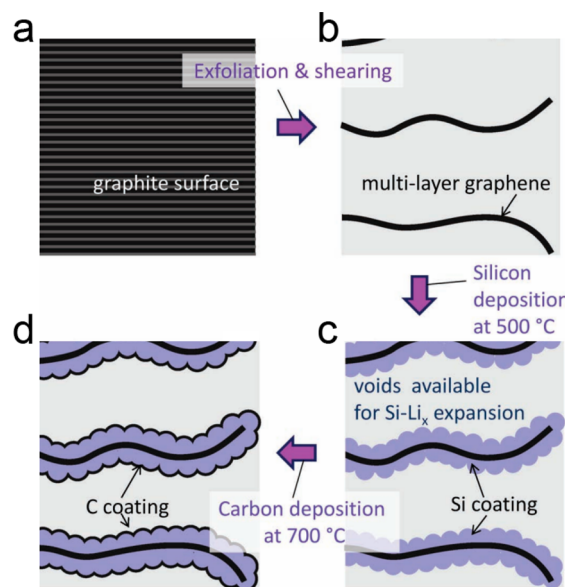


**Figure 43.** Schematic illustration to the formation of C/Si/graphene composite. (a) Natural graphite. (b) Exfoliated graphene. (c) Si nanoparticles-coated graphene. (d) A thin C layer-coated Si/graphene hybrid. Reproduced with permission from ref 343. Copyright John Wiley and Sons (2011).

change of silicon and facilitated the transport of electrons and Li ions. To further improve the surface area, porous single-crystalline silicon nanowires were synthesized through liquid-phase graphite exfoliation method and etching process and attached with graphene sheets. A high capacity of 2041 mAh/g was maintained after 20 cycles, and the capacity at 2 C was ~75% of that at 0.1 C. Besides the favorable charge-transmitting role of graphene, the kinetics-facilitating and nanostructure-stabilizing role of the porous Si nanowires were also responsible for the high performance above.<sup>338</sup> To enhance the interaction between the graphene and silicon nanowire, core–shell graphene/silicon nanowire electrodes were prepared through a vacuum filtration and used without polymer binders.<sup>346</sup> The cycle performance was enhanced with more than 90% of the initial capacity after 50 cycles because of the hybrid structure. Moreover, the use of hot-pressing which binds the electrode onto the current collector without any polymer binder also benefits the development of binder free anodes.

Graphene sheets possess a lot of in-plane vacancies that favor the cross-plane ion diffusivity and are deformable, so they can be used as three-dimensional, flexible, conducting scaffolds to improve the rate performance.<sup>340</sup> The resulting graphene/silicon electrode exhibited Li storage capacities of 3200 mAh/g at 1 A/g and 1100 mAh/g at 8 A/g. In addition, the hybrid electrode was self-supported and flexible (Figure 44), and the high rate performance was also partly contributed from the self-supported state without any polymer binder that typically exhibited a low electrical conductivity. Based on a similar strategy, a lot of reports are available for the freestanding, flexible graphene/silicon hybrid electrodes, particularly, based on solution processes.<sup>344,345</sup> For instance, Guo and co-workers prepared such hybrid electrodes through a spin-coating method,<sup>345</sup> and the capacity reached 1611 mAh/g at 1 A/g after 200 cycles. In addition, the capacity had been maintained at 74% after 200 cycles.

Due to a high theoretical capacity, easy synthesis and low cost, metal oxide is widely investigated as an active anode

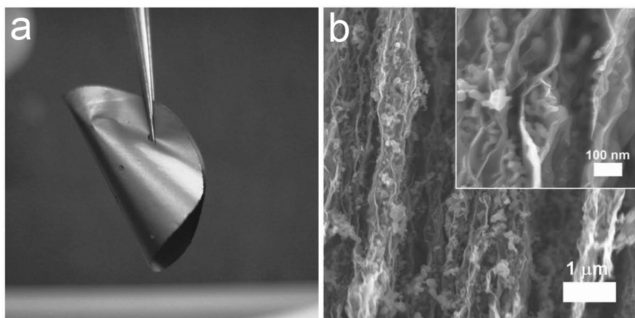


**Figure 44.** (a) Photograph and (b) SEM image of a Si/graphene hybrid paper by a side view, respectively. Si nanoparticles were uniformly embedded among graphene sheets. Reproduced with permission from ref 340. Copyright John Wiley and Sons (2011).

material. The most explored metal oxide includes  $\text{SnO}_2$ ,  $\text{Co}_3\text{O}_4$ ,  $\text{Fe}_x\text{O}_y$ ,  $\text{Mn}_x\text{O}_y$ ,  $\text{TiO}_2$ , and  $\text{NiO}$ .<sup>323,352</sup> Six structures are generally developed for graphene/metal oxide hybrid materials (Figure 45), i.e., metal oxide nanoparticles anchored on

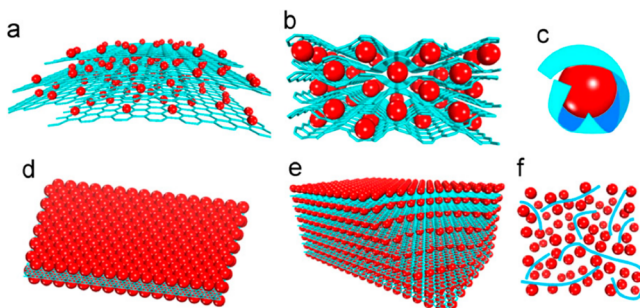
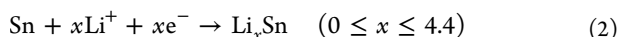
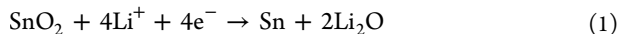


**Figure 45.** Schematic illustration to the structural models of graphene/metal oxide hybrids: (a) anchored model, (b) wrapped model, (c) encapsulated model, (d) sandwich-like model, (e) layered model, and (f) mixed model. Red particles stand for metal oxide particles while blue sheets or lines stand for graphene sheets. Reproduced with permission from ref 352. Copyright Elsevier (2012).

graphene sheets, graphene-wrapped metal oxide nanoparticles, graphene-encapsulated metal oxide nanoparticles, sandwiched hybrid where graphene serves as a template for the growth of metal oxides, layered hybrid, and three-dimensional conductive graphene networks among metal oxides.  $\text{SnO}_2$  with a high theoretical capacity of 1494 mAh/g had recently attracted a lot of attentions and are first explored as a demonstration.<sup>348–355</sup> The theoretical capacity is calculated from the following equations.



A series of methods have been developed to synthesize graphene/ $\text{SnO}_2$  hybrid materials on the basis of the use of graphene or GO sheets and  $\text{SnO}_2$  nanoparticles. One, they could be made by directly mixing graphene sheets and  $\text{SnO}_2$  nanoparticles, and the following aggregation of graphene nanosheets in the presence of  $\text{SnO}_2$  nanoparticles produced the required hybrid.<sup>348</sup> The hybrid electrode exhibited a reversible Li storage capacity of 810 mAh/g and enhanced cycling performance of 570 mAh/g after 30 cycles, much higher than 60 mAh/g of bare  $\text{SnO}_2$  nanoparticles after 15 cycles.

Two, to improve their interactions for uniform hybrids, graphene/ $\text{SnO}_2$  materials had been prepared through a layer-by-layer assembly by stacking oppositely charged  $\text{Sn}^{2+}$ -anchored GO and amine-functionalized graphene sheets, followed by reduction of GO sheets.<sup>355</sup> A high and stable reversible Li ion storage capability was expected during charging–discharging cycles, e.g., 872 mAh/g after 200 cycles at 0.1 A/g. Three, the graphene/ $\text{SnO}_2$  materials may be also prepared by an in situ synthesis in a GO and  $\text{SnCl}_2$  aqueous mixture solution, followed by heating to reduce GO to graphene and  $\text{Sn}^{2+}$  to Sn nanoparticles to form uniform hybrids.<sup>349</sup> Sn nanoparticles were then oxidized to  $\text{SnO}_2$  nanoparticles. The graphene/ $\text{SnO}_2$  powders were typically made into a hybrid electrode with the assistance of a binder such as PVDF. The resulting LIB exhibited reversible Li storage capacities of 765 mAh/g that was close to the theoretical capacity of 777.2 mAh/g (weight ratio of graphene/ $\text{SnO}_2$ , 60/40) at the first cycle and retained 520 mAh/g after 100 cycles. Four, to improve the synthetic efficiency, a rapid synthesis was achieved by using a microwave heater to reduce GO with  $\text{Sn}^{2+}$ ,<sup>350</sup> and the derived LIB exhibited capacities of 600 mAh/g after 50 cycles and 550 mAh/g after 100 cycles. Five, small  $\text{SnO}_2$  nanoparticles with high specific surface areas were a key to high electrochemical performances. Through a gas–liquid interfacial synthesis to make hybrid materials with small  $\text{SnO}_2$  nanoparticles (2–6 nm in diameter),<sup>351</sup> highly reversible Li ion storage capacities of 1304 mAh/g at 0.1 A/g and 748 mAh/g even at 0.1 A/g were obtained.

These hybrid materials had been also synthesized starting from CNTs that were unzipped into graphene nanoribbons. The resulting graphene/ $\text{SnO}_2$  hybrids enabled Li ion storage capacities of 825 mAh/g at 0.1 A/g after 50 cycles and 580 mAh/g at 2 A/g.<sup>349</sup> Here the LIB can be further enhanced by coating the graphene/ $\text{SnO}_2$  composite with a thin layer of polydopamine that was cross-linked with poly(acrylic acid) (PAA).<sup>353</sup> The modified graphene/ $\text{SnO}_2$  hybrid exhibited a much improved specific capacity of 718 mAh/g at 0.1 A/g after 200 cycles and good rate performances of 811, 641, and 512 mAh/g at 0.1, 0.5, and 1 A/g, respectively. The good electrochemical performance, particularly the high stability, was attributed to the cross-linked PAA/polydopamine that provided a robust network in the composite anode.

Besides the physical mixtures above,  $\text{SnO}_2$  nanocrystals had been also bonded onto N-doped graphene sheets to fabricate LIBs with high capacity, excellent rate capability, and long cycle life.<sup>354</sup> At 0.5 A/g, after the formation of SEI, the hybrid exhibited a reversible capacity of 1021 mAh/g, corresponding to 1352 mAh/g based on  $\text{SnO}_2$  that was close to its theoretical value of 1494 mAh/g. In addition, the hybrid exhibited a capacity of 1346 mAh/g after 500 cycles at 0.5 A/g and good rate performances of 994, 782, 631, and 417 mAh/g at 1, 5, 10, and 20 A/g, respectively. The excellent performance of the chemically bonded hybrid was mainly attributed to two main factors. On the one hand, Sn–N bonds between  $\text{SnO}_2$  nanocrystal and N-doped graphene sheet could well stabilize  $\text{SnO}_2$  nanocrystals and prevented aggregation of  $\text{SnO}_2$  nanoparticles during cycling. On the other hand, N-doped graphene sheets had effectively provided electrons and enhanced the Li electrochemical activity of  $\text{SnO}_2$  nanocrystals.

$\text{Co}_3\text{O}_4$  with a theoretical capacity of 890 mAh/g represents another important metal oxide as the anode material.  $\text{Co}_3\text{O}_4$  had been incorporated with graphene mainly through an in situ conversion of cobalt salts and assembly of oppositely charged

components.<sup>356–363</sup> For instance, the graphene/Co<sub>3</sub>O<sub>4</sub> composite was synthesized from an intermediate product of Co(OH)<sub>2</sub>,<sup>356</sup> and it exhibited a Li storage capacity of 935 mAh/g after 30 cycles at 0.05 A/g; positively charged Co<sub>3</sub>O<sub>4</sub> nanoparticles and GO were mixed and alternately stacked into hybrid materials by their electrostatic interactions, followed by reduction of GO/Co<sub>3</sub>O<sub>4</sub> into graphene/Co<sub>3</sub>O<sub>4</sub>.<sup>357</sup> The composite produced a higher capacity of 1100 mAh/g at 0.074 A/g and 1000 mAh/g after 130 cycles possibly due to the layered structure.

The other methods were also explored to synthesize graphene/Co<sub>3</sub>O<sub>4</sub> hybrid materials. Wang and co-workers developed a microwave-assisted synthesis to prepare graphene/Co<sub>3</sub>O<sub>4</sub> sheet-on-sheet hybrid with a high capacity of 1162 mAh/g at 0.445 A/g and high rate capacity of 931 mAh/g at 5 C (4.45 A/g).<sup>358</sup> The improvements were attributed to the synergistic interactions of graphene and Co<sub>3</sub>O<sub>4</sub> nanosheets. More specifically, the aggregation of graphene nanosheets was prevented by Co<sub>3</sub>O<sub>4</sub> nanosheets, and the electrical conductivity and mechanical stability of graphene/Co<sub>3</sub>O<sub>4</sub> nanosheet hybrids were also enhanced in a comparison to Co<sub>3</sub>O<sub>4</sub> nanosheets. Through a one-step hydrothermal method, Xiao and co-workers synthesized three kinds of Co<sub>3</sub>O<sub>4</sub> crystals with different structures.<sup>359</sup> The shape control of Co<sub>3</sub>O<sub>4</sub> and effect of the crystal plane on the electrochemical performance were carefully investigated. Compared with a cube with the (001) plane and a truncated octahedron with (001), the Co<sub>3</sub>O<sub>4</sub> octahedron with the (111) plane exhibited a better electrochemical performance with the highest capacity and best rate capability. These hybrid materials could be also synthesized through a hydrothermal method via direct reactions between GO and Co powder, and GO was reduced by the metal powder in water.<sup>360</sup> This hybrid enabled a reversible capacity of ~800 mAh/g after 100 cycles. Recently, a binder-free and freestanding graphene/Co<sub>3</sub>O<sub>4</sub> hybrid film had been achieved through vacuum filtration and thermal treating,<sup>362</sup> and graphene and Co<sub>3</sub>O<sub>4</sub> were assembled together via electrostatic interactions. A high specific capacity of 1400 mAh/g at 0.1 A/g and excellent cyclic stability were produced in the resulting LIBs.

The other metal oxide includes Fe<sub>3</sub>O<sub>4</sub>,<sup>364–368</sup> Fe<sub>2</sub>O<sub>3</sub>,<sup>369,370</sup> MnO,<sup>371</sup> Mn<sub>3</sub>O<sub>4</sub>,<sup>372,373</sup> NiO,<sup>374</sup> MoO<sub>2</sub>,<sup>375</sup> CuO,<sup>376</sup> and TiO<sub>2</sub>.<sup>377</sup> Among them, Fe<sub>3</sub>O<sub>4</sub> has been widely studied due to a low cost, abundance, easy synthesis and high theoretical capacity of 926 mAh/g. Similarly, a lot of methods had been investigated to synthesize graphene/Fe<sub>3</sub>O<sub>4</sub> composites to realize high-performance LIBs.<sup>364–368</sup> They were generally prepared through an in situ reduction of iron hydroxide on reduced GO and exhibited a high capacity of 1026 mAh/g after 30 cycles at 0.035 A/g.<sup>364</sup> The higher capacity than the theoretical value was attributed to the reaction of oxygen-containing functional groups on reduced GO sheets with lithium ions. Some modifications were explored to further improve the electrochemical performance. Wu and Cao had incorporated carbon onto the graphene/Fe<sub>3</sub>O<sub>4</sub> hybrid with a core–shell nanostructure where the carbon shell can tackle the deformation of Fe<sub>3</sub>O<sub>4</sub> nanoparticles without decrease of the conductivity and catalytic activity of graphene/Fe<sub>3</sub>O<sub>4</sub> hybrid.<sup>367,368</sup> As a result, the cyclic stability had been improved with the capacity of 900 mAh/g after 100 cycles at 0.2 A/g. In contrast, the graphene/Fe<sub>3</sub>O<sub>4</sub> hybrid without the carbon shell can only maintain a capacity of 450 mAh/g under the same condition. Recently, Feng and co-workers designed a graphene/Fe<sub>3</sub>O<sub>4</sub> hybrid by cross-linking three-dimensional graphene

foams with pre-encapsulated Fe<sub>3</sub>O<sub>4</sub> nanospheres. Fe<sub>3</sub>O<sub>4</sub> nanospheres were first wrapped by graphene sheets and then confined within continuous graphene networks. Therefore, a double protection was provided against the volume changes of Fe<sub>3</sub>O<sub>4</sub> nanospheres during charging–discharging processes. The networked graphene/Fe<sub>3</sub>O<sub>4</sub> hybrid exhibited a reversible capacity of 1059 mAh/g after 150 cycles at 0.093 A/g and a rate capacity of 363 mAh/g at 4.8 A/g.

To summarize, in the graphene/metal oxide hybrid anode, graphene serves as a flexible and conductive substrate with high specific surface area to load metal oxide moieties and prevent their aggregations and volume changes; metal oxide prohibits the restacking of graphene sheets and provides a high lithium storage capacity. The synergistic effects of graphene and metal oxide provide high lithium storage performances. In many hybrids, a porous nanostructure is often designed to further facilitate the lithium ion transport. However, there remain several critical problems, the volume change needs to be further effectively prohibited to improve the cyclic stability, the electrical conductivity should be enhanced to reach higher rate performance and power density, and the hybrid electrode is required to be lighter and smaller.

**4.1.2.2. Cathode.** Similar to the CNT, bare graphene does not provide a capacity for lithium storage as a cathode as the bare carbon materials store lithium with a potential around 0.05 V, which is too low to meet the requirement of a cathode.<sup>323</sup> However, functionalized graphene may exhibit specific capacities up to 250 mAh/g at a potential range of 1.5–4.5 V.<sup>378,379</sup> The introduced functional groups on graphene nanoplatelets can serve as redox centers to show high performances in cathode applications. Besides, graphene generally acts as a conductive agent to improve the electrical conductivity of the cathode. It can also prevent the aggregation of the active components. In addition, due to the excellent mechanical property, graphene can simultaneously serve as a binder to prepare flexible binder-free electrodes.

Among various active cathode materials, the most investigated systems include LiMO<sub>2</sub> (M = Co, Mn, and Ni), LiM<sub>2</sub>O<sub>4</sub> (M = Mn, Co, and Ni), and LiMPO<sub>4</sub> (M = Fe, Co, Ni, and Mn).<sup>323–325,380,381</sup> Here graphene hybrids with LiMn<sub>2</sub>O<sub>4</sub> and LiFePO<sub>4</sub>, two main cathode materials for electric vehicles, are taken as examples and mainly discussed. Similar to the graphene/metal oxide hybrid for the anode, physically mixing and *in situ* growth represent two main methods in the synthesis of graphene/LiMn<sub>2</sub>O<sub>4</sub> and graphene/LiFePO<sub>4</sub> hybrid materials.<sup>382–388</sup>

For a typical synthesis through the physically mixing method, graphene was first mixed with LiFePO<sub>4</sub> in solutions, followed by evaporation to form a composite.<sup>382</sup> Graphene acted as a conductive additive in a “plane-to-point” conducting mode and thus exhibited a better performance than CNTs that showed a lower contacting fraction. The graphene/LiFePO<sub>4</sub> hybrid electrode exhibited a specific capacity of ~150 mAh/g at 0.1 C and the capacity can be well maintained after 20 cycles. Liu and co-workers had enhanced the graphene/LiFePO<sub>4</sub> hybrid through spray-drying and annealing processes based on as-synthesized LiFePO<sub>4</sub> nanoparticles and GO nanosheets.<sup>383</sup> At 10 C charge and 20 C discharge rates, a specific capacity of ~110 mAh/g was achieved and maintained by 85% after 1000 cycles. Moreover, the specific capacity reached 70 mAh/g even at a high rate of 60 C. A high crystallization degree was maintained by the physically mixing process as the sizes and

structures of both graphene sheets and LiFePO<sub>4</sub> nanoparticles could be well controlled.

The *in situ* growth has been widely explored to synthesize more homogeneous graphene/LiFePO<sub>4</sub> hybrid materials. For instance, an *in situ* sol–gel method was used to coat carbon onto LiFePO<sub>4</sub>, followed by a thermal treatment at 700 °C in the presence of carbon sources.<sup>384</sup> The resulting hybrid was observed to be graphene-rich with a porous structure and exhibited a specific capacity of 153 mAh/g at 0.1 C. An *in situ* transformation approach to directly grow LiFePO<sub>4</sub> nanocrystals on graphene using Fe<sub>2</sub>O<sub>3</sub> as precursor also produced the high quality graphene/LiFePO<sub>4</sub> hybrid that exhibited a high specific capacities of 160 mAh/g at 1 C without fading after 100 cycles.<sup>386</sup> The specific capacity could be increased to 167.7 mAh/g that was close to the theoretical specific capacity of LiFePO<sub>4</sub> at 0.1 C through *in situ* pyrolysis and catalytic graphitization.<sup>387</sup> A uniform decoration and intimate contact between graphene and LiFePO<sub>4</sub> increased both electrical and ionic conductivities that enabled the remarkable electrochemical performance above.

Flexible LIBs had been also realized from the graphene/LiFePO<sub>4</sub> hybrid electrode (Figure 46) with LiFePO<sub>4</sub>/graphene

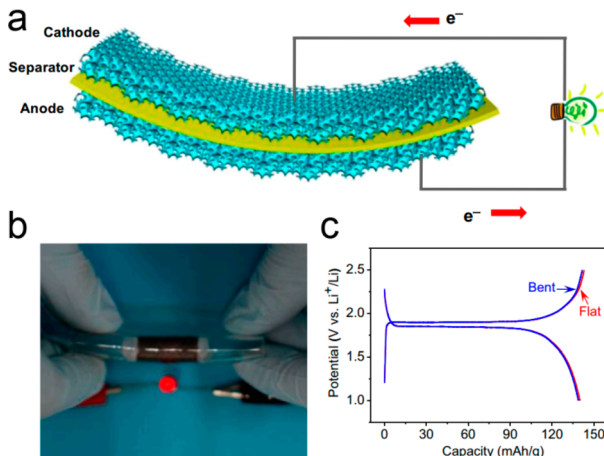


**Figure 46.** (a) Schematic illustration to the flexible LIB using LiFePO<sub>4</sub>/graphene and Li<sub>4</sub>Ti<sub>5</sub>O<sub>12</sub>/graphene as cathode and anode, respectively. (b) A red light emission diode being lightened up by a flexible LIB under bending. (c) Galvanostatic charging/discharging curves of the LIB before and after bending. Reproduced with permission from ref 388. Copyright PNAS (2012).

and Li<sub>4</sub>Ti<sub>5</sub>O<sub>12</sub>/graphene as cathode and anode, respectively.<sup>388</sup> The capacity had been well maintained under bending. These flexible LIBs are particularly promising to power various portable electronic devices and represent a new direction in the future.

**4.1.3. Mesoporous Carbon.** Porous carbon has been widely used as a conductive additive in both cathode and anode, e.g., carbon blacks like super P and XC-72 represent the most explored conductive additives.<sup>389</sup> With the tunable pore size and wall thickness, high pore volume and surface area, inner connection among pore channels and easy functionalization, porous carbon was found to be an ideal matrix to incorporate active materials. The porous structure may provide solutions to many problems in batteries such as low electrical conductivity, large volume expansion, and dissolution in electrolyte.

**4.1.3.1. Bare OMC Electrodes.** CMK-3, a widely studied OMC with ordered three-dimensional hexagonal structure, exhibited a lithium extraction potential range of 0.1–0.5 V and initial capacity of 3100 mAh/g, corresponding to a lithiated composition of Li<sub>8.4</sub>C<sub>6</sub>.<sup>390</sup> Generally, a reversible capacity of 850–1100 mAh/g was observed. It had been further found that the morphology also played a key role on the electrochemical performance of CMK-3. Yu and co-workers had recently compared rod-shaped OMC materials with different lengths and concluded that the shortest rods exhibited the highest reversible discharge capacity of 1012 mAh/g at 0.1 A/g and best cyclability with 86.6% retention of initial capacity after 100 cycles (Figure 47).<sup>391</sup> Obviously, shorter mesoporous channels

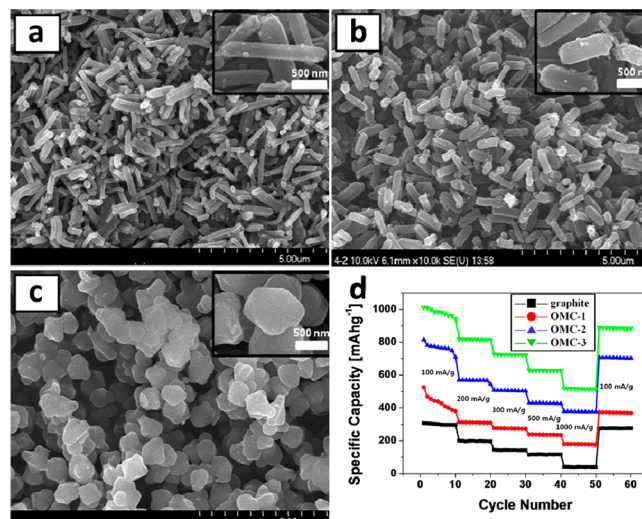


**Figure 47.** SEM images of OMC at different sizes. (a) OMC-1 with  $S_{\text{BET}}$  of  $711 \text{ m}^2 \text{ g}^{-1}$  and pore size of 3.2 nm. (b) OMC-2 with  $S_{\text{BET}}$  of  $1022 \text{ m}^2 \text{ g}^{-1}$  and pore size of 3.3 nm. (c) OMC-3 with  $S_{\text{BET}}$  of  $1220 \text{ m}^2 \text{ g}^{-1}$  and pore size of 3.4 nm. (d) Rate performances of commercial graphite and OMC at increasing current densities from 100 to 1000  $\text{mA g}^{-1}$  and then back to 100  $\text{mA g}^{-1}$ . Reproduced with permission from ref 391. Copyright American Chemical Society (2013).

provided a more rapid diffusion and transport for lithium ion and electrolyte as well as both lower solid electrolyte interphase resistance and contact resistance. Note that although the Coulombic efficiencies were relatively low at the beginning, they were rapidly improved to a high level within 10 cycles. To further increase the electrical conductivity of OMC for better electrochemical performance, it can be bridged by highly conducting CNTs.<sup>392</sup> In a typical synthesis, the electrical conductivity was increased from 138 to 645 S/m, resulting in a longer life stability and higher rate capacity in the LIB.

**4.1.3.2. OMC Based Hybrid Electrodes.** A wide variety of active materials, particularly transition metal oxides such as FeOx, SnO<sub>2</sub>, NiO, V<sub>2</sub>O<sub>5</sub>, and MoO<sub>2</sub>, have been integrated into OMC materials. In most cases, the related precursors are injected into the mesoporous channels, followed by chemical reactions to form the corresponding active oxides. These hybrids have taken the advantages of the metal oxides with high specific capacities and the OMC's three-dimensional ordered structure as both current collector and conductive agent. The OMC/metal oxide hybrid alleviates the capacity fading by restricting the volume change and reducing the surface pulverization during the lithium ion intercalation and deintercalation processes.

Table 4. OMC Materials for LIBs

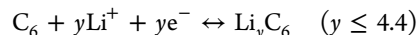
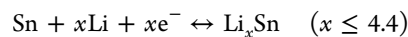
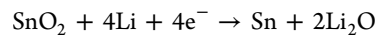
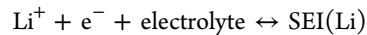
| material                                | specific capacity  | $S_{\text{bet}}$ ( $\text{m}^2 \text{ g}^{-1}$ ) | retention               | ref |
|---|--|--|-------------------------|-----|
| PPy-coated $\text{Fe}_2\text{O}_3$ /OMC | 528 $\text{mAh g}^{-1}$ at 1000 $\text{mA g}^{-1}$   | 303  | 97% (2 to 100 cycles)   | 394 |
| $\text{Fe}_2\text{O}_3$ /OMC            | 683 $\text{mAh g}^{-1}$ at 200 $\text{mA g}^{-1}$ and 430 $\text{mAh g}^{-1}$ at 1500 $\text{mA g}^{-1}$ | 688  | 99% (2 to 100 cycles)   | 395 |
| $\text{FeO}_{x'}$ /OMC                  | 660 $\text{mAh g}^{-1}$ at 100 $\text{mA g}^{-1}$ and 320 $\text{mAh g}^{-1}$ at 1600 $\text{mA g}^{-1}$ | 607  | 38% (50 cycles)         | 396 |
| $\text{SnO}_2$ /OMC                     | 978 $\text{mAh g}^{-1}$ at 200 $\text{mA g}^{-1}$ and 600 $\text{mAh g}^{-1}$ at 1500 $\text{mA g}^{-1}$ | 383  | 106% (10 to 100 cycles) | 397 |
| $\text{SnO}_2$ /OMC                     | 769 $\text{mAh g}^{-1}$ at 100 $\text{mA g}^{-1}$ and 440 $\text{mAh g}^{-1}$ at 1600 $\text{mA g}^{-1}$ | 303  | 55% (2 to 100 cycles)   | 398 |
| $\text{SnO}_2$ /OMC                     | 472.1 $\text{mAh g}^{-1}$ at 0.1 C   | 379  | 62.2% (30 cycles)       | 399 |
| $\text{NiO}$ /OMC                       | 812 $\text{mAh g}^{-1}$ at 1000 $\text{mA g}^{-1}$   | 625  | 90% (after 50 cycles)   | 400 |
| $\text{CoO}$ /OMC                       | 733 $\text{mAh g}^{-1}$ at 100 $\text{mA g}^{-1}$  | 1000   | 92% (2 to 20 cycles)    | 401 |
| $\text{CuO}$ /OMC                       | 723 $\text{mAh g}^{-1}$ at 0.1C and 171 $\text{mAh g}^{-1}$ at 25C                                       | 687  | 92% (2 to 20 cycles)    | 402 |
| $\text{V}_2\text{O}_3$ /OMC             | 536 $\text{mAh g}^{-1}$ 100 $\text{mA g}^{-1}$   | 95   | 79% (2 to 100 cycles)   | 403 |
| $\text{TiO}_2$ /OMC                     | 120 $\text{mAh g}^{-1}$ at 1000 $\text{mA g}^{-1}$   | 211  | 92% (2 to 100 cycles)   | 404 |
| $\text{MoO}_2$ /OMC                     | 401 $\text{mAh g}^{-1}$ at 2000 $\text{mA g}^{-1}$ and 689 $\text{mAh g}^{-1}$ at 50 $\text{mA g}^{-1}$  | 407  | 80% (50 cycles)         | 405 |

Here some representative applications of OMC composite materials as electrodes are summarized. The combination of cathode materials and OMC is rare due to the good anode property of the OMC, which decreases the charging voltage of the battery. However, a  $\text{FeF}_3$ /OMC hybrid has been found to achieve a better cyclability than the bare  $\text{FeF}_3$  material, and it also achieved a higher  $\text{FeF}_3$  content compared with the other carbon-based composite by incorporating CNTs and active carbon. For instance, Jung and co-workers synthesized  $\text{FeF}_3$ /OMC hybrids by an incipient-wetness impregnation of an aqueous  $\text{FeCl}_3$ /HF solution into the pores of the OMC that was used as a hard template, followed by drying and calcination under argon.<sup>393</sup> The as-synthesized  $\text{FeF}_3$ /OMC hybrid showed good rate capabilities of 165, 156, 143, 131, 117, 90, and 69  $\text{mAh/g}$  at currents of 0.1, 0.25, 0.5, 1, 2, 5, and 10 C, respectively. At current rates of 0.5 C or higher, the discharge capacities of the  $\text{FeF}_3$ /OMC hybrids were more than 3 times higher than the corresponding bulk  $\text{FeF}_3$ . In addition, when the current density was decreased to 0.1 C, the capacities of bulk  $\text{FeF}_3$  and  $\text{FeF}_3$ /OMC hybrids were maintained by 48% and 89%, respectively. Obviously, the introduction of OMC had enhanced both structural stability and capacity reversibility.

Compared with the active cathode materials, anode materials have been more extensively incorporated into OMC to form hybrid electrodes, and the electrochemical performances are markedly increased accordingly. Table 4 has compared recent OMC hybrid anodes with different metal oxides.<sup>394–405</sup> Two methods were explored to incorporate  $\text{Fe}_2\text{O}_3$  nanoparticles into OMCs as electrodes.<sup>394,406</sup> In one case, polypyrrole-coated  $\text{Fe}_2\text{O}_3$ /OMC hybrids had been prepared by introducing  $\text{Fe}_2\text{O}_3$  nanoparticles to tubular mesoporous OMC, followed by in situ surface sealing with a coated PPy layer. The use of  $\text{Fe}_2\text{O}_3$  as anodes in LIBs is hampered by the drastic volume change (over 200%), resulting in a poor capacity retention. As the  $\text{Fe}_2\text{O}_3$  particles were well dispersed within the carbon matrix and coated with PPy layers on the outer surface of the OMC, the hybrid material displayed both much higher stable cycle performance and reaction kinetics. As a result, a higher efficiency in the use of  $\text{Fe}_2\text{O}_3$ , i.e., 528  $\text{mAh/g}$  at 1 A/g, and larger volumetric capacity, i.e., 97% capacity retention against the second cycle had been achieved. In the other case, the  $\text{Fe}_2\text{O}_3$ /OMC hybrid was synthesized by ammonia treatment and subsequent pyrolysis to enable a high  $\text{Fe}_2\text{O}_3$  content and adequate buffer space for high electrochemical performances.<sup>395</sup> Indeed, a high load of 47 wt % for the  $\text{Fe}_2\text{O}_3$  in the hybrid had been produced to offer a considerably stable cycle performance, e.g., the capacity was maintained at 683  $\text{mAh/g}$  after 100 cycles

with 99% capacity retention against the second cycle, as well as a good rate capability.

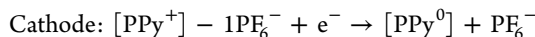
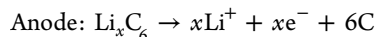
$\text{SnO}_2$  particles were incorporated into a tubular OMC through an in situ hydrolysis.<sup>397</sup> The weight percentage of  $\text{SnO}_2$  reached as high as 80%, resulting in an outstanding reversible capacity of 978  $\text{mAh/g}$  at a current density of 0.2 A/g at 0.005–3 V. The reversible capacity had been even increased up to 1039  $\text{mAh/g}$  after 100 cycles, much higher than the theoretical capacity of  $\text{SnO}_2$  (782  $\text{mAh/g}$ ). This remarkable electrochemical property was contributed from the thin carbon wall (~2 nm in thickness) and high pore volume (2.16  $\text{cm}^3/\text{g}$ ). The  $\text{SnO}_2$ /OMC hybrid electrode reacted with the electrolyte according to the following equations.



The theoretical capacity of  $\text{SnO}_2$ , i.e., 782  $\text{mAh/g}$ , is calculated on the basis of the third reaction that is reversible. As  $\text{Li}_2\text{O}$  is regarded as an electrochemically inactive material, the second reaction is considered to be an irreversible process. But in most cases, it should be reversible thermodynamically.<sup>407,408</sup> The reversibility of the second reaction has been mainly influenced by the intrinsic conductivity of  $\text{SnO}_2$ , grain size of  $\text{Li}_2\text{O}$  and Sn, degree of dispersion and contacting degree with conductive additives. Therefore, the second reaction is at least partially reversible here (6.4 Li per  $\text{SnO}_2$  based on 1133  $\text{mAh/g}$ ), which contributed to the ultrahigh reversible capacity. This conclusion was further verified by cyclic voltammograms with an oxidation peak at 1.25 V that correspond to the second reaction. The other active materials such as  $\text{NiO}$ ,<sup>400</sup>  $\text{CoO}$ ,<sup>401</sup>  $\text{CuO}$ ,<sup>402</sup>  $\text{V}_2\text{O}_3$ ,<sup>403</sup>  $\text{TiO}_2$ ,<sup>404</sup>  $\text{MoO}_2$ ,<sup>405</sup> and  $\text{SnO}$ <sup>398,399</sup> had also been introduced into the channels of OMCs, and an obvious increase in stability and rate capacity was shared.

**4.1.4. Fiber-Shaped Lithium Ion Batteries.** A flexible fiber-shaped polymer battery was reported in 2005 with a platinum wire substrate being electrodeposited with polypyrrole-hexafluorophosphate and polypyrrole-polystyrenesulfonate as active cathode and anode materials, respectively.<sup>409</sup> The capacity performance of the whole battery was as low as 10  $\text{mAh/g}$ , which had been limited by the discharge capacity of the anode (~11  $\text{mAh/g}$ ). The open circuit potential and Coulombic efficiency were 0.4 V and ~98%, respectively.

This fiber-shaped polymer battery had been further improved by replacing the anode active materials with SWCNTs. The reactions during discharge are provided below.



As SWCNTs had a much higher capacity, the discharge capacity reached 28 mAh/g. However, the polymer-based batteries suffered from a low open circuit potential and low discharge capacity, so increasing attentions are recently attracted to metal and lithium metal oxide materials.

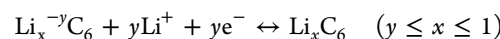
Later, a cable-type LIB was made to exhibit a high flexibility and discharge capacity.<sup>410</sup> A relatively sophisticated structure was required to fabricate the LIB cable with a diameter of millimeters. Cu wires deposited with Ni–Sn active materials were shaped into a hollow-structured anode. The anode was then subsequently wound with the modified poly(ethylene terephthalate) nonwoven separator and aluminum wire as the cathode current collector, followed by coating LiCoO<sub>2</sub> slurry to form the positive electrode. The assembled electrode was then sealed into a heat-shrinkable tube, and the aqueous electrolyte was injected to obtain the LIB cable. It exhibited a capacity of 1 mAh/cm and potential plateau at ~3.5 V. In addition, this LIB cable was flexible, and the capacity could be well maintained under bending.

To better satisfy the future development on the miniature and wearable electronic devices, it became urgent to discover one-dimensional, thin LIBs. To this end, aligned CNT fibers with diameters from several to tens of micrometers were investigated to make fiber-shaped LIBs. The existing CNT networks in the fiber acted as a skeleton for charge transport and physical support of the fiber device. The effective capacity was high without the inactive copper foil as current collector in the traditional design. The fiber-shaped micro-LIBs were then fabricated by twisting an aligned CNT/MnO<sub>2</sub> composite fiber and a lithium wire as positive and negative electrodes, respectively.<sup>411</sup> The aligned CNT fibers showed both high tensile strengths and electrical conductivities, so they could be electrochemically deposited with MnO<sub>2</sub> as the cathode. The modified fiber-shaped LIB showed a discharge platform of 1.5 V with a specific capacity of 94.37 mAh/cm<sup>3</sup> or 174.40 mAh/g at 0.002 mA. The charge and discharge power densities were 3.87 and 2.43 W/cm, respectively.

To improve the capacity performance of the electrode, aligned CNT/Si hybrid fiber anodes were further investigated.<sup>321</sup> A thin layer of silicon was coated on the outer surface of the aligned CNT sheet by electron beam evaporation to form a core–sheath structure that can effectively and simultaneously exploit the high specific capacity of the silicon and high electrical conductivity of the CNT, while the designed space with sizes of tens to hundreds of nanometers among the aligned hybrid nanotubes can effectively counterbalance the volume change of the silicon component. The hybrid sheet was further scrolled into a fiber-shaped electrode. The CNT/Si hybrid fiber was then assembled with Li wire and tested as a half battery. When the weight percentage of Si was controlled to be 38.1%, the specific capacity was 1670 mAh/g at a current density of 1.0 A/g. The operating voltage that corresponded to the lithium alloying/dealloying potential of Si was 0.4 V.

Compared with the conventional planar structure, the fiber-shaped LIB can be easily woven into flexible textile and are more likely to be used in wearable electronics. Therefore, they

are required to be both stable and safe beside having a high electrochemical performance. However, the previous use of lithium wire in the LIB had largely limited their practical applications. In particular, the fiber-shaped LIB was prone to break under bending and stretching. As a result, a novel and safe fiber-shaped LIB was made by embracing Li<sub>4</sub>Ti<sub>5</sub>O<sub>12</sub> and LiMn<sub>2</sub>O<sub>4</sub> nanoparticles into two aligned CNT fibers as anode and cathode, respectively.<sup>412,413</sup> The use of more stable and comparable Li<sub>4</sub>Ti<sub>5</sub>O<sub>12</sub> and LiMn<sub>2</sub>O<sub>4</sub> as cathode and anode had notably reduced the short circuit caused by dendritic lithium. For the most commonly used anode materials such as graphite, during the charge–discharge process, the lithium ion in the electrolyte will insert within the graphite electrode to form compounds as follows:



The lithiation potential is ranged from 0 to 0.20 V (vs Li/Li<sup>+</sup>) for the graphite anode. With the increasing current, the lithiation potential could be lowered and approaches to 0 V (vs Li/Li<sup>+</sup>), so the dendritic lithium was grown on the anode to impale the separator, finally leading to a short circuit. Here spinel Li<sub>4</sub>Ti<sub>5</sub>O<sub>12</sub> for the Li insertion took place at ~1.5 V (vs Li/Li<sup>+</sup>); the CNTs showed high conductivity and electrochemical stability. Therefore, no short circuits were found during use.

The hybrid fiber electrodes were prepared by coating the suspensions of Li<sub>4</sub>Ti<sub>5</sub>O<sub>12</sub> and LiMn<sub>2</sub>O<sub>4</sub> particles onto the aligned CNT sheet, respectively, followed by a scrolling process. The weight percentages were 78% and 90% for the Li<sub>4</sub>Ti<sub>5</sub>O<sub>12</sub> and LiMn<sub>2</sub>O<sub>4</sub> particles in the hybrid fibers, respectively.<sup>412</sup> Figure 48a,b shows typical SEM images of the resulting composite fibers. The Li<sub>4</sub>Ti<sub>5</sub>O<sub>12</sub> and LiMn<sub>2</sub>O<sub>4</sub> particles were well dispersed and incorporated within aligned

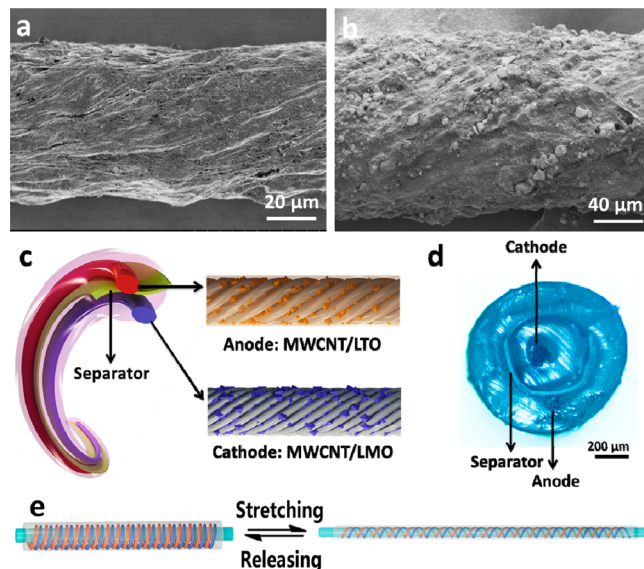


**Figure 48.** (a,b) SEM images of MWCNT/LTO and MWCNT/LMO hybrid yarns, respectively. (c) Schematic illustration to the structure of the flexible fiber-shaped LIB. The aligned MWCNT/LTO and MWCNT/LMO hybrid yarns were paired as the anode and cathode, respectively. (d) Cross-sectional micrograph of a full LIB. (e) Schematic illustration to a superstretchy fiber-shaped LIB during a stretching and releasing process. Reproduced with permission from ref 412. Copyright John Wiley and Sons (2010).

CNTs that served as effective pathways for charge transport and current collectors. The fiber-shaped anode and cathode electrodes were then assembled into a tube to obtain a full fiber-shaped LIB (Figure 48c,d), which revealed a specific capacity of 0.0028 mAh/cm (128 mAh/g), and the discharge plateau was 2.5 V at 0.01 mA. The fiber-shaped LIB was flexible and can be deformed into various shapes without physical damages and with negligible performance loss. Furthermore, when the hybrid fibers were wound around a rubber fiber in a helical structure, a stretchable LIB was further obtained (Figure 48e). This stretchable fiber-shaped LIB can be stretched by 100%, and no obvious damage in the structure was found. After stretched to 100% by 200 cycles, the specific capacity was maintained by over 80%.

The studies on the fiber-shaped LIBs are relatively less compared with the other flexible fiber-shaped devices such as solar cells and supercapacitors due to more complex fabrications enabled by the sensitive organic electrolyte. However, the fiber-shaped LIBs display many unique and promising advantages in the energy storage such as high energy densities and are currently attracting increasing attentions. More efforts are underway to develop more efficient fiber electrodes and stable electrolytes.

**4.1.5. Nanostructured Carbon for Post Li-Ion Batteries.** As a strong contender in the future batteries, lithium–sulfur batteries have gained increasing interests due to their high capacities and energy densities. Because the sulfur cannot act as a cathode itself due to the intrinsic nonconductivity and soluble property, a second component is necessary to function as the conducting matrix and sulfur host. Nanostructured carbon materials have been widely explored as a promising candidate for sulfur cathodes due to the mentioned high conductivity, porous structure, large surface area, and sufficient pathways that meet the requirements to host sulfur, provide conductivity, and suppress dissolution. As a one-dimensional material, CNTs can form a conducting network to interpenetrate with each other and thus make the sulfur cathode freestanding without the use of binders or conducting agents, which are particularly beneficial for flexible cathodes. For instance, a CNT/S composite film offered a specific capacity of 1352 mAh/g at the current rate of 1 C, and it can be maintained by 915 mAh/g after 100 cycles.<sup>414</sup>

Na is located below Li at the periodic table and is one of the most abundant elements on the earth. Compared with the lithium-ion battery, the fundamental principles of the sodium-ion battery are identical while the voltage is generally lower and the volume change upon Na removal or insertion is larger. The use of nanostructured carbon materials in sodium-ion batteries is similar to lithium-ion batteries in strategy and has been reviewed elsewhere.<sup>415</sup>

Lithium–air batteries represent a promising candidate for the next-generation batteries because of the remarkably high theoretical energy output. A lithium–air battery is composed of a lithium metal anode and an air electrode with an open structure to draw cathode active materials (i.e., oxygen) from air. The electrocatalyst in the air electrode plays a vital role in determining the electrode performance. Due to the notable merits including low cost, high electrical conductivity, large surface area, and good stability, carbonaceous materials can be used as either catalyst supports or catalytically active components. CNT and graphene have been widely explored as efficient substrates to disperse catalyst components such as Pt nanoparticles.<sup>416–419</sup> To further enhance the electrocatalytic

property, a second phase has been often incorporated into the carbon nanomaterial as a general and effective strategy. They can be made into hybrid materials to produce synergistic effects,<sup>420,421</sup> or carbon nanomaterials are doped to act as metal-free electrocatalysts for oxygen reduction.<sup>422,423</sup>

#### 4.2. Electrochemical Capacitor

Electrochemical capacitors, also known as supercapacitors or ultracapacitors, are considered to be one type of the most efficient energy storage devices. The concept was first brought up by Becker in 1957 in a filed patent and then first commercialized by Panasonic in 1978.<sup>1,424</sup> Compared with LIBs, the advantages of supercapacitors are reflected in the following four aspects: (1) higher power-delivery capability (or higher power density), (2) more rapid charging (i.e., shorter time needed for full charging), (3) longer life stability (e.g., specific capacitances without obvious decays after charging–discharging for thousands of cycles) and (4) higher Coulombic efficiencies. However, as widely recognized, supercapacitors typically show lower energy densities than LIBs.

The supercapacitor can be divided into two main types based on the difference in the storage mechanism of electric energy, i.e., electrochemical double layer capacitor (EDLC) and pseudocapacitor. The former one is similar to a traditional capacitor, e.g., both of them store energy by a means of charge separation. Differently, in an EDLC, the separation process occurs at both negative and positive electrodes to form two electric double layers, and each layer equal a traditional capacitor. However, the specific capacitance of an EDLC is several orders of magnitude higher than a traditional capacitor as, in the EDLC, the charge separation occurs across a much smaller distance in the interphase between the electrode and electrolyte, and it simply involves the movement of ions on the surface. Therefore, the capacitance of the EDLC strongly depends on the surface area of the electrode. Carbon materials including active carbon,<sup>425,426</sup> mesoporous carbon,<sup>427,428</sup> CNT,<sup>429–431</sup> and graphene,<sup>430,432,433</sup> with high specific surface areas and rapid electric transports are therefore promising for the high-performance supercapacitors.

The pseudocapacitor is quite different in the mechanism where a reversible Faradaic charge transfer takes place and a chemical redox reaction occurs within active materials on the electrode and ions in the electrolyte. The behavior of a pseudocapacitor is more like a LIB. Transitional metal oxides (e.g., MnO<sub>2</sub>,<sup>434,435</sup> NiO,<sup>436</sup> RuO<sub>2</sub>,<sup>437</sup> and V<sub>2</sub>O<sub>5</sub><sup>438</sup>) and conducting polymers (e.g., polyaniline,<sup>439,440</sup> polythiophene,<sup>440,441</sup> polypyrrole,<sup>442</sup> and derivatives<sup>440</sup>) are the two most investigated classes.

To satisfy practical applications for both high power and energy densities, supercapacitor and LIB may be combined together to realize either advantages. Typically, the hybrid capacitor combines the construction of LIB and electrochemical double layer capacitor, i.e., there is an electric double layer formed at the positive electrode and a faradaic charge-transfer reaction with Li<sup>+</sup> in the electrolyte at the negative electrode.<sup>443–445</sup> Based on this strategy, these hybrid energy storage devices have been already used in electric vehicles where the supercapacitors provide peak power for acceleration or hill climbing while LIBs provide electric power during normal driving. CNT, graphene, and OMC have been widely explored as one-, two-, and three-dimensional carbon nanomaterials for supercapacitors that are compared in Figure 49 and discussed below.

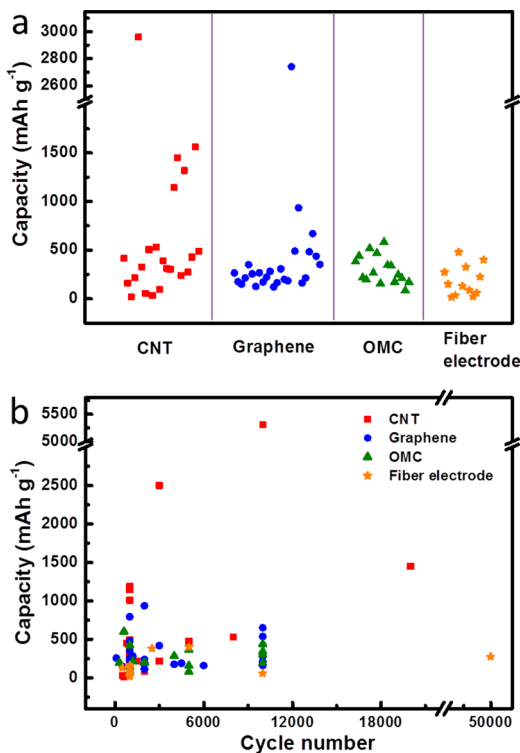


**Figure 49.** Performance overview of planar supercapacitors based on CNT, graphene, OMC, as well as their derived fiber-shaped devices. (a) The capacitance distribution. (b) The long-life stability.

**4.2.1. Carbon Nanotube.** Large specific surface areas (typically over 1500 m<sup>2</sup>/g) are a key to high specific capacitances of supercapacitors by providing an effective charge separation in the double-layered capacitors. Due to high specific surface areas as well as combined high electrical conductivity, mechanical stability and electrocatalytic activity, CNTs including both SWCNTs and MWCNTs are extensively studied for electrode materials of supercapacitors. The advantages of CNTs in the use of supercapacitors include the following: they are more efficient to percolate active particles than the traditional carbon materials; they are often made into a porous network which allows the ions to diffuse easily to the surface of the active moiety; and they can help to alleviate the volumetric change during the charge and discharge, resulting in an improved cyclic performance.<sup>446</sup> For bare CNTs, the specific capacitances are varied typically from 15 to 80 F/g<sup>447,448</sup> with energy and power densities to be 7 Wh/kg and 20 kW/kg, respectively.<sup>449,450</sup> Three methods are developed to further increase the specific capacitances of CNT-based supercapacitors. The CNTs are functionalized to introduce some functional groups and defects to offer pseudo capacitances similar to the LIB above. They are incorporated with the other carbon materials to form a hierarchical three-dimensional structure. They are incorporated with pseudocapacitor materials like metal oxides and conducting polymers.

**4.2.1.1. Bare CNT Electrodes.** CNTs tend to form a porous network due to their entanglements in preparation. MWCNTs and SWCNTs have been investigated as effective electrodes on the basis of high specific surface areas in both aqueous and nonaqueous electrolytes.<sup>456–459</sup> For the reported specific surface areas from 120 to 500 m<sup>2</sup>/g, the capacitances are ranged from 5 to 200 F/g. CNT electrodes show lower equivalent series resistances compared with the active carbon

due to a more efficient diffusion within the porous network for the electrolyte ions, so they display acceptable capacitance performances even at extremely high rates. For instance, an aligned MWCNT sheet with Al sheet as current collector produced a discharge capacity of 10–15 F/g at an extremely high current density of 200 A/g, where no discharge capacitance was obtained for the commonly used active carbon electrode under the same condition.<sup>149</sup> For SWCNTs, a specific capacitance of 180 F/g and power density of 20 kW/kg were obtained at an energy density of 7 Wh/kg.<sup>450</sup>

The effective specific surface area depends on the used electrolyte. A freestanding SWCNT film electrode was studied in aqueous gel and organic liquid electrolytes.<sup>429</sup> The aqueous gel electrolyte was composed of PVA/H<sub>3</sub>PO<sub>4</sub> electrolyte and the organic liquid electrolyte was composed of 1 M LiPF<sub>6</sub> in ethylene carbonate/diethyl carbonate (1/1, weight ratio). Some liquid electrolytes of H<sub>3</sub>PO<sub>4</sub>, H<sub>2</sub>SO<sub>4</sub> and NaCl aqueous solutions were also investigated as a comparison. Galvanostatic charge/discharge measurements were performed to evaluate the specific capacitances and internal resistances of the supercapacitors in a two-electrode configuration. There were no significant differences in the internal resistance between PVA/H<sub>3</sub>PO<sub>4</sub> gel and liquid H<sub>3</sub>PO<sub>4</sub> electrolyte, indicating that the polymer matrix did not obviously affect the internal resistance in the aqueous electrolyte. The capacitances were comparable in all aqueous electrolytes and ranged from ~90 to 120 F/g. However, the capacitance was relatively lower for the LiPF<sub>6</sub>/EC:DEC electrolyte, especially at a higher current density. This phenomenon can be explained by the fact that the ion association hindered the penetration into smaller pores, and compared with water, the higher viscosity of EC:DEC might lead to an incomplete wetting of the pores and decrease the effective surface area of the electrode. The thickness of the electrode film is another key to influence the electrolyte penetration and effective surface area, particularly for the gel electrolyte. Figure 50 shows the dependence of the capacitance per geometric area on thickness, and the capacitance was linearly increased with the increasing film thickness for the liquid electrolyte. A saturation occurred for the gel electrolyte due to a limited penetration into the porous network. On the other hand, the advantages of the LiPF<sub>6</sub>/EC:DEC electrolyte enabled a larger electrochemical stability window, which

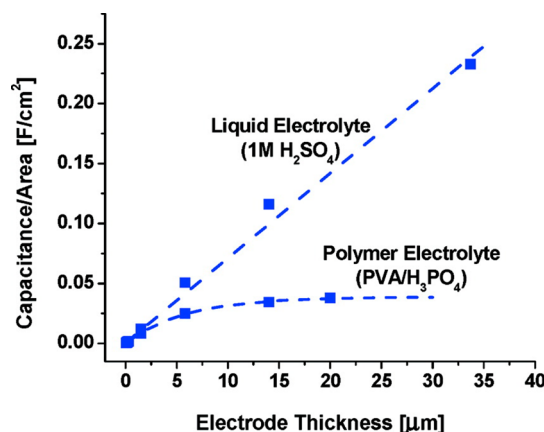


**Figure 50.** Thickness dependence of the capacitance per area for the CNT film using a liquid (1 M H<sub>2</sub>SO<sub>4</sub>) and a gel electrolyte (PVA/H<sub>3</sub>PO<sub>4</sub>). Reproduced with permission from ref 429. Copyright American Chemical Society (2009).

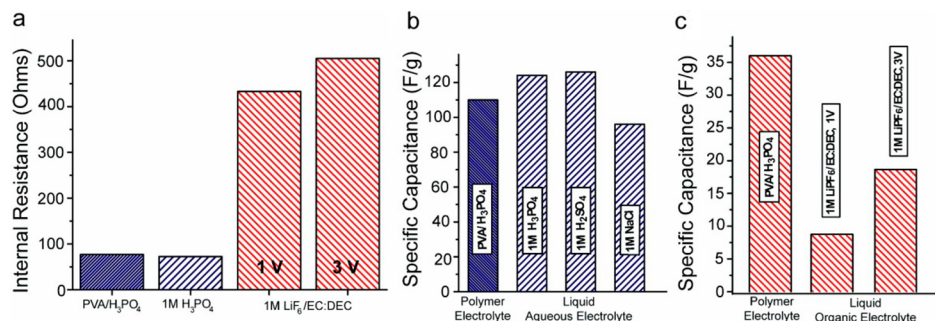


**Figure 51.** Electrochemical data of supercapacitors fabricated from different liquid and gel electrolytes based on galvanostatic charge/discharge measurements. (a) Internal resistance at a current density of  $1 \text{ mA cm}^{-2}$  ( $30 \text{ mA mg}^{-1}$ ). (b) Specific capacitances in the aqueous electrolyte at a current density of  $40 \mu\text{A cm}^{-2}$  ( $1 \text{ mA mg}^{-1}$ ). (c) Specific capacitances at a current density of  $1 \text{ mA cm}^{-2}$  ( $30 \text{ mA mg}^{-1}$ ). Reproduced with permission from ref 429. Copyright American Chemical Society (2009).

allowed for a higher operating voltage up to 3 V with both increasing power and energy densities (Figure 51).

Highly pure SWCNT materials with a nearly ideal specific surface area (i.e.,  $1300 \text{ m}^2/\text{g}$ ) had been also made to achieve their advantages as promising electrodes.<sup>451</sup> The organic electrolyte of 1 M Et<sub>4</sub>NBF<sub>4</sub>/propylene carbonate had been studied as a demonstration. A higher operation voltage of 4 V was achieved with a durable full charge–discharge cyclability. High energy density (94 Wh/kg or 47 Wh/L) and power density (210 kW/kg, 105 kW/L) were obtained and far exceeded those based on the active carbon.

It has been discussed that a higher surface area does not guarantee a higher capacitance as it is also affected by electric conductivity and pore size and distribution which is to a great extent related to the adaptability between electrode materials and electrolyte. Regardless of this issue, MWCNT materials with tunable sizes derived from anodic aluminum oxide templates were used to investigate the size effect on the capacitance.<sup>452,453</sup> The capacitance based on the CNT with a smaller diameter of 33 nm was higher than the diameter of 200 nm due to a larger specific surface area. MWCNTs with increasing outer diameters from 10 to 20 nm and inner diameters from 2 to 5 nm had been compared with increasing specific surface areas of  $128\text{--}411 \text{ m}^2/\text{g}$ , and the highest capacitance of 80 F/g occurred at the largest specific surface area in KOH aqueous electrolyte.<sup>451</sup> The CNT electrode often shows rectangular cyclic voltammograms even at very high scan rates due to a rapid charge transport and ideal double-layer performance.

Chemical activation and functionalization of the CNTs to introduce more defects and pseudocapacitances represents another general and effective strategy to improve their specific capacitances. For the SWCNT material after an electrochemical activation, a higher specific surface area of  $109.4 \text{ m}^2/\text{g}$  and larger volume of small mesopores of  $0.048 \text{ cm}^3/\text{g}$  (3.0–5.0 nm in diameter) were obtained compared with  $46.8 \text{ m}^2/\text{g}$  and  $0.026 \text{ cm}^3/\text{g}$  of the original SWCNTs without activation, respectively.<sup>454</sup> The specific capacitance had been further increased by three times. By introducing carboxyl groups to the surfaces of MWCNTs using extremely aggressive oxidizing agents such as a H<sub>2</sub>SO<sub>4</sub>/HNO<sub>3</sub> mixture, the capacitance was enhanced by 3.2 times due to the increased hydrophilicity in the aqueous electrolyte.<sup>455</sup> The hydrophilicity of MWCNTs was increased with the oxidation time for higher capacitances, but the oxidation also produced severe damages on the MWCNT surface to significantly decrease electrical conductiv-

ities of MWCNT electrodes. Therefore, a balance between hydrophilicity and conductivity was required, and it may be different in different systems.

Functional groups were introduced to the surfaces of MWCNTs after treatment in NaOH solution under heating, followed by an ultrasonic treatment in a mixed sulfuric and nitric acids. Compared with the original MWCNTs (28 F/g), a much improved specific capacitance of 85 F/g was verified in H<sub>2</sub>SO<sub>4</sub> electrolyte. A rougher surface was obtained due to the production of oxygen-containing functional groups on the surface and new generated pores during the alkali and acid treatments. After further introduction of redox active hydroquinone into the H<sub>2</sub>SO<sub>4</sub> electrolyte, the modified MWCNT electrode presented a specific capacitance as high as 3199 F/g owing to the hydroquinone redox reaction occurring on the surface of the MWCNT electrode. The oxidation process involved the adsorption of the molecule when the size of the electrochemically active hydroquinone was smaller than the average pore size of the electrode material, so the reversible reaction of the quinone/hydroquinone was available in the pores of MWCNTs.<sup>456</sup>

Note that there are also some other parameters including point of zero charge, contact resistance, and self-discharge characteristics that may also contribute to their electrochemical properties. These parameters should be considered in designing the CNT electrode by the above modifications.

#### 4.2.1.2. Carbon Nanotube/Polymer Composite Electrodes.

Depositing conducting polymers onto the CNTs represents an effective strategy to enhance the performance of CNT-based supercapacitors. Conducting polymers are good candidates for supercapacitor due to their high specific capacitances derived from rapid redox reactions and conductivities in charged states with a low equivalent series resistance and high power density. A main drawback of polymers lies in a low cycling stability suffered from shrinking, breaking, and cracking in charge–discharge processes.<sup>325</sup> On the other hand, many applications such as wearable electronic devices ask the power systems to be lightweight and small. The incorporation of second phases represents an effective solution to reduce the volume and weight with high performances. By attaching conducting polymers on the surfaces of CNTs, we may combine the advantages of conducting polymers with a high pseudocapacitance and CNTs with a rapid and efficient charge transportation. Some representative composite materials are highlighted to present a main configuration.

Uniform CNT/polymer composite materials can be synthesized after chemical reactions between them. For instance, a homogeneously grafted poly(3,4-ethylenedioxythiophene)/MWCNT composite was synthesized after *in situ* chemical polymerization in a ternary phase system.<sup>457</sup> The coaxial nanotubes contained many whorl fingerprint-like open ends that were favorable for the transport of electrons and ions. The composite electrode exhibited an energy density of 11.3 Wh/kg, over four times of the original MWCNT (2.7 Wh/kg). The parameters such as different electrolytes were also compared for supercapacitors on the basis of polypyrrole/MWCNT composite electrodes.<sup>458</sup> The polypyrrole/MWCNT composite preferred a neutral electrolyte over acidic and alkaline media. A specific capacitance of 165 F/g with high stability was obtained in a 1.0 M KCl electrolyte. For such composite materials, they could be easily made into flexible films through an *in situ* electrochemical polymerization.<sup>459</sup> Besides the three-dimensional network with large specific surface areas created by MWCNTs, the core–shell structure with an MWCNT as the core and polypyrrole as the shell enhanced the transport rate and accessibility of ions to the polypyrrole layer during the redox process. A flexible SWCNT/polyaniline composite was studied to also display a high specific capacitance of 706.7 F/g due to the dissolution of the off-lying disordered polyaniline and an increase in the number of available polycrystalline polyaniline regions.

The performance of the CNT/polymer composite material can be further improved by introducing multiple components. For one case, several polymers may be made in one electrode, e.g., an MWCNT@PEDOT/PSS composite film showed better capacitive behaviors with an areal capacitance of 98.1 mF/cm<sup>2</sup> at 5 mV/s cyclic voltammetry scan and higher cyclic stability compared with either MWCNT/PEDOT or MWCNT/PSS composites.<sup>460</sup> For another case, the other carbon component may be further incorporated into the composite electrode, e.g., a nonwoven MWCNT/graphene/polypyrrole fabric that served as an electrode produced specific capacitances up to ~319 F/g with a retention of 94.5% after 1000 cycles at a scan rate of 80 mV/s.<sup>461</sup> For the above multicomponent composite materials, synergistic effects among the multiple active materials contribute to the high performances. For the MWCNT/graphene/polypyrrole composite electrode, the graphene increased the surface area while the MWCNTs enhanced the electrical conductivity of polypyrrole. Of course, the other component besides carbon and polymer can be also designed to offer better performances. Silver nanoparticles were decorated onto a polyaniline/MWCNT composite electrode to produce a conductivity of 4.24 S/cm at room temperature and revealed a specific capacitance of 528 F/g, energy density of 187.73 Wh/kg, and power density of 4185 W/kg.<sup>462</sup>

On the other hand, conducting polymers have been widely studied as smart materials due to their obvious color changes in response to environmental stimuli, e.g., temperature, pH, ion, and solvent and ligand interaction. Therefore, they were recently developed to fabricate smart supercapacitors.<sup>463</sup> For instance, the aligned CNT/PANI composite films demonstrated chromatic transitions upon pass of electric currents with a high reversibility, and the colors could be controlled by varying the values of passed currents or used voltages (Figure 52). The as-fabricated supercapacitor could rapidly and reversibly change color among yellow, green, and blue, which can be clearly observed by the naked eyes. Besides, a specific capacitance of 308.4 F/g at 1 A/g was also maintained.

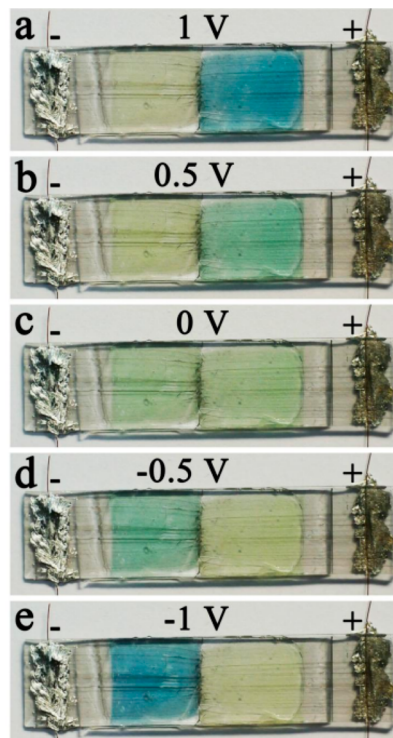


**Figure 52.** Chromatic transition during a charging–discharging process. Reproduced with permission from ref 463. Copyright John Wiley and Sons (2014).

#### 4.2.1.3. Carbon Nanotube/Metal Oxide Hybrid Electrodes.

Metal oxides or hydroxides have been widely explored for pseudocapacitors. They generally show higher energy densities than carbon materials and higher electrochemical stability than conducting polymers in electrochemical capacitors. They can store energy by formation of electrochemical double-layers and faradaic reactions. To be used as effective electrode materials, the metal oxides or hydroxides should be electronically conductive and have two or more oxidation states that can coexist at a continuous range, and the metal protons can freely intercalate into or get out of the oxide lattice during reduction or oxidation. The most investigated metal oxides for electrochemical capacitors include MnO<sub>2</sub>, RuO<sub>2</sub>, V<sub>2</sub>O<sub>5</sub>, Co<sub>3</sub>O<sub>4</sub>, NiO<sub>2</sub>, TiO<sub>2</sub>, and Fe<sub>2</sub>O<sub>3</sub>. Metal oxides are widely incorporated with CNTs as hybrid electrodes for high performance supercapacitors. When the cycling stability is decreased by the chemical or oxidization state changes in the electrodes induced by the Faradaic charge transfer during the charge–discharge process, the use of CNTs can increase the stability of the metal oxide by restricting the volume change and enhance the inner connection within the hybrid material.

A lot of CNT/metal oxide hybrid materials have been studied for supercapacitors and summarized at Table 5.<sup>464–473</sup> MnO<sub>2</sub> represents one of the most promising electrode materials for pseudocapacitors due to an abundant availability on the earth, easy synthesis, low cost, environmental compatibility, and high theoretical capacities ranged from 1100 to 1300 F/g.<sup>325</sup> The design of hierarchical structures is a key to take advantage of the remarkable properties during use. Aligned MWCNT/MnO<sub>2</sub> hybrid array electrodes were prepared by electrochemically depositing MnO<sub>2</sub> on MWCNT arrays synthesized by CVD,<sup>465</sup> and they produced a high specific capacitance of 642 F/g at a scan rate of 10 mV/s. Core–shell CNT/MnO<sub>2</sub>

**Table 5.** Metal Oxide/CNT Hybrid Materials for Supercapacitors

| material                                   | specific capacitance                             | electrolyte                           | ref |
|--|--|---------------------------------------|-----|
| MnO <sub>2</sub> /MWCNT                    | 179 F g <sup>-1</sup> at 5 mV s <sup>-1</sup>    | 1 M Na <sub>2</sub> SO <sub>4</sub>   | 465 |
| MnO <sub>2</sub> /vertically aligned MWCNT | 642 F g <sup>-1</sup> at 10 mV s <sup>-1</sup>   | 0.2 M Na <sub>2</sub> SO <sub>4</sub> | 464 |
| Ni(OH) <sub>2</sub> /MWCNT                 | 221 F g <sup>-1</sup> at 100 mV s <sup>-1</sup>  | 6 M KOH                               | 466 |
| NiO/MWCNT                                  | 1727 F g <sup>-1</sup> at 5 mA cm <sup>-2</sup>  | 2 M KOH                               | 467 |
| RuO <sub>2</sub> /MWCNT                    | 493.9 F g <sup>-1</sup> at 50 mV s <sup>-1</sup> | 1.0 M H <sub>2</sub> SO <sub>4</sub>  | 468 |
| RuO <sub>2</sub> /MWCNT                    | 1170 F g <sup>-1</sup> at 10 mV s <sup>-1</sup>  | 0.5 M H <sub>2</sub> SO <sub>4</sub>  | 469 |
| MoO <sub>2</sub> /SWCNT                    | 597 F g <sup>-1</sup> at 10 mV s <sup>-1</sup>   | 0.1 M Na <sub>2</sub> SO <sub>4</sub> | 470 |
| SnO <sub>2</sub> /SWCNT                    | 320 F g <sup>-1</sup> at 6 mV s <sup>-1</sup>    | 1 M Na <sub>2</sub> SO <sub>4</sub>   | 471 |
| Co <sub>3</sub> O <sub>4</sub> /RGO/CNT    | 378 F g <sup>-1</sup> at 2 A g <sup>-1</sup>     | 3 M KOH                               | 472 |
| V <sub>2</sub> O <sub>5</sub> /MWCNT       | 280~ F cm <sup>-1</sup> at 30 mV s <sup>-1</sup> | 1 M KHSO <sub>4</sub>                 | 473 |

nanocables had been synthesized onto a Ni foam to fabricate binder-free capacitors, both high specific capacitance of 325.5 F/g and cycling stability with a 90.5% capacitance retention after 5000 cycles were achieved due to a close contact between CNT and Ni foam for high conductivity.<sup>474</sup> Despite the high cost, RuO<sub>2</sub> has been extensively studied for supercapacitors due to a wide potential window, three distinct oxidation states and highly reversible redox reactions. Similarly, a thin, uniform ruthenium oxide layer had been deposited onto the CNT film to form a three-dimensional nanoporous structure.<sup>469</sup> It was found that RuO<sub>2</sub> can be made into a hydrated amorphous and porous structure with small size to enable a large surface area, and both high specific capacitance of 1170 F/g and high rate capability were therefore achieved.

Reddy and co-workers had further compared the supercapacitors based on MWCNT/RuO<sub>2</sub>, MWCNT/TiO<sub>2</sub>, and MWCNT/SnO<sub>2</sub> nanocrystalline hybrid electrodes that were synthesized by a chemical reduction method using functionalized MWCNTs and corresponding salts.<sup>475</sup> They were measured in a 1 M H<sub>2</sub>SO<sub>4</sub> aqueous electrolyte with the same mass in a two electrode Swagelok cell, and the MWCNT/TiO<sub>2</sub> exhibited the best performance in developing electrochemical double layer capacitors (Figure 53). A wide variety of other metal oxides had been also used to prepare CNT hybrid

electrodes including NiO, MoO<sub>2</sub>, SnO<sub>2</sub>, Co<sub>3</sub>O<sub>4</sub>, and V<sub>2</sub>O<sub>5</sub> (Table 6). Compared with bare MWCNTs, the enhanced

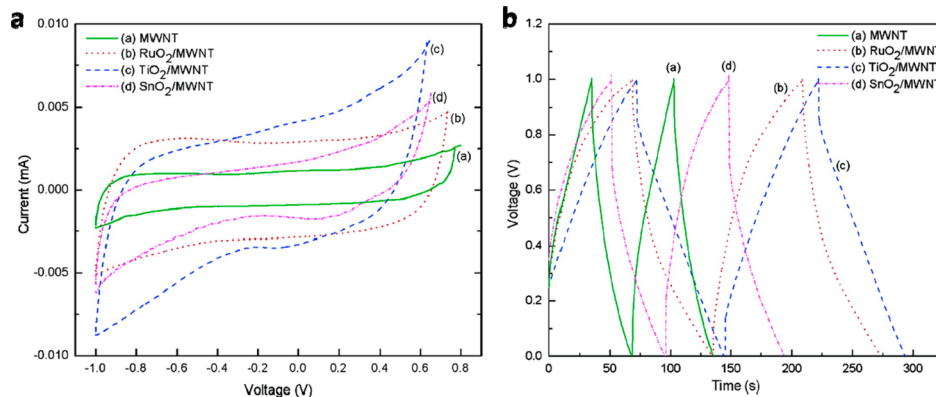
**Table 6.** Specific Supercapacitances Obtained by Different Methods<sup>a</sup>

| electrode material      | cyclic voltammetry (F g <sup>-1</sup> ) | galvanostatic charge–discharge (F g <sup>-1</sup> ) | electrochemical impedance spectroscopy (F g <sup>-1</sup> ) | average specific capacitance (F g <sup>-1</sup> ) |
|-------------------------|---|---|---|---|
| MWCNT                   | 68                                      | 69  | 64  | 67  |
| RuO <sub>2</sub> /MWCNT | 147                                     | 133   | 134   | 138   |
| TiO <sub>2</sub> /MWCNT | 166                                     | 148   | 166   | 160   |
| SnO <sub>2</sub> /MWCNT | 95                                      | 91  | 93  | 93  |

<sup>a</sup>Reproduced with permission from ref 475. Copyright American Chemical Society (2007).

specific capacitances from the MWCNT/metal oxide hybrids were derived from the progressive redox reactions occurring at the surface and bulk of transition metal oxides through a Faradaic charge transfer.

More complex composite electrodes were also explored to combine two more moieties such as conducting polymers and transition metal oxides with the CNT for better electrochemical performances. For instance, Hou and co-workers had developed a ternary nanocomposite film composed of MnO<sub>2</sub>, CNT, and PEDOT–PSS,<sup>476</sup> and a specific capacitance of 427 F/g was achieved with a capacitance retention of 99% after charge–discharge processes for 1000 cycles. Herein, CNTs provide high specific surface areas for depositing hierarchically porous MnO<sub>2</sub> nanospheres and improve the electrical conductivity and mechanical stability of the composite; PEDOT–PSS serves as an effective dispersant for CNT/MnO<sub>2</sub> hybrids and a binder material to enhance the adhesion to the substrate and connection among MnO<sub>2</sub>/CNT hybrid particles; the highly porous MnO<sub>2</sub> nanospheres with large specific surface areas offer high specific capacitances. A multicomponent nanomaterial was designed by embedding Ni(OH)<sub>2</sub> nanoparticles into CNTs as pillars for reduced graphene oxide (RGO) sheets, and high specific capacitances of 1235 and 780 F/g had been achieved at current densities of 1 and of 20 A/g, respectively.<sup>477</sup> The use of a conducting RGO substrate, the morphology of the CNT and the amount of

**Figure 53.** Electrochemical performances of MWCNT, RuO<sub>2</sub>/MWCNT, TiO<sub>2</sub>/MWCNT, and SnO<sub>2</sub>/MWCNT hybrids with the same electrode weight of 10 mg. (a) Cyclic voltammograms at a scan rate of 2 mV s<sup>-1</sup> in 1 M H<sub>2</sub>SO<sub>4</sub> aqueous electrolyte. (b) Galvanostatic charge–discharge curves at a current of 10 mA in 1 M H<sub>2</sub>SO<sub>4</sub> aqueous electrolyte. Reproduced with permission from ref 475. Copyright American Chemical Society (2007).

nickel particles are critical to the electrochemical performance of the composite material. Such three-dimensional nanostructures favored rapid ion and electron transports throughout the electrode matrix, highly accessible pseudoactive components with an efficient utilization, and strong interactions between the carbon matrix and pseudoactive material.

**4.2.2. Graphene.** Similar to the CNT, graphene exhibits both remarkable electrical, mechanical, and electrochemical properties and has been explored to fabricate effective supercapacitors. In addition, graphene can be made into various porous materials to further increase the specific capacitance.<sup>478</sup> Bare, hybrid, and composite graphene materials are all extensively investigated for the development of supercapacitors.

**4.2.2.1. Bare Graphene Electrodes.** For the electrode materials in EDLCs, specific surface area, pore structure, and electrical conductivity are three crucial factors that determine their electrochemical performances including specific capacitance, power density, and energy density.<sup>325,479</sup> The above three factors of graphene-based electrodes depend on the synthetic methods that are summarized below.

One of the most common and simple methods is to reduce GO into graphene.<sup>79,479,480</sup> Previously, the graphene materials were reduced from GO by using hydrazine hydrate as a reducing agent to offer a specific capacitance of 135 F/g. However, graphene sheets that were chemically reduced by hydrazine hydrate aggregated into particles (Figure 54).<sup>79</sup> As a

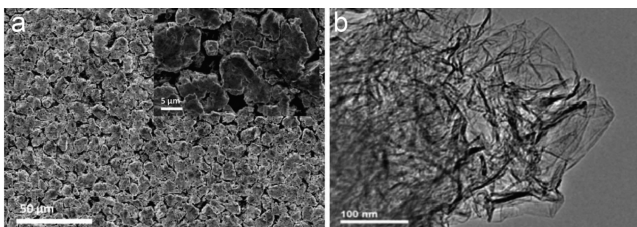


**Figure 54.** (a) SEM image of an electrode composed of graphene particles (inserted, higher resolution). (b) TEM image of individual graphene sheets. Reproduced with permission from ref 79. Copyright American Chemical Society (2008).

result, the specific surface area of the graphene-based electrode material turned out to be  $705 \text{ m}^2/\text{g}$ , much lower than  $2630 \text{ m}^2/\text{g}$  of single graphene sheets. The introduction of insulate binder also lowered the electrical conductivity of the electrode, thus decreasing specific capacitances. Besides hydrazine hydrate, there are many other reduction agents such as hydrobromic acid, hydroiodic acid and sodium carbonate.<sup>481–483</sup> Ma and co-workers had partially reduced GO into graphene by a hydrobromic acid that was a weak reductant.<sup>481</sup> This partially reduced GO had not only promoted the penetration of aqueous electrolyte but also introduced pseudocapacitances. The resulting RGO, at a current density of  $0.2 \text{ A/g}$ , offered high specific capacitances of 348 and 158 F/g in  $1 \text{ M H}_2\text{SO}_4$  and ionic liquid electrolyte of 1-butyl-3-methylimidazolium hexafluorophosphate, respectively. The specific capacitances were increased continuously until the 2000th cycle. The increased capacitances were resulted from the reduction of the residual oxygen-containing functional groups during the cycling electrochemical measurements. Actually, for the chemical reduction of GO in solution, no matter how well GO can exist as single sheets in aqueous solution, the final graphene agglomeration

seemed to be inevitable and the aggregated graphene naturally give a relatively low specific surface area.<sup>79,484,485</sup>

Graphene can be also synthesized by thermal exfoliation and reduction of GO.<sup>486–488</sup> For instance, Rao and co-workers had synthesized graphene electrodes through thermal exfoliation of GO at  $1050^\circ\text{C}$  and then fabricated the desired EDLCs.<sup>489</sup> Although a comparatively high specific surface area of  $925 \text{ m}^2/\text{g}$  was achieved, the specific capacitance still turned out to be a moderate value of 117 F/g in aqueous  $\text{H}_2\text{SO}_4$  mainly because the large proportion of micropores were inaccessible. To this end, Chen and co-workers further synthesized mesoporous graphene and improved the specific capacitance to 150 F/g.<sup>490</sup>

High temperatures were generally required with a relatively low efficiency in the above method, while high vacuum and microwave treatment had been found to be two effective assistant technologies to decrease the thermal exfoliation temperature.<sup>491–495</sup> Yang and co-workers developed a comparatively low-temperature exfoliation approach (as low as  $200^\circ\text{C}$ ) to produce graphene with the aid of a high vacuum environment (Figure 55). The high vacuum introduced a

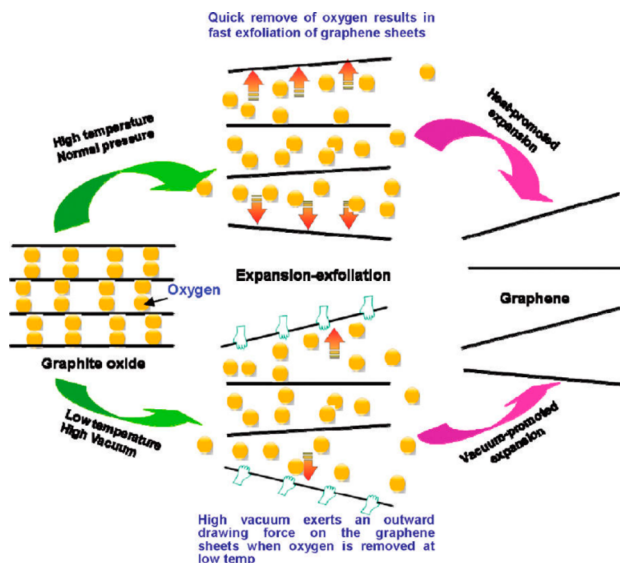


**Figure 55.** Schematic illustration to the chemical exfoliation of graphene. The high and low temperatures were above  $1000^\circ\text{C}$  and as low as  $200^\circ\text{C}$ , respectively. Reproduced with permission from ref 491. Copyright American Chemical Society (2009).

negative pressure surrounding the graphene layers and thus reduced the exfoliation temperature. The resulting graphene materials showed an electrochemical capacitance of 264 F/g.<sup>491</sup> Ruoff and co-workers developed a highly effective method to synthesize RGO from GO within 1 min through a microwave-assisted exfoliation, and the resulting RGO exhibited a specific capacitance of 191 F/g in KOH electrolyte.<sup>492</sup> Thermally exfoliating and reducing GO in high boiling-point solvent is another common strategy to realize thermal exfoliation and reduction at relatively low temperatures.<sup>496–498</sup> The exfoliation and reduction can be completed in organic solvents such as propylene carbonate (PC) and DMF without other reducing agents. Ruoff and co-workers exfoliated and reduced GO in PC at a low temperature of  $150^\circ\text{C}$ , and the RGO showed layer numbers from 2 to over 10 with an electrical conductivity of  $5230 \text{ S/m}$ .<sup>496</sup> A specific capacitance of  $\sim 120 \text{ F/g}$  can be obtained after addition of tetraethylammonium tetrafluorobo-

rate ( $\text{TEA BF}_4$ ) to the RGO/PC slurry. It should be noted that the specific capacitance was relatively higher compared with the other electrode materials with the PC-based electrolyte.<sup>499</sup>

Chemical and thermal reductions produce graphene electrodes with high quality for EDLCs. However, the resulting pores of RGO are generally not large enough, so the current density is limited to a low value as it is unavailable for the electrolyte to diffuse among small pores.<sup>500</sup> Therefore, a lot of effort had been made to further tune the porous structure, prevent agglomeration, and increase conductivity by designing a three-dimensional structure.<sup>501</sup> Three-dimensional self-assembled graphene hydrogels were recently synthesized via a hydrothermal method. The graphene hydrogel showed comparatively high mechanical, electrical and thermal properties, and a specific capacitance of 175 F/g was obtained in aqueous electrolyte. Later, 2-aminoanthraquinone (AAQ) was covalently grafted onto the surface of chemically modified graphene that can self-assemble into macroporous hydrogels.<sup>502</sup> They produced a much improved specific capacitance of 258 F/g partly derived from the additional pseudo capacitance provided by the covalently bonded AAQ moieties. Importantly, both high rate capability and cyclic stability had been simultaneously achieved due to high electrical conductivity, large specific surface area and good stability. To further improve the electrical conductivity of graphene hydrogel, Shi and co-workers combined hydrothermal and chemical reductions together.<sup>482</sup> The specific capacitance reached 220 F/g at the current density of 1 A/g for the resulting graphene hydrogel electrode, and it had been maintained at 74% when the current density was increased to 100 A/g. Accordingly, the power and energy densities were calculated to be 30 kW/kg and 5.7 Wh/kg (Figure 56), respectively. RGO hydrogels could be further

specific capacitance of 366 F/g was achieved at a current density of 2 A/g in 6 M KOH solution.

To further increase the specific capacitance, the activation had been widely used for carbon-based electrodes,<sup>506–508</sup> so do the graphene-based electrodes.<sup>432,509,510</sup> An electrical activation improved the specific capacitance from negligible to 220 F/g in 1 M  $\text{Et}_4\text{NBF}_4$ /acetonitrile electrolyte due to the increased specific surface area from 5 to 2687 m<sup>2</sup>/g after electrical activation and additional pseudo capacitance.<sup>509</sup> Remarkably, Ruoff and co-workers had activated microwave-exfoliated GO and thermally exfoliated GO by KOH and achieved a specific surface area as high as 3100 m<sup>2</sup>/g that was even higher than the claimed value of 2630 m<sup>2</sup>/g for single graphene sheets. In addition, the activation generated a three-dimensional network with both small pores of ~1 to ~10 nm and high conductivity.<sup>432</sup> Later, the same group had activated reduced GO paper by KOH to produce highly conductive porous thin films.<sup>511</sup> The resulting supercapacitor displayed a high power density of ~500 kW/kg at a current density of 10 A/g in  $\text{TEABF}_4/\text{AN}$  electrolyte, and the corresponding specific capacitance and energy density turned out to be 120 F/g and 26 Wh/kg, respectively. The specific surface area was further increased by integrating mesopores into macroporous scaffolds, and the specific capacitance reached 174 F/g or ~100 F/cm<sup>3</sup> in an ionic liquid electrolyte in acetonitrile with energy and power densities of 74 Wh/kg (44 Wh/L) and 338 kW/kg (199 kW/L), respectively.<sup>512</sup> Another general and effective strategy to improve the specific capacitance of the graphene electrode is preventing the agglomeration of RGO by introducing spacers or stabilizers.<sup>485,513–518</sup> The spacer can improve not only the accessibility of the electrolyte but the electrochemical utilization of both surfaces and nanochannels of graphene sheets. For instance, platinum nanoparticles were intercalated into partially exfoliated graphene nanosheets and the specific surface area of graphene was increased from 44 to 862 m<sup>2</sup>/g. Accordingly, the specific capacitance was increased from 14 to 269 F/g.<sup>46</sup> Surfactants could be also intercalated onto GO sheets, followed by reduction of GO to produce the graphene electrode.<sup>514</sup> The widely explored surfactants include tetrabutylammonium hydroxide (TBAOH), cetyltrimethylammonium bromide (CTAB), and sodium dodecylbenzenesulfonate (SDBS). The presence of these surfactants had not only stabilized the structure of graphene sheets during reduction but also enhanced the wettability of graphene electrodes, thus enhancing the electrochemical performance. The TBAOH-stabilized graphene material exhibited a specific capacitance of 194 F/g at a current density of 1 A/g in 2 M  $\text{H}_2\text{SO}_4$  aqueous solution.

Hybrid electrodes by incorporation with the other nanostructured carbon also represent a promising direction in supercapacitors. Carbon black was introduced to graphene sheets to prepare hybrid electrodes through ultrasonication and *in situ* reduction.<sup>515</sup> Graphene nanosheets were separated by carbon black in the resulting three-dimensional hybrid material, enabling a specific capacitance of 175 F/g at a scan rate of 10 mV/s in 6 M KOH aqueous solution. Mesoporous carbon spheres were intercalated among graphene sheets also with a three-dimensional structure,<sup>519</sup> which exhibited a lower equivalent series resistance and higher power capability than the RGO electrode, and a specific capacitance of 171 F/g can be obtained at a scan rate of 10 mV/s in 6 M KOH aqueous solution. Doping has also been well recognized as an effective route to tune electronic properties of graphene, particularly,

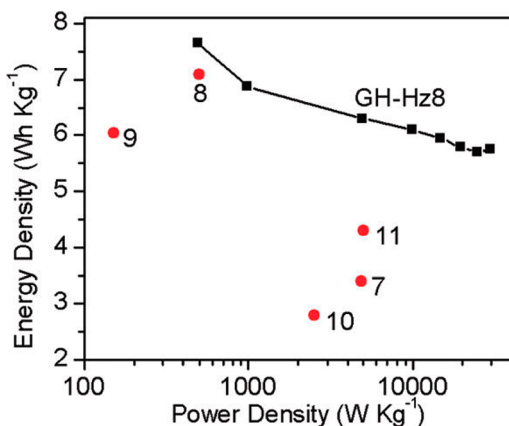


**Figure 56.** Ragone plot of the supercapacitor based on hydrazine monohydrate-reduced graphene hydrogels. Red dots stand for the highest power densities and corresponding energy densities from the literature. Note that the labeled numbers correspond to the reference numbers at ref 479, not this review article. Reproduced with permission from ref 482. Copyright American Chemical Society (2011).

incorporated into a microporous nickel foam to form a hybrid electrode.<sup>503–505</sup> As the transporting distances of ions and electrons were largely shortened, this hybrid electrode exhibited a high rate capability. The hybrid electrode based on GO hydrogel and nickel foam was also synthesized by a freeze-drying method, followed by thermal annealing.<sup>504</sup> A high

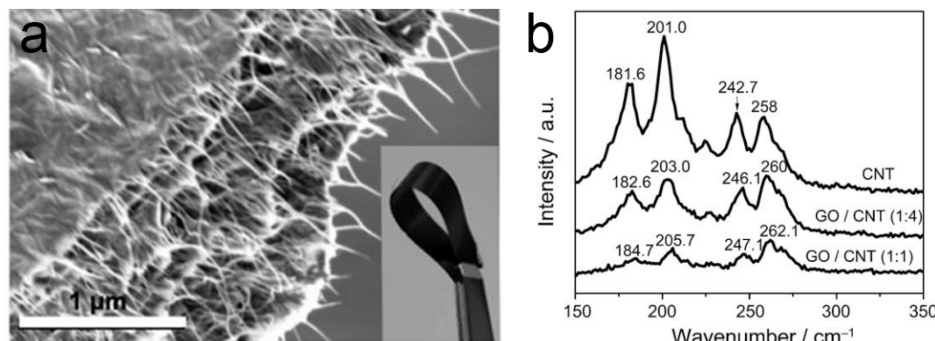


**Figure 57.** (a) SEM image of a GO/CNT hybrid film (inserted, a bent strip of the hybrid film). (b) Raman spectra of the GO/CNT film with different GO/CNT weight ratios. Reproduced with permission from ref 524. Copyright John Wiley and Sons (2010).

improving the electrical conductivity. Graphene sheets are doped with nitrogen by plasma processes and the specific capacitance reached 280 F/g at a current density of 1 A/g in 6 M KOH aqueous solution.<sup>520</sup> A N-doped three-dimensional graphene with an ultralow density of ~2.1 mg/cm<sup>3</sup> was synthesized by hydrothermally treating GO with pyrrole, followed by thermal exfoliation and reduction.<sup>226,521</sup> This N-doped graphene framework combined the unique three-dimensional porous structure of few-layer graphene sheets that favored the accessibility of electrolytes and enhanced the capacitance performance especially at a high rate. In 1 M LiClO<sub>4</sub> aqueous solution, a high specific capacitance of 484 F/g that approached the theoretical electrical double layer capacitance of 550 F/g of bare graphene was achieved. Moreover, when the current density was increased to 100 A/g, the specific capacitance was maintained at 415 F/g after 1000 cycles. Similarly, the other element such as B-doped graphene was also realized via the reduction of GO by a borane-tetrahydrofuran adduct. The B-doped graphene exhibited a specific surface area of 466 m<sup>2</sup>/g to offer a relatively high specific capacitance of 200 F/g at a current density of 0.1 A/g in 6 M KOH aqueous solution.<sup>522</sup> Of course, two elements can be also codoped onto graphene sheets. N/P-codoped RGO with a high number density of surface groups also shows a promising specific capacitance.<sup>523</sup>

CNTs served as spacers to separate graphene sheets to prevent their agglomeration for high specific surface areas.<sup>524</sup> There are strong  $\pi-\pi$  interactions between graphene sheets and CNTs, and graphene sheets bridged the CNTs to increase the electronic and mechanical properties of the hybrid electrode.<sup>525</sup> However, as both as-synthesized CNTs and graphene sheets generally exist in agglomerations, it is necessary to mix them to form a uniform hybrid nanostructure. In a representative method, pristine CNTs were first dispersed into water to form suspensions by using GO sheets as dispersants through supramolecular interactions (Figure 57).<sup>524</sup> The oxygen-containing groups on GO sheets make the nanohybrid hydrophilic and well dispersed in water, and the  $\pi-\pi$  interaction between aromatic moieties of CNTs and aromatic moieties of GO sheets make the nanohybrid stable. The resulting hybrid electrode exhibited a specific capacitance of 140 F/g at a current density of 0.1 A/g. However, GO nanosheets were insulated, so the specific capacitance was sharply decreased to 30 F/g with the increasing current density to 30 A/g. The graphene/CNT hybrid electrode could be also synthesized by assembling acid-oxidized MWCNTs and polymer-modified graphene sheets that were prepared by *in situ* reduction of exfoliated GO in the presence of cationic

poly(ethylenimine) (PEI).<sup>425</sup> The resulting composite materials showed an interconnected network and well-defined nanopores that enabled a high electrochemical property, even at a scan rate of 1000 mV/s. As expected, the design of a three-dimensional hierarchical structure generally produced a high specific capacitance around 300 F/g.<sup>526,527</sup>

There are also some other methods to improve electrochemical capacitances of graphene electrodes. Graphene sheets at one or two layers that enabled a specific surface area of 1654 m<sup>2</sup>/g were synthesized by CVD with porous MgO as the template, and the specific capacitance reached 255 F/g in 6 M KOH aqueous solution.<sup>528</sup> Injected graphene electrodes were also made through inject-printing GO aqueous dispersion onto Ti foils, followed by thermal reduction. This electrode exhibited a specific capacitance of 132 F/g in 1 M H<sub>2</sub>SO<sub>4</sub> aqueous electrolyte.<sup>529</sup> Ultrathin, transparent graphene film electrodes with a thickness of 25 nm and optical transmittance of 70% (at a wavelength of 550 nm) showed a specific capacitance of 135 F/g and high power density of 7.2 kW/kg in 2 M KCl aqueous solution.<sup>530</sup> It should be noted that, although bare graphene electrodes have reached fairly good gravimetric properties, their corresponding volumetric properties are low because of a very low density of graphene electrodes ranging from 0.05 to 0.75 g/cm<sup>3</sup>.<sup>531,532</sup> It has been proposed that the volume energy density against the whole EDLC including both electrodes, electrolyte, separator, and current collectors is more reliable to evaluate the potential of an electrode material. Thus, the gravimetric capacitance of the graphene electrode and packing density of the porous graphene are two critical factors. The gravimetric capacitance of graphene materials can be significantly improved by optimizing fabrication methods or introducing other materials with high energy densities described in section 4.2.2. However, porous yet densely packed carbon electrodes are crucial to the realization of high-density electrochemical capacitive energy storage but remain challenging. An important attempt was made to realize a subnanometer integration of graphene sheets with electrolytes to form highly compact electrodes,<sup>533</sup> and the resulting EDLC showed volumetric energy densities approaching 60 Wh/L and power densities approaching ~75 kW/L. The high electrochemical performance was derived from the continuous ion transport network. Note that the packing density of the graphene film was increased from typically 0.13 to 1.33 g/cm<sup>3</sup>, while graphite with a density of ~2.2 g/cm<sup>3</sup> delivers little capacitance as ions cannot access the interplanar space.

**4.2.2.2. Graphene Based Composite Electrodes.** Similar to CNTs, graphene shows a relatively low specific capacitance as an electrode material in the EDLC. Therefore, the other phase

with higher capacitances can be added to form composite materials for more efficient supercapacitors.

**Graphene/Conducting Polymers Composite Electrodes.** Similar to the CNT, graphene shows excellent electronic and mechanical properties that may buffer the volume changes of conducting polymers for a high stability. In addition, graphene also serves as a substrate to obtain freestanding electrodes based on conducting polymers. Typically, graphene was introduced to enhance the mechanical and electrical performance of PANI,<sup>534–536</sup> and PANI/GO composite materials are synthesized via *in situ* polymerization of aniline monomers in the presence of GO.<sup>537</sup> The ratio between PANI and GO dramatically influenced the capacitive performance of the composite electrode, e.g., a ratio of 100/1 was better than 61/1. In the following work,<sup>536</sup> the same group further found that the highest specific capacitance of 746 F/g was obtained at a mass ratio of PANI to GO as 200/1. The capacitance can be maintained by 73% after 500 cycles for the composite electrode with the PANI/GO mass ratio of 23/1, though a retention of 20% was maintained for pure PANI. The enhancements of specific capacitance and cycling life demonstrated that the synergistic interactions including electrostatic interactions, hydrogen bonding, and  $\pi-\pi$  interactions had not only affected the composite morphology but also greatly improved the electrochemical performance. Modified composite electrodes with vertically aligned PANI nanowires grown on GO sheets were further studied to compare their structures and electrochemical properties based on different ratios (Figure 58).<sup>538</sup> The morphologies of PANI nanowires were determined by the ratio of aniline to GO due to different nucleation processes. Graphene/PANI composite materials were synthesized through *in situ* polymerization.<sup>539,540</sup> Graphene mainly served as a

supporting material to provide active sites for nucleation of PANI and electron transfer. The graphene/PANI composite exhibited a specific capacitance of 1046 F/g at a scan rate of 1 mV/s in 6 M KOH aqueous solution with the energy and power densities of 39 Wh/kg and 70 kW/kg, respectively. When the scan rate was increased to 500 mV/s, the specific capacitance was decreased to ~300 F/g.

To further improve the electrochemical performance, many other strategies such as tuning the morphology of graphene with more active nucleation sites and doping the other elements have been also developed. Graphene nanoribbons were unzipped from CNTs and used to synthesize composite materials with PANI.<sup>541</sup> Here the graphene nanoribbons provided more active sites for the nucleation of PANI. Under the assistance of PTFE as the binder, the composite electrode exhibited a specific capacitance of 340 F/g in 1 M H<sub>2</sub>SO<sub>4</sub> aqueous solution, and a retention of ~90% was achieved after 4200 cycles. Cobalt-doped graphene/PANI composite electrodes were also synthesized to produce high electrochemical properties by *in situ* polymerization of aniline in the presence of graphene and cobalt<sup>542</sup> and exhibited a high specific capacitance of 989 F/g. Recently, a three-dimensional graphene/PANI composite hydrogel was synthesized after a self-assembling process and *in situ* polymerization.<sup>543</sup> The composite hydrogel could be made into freestanding films to serve as electrodes without binders. Multilayered graphene/PANI composite films were constructed by layer-by-layer assembly of positively charged PANI and negatively charged GO sheets through electrostatic interactions, followed by reduction of GO into graphene.<sup>544</sup> These kinds of freestanding films were used for flexible thin film supercapacitors.<sup>543–545</sup> The synergistic interaction between graphene and PANI offered both high electrical conductivity and chemical stability, thus resulting in a specific capacitance of 375.2 F/g in 1 M H<sub>2</sub>SO<sub>4</sub> aqueous electrolyte, which was well maintained by 90.7% after 500 cycles at a high current density of 3 A/g.

PPy/graphene composite had been directly prepared by mixing PPy nanotubes and RGO together.<sup>546</sup> The composite exhibited a specific capacitance of 400 F/g at 0.3 A/g. More uniform PPy/GO composites could be synthesized via *in situ* chemical polymerization using FeCl<sub>3</sub> as oxidant,<sup>547</sup> and a specific capacitance of 421.42 F/g was achieved. By optimizing the oxidant, Xie and co-workers improved specific capacitances to 728 F/g at 0.5 A/g in 1 M KCl aqueous solution.<sup>548</sup> PPy/RGO composite electrodes had been also synthesized by chemical reduction of GO.<sup>549</sup> Compared with the PPy/GO composite, a lower specific capacitance of 267 F/g was produced while the cyclic stability of graphene was higher than GO, so a high capacitance retention of 90% was obtained after 500 cycles. PPy/graphene composite electrodes could be also prepared through electrostatic interactions. Layered GO sheets were sandwiched between PPy through an electrostatic interaction between negatively charged GO sheets and positively charged surfactant micelles and polymerization of pyrrole monomer in the micelles (Figure 59).<sup>550</sup> The electrochemical performances were varied depending on their morphologies. The highest specific capacitance of 510 F/g was achieved at 0.3 A/g in 2 M H<sub>2</sub>SO<sub>4</sub> aqueous solution, and it was maintained at 351 F/g at 5 A/g with 70% retention after 1000 charging–discharging cycles.

Electropolymerization represents another general and effective route to synthesize PPy materials. For instance, PPy was incorporated into a three-dimensional graphene foam

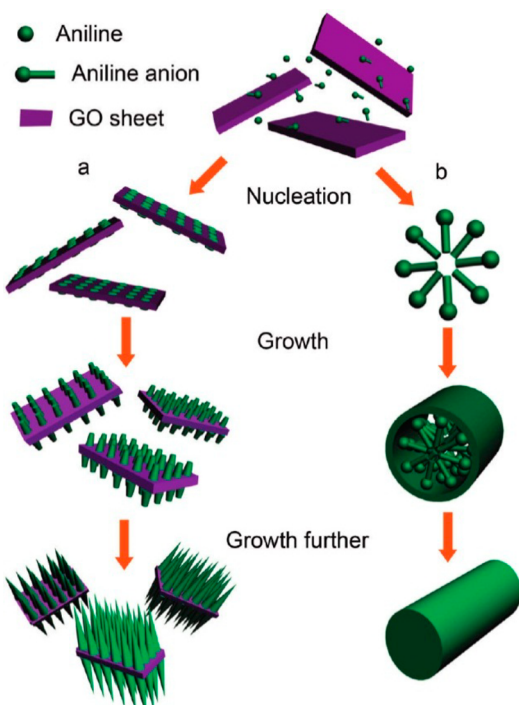


**Figure 58.** Schematic illustration to (a) the heterogeneous nucleation on GO nanosheets and (b) homogeneous nucleation in bulk solution for the growth of PANI nanowires. Reproduced with permission from ref 538. Copyright American Chemical Society (2010).

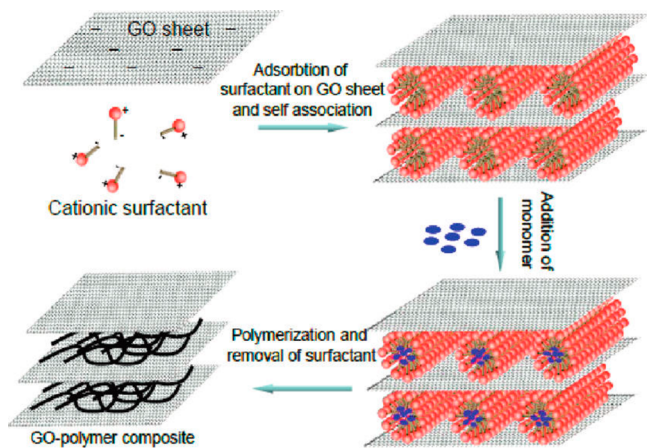


**Figure 59.** Schematic illustration to the formation of a GO/PPy composite. Reproduced with permission from ref 550. Copyright American Chemical Society (2010).

through electropolymerization.<sup>551</sup> Pyrrole monomers were first dispersed in a GO aqueous suspension to form a homogeneous solution that was then hydrothermally treated to reduce GO to RGO. The absorbed pyrrole monomers in the graphene foam were converted to PPy after electropolymerization. The composite foams demonstrated stable mechanical properties and exhibited a specific capacitance of 350 F/g at 1.5 A/g in 3 M NaClO<sub>4</sub> aqueous electrolyte. In particular, the capacitance had been maintained by nearly 100% after 1000 cycles. Thin PPy/graphene composite films were recently prepared by electrophoretic deposition of graphene on a titanium metal substrate and electropolymerization of PPy on graphene.<sup>552</sup> An ultrahigh specific capacitance of 1510 F/g (151 mF/cm<sup>2</sup>, 151 F/cm<sup>3</sup>) was obtained at a scan rate of 10 mV/s. The remarkable electrochemical performance was derived from the highly porous structure and effective utilization of the surface area. Moreover, the mode of polymerization exposed maximal surface sites for Faradaic redox reactions.

**Graphene/Metal Oxide or Hydroxide Hybrid Electrodes.** GO/MnO<sub>2</sub> hybrid materials could be synthesized by a mild chemical reaction carried out in a water-isopropyl alcohol solvent mixture (Figure 60).<sup>553,554</sup> MnO<sub>2</sub> nanoneedles on GO sheets were formed through intercalation and adsorption of manganese ions, followed by nucleation and growth of nanoneedle crystal. This process also led to the exfoliation of GO sheets. Compared with the bare GO, the hybrid exhibited much enhanced electrochemical performance with a specific capacitance of 216 F/g and was maintained by 84.1% after 1000

cycles. To increase the uniformity and stability of the hybrid, polymer brushes were modified on the composite aggregates by perpendicularly grafting poly(sodium methacrylic acid) (PMANa) to GO or RGO sheets and then using the composite sheets as templates to load MnO<sub>2</sub> nanoparticles (Figure 61).<sup>555</sup> The hybrid was then mixed with acetylene black and PTFE binder and assembled into a two-electrode cell in 1 M Li<sub>2</sub>SO<sub>4</sub> aqueous electrolyte. It exhibited an outstanding electrochemical performance with a specific capacitance of 372 F/g at a current density of 0.5 A/g, and only a slight drop of 8% was observed after 4000 cycles. The formation of porous structures with higher specific surface areas represents an efficient strategy to further enhance the electrochemical performance. Porous “activated microwave expanded graphite oxide” was used to deposit MnO<sub>2</sub> nanoparticles with sizes of 2–3 nm to form the desired hybrid (Figure 62).<sup>556</sup> This hybrid material based symmetric electrochemical capacitor revealed a capacitance of 256 F/g (640 F/cm<sup>3</sup>) and yielded power and energy densities of 32.3 kW/kg and 20.8 Wh/kg, respectively.

Aiming at practical applications, Fan and co-workers had developed a rapid and effective method to synthesize graphene/MnO<sub>2</sub> hybrids through self-limiting deposition of MnO<sub>2</sub> on graphene under microwave irradiation (Figure 63).<sup>434</sup> The nanostructured graphene/MnO<sub>2</sub> hybrid material was mixed with carbon black and PTFE to prepare an electrode with a specific capacitance of 310 F/g at 2 mV/s in 1 M Na<sub>2</sub>SO<sub>4</sub> aqueous electrolyte. The capacitance could be maintained at 228 F/g at 500 mV/s, indicating a high rate performance.

Besides MnO<sub>2</sub>, Mn<sub>3</sub>O<sub>4</sub> was also incorporated into graphene to improve the capability.<sup>557–559</sup> Graphene/Mn<sub>3</sub>O<sub>4</sub> hybrids had been synthesized through a one-step method, and the specific capacitance can reach 271.5 F/g at a current density of 0.1 A/g.<sup>559</sup> Moreover, a specific capacitance of 180 F/g had been maintained when the current density was increased to 10 A/g, and the capacitance was held by 100% after 20 000 cycles. However, the graphene/Mn<sub>3</sub>O<sub>4</sub> hybrid materials are generally not freestanding, and insulated binders that decrease the electrochemical performance need to be added in the preparation of electrodes. Moreover, they are mainly tested in three-electrode systems and need a current collector during measurements. Recently, an attempt was made to synthesize freestanding graphene/Mn<sub>3</sub>O<sub>4</sub> papers by filtration, and the hybrid paper could be assembled into flexible asymmetric supercapacitors (Figure 64).<sup>560</sup>

Cheng and co-workers had synthesized graphene/RuO<sub>2</sub> hybrid materials with different contents of Ru through sol-gel and low-temperature annealing processes.<sup>561</sup> Graphene sheets were well separated by RuO<sub>2</sub> nanoparticles, and RuO<sub>2</sub> nanoparticles had been also well anchored onto graphene sheets. The synergistic interactions between graphene sheets and RuO<sub>2</sub> nanoparticles provided the hybrid with a remarkable electrochemical property. A high specific capacitance of 570 F/g was achieved at Ru weight percentage of 38.3%; the capacitance can be maintained up to 97.9% after 1000 cycles with high energy density of 20.1 Wh/kg at 0.1 A/g; a reasonable energy density of 4.3 Wh/kg was obtained at a high power density of 10 kW/kg. Similar to the manganese oxide, flexible supercapacitors had been realized from the modified graphene/Nafion/RuO<sub>2</sub> electrode.<sup>562</sup>

Co<sub>3</sub>O<sub>4</sub> has also attracted increasing attentions for large specific surface area, reversible redox behavior, high conductivity, and long-term performance.<sup>553</sup> The hybrid composed of graphene and Co<sub>3</sub>O<sub>4</sub> nanoparticles could be typically

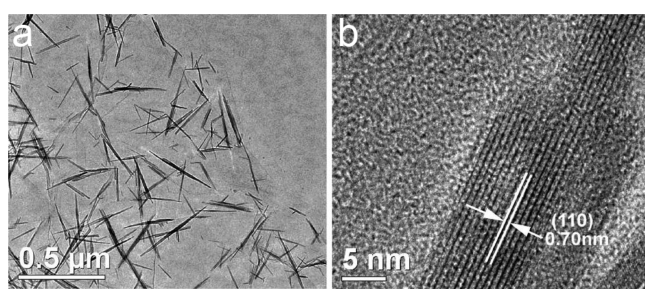


**Figure 60.** (a) TEM image of a GO/MnO<sub>2</sub> hybrid nanoneedle. (b) TEM image of a MnO<sub>2</sub> nanoneedle at a higher resolution. Reproduced with permission from ref 554. Copyright American Chemical Society (2010).

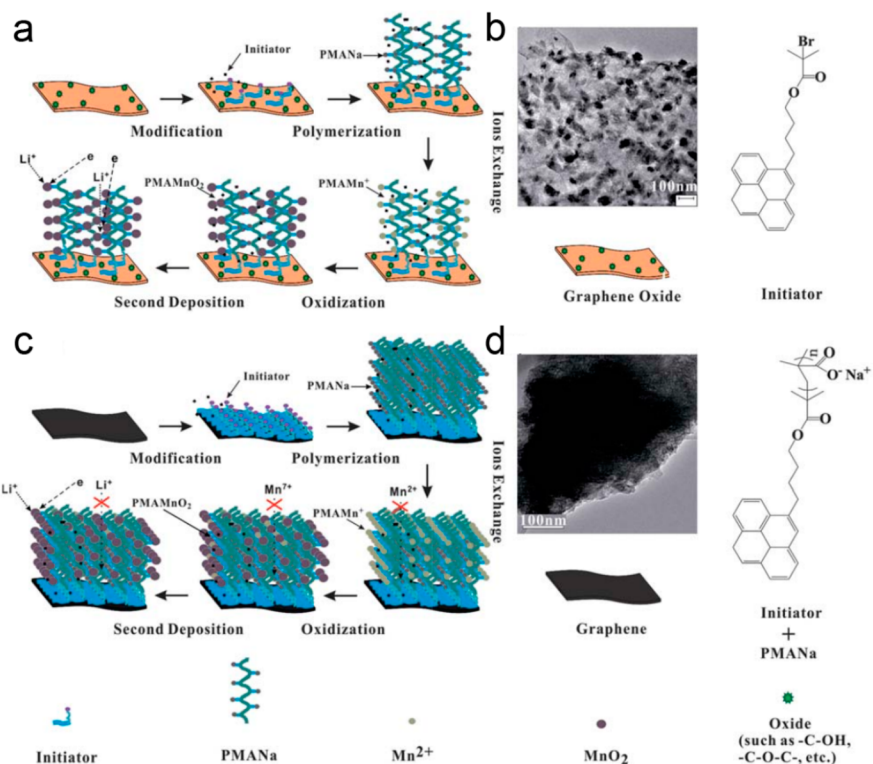


**Figure 61.** (a) Schematic illustration to the formation process and (b) TEM image of graphene oxide/polymer brush/ $\text{MnO}_2$  composite. (c) Schematic illustration to the formation process and (d) TEM image of graphene/polymer brush/ $\text{MnO}_2$  composite. Reproduced with permission from ref 555. Copyright Royal Society of Chemistry (2013).

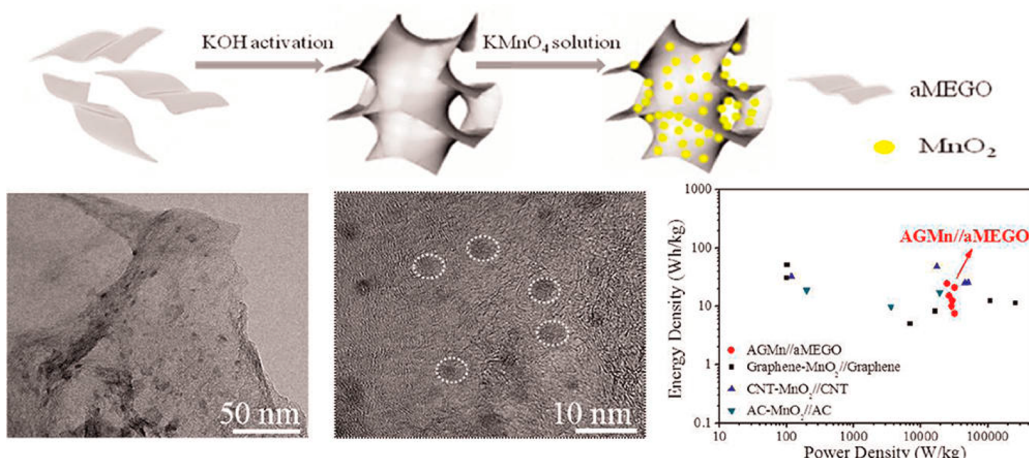


**Figure 62.** Schematic illustration to the deposition of  $\text{MnO}_2$  in activated microwave-expanded GO and TEM images of resulting  $\text{MnO}_2$  nanoparticles. The right, bottom graph shows the Ragone plot of the hybrid supercapacitor. Reproduced with permission from ref 556. Copyright American Chemical Society (2012).

synthesized through a microwave-assisted method.<sup>563</sup> The hybrid exhibited a specific capacitance of 243.2 F/g. Graphene/ $\text{Co}_3\text{O}_4$  nanoplate hybrids were made by hydrothermal treatment and subsequent calcination aimed at improved electrochemical performances.<sup>564</sup> The  $\text{Co}_3\text{O}_4$  nanoplates were homogeneously distributed on the surfaces of graphene sheets with lengths of 0.5–1  $\mu\text{m}$  and widths of 100–300 nm. For the graphene load of 7 wt %, a maximal specific capacitance of 472.5 F/g was produced. However, the capacitance was increased by 25.2% after 450 cycles and then decreased slightly in the following 550 cycles. This phenomenon should be ascribed to the gradual activation of the

nanostructures at the initial 450 cycles and following capacitance fading of the fully activated  $\text{Co}_3\text{O}_4$  nanoplates after continuous charge–discharge cycling. Another Co-based sheet-on-sheet graphene/ $\text{Co(OH)}_2$  composite was synthesized through in situ one-step hydrothermal growth.<sup>565</sup> This hybrid realized a high specific capacitance of 540 F/g at a current density of 10 A/g in 1 M KOH aqueous solution. Moreover, the capacitance was increased to 810 F/g during the first 1000 cycles and then maintained at 651 F/g after 10 000 cycles.

The other metal oxide or hydroxide materials such as  $\text{Ni(OH)}_2$ ,  $\text{Fe}_2\text{O}_3$  or  $\text{Fe}_3\text{O}_4$ ,  $\text{TiO}_2$ , and  $\text{ZnO}$  have also been incorporated with graphene to prepare electrodes for super-

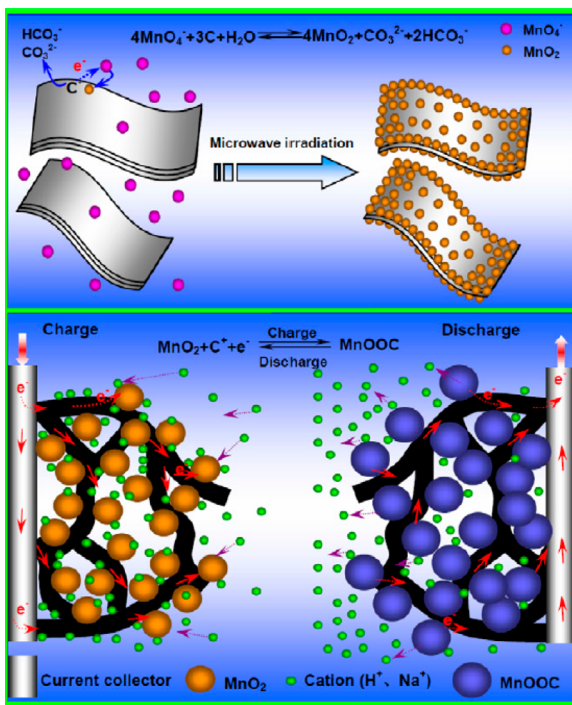


**Figure 63.** Schematic illustration to the synthesis and electrochemical energy storage process of graphene/MnO<sub>2</sub> hybrid. Reproduced with permission from ref 434. Copyright Elsevier (2010).

capacitors with high performances.<sup>478,553,566–571</sup> A graphene/Ni(OH)<sub>2</sub> nanocrystal hybrid exhibited a very high specific capacitance of 1335 F/g at a current density of 2.8 A/g.<sup>543</sup> The good cyclic stability was also verified at a high current density of 28.6 A/g without obvious decrease in capacitance after 2000 cycles. Recently, more and more attention has been paid to explore ternary systems such as graphene/CNT/conducting polymer, graphene/CNT/metal oxide, and graphene/conducting polymer/metal oxide for better electrochemical performances.<sup>572–574</sup> They are designed to not only effectively take advantages of each moieties but also realize their synergistic interactions.

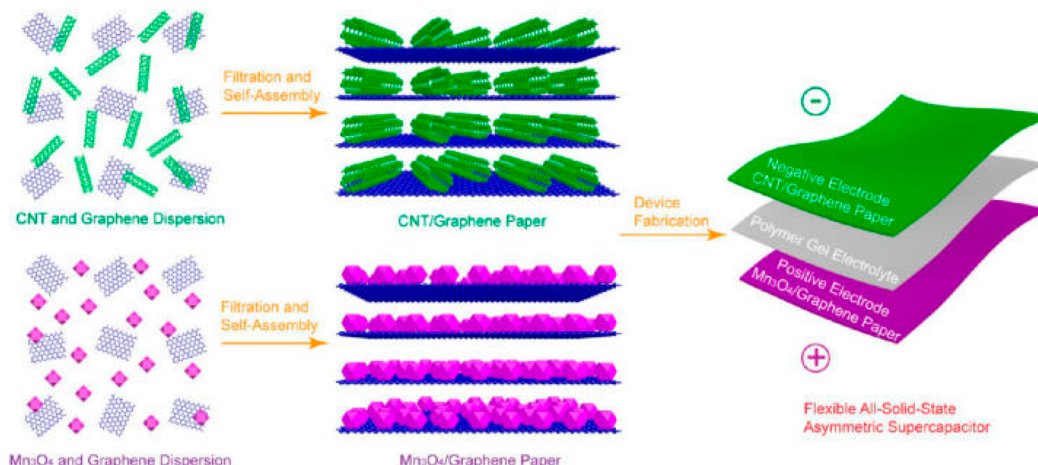


**Figure 64.** Schematic illustration to the fabrication of all-solid-state flexible asymmetric supercapacitors using polymer gel electrolyte and freestanding CNT/graphene and Mn<sub>3</sub>O<sub>4</sub>/graphene paper electrodes. Reproduced with permission from ref 560. Copyright American Chemical Society (2012).

**4.2.3. Mesoporous Carbon.** Activated carbon is still mainly used as electrode materials of EDLCs due to a low cost but limited by an abundant proportion of micropores (diameters of less than 2 nm) that are not easily wetted by the electrolyte for charge storage. Moreover, even in the situation where the micropores can be wetted by the electrolyte, the ionic transport in such small pores is so slow that the high rate capability, one of the advantages of EDLCs, may not be realized. In contrast, mesoporous carbon is demonstrated for a large specific surface area that is favorable for high charge accumulation, effective electrolyte wetting, and rapid ionic transport. In particular, they can be designed with tunable pore sizes and size distributions according to the dimensions of electrolytes and ions to enhance the charge accumulation and transport. The regularly interconnected mesopores (larger than 2 nm) produced both high charge storage and rate capability that are also unavailable for the randomly connected pores in the activated carbon.

**4.2.3.1. Bare OMC Electrodes.** Mesoporous carbon materials are typically prepared using mesoporous silica as the template. Therefore, two-dimensional hexagonal and three-dimensional cubic mesoporous silica produce two- and three-dimensional ordered mesoporous carbon materials, respectively. A lot of effort was previously made to enhance the pore volume in activated carbon by increasing the specific surface area and refining the activation process. However, the results suggested that there was not a linear relationship between the specific surface area and capacitance, and the effects differed for different kinds of electrolytes in the case of different pore sizes.<sup>575,576</sup> For instance, in organic electrolytes, the pores smaller than 1 nm may not be accessible to the solvated ions, whose sizes are larger than 1 nm.<sup>577</sup> Even the hydrated ions also required a pore size of at least 0.5 nm. The ions owned a dynamic sheath of solvent molecules, and hundreds of kilojoules per mole were required to remove it in aqueous solutions. A pore size distribution in the range of 2–5 nm, which is larger than the sizes of two solvated ions, was preferred to improve the energy density and power capability.<sup>576</sup> It was also found that there existed a balance between micropores and mesopores to maximize the specific capacitance. Too high an amount of mesopores can diminish the volumetric capacitance due to a lower density of the carbon material.<sup>578,579</sup> It was also

suggested that a partial desolvation of ions could occur, allowing for the access to small pores (less than 2 nm).<sup>427</sup> High capacitance was observed for a mesoporous carbon containing large numbers of small micropores, indicating that a partial ion desolvation could lead to an improved capacitance.<sup>425,580</sup> Despite all of these efforts, only a moderate improvement in the electrochemical property of the mesoporous carbon had been made, and gravimetric capacitances in the ranges of 100–120 and 150–200 F/g in organic and aqueous electrolytes were achieved, respectively.<sup>581,582</sup>

The work from Frackowiak and co-workers is highlighted for a better understanding of the impact of pore sizes on the electrochemical performance above.<sup>427</sup> Two highly ordered mesoporous carbons with narrow dispersed pore sizes of 3 and 8 nm (Figure 65) were synthesized from a mesostructured

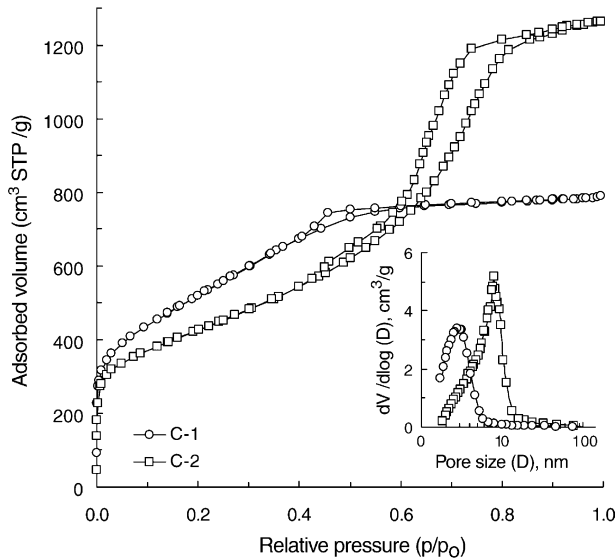


**Figure 65.** Nitrogen adsorption/desorption isotherms at 77 K (inset, pore size distribution of the carbon). Reproduced with permission from ref 427. Copyright Elsevier (2005).

SBA-16 silica template and polyfurfuryl alcohol carbon precursor, respectively. The above mesopores displayed large equivalent BET-surface areas of 1880 and 1510 m<sup>2</sup>/g and were labeled as C-1 and C-2, respectively (Table 7). For C-1, a remarkable presence of micropores with sizes below 2 nm was also observed, which explained the prominent surface area. C-1 and C-2 were then tested in various electrolytic solutions (acidic, alkaline, and aprotic) by the two-electrode method. Table 8 presents the capacitances for both C-1 and C-2 in different media estimated by impedance spectroscopy at 1 mHz, galvanostatic discharges at a current density range from 0.1 to 1 A/g, and voltammetry cycling at scan rates from 1 to 20 mV/s. Sample C-1 demonstrated a higher capacitance than C-2 in all three electrolytic solutions, which agreed with the higher

**Table 8. Specific Capacitances (F g<sup>-1</sup>) of the Mesoporous Carbon Materials, i.e., C-1 and C-2, Prepared through the Template Method<sup>a</sup>**

|                         | 1 mol L <sup>-1</sup> H <sub>2</sub> SO <sub>4</sub> (F g <sup>-1</sup> ) |     | 6 mol L <sup>-1</sup> KOH (F g <sup>-1</sup> ) |     | aprotic medium (F g <sup>-1</sup> ) |     |
|-------------------------|---|-----|--|-----|-------------------------------------|-----|
|                         | C-1   | C-2 | C-1  | C-2 | C-1                                 | C-2 |
| impedance 1 mHz         | 145   | 127 | 137  | 115 | 91                                  | 83  |
| 100 mA g <sup>-1</sup>  | 191   | 161 | 184  | 134 | 97                                  | 93  |
| 200 mA g <sup>-1</sup>  | 172   | 154 | 169  | 121 | 96                                  | 89  |
| 500 mA g <sup>-1</sup>  | 155   | 144 | 145  | 87  | 90                                  | 86  |
| 1000 mA g <sup>-1</sup> | 143   | 132 | 133  | 67  | 86                                  | 80  |
| 1 mV s <sup>-1</sup>    | 199   | 164 | 205  | 160 | 113                                 | 109 |
| 2 mV s <sup>-1</sup>    | 178   | 158 | 186  | 143 | 108                                 | 99  |
| 5 mV s <sup>-1</sup>    | 163   | 156 | 156  | 136 | 100                                 | 97  |
| 10 mV s <sup>-1</sup>   | 154   | 143 | 148  | 69  | 98                                  | 96  |
| 20 mV s <sup>-1</sup>   | 144   | 134 | 132  | 47  | 94                                  | 95  |

<sup>a</sup>Reproduced with permission from ref 427. Copyright Elsevier (2005). The specific capacitances were calculated from galvanostatic charge–discharge curves based on the impedance spectroscopy at 1 mHz.

surface area of C-1 (1880 m<sup>2</sup>/g in comparison to 1510 m<sup>2</sup>/g). For both C-1 and C-2, the capacitances in an acidic medium were higher than those in an alkaline medium. Unexpectedly, C-2 dramatically lost the ability for charge accumulation at high current densities in alkaline medium, e.g., only 87 F/g at a current density of 0.5 A/g, while a much higher capacitance of 145 F/g was maintained for C-1. The sharp decrease in C-2 could be explained by a worse connectivity among pores compared with C-1. However, the two samples shared a moderate decrease in capacitance with the increasing scan rate or current density in the acidic or nonaqueous electrolyte. The capacitances were close to 100 F/g in the nonaqueous electrolyte, relatively high values for organic solutions. To summarize, the mesoporous carbon with a smaller average pore size of 3 nm showed an obviously better performance than the larger pore with average diameter of 8 nm.

**4.2.3.2. Functionalized OMC Electrodes.** A good charge propagation and capability for high current loads requires the presence of small mesopores (2–4 nm), while the microspores play an important role in the electrically charging process. Therefore, it is also necessary to introduce the micropores into the mesoporous carbon, which has been generally realized through an activation process. For instance, the capacitance was increased from 115 to 223 F/g after the CO<sub>2</sub> activation.<sup>583</sup> When sulfuric acid, nitric acid, or ammonium persulfate solution was used as the activation agent, a variety of functional groups are also produced, which further benefit the adsorption of ions and improve the hydrophilicity or lipophilicity. Therefore, it can not only introduce the additional pseudocapacitance to enhance the capacitance greatly but also facilitate a better wetting process between the electrolyte and carbon electrode and speed the ion transport within the

**Table 7. Porous Carbons Synthesized by a Template Method<sup>a</sup>**

| carbon | $S_{\text{BET}}$ (m <sup>2</sup> g <sup>-1</sup> ) | total pore volume (cm <sup>3</sup> g <sup>-1</sup> ) | $\alpha$ -analysis                                 |  | maximum of pore size distribution (nm) | fwhm (nm) <sup>b</sup> |
|--------|--|--|--|--|--|------------------------|
|        |  |  | mesopore volume (cm <sup>3</sup> g <sup>-1</sup> ) | $S_{\text{ext}}$ (m <sup>2</sup> g <sup>-1</sup> ) |  |                        |
| C-1    | 1880   | 1.22   | 1.08   | 20   | 2.8                                    | 2.5                    |
| C-2    | 1510   | 1.96   | 1.79   | 50   | 8                                      | 5                      |

<sup>a</sup>Reproduced with permission from ref 427. Copyright Elsevier (2005). <sup>b</sup>Full width at a half-maximum.

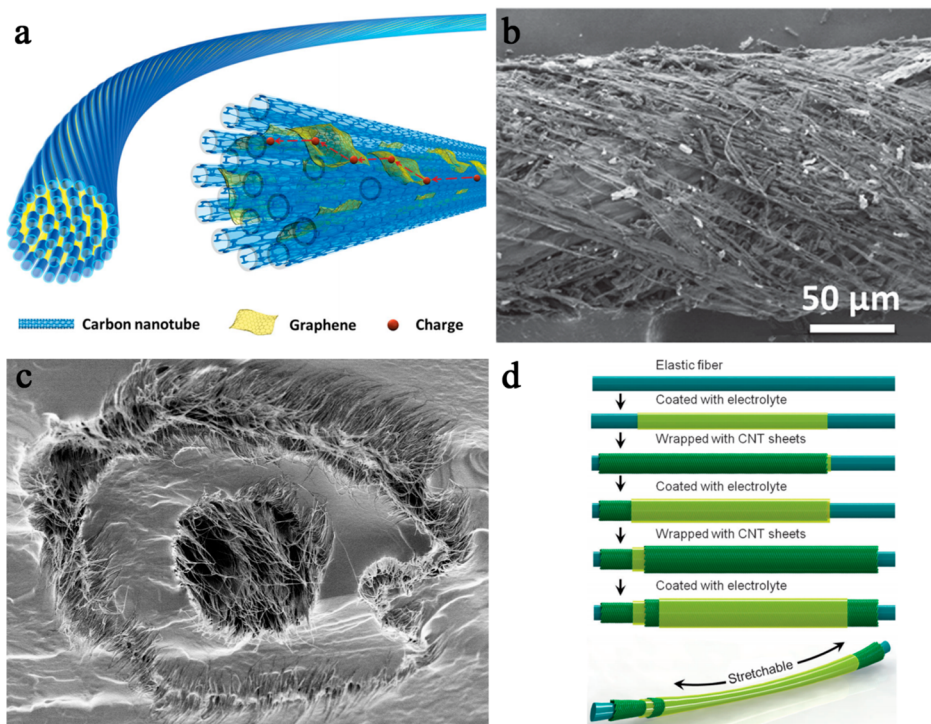
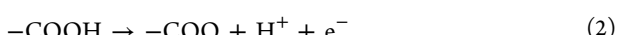
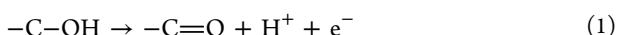


**Figure 66.** (a) Structure of the graphene/CNT fiber. Reproduced with permission from ref 589. Copyright John Wiley and Sons (2014). (b) SEM image of OMC/CNT hybrid fiber. Reproduced with permission from ref 590. Copyright John Wiley and Sons (2013). (c) Cross-sectional SEM image of the coaxial supercapacitor. Reproduced with permission from ref 591. Copyright John Wiley and Sons (2013). (d) Schematic illustration to the fabricating process of the stretchable fiber-shaped supercapacitor. Reproduced with permission from ref 592. Copyright John Wiley and Sons (2013).

micropores. For instance, an OMC material was activated by nitric acid to produce both small mesopores and functional groups of  $-\text{OH}$ ,  $-\text{COOH}$ , and/or  $-\text{C}=\text{O}$  on the surface.<sup>584</sup> A bimodal pore size distribution of 2.1–2.3 and 5.3 nm was observed to provide a specific surface area of 465–578 m<sup>2</sup>/g. Compared with the original OMC, the introduced functional groups offered a pseudocapacitance to increase the specific capacitance from 117 to 295 F/g at a scan rate of 10 mV/s in 6 M KOH aqueous solution. The following redox reactions can explain the caused pseudocapacitance by the mentioned functional groups. A high cycling stability with capacitance retention of 85% was discovered for over 500 cycles.



Nitrogen doping has been also widely used to enhance the electrochemical properties of OMC materials in supercapacitors. An N-doped OMC can be synthesized by using soluble resol as a carbon source, dicyandiamide as a nitrogen source, and commercial triblock copolymer F127 as a soft template via solvent evaporation induced self-assembly process.<sup>585</sup> The as-synthesized OMC showed a  $p6m$  and  $I\bar{m}3m$  symmetry mesostructures with pore sizes of 3.1–17.6 nm, specific surface areas of 494–586 m<sup>2</sup>/g, and high nitrogen weight percentages up to 13.1%. The nitrogen doping can enhance the surface polarity, electrical conductivity, and electron donor tendency of the mesoporous carbon, leading to a promising capacitor performance. A specific capacitance of 262 F/g was achieved at a current density of 0.2 A/g.

Besides the pore sizes and surface modifications, the channel structure is also an important factor to the capacitivity of OMC. For instance, two-dimensional hexagonal mesoporous and three-dimensional cubic mesoporous carbon materials were prepared from SBA-15 and MCM-48 silica templates, respectively.<sup>109</sup> When they were used as electrodes, the three-dimensional networked structure produced a better performance than the former one due to a lower ion-transfer resistance.<sup>586</sup>

**4.2.3.3. OMC Based Composite or Hybrid Electrodes.** The OMC materials have been also incorporated with the other moieties for better electrochemical properties, and a broad spectrum of pseudocapacitor materials such as conducting polymers and metal oxides are widely investigated. For instance, a family of hierarchical PANI nanowire/ordered bimodal mesoporous carbon (PANI/OBMC) composites were synthesized by a chemical oxidative polymerization.<sup>587</sup> The composite material showed a specific surface area of 599 m<sup>2</sup>/g with a combination of smaller mesopores (2.4 nm in diameter) and larger mesopores (5.0 nm in diameter). The PANI nanowires with diameters of 20–30 nm were formed after polymerization. This composite material displayed a decent specific capacitance of 517 F/g and an outstanding cycling stability with 91.5% retention after 1000 charge–discharge cycles. The coexistence of both large and small mesopores were believed to be favorable for the penetration of electrolyte, while the unique hierarchical structure shortened the charge transfer distance, which was crucial to the facilitation of ion diffusions.

**4.2.4. Fiber-Shaped Electrochemical Capacitors.** Similar to the other fiber-shaped energy devices such as PSCs, DSSCs, and LIBs, the fiber-shaped supercapacitors are also flexible, lightweight, integratable, and wearable. Different from

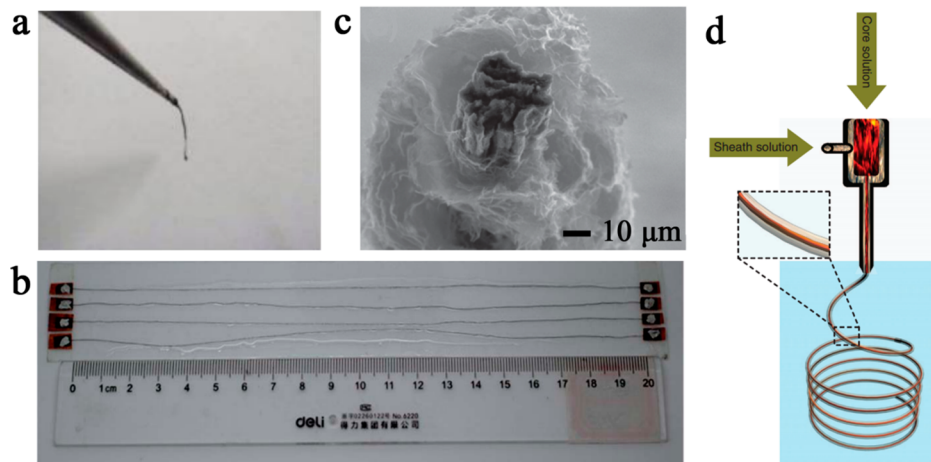


**Figure 67.** (a) Photograph of a graphene fiber made by CVD. Reproduced with permission from ref 595. Copyright American Chemical Society (2011). (b) Photograph of a graphene fiber made by reduction of a wet-spun GO fiber. Reproduced with permission from ref 597. Copyright Royal Society of Chemistry (2013). (c) Cross-sectional SEM image of the porous graphene-coated graphene fiber. Reproduced with permission from ref 598. Copyright John Wiley and Sons (2013). (d) Schematic illustration to the coaxial spinning process. Adapted from refs and 597–599. Reproduced with permission from ref 599. Copyright Nature Publishing Group (2013).

the fiber-shaped DSSCs, PSCs, and LIBs that require strict conditions such as oxygen- and water-free atmospheres, the fiber-shaped supercapacitors can be more easily fabricated by directly twisting two fiber electrodes or wrapping two electrodes on fiber substrate to form a coaxial structure in the air under mild conditions; they can be also more stably operated with long lifetime during use.

Previously, two aligned CNT fibers coated with gel electrolyte were twisted into a supercapacitor based on the combined high electrical conductivity and mechanical strength of CNT fibers besides being flexible.<sup>588</sup> The bare CNT fiber-based supercapacitor was typically a classical EDLC with a relatively low specific capacitance of 13.3 F/g (3.01 mF/cm<sup>2</sup> or 0.015 mF/cm). To enhance the specific capacitance of the fiber-shaped supercapacitor, graphene was incorporated into aligned CNT fibers by soaking aligned CNT sheets with graphene oxide solution, followed by twisting the GO/CNT hybrid sheet into fibers and reduction of GO into graphene (Figure 66a).<sup>589</sup> Here graphene sheets served as effective bridges among neighboring CNTs and improved the charge transport due to the π–π interactions between graphene sheets and CNTs. Therefore, compared with the bare CNT fiber, the graphene/CNT hybrid fiber possessed higher conductivity and produced a higher specific capacitance of 31.5 F/g (4.97 mF/cm<sup>2</sup> or 0.027 mF/cm) that can be well maintained after 5000 cycles. Similarly, OMC particles were also introduced into CNT sheets and then spun into CNT fibers containing OMC (Figure 66b).<sup>590</sup> The use of OMC particles with tunable pores offered larger specific surface area for higher specific capacitances, while the continuous aligned CNTs with high electrical conductivity ensured rapid charge transports in the hybrid fiber. At the OMC weight percentage of 87%, a specific capacitance of 39.67 mF/cm<sup>2</sup> (1.91 mF/cm) was achieved in the resulting fiber-shaped supercapacitor. In contrast, a much lower capacitance of 1.97 mF/cm<sup>2</sup> (0.017 mF/cm) was obtained for the bare CNT fiber. Note that the aligned CNT/OMC hybrid fiber also showed much higher electrochemical performance than the bare OMC discussed above.

The fiber-shaped supercapacitor could be also made into a coaxial structure. For instance, an aligned CNT fiber served as the inner electrode while an aligned CNT sheet wrapped as the

sheath acted as the outer electrode with a gel electrolyte being sandwiched between them (Figure 66c).<sup>591</sup> Compared with the twisting structure, this coaxial structure decreased the internal resistance of the supercapacitor and thus improved the energy storing properties with a specific capacitance of 59 F/g. The coaxial fiber-shaped supercapacitor could be bent, knotted and woven into textiles without obvious damages or breaking in structure and loss in capacitance. For instance, the capacitance was maintained by 97.2% after bending at the angle of 180° for 100 cycles. However, a large decrease of the capacitance (~20%) occurred after stretching for 75 cycles at a strain of 10%, which had largely limited their practical applications in portable and wearable electronic devices. To this end, elastic fiber electrodes were further developed by winding aligned CNT sheets onto stretchable polymer fibers (Figure 66d).<sup>592</sup> After deposition of gel electrolyte on the elastic fiber electrode, another layer of CNT sheets was wound onto the surface and served as the other electrode. The resulting fiber-shaped supercapacitor can be stretched by 75% for 100 cycles and the capacitance had been maintained by above 95%. In addition, the capacitance was maintained by over 90% after 1000 charge–discharge cycles under a stretched state.

To further improve the capacitance of the fiber-shaped supercapacitors, conducting polymers have been also introduced to fabricate pseudo capacitor. For instance, PANI/CNT composite fibers were easily synthesized through electrochemical polymerization of aniline.<sup>593</sup> Because of the pseudo capacitance of PANI, the specific capacitance was increased to 274 F/g or 263 mF/cm. Moreover, because PANI was electrochemically deposited onto aligned CNTs through *in situ* polymerization, the composite fiber inherited high flexibility of the CNT fiber and can be woven into clothes. After 50 cycles of bending, the capacitance remained by 97%, indicating a high stability of the supercapacitor under bending. PANI array can be also deposited onto CNT fibers through dilute polymerization process.<sup>594</sup> Due to the larger surface area of the PANI array, the specific capacitance reached 38 mF/cm<sup>2</sup> that was 16 times of the bare CNT fiber (2.3 mF/cm<sup>2</sup>). As expected, transition metal oxide such as MnO<sub>2</sub> with a high pseudo capacitance could be also introduced to aligned CNT

fibers.<sup>588</sup> The capacitance was improved to 3.707 mF/cm<sup>2</sup> compared with 3.010 mF/cm<sup>2</sup> in the bare CNT fiber.

Graphene fibers that are lightweight, flexible, strong, and conductive can be also used as fiber electrodes to fabricate fiber-shaped supercapacitors typically with an electrical double layer capacitance. Graphene fibers with a porous and crumpled structure were first assembled from graphene synthesized by CVD.<sup>595</sup> The electrochemical properties were measured in a three-electrode system and liquid electrolyte. A low specific capacitance of 1.4 mF/cm<sup>2</sup> was produced. Two graphene fibers were then twisted into an all-solid-state fiber-shaped supercapacitor in a gel electrolyte, and the specific capacitance turned out to be 2.13 mF/cm<sup>2</sup>.<sup>596</sup> The prepared fiber was relatively short (Figure 67a).<sup>572</sup> Long graphene fibers were later synthesized by wet spinning of GO sheets, followed by reduction into graphene fiber (Figure 67b).<sup>597</sup> The resulting fiber-shaped supercapacitor exhibited a specific capacitance of 3.3 mF/cm<sup>2</sup> without fatigue even after 5000 charge–discharge cycles or 5000 bending cycles. To improve the electrical double layer capacitance, a unique all-graphene core–sheath fiber was designed and fabricated with a graphene fiber as the core and three-dimensional porous graphene framework as the sheath (Figure 67c).<sup>598</sup> The core graphene fiber endowed a high conductivity, and the porous network-like graphene in the sheath offered a high specific surface area. As a result, a specific capacitance of 40 F/g (1.7 mF/cm<sup>2</sup>) was achieved. Recently, a modified coaxial fiber shape was realized to reach high electrochemical performances (Figure 67d).<sup>599</sup> In this novel coaxial structure, the core graphene fiber was reduced from a GO fiber, and the sheath was composed of sodium carbonymethyl cellulose that was ionically conductive but electrically insulated. The specific capacitance was greatly improved to 177 mF/cm<sup>2</sup>. Moreover, the protocol was simple and industrially viable for a scalable fabrication of wearable supercapacitor.

Conductive polymers and metal oxides are also incorporated into graphene fibers to provide pseudocapacitances. PANI nanoparticles can be deposited onto graphene sheets by *in situ* chemical polymerization of aniline. The specific capacitance can be increased to 66.6 mF/cm<sup>2</sup> from 3.3 mF/cm<sup>2</sup> of the bare graphene fiber.<sup>597</sup> When the graphene fiber was decorated with MnO<sub>2</sub> nanoparticles, the specific capacitance was enhanced from 2.13 to 42 mF/cm<sup>2</sup> at the scan rate of 10 mV/s.<sup>596</sup>

#### 4.3. Summary

Advanced electrical storage technology has greatly affected the progress of our society. Carbon nanomaterials like CNT, graphene, and OMC demonstrate high potentials in energy storage due to large specific surface areas and high electrical conductivities. The main efforts are paid to their applications as cathodes and additives to promote the transport of both lithium ions and electrons in LIBs, or to increase the specific surface area and conductivities in EDLC, or to be used as a skeleton to fabricate freestanding electrodes (without metal substrate or binder). Moreover, CNT, graphene, and OMC can also be composited with conducting polymers or metal oxides to fabricate hybrid electrodes in energy storage devices with high specific capacitances and power densities.

Besides unremitting efforts in developing materials with high energy storage capabilities, increasing attention is paid to the application in the wearable and portable electronics, which requires flexible and lightweight energy storage systems to power them. Learning from the old textile technology, LIBs and supercapacitors in a new fiber format have been summarized

above, and these fiber-shaped energy storage systems can be further woven into clothes or other flexible structures. It is recognized that the fiber electrode plays a vital role in constructing fiber-shaped batteries and supercapacitors. At present, both continuous CNT and graphene fibers had been synthesized with high strengths and conductivities. The resulting LIBs and supercapacitors based on those fiber electrodes were lightweight, flexible, weaveable, and wearable. They could even be highly stretchable to achieve better adaptability to the movement of our bodies.

## 5. INTEGRATED ENERGY CONVERSION AND STORAGE DEVICES

Converted solar energy needs to be stored effectively for future applications. Traditionally, solar cells can be connected with an energy storage device by external electrical wires. However, it is not convenient and also reduces the use efficiency of the produced solar energy. To this end, some integrated devices were developed by integrating solar cells and storage devices together.<sup>600–603</sup>

### 5.1. Planar Structure

An integrated device named a “photocapacitor” was previously realized by designing a sandwich structure where a redox-free liquid electrolyte had been sandwiched between a photoanode and an activated carbon-based capacitor. This photocapacitor showed a specific capacitance of 690 mF/cm<sup>2</sup>.<sup>600</sup> Later, a printable and all-solid-state integrated device was made by stacking a PSC and a supercapacitor together (Figure 68). This design can reduce the internal resistance by 43% compared with the case where the PSC and supercapacitor were connected by external conducting wires.<sup>601</sup>

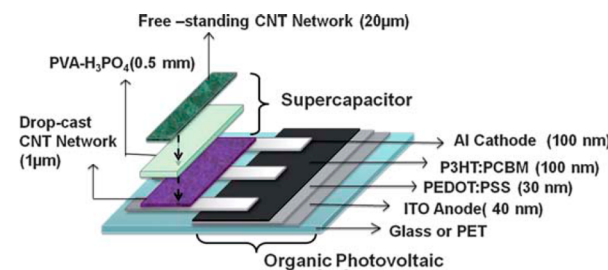


**Figure 68.** Schematic illustration of a self-powered integrated device fabricated by integrating a PSC and a supercapacitor. Reproduced with permission from ref 601. Copyright Royal Society of Chemistry (2010).

After several years of optimizations, an all-solid-state self-powering integrated device was fabricated by integrating a DSSC and a supercapacitor based on penetrated and aligned CNT films (Figure 69).<sup>602</sup> These CNT films were prepared by a pressing method from CNT arrays with remarkable electronic and catalytic properties. The working mechanism of the integrated device is summarized below. Upon illumination, the generated electrons from dye molecules are injected into the conduction band of TiO<sub>2</sub> and flow to the outer MWCNT electrode, which provide a potential for charging the supercapacitor. The photoelectrical conversion part showed a  $V_{OC}$  of 0.750 V,  $J_{SC}$  of 13.41 mA/cm<sup>2</sup>, and FF of 0.61, which produced an energy conversion efficiency of 6.10%. The energy storage part exhibited a specific capacitance of 26 F/g with energy storage efficiency of ~84%. Herein, the entire energy conversion and storage efficiency was calculated to be ~5.12%.

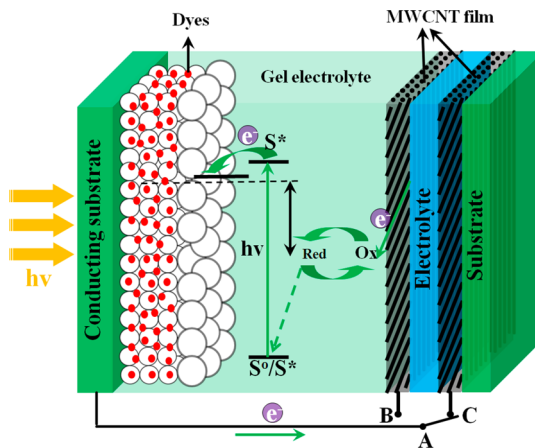


**Figure 69.** Schematic illustration of a self-powering integrated device by sharing a penetrated and aligned MWCNT film electrode in energy conversion and storage parts. Reproduced with permission from ref 602. Copyright Royal Society of Chemistry (2013).

## 5.2. Fiber Shape

Similarly, a fiber-shaped self-powered integrated device can be also fabricated by integrating a solar cell with a supercapacitor. In general, they can be divided into two main types. In one case, the photoelectric conversion and energy storage parts share one electrode along the axial direction.<sup>336,604,605</sup> In the other case, the electric conversion and energy storage parts are coaxially coated onto a fiber sequentially.<sup>144</sup>

It is relatively easy to fabricate the first type of self-powering integrated devices. For instance, a solar cell, nanogenerator and supercapacitor had been fabricated onto a fiber for both energy conversion and storage.<sup>604</sup> More specifically, it can gather both mechanical and solar energy and then store the generated energy in the integrated fiber-shaped supercapacitor (Figure 70). The three parts shared the same modified Kevlar fiber electrode with ZnO nanowires perpendicularly grown on the surface. Graphene was wound on the modified Kevlar fiber to serve as the other electrode in the integrated energy device. The energy conversion efficiency was relatively low at 0.02%,

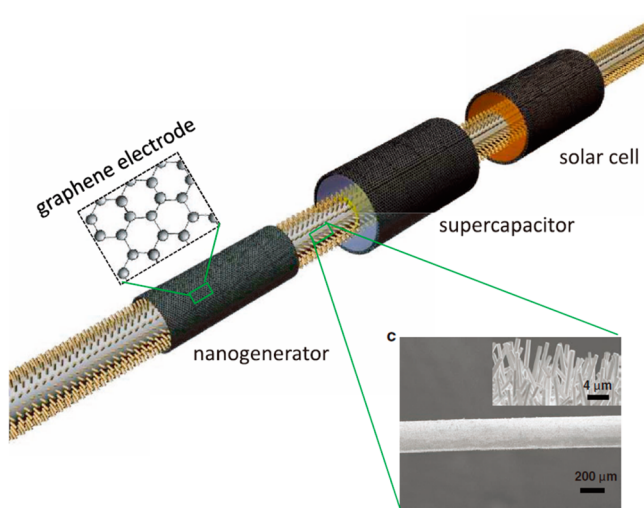


**Figure 70.** Schematic illustration of a self-powering fiber-shaped integrated device by integrating the solar cell, nanogenerator, and supercapacitor together. Reproduced with permission from ref 604. Copyright John Wiley and Sons (2011).

and the supercapacitor showed specific capacitance of 0.4 mF/cm<sup>2</sup> or ~0.025 mF/cm.

This integrated energy device has taken advantage of various nanostructured materials. Graphene was used as the outer electrode with large specific surface area, high conductivity, and optical transmittance, while the modified Kevlar fiber with ZnO nanowires exhibited a proper working function for nanogenerator and acceptable specific surface area for dye absorption in DSSC and charge storage in supercapacitor. However, a relatively poor performance had been observed in the integrated energy device due to the difficulty in the control and fabrication optimization. The graphene was coated on the Cu mesh and was not highly transparent, resulting in a significant loss in the transmission of incident light to the dyes in DSSC. The specific surface area of ZnO nanowires was not high enough to offer remarkable electrochemical performance in the supercapacitor.

Recently, a fiber-shaped integrated device had been realized by integrating a DSSC with a supercapacitor based on an aligned CNT fiber and modified titanium wire.<sup>336</sup> Specifically, the photoelectric conversion and energy storage parts shared a titanium wire electrode that was perpendicularly grown with aligned TiO<sub>2</sub> nanotubes. Here the aligned TiO<sub>2</sub> nanotubes not only improved the charge separation and transport in the photoelectric conversion part but also increased the specific surface area in the energy storage part. Two aligned CNT fibers were separately wrapped for the photoelectric conversion and energy storage parts. The energy conversion efficiency reached 2.2% from the photoelectric conversion part, and a specific capacitance was about 0.6 mF/cm<sup>2</sup> in the energy storage part. The energy storage part can be rapidly charged to a voltage which was close to the open-circuit voltage of the photoelectric conversion part upon light irradiation. The energy storage efficiency reached 68.4%, and the entire photoelectric conversion and storage efficiency was therefore calculated to be 1.5% by multiplying the energy conversion efficiency and energy storage efficiency. The charging process of the integrated energy device was schematically shown in Figure 71.

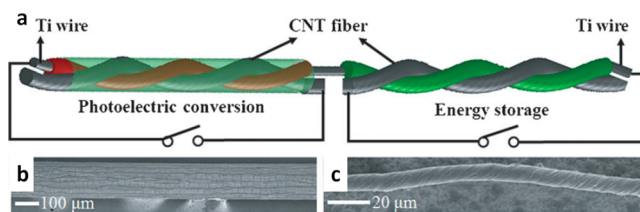


**Figure 71.** (a) Schematic illustration of the integrated fiber-shaped device for photoelectric conversion and energy storage based on a series connection. (b, c) SEM images of the working electrode in the photoelectric conversion part and CNT fiber, respectively. Reproduced with permission from ref 336. Copyright John Wiley and Sons (2012).

Fiber-shaped integrated devices in a coaxial structure have been also developed with the solar cell in the outer sheath while a supercapacitor in the inner sheath (Figure 72).<sup>606</sup> A polymer separation tube between the photo anode and supercapacitor was used to prevent the infiltration of electrolyte into the supercapacitor, and aligned CNT sheets were wrapped on the separation tube acting as the counter electrode. At the outermost part, another polymer separation tube was used to stabilize the liquid electrolyte and protect the whole device.

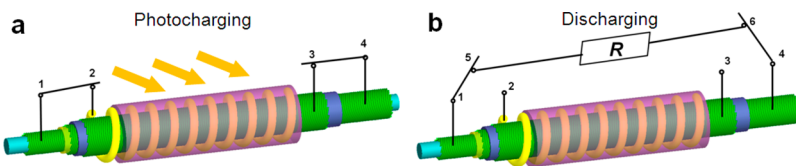


**Figure 72.** (a, b) Schematic illustration of the photocharge and discharge for the self-powering energy fiber based on a coaxial structure, respectively. Reproduced with permission from ref 606. Copyright John Wiley and Sons (2014).

Compared with the integrated device by connecting photovoltaic and storing devices in series, it was not easy for this coaxial structure to break in the connected part and showed higher photoelectric conversion efficiency under the same device area. The entire energy conversion and storage efficiency was calculated to be 1.83% and can be well maintained under stretching. The realization of stretchability here is a great breakthrough and promoted the integrated devices toward practical applications.

## 6. SUMMARY AND PERSPECTIVE

Four dimensions of carbon nanomaterials, i.e., zero-dimensional fullerene, one-dimensional CNTs, two-dimensional graphene, and three-dimensional OMC, have been developed in both energy conversion and storage devices. For the energy conversion devices such as solar cells, CNTs and graphene are widely studied as alternative materials to replace the traditional transparent conducting electrode (i.e., ITO); fullerene derivatives are still the best electron acceptor in PSCs to date; CNTs and graphene were prepared as counter electrodes to replace the platinum electrodes due to their high catalytic activity, stability, and flexibility in DSSCs. The carbon nanomaterials also demonstrate high potentials in energy storage due to large specific surface areas and high electrical conductivities. For instance, CNT, graphene, and OMC have been widely used as cathodes and additives to promote the transport of both lithium ions and electrons in LIBs. In addition, they can also be used as electrodes in supercapacitors with high specific capacitances and power densities.

To summarize the recent study, the main efforts have been made and will be continuously made to develop general and effective methods in the synthesis of carbon nanomaterials, design and accurately control their structures, and enhance their chemical and physical properties.<sup>607</sup> For the synthesis, it is difficult to produce fullerene derivatives at a large scale, so the cost remains high for practical applications. Although CNTs have been extensively explored for over two decades at both the academy and industry and the costs have been largely decreased to synthesize them, it is challenging to achieve a high purity, particularly, SWCNTs, for various applications, and the purifying process increases the complexity and cost. Compared with the CNT, graphene is studied on the synthesis for a much shorter time but has been shown to be much cheaper, so it seems available for a large-scale application. However, the realization of high-quality graphene materials with close and repeating sizes remains challenging. In contrast, the synthesis of OMC materials is still limited to a lab scale.

It is always important, although not easy, to control the structures of nanoscaled materials, particularly, at an application scale. Although CNTs have been extensively explored, it is still unavailable to accurately control and repeat the structures of SWCNTs, and there typically exist a lot of defects particularly for MWCNTs. Similarly, although it has been demonstrated to synthesize single-layered graphene sheets with designed

dimensions, it remains difficult to control the sizes and layer numbers of graphene sheets at large scales. In contrast, the available control on the pore morphology and size in OMC materials seems already efficient in satisfying energy storage applications, more effort is needed to control the sizes of aggregates that typically appear for OMC materials. On the other hand, it is typically necessary to prepare uniform materials for high properties and stable performances in use. However, carbon nanomaterials tend to aggregate into island-like or networked structures depending on their morphologies during preparation. The zero-dimensional fullerene derivatives form large aggregates, one-dimensional CNTs often appear in networks, while two-dimensional graphene sheets are more likely to stack into thicker plates.

Carbon nanomaterials are often modified with the other functional organic or inorganic moieties to prevent the above aggregation for uniform structures. In most cases, their physical properties will be decreased after modification, e.g., both mechanical strengths and electrical conductivities of CNTs and graphene sheets are obviously decreased after the connection of polymers on their surfaces by chemical reactions. On the other hand, the properties of carbon nanomaterials may be also enhanced after the specifically designed modifications. For instance, the catalytic properties of CNTs were greatly improved for high-capacitance supercapacitors after doping with nitrogen in the wall, the cross-linked polymers among neighboring CNTs in fact increased the tensile strengths of CNT fibers, and the electrochemical deposition of platinum nanoparticles on the surfaces of graphene sheets in a fiber produced the highest power conversion efficiency of the DSSC. Therefore, it is a key to design the second component and connection format in modification for higher properties.

Besides the continuous efforts on the effective synthesis, structure control, and property optimization, increasing attention has also been made to incorporate different dimensions of carbon nanomaterials to more efficiently take their advantages. For instance, graphene sheets were coated onto aligned CNTs to serve as bridges to rapidly transport charges, which obviously increased the power conversion efficiency of the resulting DSSC. OMC materials had been wrapped into aligned CNTs to produce hybrid fibers where both high specific surface area of OMC and high electrical conductivity of CNT were integrated to achieve a synergistic effect. As a result, when they were used as electrodes to fabricate supercapacitors, a much improved specific capacitance had been achieved in a comparison to either bare CNT or OMC material. The above design may represent a general and effective strategy in the development of carbon nanomaterials for energy applications with high performances.

With the rapid development on the portable and wearable electronic devices in the near future, it becomes critical to find soft, lightweight, and integratable energy systems to power them. In principle, the conventional rigid, planar energy conversion and storage cannot meet the above requirements.

Fortunately, learning from the history of the old textile technology, several groups have created solar cells, LIBs, and supercapacitors in a new fiber format, and these fiber-shaped energy systems can be further woven into clothes or other flexible structures. Aiming at practical applications, it is necessary to enhance the conversion or storage efficiency with low cost. Several attempts showed that carbon nanomaterials played a critical or even indispensable role along this direction. For instance, both continuous CNT and graphene fibers had been synthesized with high strengths and conductivities to well satisfy both energy conversion and storage applications. The resulting solar cells, LIBs, and supercapacitors were lightweight, weaveable, and flexible. They could even be made to be stretchable to match the curved surfaces of our bodies.

Nevertheless, a lot of problems need to be solved, although inspiring results have been made in just a few years. One, electrical conductivities of nanostructured carbon fibers are required to be largely enhanced. At the current level of  $10^4$ – $10^5$  S/m, the energy conversion and storage efficiencies were sharply decreased for continuous fiber-shaped devices at lengths of meters. Two, although fiber-shaped energy devices can be carefully woven into textiles at lab, it remains challenging to develop general and effective approaches to weave them at an applicable scale at industry. Obviously, the fiber-shaped solar cells, LIBs, and supercapacitors have to be much more carefully handled compared with chemical fibers. Three, there exist hundreds to thousands of fiber electrodes or even more, and it is highly desired to find efficient methods to connect them together. Four, it is easy to produce short circuits for the fiber-shaped energy devices during use, so they may fail to work in a short period, which remains a challenge and may be overcome by the microelectronic design. Last but not least, it is also important to produce continuous, stable nanostructured fibers with low costs to make the fiber-shaped energy devices scalable soon. This direction represents a new and promising platform for the development of carbon nanomaterials and will attract broad interests in various fields to further push it forward.

## AUTHOR INFORMATION

### Corresponding Author

\*E-mail: penghs@fudan.edu.cn.

### Notes

The authors declare no competing financial interest.

### Biographies



Zhibin Yang received his B.S. in Applied Physics from East China University of Science and Technology in 2009 and Ph.D. in

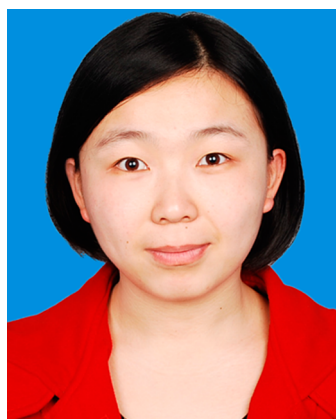
Macromolecular Chemistry and Physics at Fudan University in 2014. His research centers on fiber-shaped solar cells, supercapacitors, and their integrated energy devices. He is currently a postdoctoral fellow at the University of Washington in the United States.



Jing Ren received her B.S. in Chemistry at Lanzhou University in 2011. She is currently a Ph.D. student majoring in Macromolecular Chemistry and Physics at Fudan University. She is developing fiber-shaped lithium ion batteries and supercapacitors based on carbon nanomaterials and their applications in sensing.



Zhitao Zhang received his B.S. in Polymer Material and Engineering from East China University of Science and Technology in 2012. He is currently a Ph.D. student majoring in Macromolecular Chemistry and Physics at Fudan University. His work focuses on the synthesis of carbon nanomaterials and their applications in optoelectronic devices.



Xuli Chen received her B.S. in Physics at Shanxi Normal University in 2009 and Ph.D. in Macromolecular Chemistry and Physics at Fudan University in 2014. Her research focuses on the development of smart

polymer materials and supercapacitors. She is currently a postdoctoral fellow at Department of Macromolecular Science and Engineering, Case Western Reserve University in the United States.



Guozhen Guan received his B.S. in Polymer Material and Engineering from Shanghai Jiao Tong University in 2010. He is currently a Ph.D. student majoring in Macromolecular Chemistry and Physics at Fudan University. His work focuses on the synthesis of novel carbon nanomaterials and their applications in DSSCs and lithium ion batteries.



Longbin Qiu received his B.S. in Polymer Material and Engineering from Sun Yat-Sen University in 2011. He is currently a Ph.D. student majoring in Macromolecular Chemistry and Physics at Fudan University. His work focuses on the synthesis of carbon nanomaterials and their applications in dye-sensitized and perovskite solar cells.



Ye Zhang received her B.S. in Polymer Material and Engineering from Zhengzhou University in 2013. She is currently a graduate student majoring in Macromolecular Chemistry and Physics at Fudan University. Her work focuses on developing fiber-shaped lithium ion batteries and supercapacitors based on carbon nanomaterials.



Huisheng Peng is currently a Professor in the Department of Macromolecular Science and Laboratory of Advanced Materials at Fudan University. He received his B.E. in Polymer Materials at Donghua University in China in 1999, M.S. in Macromolecular Chemistry and Physics at Fudan University in China in 2003 and Ph.D. in Chemical Engineering at Tulane University in the United States in 2006. He then worked at Los Alamos National Laboratory before joining Fudan University in 2008. His research focuses on the development of novel energy materials and devices particularly based on polymers and has published over 120 peer-reviewed papers.

## ACKNOWLEDGMENTS

This work was supported by MOST (2011CB932503), NSFC (21225417), STCSM (12 nm0503200), the Fok Ying Tong Education Foundation, the Program for Special Appointments of Professors at Shanghai Institutions of Higher Learning, and the Program for Outstanding Young Scholars from the Organization Department of the CPC Central Committee.

## REFERENCES

- (1) Dai, L.; Chang, D. W.; Baek, J. B.; Lu, W. *Small* **2012**, *8*, 1130–1166.
- (2) Brennan, L. J.; Byrne, M. T.; Bari, M.; Gun'ko, Y. K. *Adv. Energy Mater.* **2011**, *1*, 472–485.
- (3) Dillon, A. *Chem. Rev.* **2010**, *110*, 6856–6872.
- (4) Yu, Y.; Cui, C.; Qian, W.; Xie, Q.; Zheng, C.; Kong, C.; Wei, F. *Asia-Pac. J. Chem. Eng.* **2013**, *8*, 234–245.
- (5) Candelaria, S. L.; Shao, Y.; Zhou, W.; Li, X.; Xiao, J.; Zhang, J.-G.; Wang, Y.; Liu, J.; Li, J.; Cao, G. *Nano Energy* **2012**, *1*, 195–220.
- (6) Zhai, Y.; Dou, Y.; Zhao, D.; Fulvio, P. F.; Mayes, R. T.; Dai, S. *Adv. Mater.* **2011**, *23*, 4828–4850.
- (7) He, Y.; Chen, H.-Y.; Hou, J.; Li, Y. *J. Am. Chem. Soc.* **2010**, *132*, 1377–1382.
- (8) Chen, L.-M.; Hong, Z.; Li, G.; Yang, Y. *Adv. Mater.* **2009**, *21*, 1434–1449.
- (9) Li, C.-Z.; Yip, H.-L.; Jen, A. K. Y. *J. Mater. Chem.* **2012**, *22*, 4161–4177.
- (10) Zhu, S.-E.; Li, F.; Wang, G.-W. *Chem. Soc. Rev.* **2013**, *42*, 7535–7570.
- (11) Zhang, J.; Bowles, F. L.; Bearden, D. W.; Ray, W. K.; Fuhrer, T.; Ye, Y.; Dixon, C.; Harich, K.; Helm, R. F.; Olmstead, M. M.; Balch, A. L.; Dorn, H. C. *Nat. Chem.* **2013**, *5*, 880–885.
- (12) Peng, K.-J.; Liu, Y.-L. *Macromolecules* **2011**, *44*, 5006–5012.
- (13) Chuvalin, A.; Kaiser, U.; Bichoutskaia, E.; Besley, N. A.; Khlobystov, A. N. *Nat. Chem.* **2010**, *2*, 450–453.
- (14) Chen, L.; Chen, W.; Huang, H.; Zhang, H. L.; Yuhara, J.; Wee, A. T. S. *Adv. Mater.* **2008**, *20*, 484–488.
- (15) Vasil'ev, Y. V.; Hirsch, A.; Taylor, R.; Drewello, T. *Chem. Commun.* **2004**, 1752–1753.
- (16) Sugunan, S. K.; Greenwald, C.; Paige, M. F.; Steer, R. P. *J. Phys. Chem. C* **2013**, *117*, 5419–5427.

- (17) Kim, Y.; Cook, S.; Tuladhar, S. M.; Choulis, S. A.; Nelson, J.; Durrant, J. R.; Bradley, D. D. C.; Giles, M.; McCulloch, I.; Ha, C.-S.; Ree, M. *Nat. Mater.* **2006**, *5*, 197–203.
- (18) Dou, L.; You, J.; Hong, Z.; Xu, Z.; Li, G.; Street, R. A.; Yang, Y. *Adv. Mater.* **2013**, *25*, 6642–6671.
- (19) Günes, S.; Neugebauer, H.; Sariciftci, N. S. *Chem. Rev.* **2007**, *107*, 1324–1338.
- (20) Yang, L.; Yan, L.; You, W. *J. Phys. Chem. Lett.* **2013**, *4*, 1802–1810.
- (21) Gan, L.; Yang, D.; Zhang, Q.; Huang, H. *Adv. Mater.* **2010**, *22*, 1498–1507.
- (22) Oriana, S.; Aroua, S.; Sollner, J. O. B.; Ma, X.-J.; Iwamoto, Y.; Yamakoshi, Y. *Chem. Commun.* **2013**, *49*, 9302–9304.
- (23) Mendes, R. G.; Bachmatiuk, A.; Buchner, B.; Cuniberti, G.; Rummeli, M. H. *J. Mater. Chem.* **2013**, *1*, 401–428.
- (24) Roy, X.; Lee, C.-H.; Crowther, A. C.; Schenck, C. L.; Besara, T.; Lalancette, R. A.; Siegrist, T.; Stephens, P. W.; Brus, L. E.; Kim, P.; Steigerwald, M. L.; Nuckolls, C. *Science* **2013**, *341*, 157–160.
- (25) Iijima, S. *Nature* **1991**, *354*, 56–58.
- (26) Graham, A. P.; Duesberg, G. S.; Hoenlein, W.; Kreupl, F.; Liebau, M.; Martin, R.; Rajasekharan, B.; Pamler, W.; Seidel, R.; Steinhoegl, W.; Unger, E. *Appl. Phys. A: Mater. Sci. Process.* **2005**, *80*, 1141–1151.
- (27) Odom, T. W.; Huang, J. L.; Kim, P.; Lieber, C. M. *Nature* **1998**, *391*, 62–64.
- (28) Dai, H. J. *Acc. Chem. Res.* **2002**, *35*, 1035–1044.
- (29) Bethune, D. S.; Kiang, C. H.; Devries, M. S.; Gorman, G.; Savoy, R.; Vazquez, J.; Beyers, R. *Nature* **1993**, *363*, 605–607.
- (30) Iijima, S.; Ichihashi, T. *Nature* **1993**, *363*, 603–605.
- (31) Guo, T.; Nikolaev, P.; Thess, A.; Colbert, D. T.; Smalley, R. E. *Chem. Phys. Lett.* **1995**, *243*, 49–54.
- (32) Dal, H. J.; Rinzler, A. G.; Nikolaev, P.; Thess, A.; Colbert, D. T.; Smalley, R. E. *Chem. Phys. Lett.* **1996**, *260*, 471–475.
- (33) Fan, S. S.; Chapline, M. G.; Franklin, N. R.; Tombler, T. W.; Cassell, A. M.; Dai, H. J. *Science* **1999**, *283*, 512–514.
- (34) Reina, A.; Hofmann, M.; Zhu, D.; Kong, J. *J. Phys. Chem. C* **2007**, *111*, 7292–7297.
- (35) Hata, K.; Futaba, D. N.; Mizuno, K.; Namai, T.; Yumura, M.; Iijima, S. *Science* **2004**, *306*, 1362–1364.
- (36) Yamada, T.; Namai, T.; Hata, K.; Futaba, D. N.; Mizuno, K.; Fan, J.; Yudasaka, M.; Yumura, M.; Iijima, S. *Nat. Nanotechnol.* **2006**, *1*, 131–136.
- (37) Seah, C.-M.; Chai, S.-P.; Mohamed, A. R. *Carbon* **2011**, *49*, 4613–4635.
- (38) Nessim, G. D. *Nanoscale* **2010**, *2*, 1306–1323.
- (39) Yu, M. F.; Files, B. S.; Arepalli, S.; Ruoff, R. S. *Phys. Rev. Lett.* **2000**, *84*, 5552–5555.
- (40) Demczyk, B. G.; Wang, Y. M.; Cummings, J.; Hetman, M.; Han, W.; Zettl, A.; Ritchie, R. O. *Mater. Sci. Eng., A* **2002**, *334*, 173–178.
- (41) Ebbesen, T. W.; Lezec, H. J.; Hiura, H.; Bennett, J. W.; Ghaemi, H. F.; Thio, T. *Nature* **1996**, *382*, 54–56.
- (42) Pop, E.; Mann, D.; Wang, Q.; Goodson, K. E.; Dai, H. J. *Nano Lett.* **2006**, *6*, 96–100.
- (43) Kim, P.; Shi, L.; Majumdar, A.; McEuen, P. L. *Phys. Rev. Lett.* **2001**, *87*, 215502.
- (44) Chen, T.; Cai, Z.; Yang, Z.; Li, L.; Sun, X.; Huang, T.; Yu, A.; Kia, H. G.; Peng, H. *Adv. Mater.* **2011**, *23*, 4620–4625.
- (45) Yang, Z.; Li, L.; Lin, H.; Luo, Y.; He, R.; Qiu, L.; Ren, J.; Peng, H. *Chem. Phys. Lett.* **2012**, *549*, 82–85.
- (46) Moniruzzaman, M.; Winey, K. I. *Macromolecules* **2006**, *39*, S194–S205.
- (47) Vigolo, B.; Penicaud, A.; Coulon, C.; Sauder, C.; Pailler, R.; Journet, C.; Bernier, P.; Poulin, P. *Science* **2000**, *290*, 1331–1334.
- (48) Dalton, A. B.; Collins, S.; Razal, J.; Munoz, E.; Ebron, V. H.; Kim, B. G.; Coleman, J. N.; Ferraris, J. P.; Baughman, R. H. *J. Mater. Chem.* **2004**, *14*, 1–3.
- (49) Ericson, L. M.; Fan, H.; Peng, H.; Davis, V. A.; Zhou, W.; Sulpizio, J.; Wang, Y.; Booker, R.; Vavro, J.; Guthy, C.; Parra-Vasquez, A. N.; Kim, M. J.; Ramesh, S.; Saini, R. K.; Kittrell, C.; Lavin, G.; Schmidt, H.; Adams, W. W.; Billups, W. E.; Pasquali, M.; Hwang, W. F.; Hauge, R. H.; Fischer, J. E.; Smalley, R. E. *Science* **2004**, *305*, 1447–1450.
- (50) Davis, V. A.; Parra-Vasquez, A. N. G.; Green, M. J.; Rai, P. K.; Behabtu, N.; Prieto, V.; Booker, R. D.; Schmidt, J.; Kesselman, E.; Zhou, W.; Fan, H.; Adams, W. W.; Hauge, R. H.; Fischer, J. E.; Cohen, Y.; Talmon, Y.; Smalley, R. E.; Pasquali, M. *Nat. Nanotechnol.* **2009**, *4*, 830–834.
- (51) Zhang, S.; Koziol, K. K.; Kinloch, I. A.; Windle, A. H. *Small* **2008**, *4*, 1217–1222.
- (52) Behabtu, N.; Young, C. C.; Tsentalovich, D. E.; Kleinerman, O.; Wang, X.; Ma, A. W.; Bengio, E. A.; ter Waarbeek, R. F.; de Jong, J. J.; Hoogerwerf, R. E.; Fairchild, S. B.; Ferguson, J. B.; Maruyama, B.; Kono, J.; Talmon, Y.; Cohen, Y.; Otto, M. J.; Pasquali, M. *Science* **2013**, *339*, 182–186.
- (53) Jiang, K. L.; Li, Q. Q.; Fan, S. S. *Nature* **2002**, *419*, 801–801.
- (54) Zhang, M.; Atkinson, K. R.; Baughman, R. H. *Science* **2004**, *306*, 1358–1361.
- (55) Zhang, X.; Jiang, K.; Feng, C.; Liu, P.; Zhang, L.; Kong, J.; Zhang, T.; Li, Q.; Fan, S. *Adv. Mater.* **2006**, *18*, 1505–1510.
- (56) Liu, K.; Sun, Y.; Zhou, R.; Zhu, H.; Wang, J.; Liu, L.; Fan, S.; Jiang, K. *Nanotechnology* **2010**, *21*, 045708.
- (57) Liu, K.; Zhu, F.; Liu, L.; Sun, Y.; Fan, S.; Jiang, K. *Nanoscale* **2012**, *4*, 3389–3393.
- (58) Zheng, L. X.; O'Connell, M. J.; Doorn, S. K.; Liao, X. Z.; Zhao, Y. H.; Akhadov, E. A.; Hoffbauer, M. A.; Roop, B. J.; Jia, Q. X.; Dye, R. C.; Peterson, D. E.; Huang, S. M.; Liu, J.; Zhu, Y. T. *Nat. Mater.* **2004**, *3*, 673–676.
- (59) Zhang, R. F.; Zhang, Y. Y.; Zhang, Q.; Xie, H. H.; Qian, W. Z.; Wei, F. *ACS Nano* **2013**, *7*, 6156–6161.
- (60) Zhu, H. W.; Xu, C. L.; Wu, D. H.; Wei, B. Q.; Vajtai, R.; Ajayan, P. M. *Science* **2002**, *296*, 884–886.
- (61) Li, Y. L.; Kinloch, I. A.; Windle, A. H. *Science* **2004**, *304*, 276–278.
- (62) Zhong, X. H.; Li, Y. L.; Liu, Y. K.; Qiao, X. H.; Feng, Y.; Liang, J.; Jin, J.; Zhu, L.; Hou, F.; Li, J. Y. *Adv. Mater.* **2010**, *22*, 692–696.
- (63) Koziol, K.; Vilatela, J.; Moisala, A.; Motta, M.; Cunniff, P.; Sennett, M.; Windle, A. *Science* **2007**, *318*, 1892–1895.
- (64) Motta, M.; Moisala, A.; Kinloch, I. A.; Windle, A. H. *Adv. Mater.* **2007**, *19*, 3721–3726.
- (65) Novoselov, K. S.; Geim, A. K.; Morozov, S.; Jiang, D.; Zhang, Y.; Dubonos, S.; Grigorieva, I.; Firsov, A. *Science* **2004**, *306*, 666–669.
- (66) Geim, A. K.; Novoselov, K. S. *Nat. Mater.* **2007**, *6*, 183–191.
- (67) Balandin, A. A. *Nat. Mater.* **2011**, *10*, 569–581.
- (68) Park, S.; Ruoff, R. S. *Nat. Nanotechnol.* **2009**, *4*, 217–224.
- (69) Sutter, P. W.; Flege, J.-I.; Sutter, E. A. *Nat. Mater.* **2008**, *7*, 406–411.
- (70) Berger, C.; Song, Z.; Li, X.; Wu, X.; Brown, N.; Naud, C.; Mayou, D.; Li, T.; Hass, J.; Marchenkov, A. N. *Science* **2006**, *312*, 1191–1196.
- (71) Reina, A.; Jia, X.; Ho, J.; Nezich, D.; Son, H.; Bulovic, V.; Dresselhaus, M. S.; Kong, J. *Nano Lett.* **2008**, *9*, 30–35.
- (72) Kim, K. S.; Zhao, Y.; Jang, H.; Lee, S. Y.; Kim, J. M.; Kim, K. S.; Ahn, J.-H.; Kim, P.; Choi, J.-Y.; Hong, B. H. *Nature* **2009**, *457*, 706–710.
- (73) Bae, S.; Kim, H.; Lee, Y.; Xu, X.; Park, J.-S.; Zheng, Y.; Balakrishnan, J.; Lei, T.; Kim, H. R.; Song, Y. I. *Nat. Nanotechnol.* **2010**, *5*, 574–578.
- (74) Li, X.; Cai, W.; An, J.; Kim, S.; Nah, J.; Yang, D.; Piner, R.; Velamakanni, A.; Jung, I.; Tutuc, E. *Science* **2009**, *324*, 1312–1314.
- (75) Dikin, D. A.; Stankovich, S.; Zimney, E. J.; Piner, R. D.; Domke, G. H.; Evmenenko, G.; Nguyen, S. T.; Ruoff, R. S. *Nature* **2007**, *448*, 457–460.
- (76) Kosynkin, D. V.; Higginbotham, A. L.; Sinitkii, A.; Lomeda, J. R.; Dimiev, A.; Price, B. K.; Tour, J. M. *Nature* **2009**, *458*, 872–876.
- (77) Lee, C.; Wei, X.; Kysar, J. W.; Hone, J. *Science* **2008**, *321*, 385–388.

- (78) Bolotin, K. I.; Sikes, K.; Jiang, Z.; Klima, M.; Fudenberg, G.; Hone, J.; Kim, P.; Stormer, H. *Solid State Commun.* **2008**, *146*, 351–355.
- (79) Stoller, M. D.; Park, S.; Zhu, Y.; An, J.; Ruoff, R. S. *Nano Lett.* **2008**, *8*, 3498–3502.
- (80) Balandin, A. A.; Ghosh, S.; Bao, W.; Calizo, I.; Teweldebrhan, D.; Miao, F.; Lau, C. N. *Nano Lett.* **2008**, *8*, 902–907.
- (81) Xu, Z.; Gao, C. *Nat. Commun.* **2011**, *2*, 571.
- (82) Cruz-Silva, R.; Morelos-Gomez, A.; Kim, H. I.; Jang, H. K.; Tristan, F.; Vega-Diaz, S.; Rajukumar, L. P.; Elias, A. L.; Perea-Lopez, N.; Suhr, J.; Endo, M.; Terrones, M. *ACS Nano* **2014**, *8*, 5959–5967.
- (83) Dong, Z.; Jiang, C.; Cheng, H.; Zhao, Y.; Shi, G.; Jiang, L.; Qu, L. *Adv. Mater.* **2012**, *24*, 1856–1861.
- (84) Carretero-Gonzalez, J.; Castillo-Martinez, E.; Dias-Lima, M.; Acik, M.; Rogers, D. M.; Sovich, J.; Haines, C. S.; Lepro, X.; Kozlov, M.; Zhakidov, A.; Chabal, Y.; Baughman, R. H. *Adv. Mater.* **2012**, *24*, 5695–5701.
- (85) Ma, T. Y.; Liu, L.; Yuan, Z. Y. *Chem. Soc. Rev.* **2013**, *42*, 3977–4003.
- (86) Ryoo, R.; Joo, S. H.; Jun, S. *J. Phys. Chem. B* **1999**, *103*, 7743–7746.
- (87) Joo, S. H.; Choi, S. J.; Oh, I.; Kwak, J.; Liu, Z.; Terasaki, O.; Ryoo, R. *Nature* **2001**, *412*, 169–172.
- (88) Jun, S.; Joo, S. H.; Ryoo, R.; Kruck, M.; Jaroniec, M.; Liu, Z.; Ohsuna, T.; Terasaki, O. *J. Am. Chem. Soc.* **2000**, *122*, 10712–10713.
- (89) Li, F.; Song, J. X.; Shan, C. S.; Gao, D. M.; Xu, X. Y.; Niu, L. *Biosens. Bioelectron.* **2010**, *25*, 1408–1413.
- (90) Li, J.; Guo, S. J.; Zhai, Y. M.; Wang, E. K. *Anal. Chim. Acta* **2009**, *649*, 196–201.
- (91) Liang, C. D.; Dai, S. *J. Am. Chem. Soc.* **2006**, *128*, 5316–5317.
- (92) Fang, Y.; Gu, D.; Zou, Y.; Wu, Z. X.; Li, F. Y.; Che, R. C.; Deng, Y. H.; Tu, B.; Zhao, D. Y. *Angew. Chem., Int. Ed.* **2010**, *49*, 7987–7991.
- (93) Ryoo, R.; Ko, C. H.; Kruck, M.; Antochshuk, V.; Jaroniec, M. J. *Phys. Chem. B* **2000**, *104*, 11465–11471.
- (94) Hou, Y.; Ndamanisha, J. C.; Guo, L. P.; Peng, X. J.; Bai, J. *Electrochim. Acta* **2009**, *54*, 6166–6171.
- (95) Beck, J. S.; Vartuli, J. C.; Roth, W. J.; Leonowicz, M. E.; Kresse, C. T.; Schmitt, K. D.; Chu, C. T. W.; Olson, D. H.; Sheppard, E. W.; McCullen, S. B.; Higgins, J. B.; Schlenker, J. L. *J. Am. Chem. Soc.* **1992**, *114*, 10834–10843.
- (96) Bedia, J.; Rosas, J. M.; Marquez, J.; Rodriguez-Mirasol, J.; Cordero, T. *Carbon* **2009**, *47*, 286–294.
- (97) Al-Muhtaseb, S. A.; Ritter, J. A. *Adv. Mater.* **2003**, *15*, 101–114.
- (98) Joo, S. H.; Ryoo, R.; Kruck, M.; Jaroniec, M. *J. Phys. Chem. B* **2002**, *106*, 4640–4646.
- (99) Banham, D.; Feng, F. X.; Burt, J.; Alsrayheen, E.; Birss, V. *Carbon* **2010**, *48*, 1056–1063.
- (100) Wang, K. Q.; Yang, H.; Zhu, L.; Ma, Z. S.; Xing, S. Y.; Lv, Q.; Liao, J. H.; Liu, C. P.; Xing, W. *Electrochim. Acta* **2009**, *54*, 4626–4630.
- (101) Wang, J. X.; Xue, C. F.; Lv, Y. Y.; Zhang, F.; Tu, B.; Zhao, D. Y. *Carbon* **2011**, *49*, 4580–4588.
- (102) Liang, C. D.; Hong, K. L.; Guiochon, G. A.; Mays, J. W.; Dai, S. *Angew. Chem., Int. Ed.* **2004**, *43*, 5785–5789.
- (103) Tanaka, S.; Nishiyama, N.; Egashira, Y.; Ueyama, K. *Chem. Commun.* **2005**, 2125–2127.
- (104) Huang, C. H.; Doong, R. A.; Gu, D.; Zhao, D. Y. *Carbon* **2011**, *49*, 3055–3064.
- (105) Zhao, D.; Huo, Q.; Feng, J.; Chmelka, B. F.; Stucky, G. D. *J. Am. Chem. Soc.* **1998**, *120*, 6024–6036.
- (106) Hulicova, D.; Kodama, M.; Hatori, H. *Chem. Mater.* **2006**, *18*, 2318–2326.
- (107) Hulicova, D.; Yamashita, J.; Soneda, Y.; Hatori, H.; Kodama, M. *Chem. Mater.* **2005**, *17*, 1241–1247.
- (108) Hulicova-Jurcakova, D.; Kodama, M.; Shiraishi, S.; Hatori, H.; Zhu, Z. H.; Lu, G. Q. *Adv. Funct. Mater.* **2009**, *19*, 1800–1809.
- (109) Inagaki, M.; Konno, H.; Tanaike, O. *J. Power Sources* **2010**, *195*, 7880–7903.
- (110) Itoi, H.; Nishihara, H.; Kogure, T.; Kyotani, T. *J. Am. Chem. Soc.* **2011**, *133*, 1165–1167.
- (111) Jain, P.; Fonseca, D. A.; Schaible, E.; Lueking, A. D. *J. Phys. Chem. C* **2007**, *111*, 1788–1800.
- (112) Ndamanisha, J.-C.; Guo, L. *Anal. Chim. Acta* **2012**, *747*, 19–28.
- (113) Hu, Q. Y.; Lu, Y. F.; Meisner, G. P. *J. Phys. Chem. C* **2008**, *112*, 1516–1523.
- (114) Ellmer, K. *Nat. Photonics* **2012**, *6*, 809–817.
- (115) Hecht, D. S.; Hu, L.; Irvin, G. *Adv. Mater.* **2011**, *23*, 1482–1513.
- (116) Graupner, R.; Abraham, J.; Vencelova, A.; Seyller, T.; Hennrich, F.; Kappes, M. M.; Hirsch, A.; Ley, L. *Phys. Chem. Chem. Phys.* **2003**, *5*, 5472–5476.
- (117) Hecht, D. S.; Hu, L.; Irvin, G. *Adv. Mater.* **2011**, *23*, 1482–1513.
- (118) Wirth, I.; Eisebitt, S.; Kann, G.; Eberhardt, W. *Phys. Rev. B* **2000**, *61*, 5719–5723.
- (119) Geng, H.-Z.; Kim, K. K.; So, K. P.; Lee, Y. S.; Chang, Y.; Lee, Y. H. *J. Am. Chem. Soc.* **2007**, *129*, 7758–7759.
- (120) Blighe, F. M.; Lyons, P. E.; De, S.; Blau, W. J.; Coleman, J. N. *Carbon* **2008**, *46*, 41–47.
- (121) Bergin, S. D.; Nicolosi, V.; Streich, P. V.; Giordani, S.; Sun, Z.; Windle, A. H.; Ryan, P.; Niraj, N. P. P.; Wang, Z.-T. T.; Carpenter, L.; Blau, W. J.; Boland, J. J.; Hamilton, J. P.; Coleman, J. N. *Adv. Mater.* **2008**, *20*, 1876–1881.
- (122) Liu, J.; Casavant, M. J.; Cox, M.; Walters, D. A.; Boul, P.; Lu, W.; Rimberg, A. J.; Smith, K. A.; Colbert, D. T.; Smalley, R. E. *Chem. Phys. Lett.* **1999**, *303*, 125–129.
- (123) Sun, Z.; Nicolosi, V.; Bergin, S. D.; Coleman, J. N. *Nanotechnology* **2008**, *19*, 485702.
- (124) Bergin, S. D.; Nicolosi, V.; Giordani, S.; Gromard, A. d.; Carpenter, L.; Blau, W. J.; Coleman, J. N. *Nanotechnology* **2007**, *18*, 455705.
- (125) Backes, C.; Schmidt, C. D.; Hauke, F.; Böttcher, C.; Hirsch, A. *J. Am. Chem. Soc.* **2009**, *131*, 2172–2184.
- (126) Holzinger, M.; Steinmetz, J.; Samaille, D.; Glerup, M.; Paillet, M.; Bernier, P.; Ley, L.; Graupner, R. *Carbon* **2004**, *42*, 941–947.
- (127) Coleman, J. N.; Blau, W. J.; Dalton, A. B.; Muñoz, E.; Collins, S.; Kim, B. G.; Razal, J.; Selvidge, M.; Vieiro, G.; Baughman, R. H. *Appl. Phys. Lett.* **2003**, *82*, 1682.
- (128) Frizzell, C.; in het Panhuis, M.; Coutinho, D.; Balkus, K.; Minett, A.; Blau, W.; Coleman, J. *Phys. Rev. B* **2005**, *72*, 245420.
- (129) Bartholome, C.; Derre, A.; Roubeau, O.; Zakri, C.; Poulin, P. *Nanotechnology* **2008**, *19*, 325501.
- (130) Pham, G. T.; Park, Y. B.; Wang, S.; Liang, Z.; Wang, B.; Zhang, C.; Funchess, P.; Kramer, L. *Nanotechnology* **2008**, *19*, 325705.
- (131) Zhou, Y.; Hu, L.; Grüner, G. *Appl. Phys. Lett.* **2006**, *88*, 123109.
- (132) Kaempgen, M.; Duesberg, G. S.; Roth, S. *Appl. Surf. Sci.* **2005**, *252*, 425–429.
- (133) Tenent, R. C.; Barnes, T. M.; Bergeson, J. D.; Ferguson, A. J.; To, B.; Gedvilas, L. M.; Heben, M. J.; Blackburn, J. L. *Adv. Mater.* **2009**, *21*, 3210–3216.
- (134) Song, Y. I.; Yang, C. M.; Kim, D. Y.; Kanoh, H.; Kaneko, K. *J. Colloid Interface Sci.* **2008**, *318*, 365–371.
- (135) Manivannan, S.; Ryu, J. H.; Lim, H. E.; Nakamoto, M.; Jang, J.; Park, K. C. *J. Mater. Sci.: Mater. Electron.* **2009**, *21*, 72–77.
- (136) Zhang, D.; Ryu, K.; Liu, X.; Polikarpov, E.; Ly, J.; Tompson, M. E.; Zhou, C. *Nano Lett.* **2006**, *6*, 1880–1886.
- (137) Dettlaff-Welikowska, U.; Skákalová, V.; Graupner, R.; Jhang, S. H.; Kim, B. H.; Lee, H. J.; Ley, L.; Park, Y. W.; Berber, S.; Tománek, D.; Roth, S. *J. Am. Chem. Soc.* **2005**, *127*, 5125–5131.
- (138) Graupner, R.; Abraham, J.; Vencelova, A.; Seyller, T.; Hennrich, F.; Kappes, M. M.; Hirsch, A.; Ley, L. *Phys. Chem. Chem. Phys.* **2003**, *5*, 5472.
- (139) Byrne, M. T.; Hanley, C. A.; Gun'ko, Y. K. *J. Mater. Chem.* **2010**, *20*, 2949–2951.
- (140) Zhang, M.; Fang, S.; Zakhidov, A. A.; Lee, S. B.; Aliev, A. E.; Williams, C. D.; Atkinson, K. R.; Baughman, R. H. *Science* **2005**, *309*, 1215–1219.
- (141) Yang, Z.; Chen, T.; He, R.; Guan, G.; Li, H.; Qiu, L.; Peng, H. *Adv. Mater.* **2011**, *23*, 5436–5439.

- (142) Huang, S.; Yang, Z.; Zhang, L.; He, R.; Chen, T.; Cai, Z.; Luo, Y.; Lin, H.; Cao, H.; Zhu, X.; Peng, H. *J. Mater. Chem.* **2012**, *22*, 16833–16838.
- (143) Zhang, Z.; Chen, X.; Chen, P.; Guan, G.; Qiu, L.; Lin, H.; Yang, Z.; Bai, W.; Luo, Y.; Peng, H. *Adv. Mater.* **2014**, *26*, 466–470.
- (144) Chen, X.; Sun, H.; Yang, Z.; Guan, G.; Zhang, Z.; Qiu, L.; Peng, H. *J. Mater. Chem.* **2014**, *2*, 1897–1902.
- (145) Sun, H.; You, X.; Yang, Z.; Deng, J.; Peng, H. *J. Mater. Chem.* **2013**, *1*, 12422–12425.
- (146) Chen, X.; Lin, H.; Chen, P.; Guan, G.; Deng, J.; Peng, H. *Adv. Mater.* **2014**, *26*, 4444–4449.
- (147) Ellmer, K. *Nat. Photon.* **2012**, *6*, 809–817.
- (148) Eda, G.; Fanchini, G.; Chhowalla, M. *Nat. Nanotechnol.* **2008**, *3*, 270–274.
- (149) Tashima, D.; Kurosawatsu, K.; Uota, M.; Karashima, T.; Otsubo, M.; Honda, C.; Sung, Y. M. *Thin Solid Films* **2007**, *515*, 4234–4239.
- (150) Chen, T.; Xue, Y.; Roy, A. K.; Dai, L. *ACS Nano* **2013**, *8*, 1039–1046.
- (151) De, S.; Coleman, J. N. *ACS Nano* **2010**, *4*, 2713–2720.
- (152) Ito, Y.; Christodoulou, C.; Nardi, M. V.; Koch, N.; Sachdev, H.; Müllen, K. *ACS Nano* **2014**, *8*, 3337–3346.
- (153) Hummelen, J. C.; Knight, B. W.; LePeeq, F.; Wudl, F.; Yao, J.; Wilkins, C. L. *J. Org. Chem.* **1995**, *60*, 532–538.
- (154) Sariciftci, N. S.; Smilowitz, L.; Heeger, A. J.; Wudl, F. *Science* **1992**, *258*, 1474–1476.
- (155) Sariciftci, N. S.; Smilowitz, L.; Heeger, A. J.; Wudl, F. *Synth. Met.* **1993**, *59*, 333–352.
- (156) Hiramoto, M.; Fujiwara, H.; Yokoyama, M. *J. Appl. Phys.* **1992**, *72*, 3781–3787.
- (157) Yu, G.; Gao, J.; Hummelen, J.; Wudl, F.; Heeger, A. *Science-AAAS-Wkly. Pap. Ed.* **1995**, *270*, 1789–1790.
- (158) Halls, J.; Walsh, C.; Greenham, N.; Marseglia, E.; Friend, R.; Moratti, S.; Holmes, A. *Nature* **1995**, *376*, 498–500.
- (159) Kim, J. Y.; Lee, K.; Coates, N. E.; Moses, D.; Nguyen, T.-Q.; Dante, M.; Heeger, A. J. *Science* **2007**, *317*, 222–225.
- (160) Li, G.; Zhu, R.; Yang, Y. *Nat. Photonics* **2012**, *6*, 153–161.
- (161) Pasquier, A. D.; Unalan, H. E.; Kanwal, A.; Miller, S.; Chhowalla, M. *Appl. Phys. Lett.* **2005**, *87*, 203511–203513.
- (162) Wu, Z.; Chen, Z.; Du, X.; Logan, J. M.; Sippel, J.; Nikolou, M.; Kamaras, K.; Reynolds, J. R.; Tanner, D. B.; Hebard, A. F.; Rinzler, A. G. *Science* **2004**, *305*, 1273–1276.
- (163) Kymakis, E.; Stratakis, E.; Koudoumas, E. *Thin Solid Films* **2007**, *515*, 8598–8600.
- (164) Feng, Y.; Ju, X.; Feng, W.; Zhang, H.; Cheng, Y.; Liu, J.; Fujii, A.; Ozaki, M.; Yoshino, K. *Appl. Phys. Lett.* **2009**, *94*, 123302.
- (165) Kim, J.; Tung, V. C.; Huang, J. *Adv. Energy. Mater.* **2011**, *1*, 1052–1057.
- (166) Salvatierra, R. V.; Cava, C. E.; Roman, L. S.; Zarbin, A. J. G. *Adv. Funct. Mater.* **2013**, *23*, 1490–1499.
- (167) Yin, Z.; Sun, S.; Salim, T.; Wu, S.; Huang, X.; He, Q.; Lam, Y. M.; Zhang, H. *ACS Nano* **2010**, *4*, 5263–5268.
- (168) Huang, J.-H.; Fang, J.-H.; Liu, C.-C.; Chu, C.-W. *ACS Nano* **2011**, *5*, 6262–6271.
- (169) Lee, Y.-Y.; Tu, K.-H.; Yu, C.-C.; Li, S.-S.; Hwang, J.-Y.; Lin, C.-C.; Chen, K.-H.; Chen, L.-C.; Chen, H.-L.; Chen, C.-W. *ACS Nano* **2011**, *5*, 6564–6570.
- (170) Zhang, D.; Choy, W. C. H.; Wang, C. C. D.; Li, X.; Fan, L.; Wang, K.; Zhu, H. *Appl. Phys. Lett.* **2011**, *99*, 223302.
- (171) Gomez De Arco, L.; Zhang, Y.; Schlenker, C. W.; Ryu, K.; Thompson, M. E.; Zhou, C. *ACS Nano* **2010**, *4*, 2865–2873.
- (172) Wang, Y.; Tong, S. W.; Xu, X. F.; Özyilmaz, B.; Loh, K. P. *Adv. Mater.* **2011**, *23*, 1514–1518.
- (173) Hsu, C.-L.; Lin, C.-T.; Huang, J.-H.; Chu, C.-W.; Wei, K.-H.; Li, L.-J. *ACS Nano* **2012**, *6*, 5031–5039.
- (174) Liu, Z.; Li, J.; Sun, Z.-H.; Tai, G.; Lau, S.-P.; Yan, F. *ACS Nano* **2011**, *6*, 810–818.
- (175) Liu, D.; Li, Y.; Zhao, S.; Cao, A.; Zhang, C.; Liu, Z.; Bian, Z.; Liu, Z.; Huang, C. *RSC Adv.* **2013**, *3*, 13720–13727.
- (176) Chaudhary, S.; Lu, H.; Müller, A. M.; Bardeen, C. J.; Ozkan, M. *Nano Lett.* **2007**, *7*, 1973–1979.
- (177) Kim, D.-H.; Park, J.-G. *Nanotechnology* **2012**, *23*, 325401.
- (178) Nam, C.-Y.; Wu, Q.; Su, D.; Chiu, C.-y.; Tremblay, N. J.; Nuckolls, C.; Black, C. T. *J. Appl. Phys.* **2011**, *110*, 064307.
- (179) Chen, Y.; Gao, H.; Luo, Y. *Appl. Phys. Lett.* **2011**, *99*, 143309.
- (180) Stylianakis, M. M.; Kymakis, E. *Appl. Phys. Lett.* **2012**, *100*, 093301.
- (181) Li, S.-S.; Tu, K.-H.; Lin, C.-C.; Chen, C.-W.; Chhowalla, M. *ACS Nano* **2010**, *4*, 3169–3174.
- (182) Gao, Y.; Yip, H.-L.; Hau, S. K.; O’Malley, K. M.; Cho, N. C.; Chen, H.; Jen, A. K.-Y. *Appl. Phys. Lett.* **2010**, *97*, 203306.
- (183) Yun, J.-M.; Yeo, J.-S.; Kim, J.; Jeong, H.-G.; Kim, D.-Y.; Noh, Y.-J.; Kim, S.-S.; Ku, B.-C.; Na, S.-I. *Adv. Mater.* **2011**, *23*, 4923–4928.
- (184) Jeon, Y.-J.; Yun, J.-M.; Kim, D.-Y.; Na, S.-I.; Kim, S.-S. *Sol. Energy Mater. Sol. Cells* **2012**, *105*, 96–102.
- (185) Valentini, L.; Cardinali, M.; Bittolo Bon, S.; Bagnis, D.; Verdejo, R.; Lopez-Manchado, M. A.; Kenny, J. M. *J. Mater. Chem.* **2010**, *20*, 995–1000.
- (186) Fan, G.-Q.; Zhuo, Q.-Q.; Zhu, J.-J.; Xu, Z.-Q.; Cheng, P.-P.; Li, Y.-Q.; Sun, X.-H.; Lee, S.-T.; Tang, J.-X. *J. Mater. Chem.* **2012**, *22*, 15614–15619.
- (187) Liu, J.; Xue, Y.; Dai, L. *J. Phys. Chem. Lett.* **2012**, *3*, 1928–1933.
- (188) Liu, J.; Kim, G.-H.; Xue, Y.; Kim, J. Y.; Baek, J.-B.; Durstock, M.; Dai, L. *Adv. Mater.* **2013**, *26*, 786–790.
- (189) Bindl, D. J.; Safron, N. S.; Arnold, M. S. *ACS Nano* **2010**, *4*, 5657–5664.
- (190) Lee, R.-H.; Lee, L.-Y.; Huang, J.-L.; Huang, C.-C.; Hwang, J.-C. *Colloid Polym. Sci.* **2011**, *289*, 1633–1641.
- (191) Jun, G. H.; Jin, S. H.; Park, S. H.; Jeon, S.; Hong, S. H. *Carbon* **2012**, *50*, 40–46.
- (192) Lu, L.; Xu, T.; Chen, W.; Lee, J. M.; Luo, Z.; Jung, I. H.; Park, H. I.; Kim, S. O.; Yu, L. *Nano Lett.* **2013**, *13*, 2365–2369.
- (193) Jung, Y. S.; Hwang, Y.-H.; Javey, A.; Pyo, M. *J. Electrochem. Soc.* **2011**, *158*, A237–A240.
- (194) Mallajosyula, A. T.; Iyer, S. S. K.; Mazhari, B. *J. Appl. Phys.* **2011**, *109*, 124908–124910.
- (195) Liu, J.; Xue, Y.; Gao, Y.; Yu, D.; Durstock, M.; Dai, L. *Adv. Mater.* **2012**, *24*, 2228–2233.
- (196) Qu, S.; Li, M.; Xie, L.; Huang, X.; Yang, J.; Wang, N.; Yang, S. *ACS Nano* **2013**, *7*, 4070–4081.
- (197) Kymakis, E.; Amaratunga, G. A. *J. Appl. Phys. Lett.* **2002**, *80*, 112–114.
- (198) Kymakis, E.; Amaratunga, G. A. *Rev. Adv. Mater. Sci.* **2005**, *10*, 300–305.
- (199) Kymakis, E.; Koudoumas, E.; Franghiadakis, I.; Amaratunga, G. A. *J. Phys. D: Appl. Phys.* **2006**, *39*, 1058–1062.
- (200) Patyk, R. L.; Lomba, B. S.; Nogueira, A. F.; Furtado, C. A.; Santos, A. P.; Mello, R. M. Q.; Micaroni, L.; Hümmelgen, I. A. *Phys. Status Solidi RRL* **2007**, *1*, R43–R45.
- (201) Mallajosyula, A. T.; Iyer, S.; Mazhari, B. *Jpn. J. Appl. Phys.* **2009**, *48*, 011503.
- (202) Geng, J.; Zeng, T. *J. Am. Chem. Soc.* **2006**, *128*, 16827–16833.
- (203) Mallajosyula, A. T.; Iyer, S. S. K.; Mazhari, B. *J. Appl. Phys.* **2010**, *108*, 094902.
- (204) Liu, Z.; Liu, Q.; Huang, Y.; Ma, Y.; Yin, S.; Zhang, X.; Sun, W.; Chen, Y. *Adv. Mater.* **2008**, *20*, 3924–3930.
- (205) Liu, Q.; Liu, Z.; Zhang, X.; Zhang, N.; Yang, L.; Yin, S.; Chen, Y. *Appl. Phys. Lett.* **2008**, *92*, 223303.
- (206) Liu, Q.; Liu, Z.; Zhang, X.; Yang, L.; Zhang, N.; Pan, G.; Yin, S.; Chen, Y.; Wei, J. *Adv. Funct. Mater.* **2009**, *19*, 894–904.
- (207) Liu, Z.; Liu, L.; Li, H.; Dong, Q.; Yao, S.; Kidd, A. B., IV; Zhang, X.; Li, J.; Tian, W. *Sol. Energy Mater. Sol. Cells* **2012**, *97*, 28–33.
- (208) Chen, T.; Wang, S.; Yang, Z.; Feng, Q.; Sun, X.; Li, L.; Wang, Z.; Peng, H. *Angew. Chem., Int. Ed.* **2011**, *50*, 1815–1819.
- (209) Chen, T.; Qiu, L.; Cai, Z.; Gong, F.; Yang, Z.; Wang, Z.; Peng, H. *Nano Lett.* **2012**, *12*, 2568–2572.
- (210) Chen, T.; Qiu, L.; Kia, H. G.; Yang, Z.; Peng, H. *Adv. Mater.* **2012**, *24*, 4623–4628.

- (211) Zhang, S.; Ji, C.; Bian, Z.; Yu, P.; Zhang, L.; Liu, D.; Shi, E.; Shang, Y.; Peng, H.; Cheng, Q. *ACS Nano* **2012**, *6*, 7191–7198.
- (212) Pan, S.; Yang, Z.; Li, H.; Qiu, L.; Sun, H.; Peng, H. *J. Am. Chem. Soc.* **2013**, *135*, 10622–10625.
- (213) Hagfeldt, A.; Boschloo, G.; Sun, L.; Kloo, L.; Pettersson, H. *Chem. Rev.* **2010**, *110*, 6595–6663.
- (214) Murakami, T. N.; Ito, S.; Wang, Q.; Nazeeruddin, M. K.; Bessho, T.; Cesari, I.; Liska, P.; Humphry-Baker, R.; Comte, P.; Péchy, P. *J. Electrochem. Soc.* **2006**, *153*, A2255–A2261.
- (215) Yue, G.; Wu, J.; Xiao, Y.; Lin, J.; Huang, M. *Electrochim. Acta* **2012**, *67*, 113–118.
- (216) Park, S.-H.; Jung, H.-R.; Lee, W.-J. *Electrochim. Acta* **2013**, *102*, 423–428.
- (217) Lee, W. J.; Ramasamy, E.; Lee, D. Y.; Song, J. S. *ACS Appl. Mater. Interfaces* **2009**, *1*, 1145–1149.
- (218) Han, J.; Kim, H.; Kim, D. Y.; Jo, S. M.; Jang, S.-Y. *ACS Nano* **2010**, *4*, 3503–3509.
- (219) Ramasamy, E.; Lee, W. J.; Lee, D. Y.; Song, J. S. *Electrochim. Commun.* **2008**, *10*, 1087–1089.
- (220) Lin, J.-Y.; Lien, C.-H.; Chou, S.-W. *J. Solid State Electrochem.* **2012**, *16*, 1415–1421.
- (221) Kim, H.; Choi, H.; Hwang, S.; Kim, Y.; Jeon, M. *Nanoscale Res. Lett.* **2012**, *7*, 1–4.
- (222) Mei, X.; Cho, S. J.; Fan, B.; Ouyang, J. *Nanotechnology* **2010**, *21*, 395202.
- (223) Yang, Z.; Chen, T.; He, R.; Guan, G.; Li, H.; Qiu, L.; Peng, H. *Adv. Mater.* **2011**, *23*, 5436–5439.
- (224) Lee, K. S.; Lee, W. J.; Park, N.-G.; Kim, S. O.; Park, J. H. *Chem. Commun.* **2011**, *47*, 4264–4266.
- (225) Nam, J. G.; Park, Y. J.; Kim, B. S.; Lee, J. S. *Scr. Mater.* **2010**, *62*, 148–150.
- (226) Zhao, Y.; Hu, C.; Hu, Y.; Cheng, H.; Shi, G.; Qu, L. *Angew. Chem., Int. Ed.* **2012**, *51*, 11371–11375.
- (227) Dong, P.; Pint, C. L.; Hainey, M.; Mirri, F.; Zhan, Y.; Zhang, J.; Pasquali, M.; Hauge, R. H.; Verduzco, R.; Jiang, M. *ACS Appl. Mater. Interfaces* **2011**, *3*, 3157–3161.
- (228) Wu, J.; Yue, G.; Xiao, Y.; Huang, M.; Lin, J.; Fan, L.; Lan, Z.; Lin, J.-Y. *ACS Appl. Mater. Interfaces* **2012**, *4*, 6530–6536.
- (229) Li, G. R.; Wang, F.; Jiang, Q. W.; Gao, X. P.; Shen, P. W. *Angew. Chem., Int. Ed.* **2010**, *49*, 3653–3656.
- (230) Jo, Y.; Cheon, J. Y.; Yu, J.; Jeong, H. Y.; Han, C.-H.; Jun, Y.; Joo, S. H. *Chem. Commun.* **2012**, *48*, 8057–8059.
- (231) Lin, J.-Y.; Liao, J.-H.; Hung, T.-Y. *Electrochim. Commun.* **2011**, *13*, 977–980.
- (232) Peng, S.; Wu, Y.; Zhu, P.; Thavasi, V.; Mhaisalkar, S. G.; Ramakrishna, S. *J. Photochem. Photobiol. A* **2011**, *223*, 97–102.
- (233) Wang, H.-Y.; Wang, F.-M.; Wang, Y.-Y.; Wan, C.-C.; Hwang, B.-J.; Santhanam, R.; Rick, J. *J. Phys. Chem. C* **2011**, *115*, 8439–8446.
- (234) Velten, J.; Mozer, A. J.; Li, D.; Officer, D.; Wallace, G.; Baughman, R.; Zakhidov, A. *Nanotechnology* **2012**, *23*, 085201.
- (235) Luo, J.; Niu, H.-j.; Wu, W.-j.; Wang, C.; Bai, X.-d.; Wang, W. *Solid State Sci.* **2012**, *14*, 145–149.
- (236) Zhu, G.; Pan, L.; Lu, T.; Xu, T.; Sun, Z. *J. Mater. Chem.* **2011**, *21*, 14869–14875.
- (237) Wang, G.; Xing, W.; Zhuo, S. *Electrochim. Acta* **2012**, *66*, 151–157.
- (238) Yen, M.-Y.; Teng, C.-C.; Hsiao, M.-C.; Liu, P.-I.; Chuang, W.-P.; Ma, C.-C. M.; Hsieh, C.-K.; Tsai, M.-C.; Tsai, C.-H. *J. Mater. Chem.* **2011**, *21*, 12880–12888.
- (239) Wen, Z.; Cui, S.; Pu, H.; Mao, S.; Yu, K.; Feng, X.; Chen, J. *Adv. Mater.* **2011**, *23*, 5445–5450.
- (240) Hong, W.; Xu, Y.; Lu, G.; Li, C.; Shi, G. *Electrochim. Commun.* **2008**, *10*, 1555–1558.
- (241) Lin, J.-Y.; Chan, C.-Y.; Chou, S.-W. *Chem. Commun.* **2013**, *49*, 1440–1442.
- (242) Kavan, L.; Yum, J.-H.; Nazeeruddin, M. K.; Grätzel, M. *ACS Nano* **2011**, *5*, 9171–9178.
- (243) Kavan, L.; Yum, J.-H.; Grätzel, M. *Nano Lett.* **2011**, *11*, 5501–5506.
- (244) Muduli, S.; Lee, W.; Dhas, V.; Mujawar, S.; Dubey, M.; Vijayamohanan, K.; Han, S.-H.; Ogale, S. *ACS Appl. Mater. Interfaces* **2009**, *1*, 2030–2035.
- (245) Tettey, K. E.; Yee, M. Q.; Lee, D. *ACS Appl. Mater. Interfaces* **2010**, *2*, 2646–2652.
- (246) Sawatsuk, T.; Chindaduang, A.; Sae-Kung, C.; Pratontep, S.; Tumcharern, G. *Diamond Relat. Mater.* **2009**, *18*, 524–527.
- (247) Du, P.; Song, L.; Xiong, J.; Li, N.; Wang, L.; Xi, Z.; Wang, N.; Gao, L.; Zhu, H. *Electrochim. Acta* **2013**, *8*, 651–656.
- (248) Peining, Z.; Nair, A. S.; Shengyuan, Y.; Shengjie, P.; Elumalai, N. K.; Ramakrishna, S. *J. Photochem. Photobiol. A* **2012**, *231*, 9–18.
- (249) Khamwannah, J.; Noh, S. Y.; Frandsen, C.; Zhang, Y.; Kim, H.; Kong, S. D.; Jin, S. *J. Renew. Sustain. Ener.* **2012**, *4*, 023116.
- (250) Kongkanand, A.; Martínez Domínguez, R.; Kamat, P. V. *Nano Lett.* **2007**, *7*, 676–680.
- (251) Lee, K.-M.; Hu, C.-W.; Chen, H.-W.; Ho, K.-C. *Sol. Energy Mater. Sol. Cells* **2008**, *92*, 1628–1633.
- (252) Tang, Y.-B.; Lee, C.-S.; Xu, J.; Liu, Z.-T.; Chen, Z.-H.; He, Z.; Cao, Y.-L.; Yuan, G.; Song, H.; Chen, L. *ACS Nano* **2010**, *4*, 3482–3488.
- (253) Yang, N.; Zhai, J.; Wang, D.; Chen, Y.; Jiang, L. *ACS Nano* **2010**, *4*, 887–894.
- (254) Bell, N. J.; Ng, Y. H.; Du, A.; Coster, H.; Smith, S. C.; Amal, R. *J. Phys. Chem. C* **2011**, *115*, 6004–6009.
- (255) Neo, C. Y.; Ouyang, J. *J. Power Sources* **2013**, *222*, 161–168.
- (256) Grätzel, M. *Nature* **2001**, *414*, 338–344.
- (257) Gao, F.; Wang, Y.; Shi, D.; Zhang, J.; Wang, M.; Jing, X.; Humphry-Baker, R.; Wang, P.; Zakeeruddin, S. M.; Grätzel, M. *J. Am. Chem. Soc.* **2008**, *130*, 10720–10728.
- (258) Yella, A.; Lee, H.-W.; Tsao, H. N.; Yi, C.; Chandiran, A. K.; Nazeeruddin, M. K.; Diau, E. W.-G.; Yeh, C.-Y.; Zakeeruddin, S. M.; Grätzel, M. *Science* **2011**, *334*, 629–634.
- (259) Rogers, R. D.; Seddon, K. R. *Science* **2003**, *302*, 792–793.
- (260) Zhang, Q.; Liu, X. *Small* **2012**, *8*, 3711–3713.
- (261) Wang, P.; Zakeeruddin, S. M.; Exnar, I.; Grätzel, M. *Chem. Commun.* **2002**, 2972–2973.
- (262) Neo, C. Y.; Ouyang, J. *Carbon* **2013**, *54*, 48–57.
- (263) Gun, J.; Kulkarni, S. A.; Xiu, W.; Batabyal, S. K.; Sladkevich, S.; Prikhodchenko, P. V.; Gutkin, V.; Lev, O. *Electrochim. Commun.* **2012**, *19*, 108–110.
- (264) Zhang, Y.; Zhao, J.; Sun, B.; Chen, X.; Li, Q.; Qiu, L.; Yan, F. *Electrochim. Acta* **2012**, *61*, 185–190.
- (265) Ahmad, I.; Khan, U.; Gun'ko, Y. K. *K. J. Mater. Chem.* **2011**, *21*, 16990–16996.
- (266) Jung, M.-H.; Kang, M. G.; Chu, M.-J. *J. Mater. Chem.* **2012**, *22*, 16477–16483.
- (267) Kubo, W.; Kambe, S.; Nakade, S.; Kitamura, T.; Hanabusa, K.; Wada, Y.; Yanagida, S. *J. Phys. Chem. C* **2003**, *107*, 4374–4381.
- (268) Benedetti, J. E.; Correa, A. A.; Carmello, M.; Almeida, L. C.; Goncalves, A. S.; Nogueira, A. F. *J. Power Sources* **2012**, *208*, 263–270.
- (269) Shaheer Akhtar, M.; Park, J.-G.; Lee, H.-C.; Lee, S.-K.; Yang, O. *Electrochim. Acta* **2010**, *55*, 2418–2423.
- (270) Akhtar, M. S.; Li, Z. Y.; Park, D. M.; Oh, D. W.; Kwak, D.-H.; Yang, O. *Electrochim. Acta* **2011**, *56*, 9973–9979.
- (271) Wei, J.; Jia, Y.; Shu, Q.; Gu, Z.; Wang, K.; Zhuang, D.; Zhang, G.; Wang, Z.; Luo, J.; Cao, A. *Nano Lett.* **2007**, *7*, 2317–2321.
- (272) Jia, Y.; Wei, J.; Wang, K.; Cao, A.; Shu, Q.; Gui, X.; Zhu, Y.; Zhuang, D.; Zhang, G.; Ma, B.; Wang, L.; Liu, W.; Wang, Z.; Luo, J.; Wu, D. *Adv. Mater.* **2008**, *20*, 4594–4598.
- (273) Wadhwa, P.; Liu, B.; McCarthy, M. A.; Wu, Z.; Rinzler, A. G. *Nano Lett.* **2010**, *10*, 5001–5005.
- (274) Jia, Y.; Cao, A.; Bai, X.; Li, Z.; Zhang, L.; Guo, N.; Wei, J.; Wang, K.; Zhu, H.; Wu, D. *Nano Lett.* **2011**, *11*, 1901–1905.
- (275) Wadhwa, P.; Seol, G.; Petterson, M. K.; Guo, J.; Rinzler, A. G. *Nano Lett.* **2011**, *11*, 2419–2423.
- (276) Miao, X.; Tongay, S.; Petterson, M. K.; Berke, K.; Rinzler, A. G.; Appleton, B. R.; Hebard, A. F. *Nano Lett.* **2012**, *12*, 2745–2750.
- (277) Shi, E.; Zhang, L.; Li, Z.; Li, P.; Shang, Y.; Jia, Y.; Wei, J.; Wang, K.; Zhu, H.; Wu, D. *Sci. Rep.* **2012**, *2*, 884.

- (278) Tune, D. D.; Flavel, B. S.; Krupke, R.; Shapter, J. G. *Adv. Energy Mater.* **2012**, *2*, 1043–1055.
- (279) Di, J.; Yong, Z.; Zheng, X.; Sun, B.; Li, Q. *Small* **2013**, *9*, 1367–1372.
- (280) Shi, E.; Li, H.; Yang, L.; Zhang, L.; Li, Z.; Li, P.; Shang, Y.; Wu, S.; Li, X.; Wei, J.; Wang, K.; Zhu, H.; Wu, D.; Fang, Y.; Cao, A. *Nano Lett.* **2013**, *13*, 1776–1781.
- (281) NREL Research cell efficiency records (accessed January 2015).
- (282) (a) Mei, A.; Li, X.; Liu, L.; Ku, Z.; Liu, T.; Rong, Y.; Xu, M.; Hu, M.; Chen, J.; Yang, Y. *Science* **2014**, *345*, 295–298. (b) Habisreutinger, S. N.; Leijtens, T.; Eperon, G. E.; Stranks, S. D.; Nicholas, R. J.; Snaith, H. J. *Nano Lett.* **2014**, *14*, 5561–5568.
- (283) Li, Z.; Kulkarni, S. A.; Boix, P. P.; Shi, E.; Cao, A.; Fu, K.; Batabyal, S. K.; Zhang, J.; Xiong, Q.; Wong, L. H. *ACS Nano* **2014**, *8*, 6797–6804.
- (284) Sun, H.; Yang, Z.; Chen, X.; Qiu, L.; You, X.; Chen, P.; Peng, H. *Angew. Chem., Int. Ed.* **2013**, *52*, 8276–8280.
- (285) Yang, Z.; Sun, H.; Chen, T.; Qiu, L.; Luo, Y.; Peng, H. *Angew. Chem., Int. Ed.* **2013**, *52*, 7545–7548.
- (286) (a) Yang, Z.; Deng, J.; Sun, X.; Li, H.; Peng, H. *Adv. Mater.* **2014**, *26*, 2643–2647. (b) Zhang, Z.; Yang, Z.; Wu, Z.; Guan, G.; Pan, S.; Zhang, Y.; Li, H.; Deng, J.; Sun, B.; Peng, H. *Adv. Energy Mater.* **2014**, *4*, 1301750. (c) Qiu, L.; Deng, J.; Lu, X.; Yang, Z.; Peng, H. *Angew. Chem., Int. Ed.* **2014**, *53*, 10425–10428.
- (287) (a) Sun, H.; You, X.; Jiang, Y.; Guan, G.; Fang, X.; Deng, J.; Chen, P.; Luo, Y.; Peng, H. *Angew. Chem., Int. Ed.* **2014**, *53*, 9526–9531. (b) Pan, S.; Yang, Z.; Chen, P.; Deng, J.; Li, H.; Peng, H. *Angew. Chem., Int. Ed.* **2014**, *53*, 6110–6114. (c) Zhang, Z.; Li, X.; Guan, G.; Pan, S.; Zhu, Z.; Ren, D.; Peng, H. *Angew. Chem., Int. Ed.* **2014**, *126*, 11755–11758.
- (288) Landi, B. J.; Ganter, M. J.; Cress, C. D.; DiLeo, R. A.; Raffaelle, R. P. *Energy Environ. Sci.* **2009**, *2*, 638–654.
- (289) Aragane, J.; Matsui, K.; Andoh, H.; Suzuki, S.; Fukuda, H.; Ikeya, H.; Kitaba, K.; Ishikawa, R. *J. Power Sources* **1997**, *68*, 13–18.
- (290) Aurbach, D.; Markovsky, B.; Shechter, A.; EinEli, Y.; Cohen, H. *J. Electrochem. Soc.* **1996**, *143*, 3809–3820.
- (291) Aurbach, D.; Eineli, Y.; Chusid, O.; Carmeli, Y.; Babai, M.; Yamin, H. *J. Electrochem. Soc.* **1994**, *141*, 603–611.
- (292) Armstrong, G.; Armstrong, A. R.; Canales, J.; Bruce, P. G. *Chem. Commun.* **2005**, 2454–2456.
- (293) Bavykin, D. V.; Friedrich, J. M.; Walsh, F. C. *Adv. Mater.* **2006**, *18*, 2807–2824.
- (294) Li, X. L.; Kang, F. Y.; Bai, X. D.; Shen, W. *Electrochem. Commun.* **2007**, *9*, 663–666.
- (295) Liu, Y.; Yukawa, H.; Morinaga, M. *Comput. Mater. Sci.* **2004**, *30*, 50–56.
- (296) Kumar, T. P.; Stephan, A. M.; Thayananth, P.; Subramanian, V.; Gopukumar, S.; Renganathan, N. G.; Raghavan, M.; Muniyandi, N. *J. Power Sources* **2001**, *97*, 118–121.
- (297) Maurin, G.; Bousquet, C.; Henn, F.; Bernier, P.; Almairac, R.; Simon, B. *Chem. Phys. Lett.* **1999**, *312*, 14–18.
- (298) Guo, Z. P.; Zhao, Z. W.; Liu, H. K.; Dou, S. X. *Carbon* **2005**, *43*, 1392–1399.
- (299) Skakalova, V.; Kaiser, A. B.; Osvath, Z.; Vertes, G.; Biro, L. P.; Roth, S. *Appl. Phys. A-Mater. Sci. Process.* **2008**, *90*, 597–602.
- (300) Li, X. F.; Yang, J. L.; Hu, Y. H.; Wang, J. J.; Li, Y. L.; Cai, M.; Li, R. Y.; Sun, X. L. *J. Mater. Chem.* **2012**, *22*, 18847–18853.
- (301) Senami, M.; Ikeda, Y.; Fukushima, A.; Tachibana, A. *AIP Adv.* **2011**, *1*, 042106.
- (302) Wang, X. X.; Wang, J. N.; Chang, H.; Zhang, Y. F. *Adv. Funct. Mater.* **2007**, *17*, 3613–3618.
- (303) Li, L.; Yang, Z. B.; Gao, H. J.; Zhang, H.; Ren, J.; Sun, X. M.; Chen, T.; Kia, H. C.; Peng, H. S. *Adv. Mater.* **2011**, *23*, 3730–3735.
- (304) Ren, Z. F.; Huang, Z. P.; Xu, J. W.; Wang, J. H.; Bush, P.; Siegal, M. P.; Provencio, P. N. *Science* **1998**, *282*, 1105–1107.
- (305) Kaiser, A. B.; Skakalova, V.; Roth, S. *Physica E* **2008**, *40*, 2311–2318.
- (306) Udomvech, A.; Kerdcharoen, T.; Osotchan, T. *Chem. Phys. Lett.* **2005**, *406*, 161–166.
- (307) Sheem, K.; Lee, Y. H.; Lim, H. S. *J. Power Sources* **2006**, *158*, 1425–1430.
- (308) Shin, H. C.; Liu, M. L.; Sadanandan, B.; Rao, A. M. *J. Power Sources* **2002**, *112*, 216–221.
- (309) Sotowa, C.; Origgi, G.; Takeuchi, M.; Nishimura, Y.; Takeuchi, K.; Jang, I. Y.; Kim, Y. J.; Hayashi, T.; Kim, Y. A.; Endo, M.; Dresselhaus, M. S. *ChemSusChem* **2008**, *1*, 911–915.
- (310) Yun, Y. S.; Park, H. H.; Jin, H. J. *Materials* **2012**, *5*, 1258–1266.
- (311) Li, X. L.; Kang, F. Y.; Shen, W. C. *Carbon* **2006**, *44*, 1334–1336.
- (312) Liu, Z. L.; Lee, J. Y.; Lindner, H. J. *J. Power Sources* **2001**, *97*–8, 361–365.
- (313) Kato, F.; Koshina, H. Lithium-ion rechargeable battery. US2004248010, 2004.
- (314) Toprakci, O.; Toprakci, H. A. K.; Ji, L. W.; Xu, G. J.; Lin, Z.; Zhang, X. W. *ACS Appl. Mater. Interfaces* **2012**, *4*, 1273–1280.
- (315) Zhou, Y. K.; Wang, J.; Hu, Y. Y.; O’Hayre, R.; Shao, Z. P. *Chem. Commun.* **2010**, *46*, 7151–7153.
- (316) Reddy, A. L. M.; Shajumon, M. M.; Gowda, S. R.; Ajayan, P. M. *Nano Lett.* **2009**, *9*, 1002–1006.
- (317) Cao, F. F.; Guo, Y. G.; Zheng, S. F.; Wu, X. L.; Jiang, L. Y.; Bi, R. R.; Wan, L. J.; Maier, J. *Chem. Mater.* **2010**, *22*, 1908–1914.
- (318) Wang, Z. Y.; Chen, G.; Xia, D. G. *J. Power Sources* **2008**, *184*, 432–436.
- (319) Shu, J.; Li, H.; Yang, R. Z.; Shi, Y.; Huang, X. *J. Electrochem. Commun.* **2006**, *8*, 51–54.
- (320) Lin, H.; Weng, W.; Ren, J.; Qiu, L.; Zhang, Z.; Chen, P.; Chen, X.; Deng, J.; Wang, Y.; Peng, H. *Adv. Mater.* **2014**, *26*, 1217–1222.
- (321) Weng, W.; Sun, Q.; Zhang, Y.; Lin, H.; Ren, J.; Lu, X.; Wang, M.; Peng, H. *Nano Lett.* **2014**, *14*, 3432–3438.
- (322) Weng, W.; Lin, H.; Chen, X.; Ren, J.; Zhang, Z.; Qiu, L.; Guan, G.; Peng, H. *J. Mater. Chem. A* **2014**, *2*, 9306–9312.
- (323) Han, S.; Wu, D.; Li, S.; Zhang, F.; Feng, X. *Small* **2013**, *9*, 1173–1187.
- (324) Xu, C.; Xu, B.; Gu, Y.; Xiong, Z.; Sun, J.; Zhao, X. S. *Energy Environ. Sci.* **2013**, *6*, 1388–1414.
- (325) Sun, Y.; Wu, Q.; Shi, G. *Energy Environ. Sci.* **2011**, *4*, 1113–1132.
- (326) Lung-Hao, H. B.; Wu, F.-Y.; Lin, C.-T.; Khlobystov, A. N.; Li, L.-J. *Nat. Commun.* **2013**, *4*, 1687.
- (327) Dahn, J. R.; Zheng, T.; Liu, Y.; Xue, J. S. *Science* **1995**, *270*, 590–593.
- (328) Gerouki, A.; Goldner, M. A.; Goldner, R. B.; Haas, T. E.; Liu, T. Y.; Slaven, S. *J. Electrochem. Soc.* **1996**, *143*, L262–L263.
- (329) Yoo, E.; Kim, J.; Hosono, E.; Zhou, H.-s.; Kudo, T.; Honma, I. *Nano Lett.* **2008**, *8*, 2277–2282.
- (330) Chen, S.; Bao, P.; Xiao, L.; Wang, G. *Carbon* **2013**, *64*, 158–169.
- (331) Wang, G.; Shen, X.; Yao, J.; Park, J. *Carbon* **2009**, *47*, 2049–2053.
- (332) Reddy, A. L. M.; Srivastava, A.; Gowda, S. R.; Gullapalli, H.; Dubey, M.; Ajayan, P. M. *ACS Nano* **2010**, *4*, 6337–6342.
- (333) Wu, Z.-S.; Ren, W.; Xu, L.; Li, F.; Cheng, H.-M. *ACS Nano* **2011**, *5*, 5463–5471.
- (334) Yu, Y. X. *Phys. Chem. Chem. Phys.* **2013**, *15*, 16819–16827.
- (335) Chen, S.; Chen, P.; Wang, Y. *Nanoscale* **2011**, *3*, 4323–4329.
- (336) Chen, T.; Qiu, L.; Yang, Z.; Cai, Z.; Ren, J.; Li, H.; Lin, H.; Sun, X.; Peng, H. *Angew. Chem., Int. Ed.* **2012**, *51*, 11977–11980.
- (337) Hu, Y.; Li, X.; Wang, J.; Li, R.; Sun, X. *J. Power Sources* **2013**, *237*, 41–46.
- (338) Wang, X. L.; Han, W. Q. *ACS Appl. Mater. Interfaces* **2010**, *2*, 3709–3713.
- (339) Lee, J. K.; Smith, K. B.; Hayner, C. M.; Kung, H. H. *Chem. Commun.* **2010**, *46*, 2025–2027.
- (340) Zhao, X.; Hayner, C. M.; Kung, M. C.; Kung, H. H. *Adv. Energy. Mater.* **2011**, *1*, 1079–1084.

- (341) Xiang, H.; Zhang, K.; Ji, G.; Lee, J. Y.; Zou, C.; Chen, X.; Wu, J. *Carbon* **2011**, *49*, 1787–1796.
- (342) Zhou, X.; Yin, Y.-X.; Wan, L.-J.; Guo, Y.-G. *Adv. Energy. Mater.* **2012**, *2*, 1086–1090.
- (343) Evanoff, K.; Magasinski, A.; Yang, J.; Yushin, G. *Adv. Energy. Mater.* **2011**, *1*, 495–498.
- (344) Wang, J.-Z.; Zhong, C.; Chou, S.-L.; Liu, H.-K. *Electrochim. Commun.* **2010**, *12*, 1467–1470.
- (345) Zhou, X.; Cao, A.-M.; Wan, L.-J.; Guo, Y.-G. *Nano Research* **2012**, *5*, 845–853.
- (346) Lee, S. E.; Kim, H. J.; Kim, H.; Park, J. H.; Choi, D. G. *Nanoscale* **2013**, *5*, 8986–8991.
- (347) Wang, B.; Li, X.; Luo, B.; Jia, Y.; Zhi, L. *Nanoscale* **2013**, *5*, 1470–1474.
- (348) Paek, S.-M.; Yoo, E.; Honma, I. *Nano Lett.* **2008**, *9*, 72–75.
- (349) Yao, J.; Shen, X.; Wang, B.; Liu, H.; Wang, G. *Electrochim. Commun.* **2009**, *11*, 1849–1852.
- (350) Zhang, M.; Lei, D.; Du, Z.; Yin, X.; Chen, L.; Li, Q.; Wang, Y.; Wang, T. *J. Mater. Chem.* **2011**, *21*, 1673–1676.
- (351) Lian, P.; Zhu, X.; Liang, S.; Li, Z.; Yang, W.; Wang, H. *Electrochim. Acta* **2011**, *S6*, 4532–4539.
- (352) Wu, Z.-S.; Zhou, G.; Yin, L.-C.; Ren, W.; Li, F.; Cheng, H.-M. *Nano Energy* **2012**, *1*, 107–131.
- (353) Wang, L.; Wang, D.; Dong, Z.; Zhang, F.; Jin, J. *Nano Lett.* **2013**, *13*, 1711–1716.
- (354) Zhou, X.; Wan, L. J.; Guo, Y. G. *Adv. Mater.* **2013**, *25*, 2152–2157.
- (355) Prabakar, S. J.; Hwang, Y. H.; Bae, E. G.; Shim, S.; Kim, D.; Lah, M. S.; Sohn, K. S.; Pyo, M. *Adv. Mater.* **2013**, *25*, 3307–3312.
- (356) Wu, Z.-S.; Ren, W.; Wen, L.; Gao, L.; Zhao, J.; Chen, Z.; Zhou, G.; Li, F.; Cheng, H.-M. *ACS Nano* **2010**, *4*, 3187–3194.
- (357) Yang, S.; Feng, X.; Ivanovici, S.; Mullen, K. *Angew. Chem., Int. Ed. Engl.* **2010**, *49*, 8408–8411.
- (358) Chen, S. Q.; Wang, Y. *J. Mater. Chem.* **2010**, *20*, 9735–9739.
- (359) Xiao, X.; Liu, X.; Zhao, H.; Chen, D.; Liu, F.; Xiang, J.; Hu, Z.; Li, Y. *Adv. Mater.* **2012**, *24*, 5762–5766.
- (360) Zhao, C.; Chou, S.-L.; Wang, Y.; Zhou, C.; Liu, H.-K.; Dou, S.-X. *RSC Adv.* **2013**, *3*, 16597–16603.
- (361) Yue, W.; Lin, Z.; Jiang, S.; Yang, X. *J. Mater. Chem.* **2012**, *22*, 16318–16323.
- (362) Wang, R.; Xu, C.; Sun, J.; Liu, Y.; Gao, L.; Lin, C. *Nanoscale* **2013**, *5*, 6960–6967.
- (363) Zhu, J.; Bai, L.; Sun, Y.; Zhang, X.; Li, Q.; Cao, B.; Yan, W.; Xie, Y. *Nanoscale* **2013**, *5*, 5241–5246.
- (364) Zhou, G.; Wang, D.-W.; Li, F.; Zhang, L.; Li, N.; Wu, Z.-S.; Wen, L.; Lu, G. Q.; Cheng, H.-M. *Chem. Mater.* **2010**, *22*, 5306–5313.
- (365) Chen, W.; Li, S.; Chen, C.; Yan, L. *Adv. Mater.* **2011**, *23*, 5679–5683.
- (366) Behera, S. K. *Chem. Commun.* **2011**, *47*, 10371–10373.
- (367) Su, Y.; Li, S.; Wu, D.; Zhang, F.; Liang, H.; Gao, P.; Cheng, C.; Feng, X. *ACS Nano* **2012**, *6*, 8349–8356.
- (368) Li, B.; Cao, H. S.; Jin, Q. *M. Chem. Commun.* **2011**, *47*, 10374–10376.
- (369) Zhu, X.; Zhu, Y.; Murali, S.; Stoller, M. D.; Ruoff, R. S. *ACS Nano* **2011**, *5*, 3333–3338.
- (370) Wang, G.; Wang, H.; Cai, S.; Bai, J.; Ren, Z.; Bai, J. *J. Power Sources* **2013**, *239*, 37–44.
- (371) Zhang, K.; Han, P.; Gu, L.; Zhang, L.; Liu, Z.; Kong, Q.; Zhang, C.; Dong, S.; Zhang, Z.; Yao, J.; Xu, H.; Cui, G.; Chen, L. *ACS Appl. Mater. Interfaces* **2012**, *4*, 658–664.
- (372) Wang, H.; Cui, L.-F.; Yang, Y.; Sanchez Casalongue, H.; Robinson, J. T.; Liang, Y.; Cui, Y.; Dai, H. *J. Am. Chem. Soc.* **2010**, *132*, 13978–13980.
- (373) Nam, I.; Kim, N. D.; Kim, G.-P.; Park, J.; Yi, J. *J. Power Sources* **2013**, *244*, 56–62.
- (374) Zou, Y.; Wang, Y. *Nanoscale* **2011**, *3*, 2615–2620.
- (375) Sun, Y.; Hu, X.; Luo, W.; Huang, Y. *ACS Nano* **2011**, *5*, 7100–7107.
- (376) Wang, B.; Wu, X.-L.; Shu, C.-Y.; Guo, Y.-G.; Wang, C.-R. *J. Mater. Chem.* **2010**, *20*, 10661–10664.
- (377) Ding, S.; Chen, J. S.; Luan, D.; Boey, F. Y. C.; Madhavi, S.; Lou, X. W. *Chem. Commun.* **2011**, *47*, 5780–5782.
- (378) Kim, H.; Lim, H.-D.; Kim, S.-W.; Hong, J.; Seo, D.-H.; Kim, D.-C.; Jeon, S.; Park, S.; Kang, K. *Sci. Rep.* **2013**, *3*, 1506.
- (379) Kucinskas, G.; Bajars, G.; Kleperis, J. *J. Power Sources* **2013**, *240*, 66–79.
- (380) Choi, N. S.; Chen, Z.; Freunberger, S. A.; Ji, X.; Sun, Y. K.; Amine, K.; Yushin, G.; Nazar, L. F.; Cho, J.; Bruce, P. G. *Angew. Chem., Int. Ed.* **2012**, *51*, 9994–10024.
- (381) Kucinskas, G.; Bajars, G.; Kleperis, J. *J. Power Sources* **2013**, *240*, 66–79.
- (382) Su, F.-Y.; You, C.; He, Y.-B.; Lv, W.; Cui, W.; Jin, F.; Li, B.; Yang, Q.-H.; Kang, F. *J. Mater. Chem.* **2010**, *20*, 9644–9650.
- (383) Zhou, X.; Wang, F.; Zhu, Y.; Liu, Z. *J. Mater. Chem.* **2011**, *21*, 3353–3358.
- (384) Kim, J.-K.; Choi, J.-W.; Chauhan, G. S.; Ahn, J.-H.; Hwang, G.-C.; Choi, J.-B.; Ahn, H.-J. *Electrochim. Acta* **2008**, *53*, 8258–8264.
- (385) Wang, L.; Wang, H.; Liu, Z.; Xiao, C.; Dong, S.; Han, P.; Zhang, Z.; Zhang, X.; Bi, C.; Cui, G. *Solid State Ionics* **2010**, *181*, 1685–1689.
- (386) Wang, R.; Xu, C.; Sun, J.; Gao, L.; Jin, J.; Lin, C. *Mater. Lett.* **2013**, *112*, 207–210.
- (387) Li, J.; Zhang, L.; Zhang, L.; Hao, W.; Wang, H.; Qu, Q.; Zheng, H. *J. Power Sources* **2014**, *249*, 311–319.
- (388) Li, N.; Chen, Z.; Ren, W.; Li, F.; Cheng, H.-M. *Proc. Natl. Acad. Sci. U.S.A.* **2012**, *109*, 17360–17365.
- (389) Zhang, K.; Hu, Z.; Chen, J. *J. Energy Chem.* **2013**, *22*, 214–225.
- (390) Nazar, L. F.; Goward, G.; Leroux, F.; Duncan, M.; Huang, H.; Kerr, T.; Gaubicher, J. *Int. J. Inorg. Mater.* **2001**, *3*, 191–220.
- (391) Kim, M. S.; Bhattacharjya, D.; Fang, B. Z.; Yang, D. S.; Bae, T. S.; Yu, J. S. *Langmuir* **2013**, *29*, 6754–6761.
- (392) Su, F.; Zhao, X. S.; Wang, Y.; Lee, J. Y. *Microporous Mesoporous Mater.* **2007**, *98*, 323–329.
- (393) Jung, H.; Shin, J.; Chae, C.; Lee, J. K.; Kim, J. *J. Phys. Chem. C* **2013**, *117*, 14939–14946.
- (394) Han, F.; Li, D.; Li, W. C.; Lei, C.; Sun, Q.; Lu, A. H. *Adv. Funct. Mater.* **2013**, *23*, 1692–1700.
- (395) Han, F.; Li, W.-C.; Li, D.; Lu, A.-H. *J. Energy Chem.* **2013**, *22*, 329–335.
- (396) Li, Z.; Wang, X.; Wang, C.; Yin, L. *RSC Adv.* **2013**, *3*, 17097–17104.
- (397) Han, F.; Li, W.-C.; Li, M.-R.; Lu, A.-H. *J. Mater. Chem.* **2012**, *22*, 9645–9651.
- (398) Wang, X.; Li, Z.; Yin, L. *CrystEngComm* **2013**, *15*, 7589–7597.
- (399) Lin, C.; Hu, Y.; Jiang, F.; Chen, G. *Mater. Lett.* **2013**, *94*, 83–85.
- (400) Cheng, M.-Y.; Hwang, B.-J. *J. Power Sources* **2010**, *195*, 4977–4973.
- (401) Zhang, H.; Tao, H.; Jiang, Y.; Jiao, Z.; Wu, M.; Zhao, B. *J. Power Sources* **2010**, *195*, 2950–2959.
- (402) Yang, M.; Gao, Q. *Microporous Mesoporous Mater.* **2011**, *143*, 230–235.
- (403) Zeng, L.; Zheng, C.; Xi, J.; Fei, H.; Wei, M. *Carbon* **2013**, *62*, 382–388.
- (404) Shen, L.; Uchaker, E.; Yuan, C.; Nie, P.; Zhang, M.; Zhang, X.; Cao, G. *ACS Appl. Mater. Interfaces* **2012**, *4*, 2985–2992.
- (405) Zeng, L.; Zheng, C.; Deng, C.; Ding, X.; Wei, M. *ACS Appl. Mater. Interfaces* **2013**, *5*, 2182–2187.
- (406) Han, F.; Li, W. C.; Li, D.; Lu, A. H. *J. Energy Chem.* **2013**, *22*, 329–335.
- (407) Xiao, L. F.; Cao, Y. L.; Xiao, J.; Schwenzer, B.; Engelhard, M. H.; Saraf, L. V.; Nie, Z. M.; Exarhos, G. J.; Liu, J. *Adv. Mater.* **2012**, *24*, 1176–1181.
- (408) Sun, X. M.; Liu, J. F.; Li, Y. D. *Chem. Mater.* **2006**, *18*, 3486–3494.
- (409) Wang, J. Z.; Too, C. O.; Wallace, G. G. *J. Power Sources* **2005**, *150*, 223–228.

- (410) Kwon, Y. H.; Woo, S. W.; Jung, H. R.; Yu, H. K.; Kim, K.; Oh, B. H.; Ahn, S.; Lee, S. Y.; Song, S. W.; Cho, J.; Shin, H. C.; Kim, J. Y. *Adv. Mater.* **2012**, *24*, 5192–5197.
- (411) Ren, J.; Li, L.; Chen, C.; Chen, X. L.; Cai, Z. B.; Qiu, L. B.; Wang, Y. G.; Zhu, X. R.; Peng, H. S. *Adv. Mater.* **2013**, *25*, 1155–1159.
- (412) Ren, J.; Zhang, Y.; Bai, W.; Chen, X.; Zhang, Z.; Fang, X.; Weng, W.; Wang, Y.; Peng, H. *Angew. Chem., Int. Ed.* **2014**, *53*, 7864–7869.
- (413) Zhang, Y.; Bai, W.; Ren, J.; Weng, W.; Lin, H.; Zhang, Z.; Peng, H. *J. Mater. Chem. A* **2014**, *2*, 11054–11059.
- (414) Su, Y.; Fu, Y.; Manthiram, A. *Phys. Chem. Chem. Phys.* **2012**, *14*, 14495–14499.
- (415) Kim, S. W.; Seo, D. H.; Ma, X.; Ceder, G.; Kang, K. *Adv. Energy Mater.* **2012**, *2*, 710–721.
- (416) Zhang, S.; Shao, Y. Y.; Yin, G. P.; Lin, Y. H. *J. Mater. Chem.* **2010**, *20*, 2826–2830.
- (417) Yuan, Y.; Smith, J. A.; Goenaga, G.; Liu, D. J.; Luo, Z. P.; Liu, J. *B. J. Power Sources* **2011**, *196*, 6160–6167.
- (418) Xie, X.; Pasta, M.; Hu, L. B.; Yang, Y.; McDonough, J.; Cha, J.; Criddle, C. S.; Cui, Y. *Energy Environ. Sci.* **2011**, *4*, 1293–1297.
- (419) Liu, R. J.; Li, S. W.; Xu, X. L.; Zhang, G. J.; Ma, Y.; Yao, J. N. *J. Mater. Chem.* **2011**, *21*, 14917–14924.
- (420) Wei, L.; Li, C. Q.; Chuand, H. B.; Li, Y. *Dalton Trans.* **2011**, *40*, 2332.
- (421) Zhang, Y. P.; Hu, Y. Y.; Li, S. Z.; Sun, J.; Hou, B. *J. Power Sources* **2011**, *196*, 9284–9289.
- (422) Fujigaya, T.; Uchinoumi, T.; Kaneko, K.; Nakashima, N. *Chem. Commun.* **2011**, *47*, 6843–6845.
- (423) Feng, L. Y.; Yan, Y. Y.; Chen, Y. G.; Wang, L. *J. Energy Environ. Sci.* **2011**, *4*, 1892–1899.
- (424) Kötz, R.; Carlen, M. *Electrochim. Acta* **2000**, *45*, 2483–2498.
- (425) Gamby, J.; Taberna, P. L.; Simon, P.; Fauvarque, J. F.; Chesneau, M. *J. Power Sources* **2001**, *101*, 109–116.
- (426) Jurewicz, K.; Pietrzak, R.; Nowicki, P.; Wachowsk, H. *Electrochim. Acta* **2008**, *53*, 5469–5475.
- (427) Fuertes, A. B.; Lota, G.; Centeno, T. A.; Frackowiak, E. *Electrochim. Acta* **2005**, *50*, 2799–2805.
- (428) Liu, H. J.; Wang, X. M.; Cui, W. J.; Dou, Y. Q.; Zhao, D. Y.; Xia, Y. Y. *J. Mater. Chem.* **2010**, *20*, 4223–4230.
- (429) Kaempgen, M.; Chan, C. K.; Ma, J.; Cui, Y.; Gruner, G. *Nano Lett.* **2009**, *9*, 1872–1876.
- (430) Yu, D. S.; Dai, L. M. *J. Phys. Chem. Lett.* **2010**, *1*, 467–470.
- (431) Frackowiak, E.; Metenier, K.; Bertagna, V.; Beguin, F. *Appl. Phys. Lett.* **2000**, *77*, 2421–2423.
- (432) Zhu, Y. W.; Murali, S.; Stoller, M. D.; Ganesh, K. J.; Cai, W. W.; Ferreira, P. J.; Pirkle, A.; Wallace, R. M.; Cychosz, K. A.; Thommes, M.; Su, D.; Stach, E. A.; Ruoff, R. S. *Science* **2011**, *332*, 1537–1541.
- (433) Wang, Y.; Shi, Z. Q.; Huang, Y.; Ma, Y. F.; Wang, C. Y.; Chen, M. M.; Chen, Y. S. *J. Phys. Chem. C* **2009**, *113*, 13103–13107.
- (434) Yan, J.; Fan, Z. J.; Wei, T.; Qian, W. Z.; Zhang, M. L.; Wei, F. *Carbon* **2010**, *48*, 3825–3933.
- (435) Wei, W. F.; Cui, X. W.; Chen, W. X.; Ivey, D. G. *Chem. Soc. Rev.* **2011**, *40*, 1697–1721.
- (436) Nam, K. W.; Kim, K. B. *J. Electrochem. Soc.* **2002**, *149*, A346–A354.
- (437) Miller, J. M.; Dunn, B.; Tran, T. D.; Pekala, R. W. *J. Electrochem. Soc.* **1997**, *144*, L309–L311.
- (438) Lee, H. Y.; Goodenough, J. B. *J. Solid State Chem.* **1999**, *148*, 81–84.
- (439) Gupta, V.; Miura, N. *Mater. Lett.* **2006**, *60*, 1466–1469.
- (440) Snook, G. A.; Kao, P.; Best, A. S. *J. Power Sources* **2011**, *196*, 1–12.
- (441) Patil, B. H.; Jagadale, A. D.; Lokhande, C. D. *Synth. Met.* **2012**, *162*, 1400–1405.
- (442) Sharma, R. K.; Rastogi, A. C.; Desu, S. B. *Electrochim. Commun.* **2008**, *10*, 268–272.
- (443) Wang, Q.; Wen, Z. H.; Li, J. H. *Adv. Funct. Mater.* **2006**, *16*, 2141–2146.
- (444) Du Pasquier, A.; Plitz, I.; Menocal, S.; Amatucci, G. *J. Power Sources* **2003**, *115*, 171–178.
- (445) Zhao, X.; Johnston, C.; Grant, P. S. *J. Mater. Chem.* **2009**, *19*, 8755–8760.
- (446) Pan, H.; Li, J. Y.; Feng, Y. P. *Nanoscale Res. Lett.* **2010**, *5*, 654–668.
- (447) Frackowiak, E.; Machnikowski, J.; Beguin, F. *NATO Sci. Ser. II* **2006**, *229*, 5–20.
- (448) Pandolfo, A. G.; Hollenkamp, A. F. *J. Power Sources* **2006**, *157*, 11–27.
- (449) Hahn, M.; Baertschi, M.; Barbieri, O.; Sauter, J. C.; Kotz, R.; Gallay, R. *Electrochim. Solid State Lett.* **2004**, *7*, A33–A36.
- (450) An, K. h.; Jeon, K. K.; Kim, W. S.; Park, Y. S.; Lim, S. C.; Bae, D. J.; Lee, Y. H. *J. Korean Phys. Soc.* **2001**, *39*, S511–S517.
- (451) Izadi-Najafabadi, A.; Yasuda, S.; Kobashi, K.; Yamada, T.; Futaba, D. N.; Hatori, H.; Yumura, M.; Iijima, S.; Hata, K. *Adv. Mater.* **2010**, *22*, E235–E241.
- (452) Mahon, P. J.; Paul, G. L.; Keshishian, S. M.; Vassallo, A. M. *J. Power Sources* **2000**, *91*, 68–76.
- (453) Jurewicz, K.; Frackowiak, E. Modified carbon materials for electrochemical capacitors. In *Vii National Symposium on Fast Ion Conductors*; Hilczer, B., Polomska, M., Eds.; Polish Academy of Sciences: Poznan, 2000; Vol. 27, pp 38–45.
- (454) Pan, H.; Poh, C. K.; Feng, Y. P.; Lin, J. Y. *Chem. Mater.* **2007**, *19*, 6120–6125.
- (455) Obreja, V. V. N. *Physica E* **2008**, *40*, 2596–2605.
- (456) Wang, G. P.; Liang, R. F.; Liu, L. X.; Zhong, B. H. *Electrochim. Acta* **2014**, *115*, 183–188.
- (457) Bai, X. X.; Hu, X. J.; Zhou, S. Y.; Yan, J.; Sun, C. H.; Chen, P.; Li, L. F. *Electrochim. Acta* **2013**, *87*, 394–400.
- (458) Paul, S.; Choi, K. S.; Lee, D. J.; Sudhagar, P.; Kang, Y. S. *Electrochim. Acta* **2012**, *78*, 649–655.
- (459) Yang, M. M.; Cheng, B.; Song, H. H.; Chen, X. H. *Electrochim. Acta* **2010**, *55*, 7021–7027.
- (460) Zhou, H.; Han, G.; Chang, Y.; Fu, D.; Xiao, Y. *J. Power Sources* **2015**, *274*, 229–236.
- (461) Liu, F.; Wang, S.; Han, G.; Liu, R.; Chang, Y.; Xiao, Y. *J. Appl. Polym. Sci.* **2014**, DOI: 10.1002/APP.41023.
- (462) Dhibar, S.; Das, C. K. *Ind. Eng. Chem. Res.* **2014**, *53*, 3495–3508.
- (463) Chen, X.; Lin, H.; Chen, P.; Guan, G.; Deng, J.; Peng, H. *Adv. Mater.* **2014**, *26*, 4444–4449.
- (464) Jiang, R. R.; Huang, T.; Tang, Y.; Liu, J.; Xue, L. G.; Zhuang, J. H.; Yu, A. H. *Electrochim. Acta* **2009**, *54*, 7173–7179.
- (465) Amade, R.; Jover, E.; Caglar, B.; Mutlu, T.; Bertran, E. *J. Power Sources* **2011**, *196*, 5779–5783.
- (466) Liu, C. G.; Lee, Y. S.; Kim, Y. J.; Song, I. C.; Kim, J. H. *Synth. Met.* **2009**, *159*, 2009–2012.
- (467) Gund, G. S.; Dubal, D. P.; Shinde, S. S.; Lokhande, C. D. *ACS Appl. Mater. Interfaces* **2014**, *6*, 3176–3188.
- (468) Yan, S. C.; Wang, H. T.; Qu, P.; Zhang, Y.; Xiao, Z. D. *Synth. Met.* **2009**, *159*, 158–161.
- (469) Kim, I. H.; Kim, J. H.; Kim, K. B. *Electrochim. Solid State Lett.* **2005**, *8*, A369–A372.
- (470) Gao, F. L.; Zhang, L. J.; Huang, S. M. *Mater. Lett.* **2010**, *64*, 537–540.
- (471) Li, Z. J.; Chang, T. X.; Yun, G. Q.; Jia, Y. *Powder Technol.* **2012**, *224*, 306–310.
- (472) Yuan, C. Z.; Yang, L.; Hou, L. R.; Li, J. Y.; Sun, Y. X.; Zhang, X. G.; Shen, L. F.; Lu, X. J.; Xiong, S. L.; Lou, X. W. *Adv. Funct. Mater.* **2012**, *22*, 2560–2566.
- (473) Fang, W. C. *J. Phys. Chem. C* **2008**, *112*, 11552–11555.
- (474) Huang, M.; Mi, R.; Liu, H.; Li, F.; Zhao, X.; Zhang, W.; He, S.; Zhang, Y. *J. Power Sources* **2014**, *269*, 760–767.
- (475) Reddy, A. L. M.; Ramaprabhu, S. *J. Phys. Chem. C* **2007**, *111*, 7727–7734.
- (476) Hou, Y.; Cheng, Y. W.; Hobson, T.; Liu, J. *Nano Lett.* **2010**, *10*, 2727–2733.

- (477) Zhang, L.; Xiong, Z.; Zhao, X. S. *J. Power Sources* **2013**, *222*, 326–332.
- (478) Huang, Y.; Liang, J.; Chen, Y. *Small* **2012**, *8*, 1805–1834.
- (479) Huang, X.; Zeng, Z.; Fan, Z.; Liu, J.; Zhang, H. *Adv. Mater.* **2012**, *24*, 5979–6004.
- (480) Jiang, H.; Lee, P. S.; Li, C. *Energy Environ. Sci.* **2013**, *6*, 41–53.
- (481) Chen, Y.; Zhang, X.; Zhang, D.; Yu, P.; Ma, Y. *Carbon* **2011**, *49*, 573–580.
- (482) Zhang, L.; Shi, G. *J. Phys. Chem. C* **2011**, *115*, 17206–17212.
- (483) Jin, Y.; Huang, S.; Zhang, M.; Jia, M.; Hu, D. *Appl. Surf. Sci.* **2013**, *268*, 541–546.
- (484) Stankovich, S.; Dikin, D. A.; Piner, R. D.; Kohlhaas, K. A.; Kleinhammes, A.; Jia, Y.; Wu, Y.; Nguyen, S. T.; Ruoff, R. S. *Carbon* **2007**, *45*, 1558–1565.
- (485) Si, Y.; Samulski, E. T. *Chem. Mater.* **2008**, *20*, 6792–6797.
- (486) Schniepp, H. C.; Li, J.-L.; McAllister, M. J.; Sai, H.; Herrero-Alonso, M.; Adamson, D. H.; Prud'homme, R. K.; Car, R.; Saville, D. A.; Aksay, I. A. *J. Phys. Chem. C* **2006**, *110*, 8535–8539.
- (487) Wang, P.; Zakeeruddin, S. M.; Comte, P.; Exnar, I.; Grätzel, M. *J. Am. Chem. Soc.* **2003**, *125*, 1166–1167.
- (488) Wu, Z.-S.; Ren, W.; Gao, L.; Liu, B.; Jiang, C.; Cheng, H.-M. *Carbon* **2009**, *47*, 493–499.
- (489) Vivekchand, S. R. C.; Rout, C.; Subrahmanyam, K. S.; Govindaraj, A.; Rao, C. N. R. *J. Chem. Sci.* **2008**, *120*, 9–13.
- (490) Du, X.; Guo, P.; Song, H.; Chen, X. *Electrochim. Acta* **2010**, *55*, 4812–4819.
- (491) Lv, W.; Tang, D.-M.; He, Y.-B.; You, C.-H.; Shi, Z.-Q.; Chen, X.-C.; Chen, C.-M.; Hou, P.-X.; Liu, C.; Yang, Q.-H. *ACS Nano* **2009**, *3*, 3730–3736.
- (492) Zhu, Y.; Murali, S.; Stoller, M. D.; Velamakanni, A.; Piner, R. D.; Ruoff, R. S. *Carbon* **2010**, *48*, 2118–2122.
- (493) Tryba, B.; Morawski, A. W.; Inagaki, M. *Carbon* **2005**, *43*, 2417–2419.
- (494) Falcao, E. H. L.; Blair, R. G.; Mack, J. J.; Viculis, L. M.; Kwon, C.-W.; Bendikov, M.; Kaner, R. B.; Dunn, B. S.; Wudl, F. *Carbon* **2007**, *45*, 1367–1369.
- (495) Du, Q.; Zheng, M.; Zhang, L.; Wang, Y.; Chen, J.; Xue, L.; Dai, W.; Ji, G.; Cao, J. *Electrochim. Acta* **2010**, *55*, 3897–3903.
- (496) Zhu, Y.; Stoller, M. D.; Cai, W.; Velamakanni, A.; Piner, R. D.; Chen, D.; Ruoff, R. S. *ACS Nano* **2010**, *4*, 1227–1233.
- (497) Lin, Z.; Liu, Y.; Yao, Y.; Hildreth, O. J.; Li, Z.; Moon, K.; Wong, C.-p. *J. Phys. Chem. C* **2011**, *115*, 7120–7125.
- (498) Murugan, A. V.; Muraliganth, T.; Manthiram, A. *Chem. Mater.* **2009**, *21*, 5004–5006.
- (499) Burke, A. *Electrochim. Acta* **2007**, *53*, 1083–1091.
- (500) Zhang, X.; Zhang, H.; Li, C.; Wang, K.; Sun, X.; Ma, Y. *RSC Adv.* **2014**, *4*, 45862–45884.
- (501) Xu, Y.; Sheng, K.; Li, C.; Shi, G. *ACS Nano* **2010**, *4*, 4324–4330.
- (502) Wu, Q.; Sun, Y.; Bai, H.; Shi, G. *Phys. Chem. Chem. Phys.* **2011**, *13*, 11193–11198.
- (503) Chen, J.; Sheng, K.; Luo, P.; Li, C.; Shi, G. *Adv. Mater.* **2012**, *24*, 4569–4573.
- (504) Ye, S.; Feng, J.; Wu, P. *ACS Appl. Mater. Interfaces* **2013**, *5*, 7122–7129.
- (505) Xu, Y.; Lin, Z.; Huang, X.; Liu, Y.; Huang, Y.; Duan, X. *ACS Nano* **2013**, *7*, 4042–4049.
- (506) Barranco, V.; Lillo-Rodenas, M. A.; Linares-Solano, A.; Oya, A.; Pico, F.; Ibañez, J.; Agullo-Rueda, F.; Amarilla, J. M.; Rojo, J. M. *J. Phys. Chem. C* **2010**, *114*, 10302–10307.
- (507) Liu, T.; Sreekumar, T. V.; Kumar, S.; Hauge, R. H.; Smalley, R. E. *Carbon* **2003**, *41*, 2440–2442.
- (508) Raymundo-Piñero, E.; Azaïs, P.; Cacciaguerra, T.; Cazorla-Amorós, D.; Linares-Solano, A.; Béguin, F. *Carbon* **2005**, *43*, 786–795.
- (509) Hantel, M. M.; Kaspar, T.; Nesper, R.; Wokaun, A.; Kötz, R. *Electrochim. Commun.* **2011**, *13*, 90–92.
- (510) Li, Y.; van Zijll, M.; Chiang, S.; Pan, N. *J. Power Sources* **2011**, *196*, 6003–6006.
- (511) Zhang, L. L.; Zhao, X.; Stoller, M. D.; Zhu, Y.; Ji, H.; Murali, S.; Wu, Y.; Perales, S.; Clevenger, B.; Ruoff, R. S. *Nano Lett.* **2012**, *12*, 1806–1812.
- (512) Kim, T.; Jung, G.; Yoo, S.; Suh, K. S.; Ruoff, R. S. *ACS Nano* **2013**, *7*, 6899–6905.
- (513) An, X.; Simmons, T.; Shah, R.; Wolfe, C.; Lewis, K. M.; Washington, M.; Nayak, S. K.; Talapatra, S.; Kar, S. *Nano Lett.* **2010**, *10*, 4295–4295.
- (514) Zhang, K.; Mao, L.; Zhang, L. L.; On Chan, H. S.; Zhao, X. S.; Wu, J. *J. Mater. Chem.* **2011**, *21*, 7302–7307.
- (515) Yan, J.; Wei, T.; Shao, B.; Ma, F.; Fan, Z.; Zhang, M.; Zheng, C.; Shang, Y.; Qian, W.; Wei, F. *Carbon* **2010**, *48*, 1731–1737.
- (516) Qin, Z.; Li, Z. J.; Zhang, M.; Yang, B. C.; Outlaw, R. A. *J. Power Sources* **2012**, *217*, 303–308.
- (517) Li, D.; Muller, M. B.; Gilje, S.; Kaner, R. B.; Wallace, G. G. *Nat. Nanotechnol.* **2008**, *3*, 101–105.
- (518) Yang, X.; Zhu, J.; Qiu, L.; Li, D. *Adv. Mater.* **2011**, *23*, 2833–2838.
- (519) Lei, Z.; Christov, N.; Zhao, X. S. *Energy Environ. Sci.* **2011**, *4*, 1866–1873.
- (520) Jeong, H. M.; Lee, J. W.; Shin, W. H.; Choi, Y. J.; Shin, H. J.; Kang, J. K.; Choi, J. W. *Nano Lett.* **2011**, *11*, 2472–2477.
- (521) Guo, H.-L.; Su, P.; Kang, X.; Ning, S.-K. *J. Mater. Chem. A* **2013**, *1*, 2255.
- (522) Han, J.; Zhang, L. L.; Lee, S.; Oh, J.; Lee, K.-S.; Potts, J. R.; Ji, J.; Zhao, X.; Ruoff, R. S.; Park, S. *ACS Nano* **2013**, *7*, 19–26.
- (523) Wang, C.; Zhou, Y.; Sun, L.; Zhao, Q.; Zhang, X.; Wan, P.; Qiu, J. *J. Phys. Chem. C* **2013**, *117*, 14912–14919.
- (524) Qiu, L.; Yang, X.; Gou, X.; Yang, W.; Ma, Z. F.; Wallace, G. G.; Li, D. *Chem.—Eur. J.* **2010**, *16*, 10653–10658.
- (525) Yang, Z.; Liu, M.; Zhang, C.; Tjiu, W. W.; Liu, T.; Peng, H. *Angew. Chem., Int. Ed. Engl.* **2013**, *52*, 3996–3999.
- (526) Lu, X.; Dou, H.; Gao, B.; Yuan, C.; Yang, S.; Hao, L.; Shen, L.; Zhang, X. *Electrochim. Acta* **2011**, *56*, 5115–5121.
- (527) Wang, Y.; Wu, Y.; Huang, Y.; Zhang, F.; Yang, X.; Ma, Y.; Chen, Y. *J. Phys. Chem. C* **2011**, *115*, 23192–23197.
- (528) Ning, G.; Fan, Z.; Wang, G.; Gao, J.; Qian, W.; Wei, F. *Chem. Commun.* **2011**, *47*, 5976–5978.
- (529) Le, L. T.; Ervin, M. H.; Qiu, H.; Fuchs, B. E.; Lee, W. Y. *Electrochim. Commun.* **2011**, *13*, 355–358.
- (530) Yu, A.; Roes, I.; Davies, A.; Chen, Z. *Appl. Phys. Lett.* **2010**, *96*, 253105.
- (531) Simon, P.; Gogotsi, Y. *Acc. Chem. Res.* **2013**, *46*, 1094–1103.
- (532) Muralia, S.; Quarles, N.; Zhang, L.; Pottsa, J.; Tan, Z.; Lu, Y.; Zhu, Y.; Ruoff, R. *Nano Energy* **2013**, *2*, 764–768.
- (533) Yang, X.; Cheng, C.; Wang, Y.; Qiu, L.; Li, D. *Science* **2013**, *341*, 534–536.
- (534) Kuila, B. K.; Nandan, B.; Bohme, M.; Janke, A.; Stamm, M. *Chem. Commun.* **2009**, 5749–5751.
- (535) Long, Y.-Z.; Li, M.-M.; Gu, C.; Wan, M.; Duvail, J.-L.; Liu, Z.; Fan, Z. *Prog. Polym. Sci.* **2011**, *36*, 1415–1442.
- (536) Wang, H.; Hao, Q.; Yang, X.; Lu, L.; Wang, X. *ACS Appl. Mater. Interfaces* **2010**, *2*, 821–828.
- (537) Wang, H.; Hao, Q.; Yang, X.; Lu, L.; Wang, X. *Electrochim. Commun.* **2009**, *11*, 1158–1161.
- (538) Xu, J.; Wang, K.; Zu, S.-Z.; Han, B.-H.; Wei, Z. *ACS Nano* **2010**, *4*, 5019–5026.
- (539) Yan, J.; Wei, T.; Shao, B.; Fan, Z.; Qian, W.; Zhang, M.; Wei, F. *Carbon* **2010**, *48*, 487–493.
- (540) Zhang, K.; Zhang, L. L.; Zhao, X. S.; Wu, J. *Chem. Mater.* **2010**, *22*, 1392–1401.
- (541) Li, L.; Raji, A. R.; Fei, H.; Yang, Y.; Samuel, E. L.; Tour, J. M. *ACS Appl. Mater. Interfaces* **2013**, *5*, 6622–6627.
- (542) Giri, S.; Ghosh, D.; Das, C. K. *J. Electroanal. Chem.* **2013**, *697*, 32–45.
- (543) Tai, Z.; Yan, X.; Xue, Q. *J. Electrochem. Soc.* **2012**, *159*, A1702–A1709.
- (544) Lee, T.; Yun, T.; Park, B.; Sharma, B.; Song, H.-K.; Kim, B.-S. *J. Mater. Chem.* **2012**, *22*, 21092–21099.

- (545) Cong, H.-P.; Ren, X.-C.; Wang, P.; Yu, S.-H. *Energy Environ. Sci.* **2013**, *6*, 1185–1191.
- (546) Liu, J.; An, J.; Ma, Y.; Li, M.; Ma, R. *J. Electrochem. Soc.* **2012**, *159*, A828–A833.
- (547) Konwer, S.; Boruah, R.; Dolui, S. K. *J. Electron. Mater.* **2011**, *40*, 2248–2255.
- (548) Li, J.; Xie, H.; Li, Y. *J. Power Sources* **2013**, *241*, 388–395.
- (549) Bose, S.; Kim, N. H.; Kuila, T.; Lau, K.-t.; Lee, J. H. *Nanotechnology* **2011**, *22*, 369502.
- (550) Zhang, L. L.; Zhao, S.; Tian, X. N.; Zhao, X. S. *Langmuir* **2010**, *26*, 17624–17328.
- (551) Zhao, Y.; Liu, J.; Hu, Y.; Cheng, H.; Hu, C.; Jiang, C.; Jiang, L.; Cao, A.; Qu, L. *Adv. Mater.* **2013**, *25*, 591–595.
- (552) Mini, P. A.; Balakrishnan, A.; Nair, S. V.; Subramanian, K. R. *Chem. Commun.* **2011**, *47*, 5753–5755.
- (553) Wang, G.; Zhang, L.; Zhang, J. *Chem. Soc. Rev.* **2012**, *41*, 797–828.
- (554) Chen, S.; Zhu, J.; Wu, X.; Han, Q.; Wang, X. *ACS Nano* **2010**, *4*, 2822–2830.
- (555) Zhang, B.; Yu, B.; Zhou, F.; Liu, W. *J. Mater. Chem. A* **2013**, *1*, 8587–8592.
- (556) Zhao, X.; Zhang, L.; Murali, S.; Stoller, M. D.; Zhang, Q.; Zhu, Y.; Ruoff, R. S. *ACS Nano* **2012**, *6*, 5404–5412.
- (557) Lee, J. W.; Hall, A. S.; Kim, J.-D.; Mallouk, T. E. *Chem. Mater.* **2012**, *24*, 1158–1164.
- (558) Wang, B.; Park, J.; Wang, C.; Ahn, H.; Wang, G. *Electrochim. Acta* **2010**, *55*, 6812–6817.
- (559) Zhu, L.; Zhang, S.; Cui, Y.; Song, H.; Chen, X. *Electrochim. Acta* **2013**, *89*, 18–23.
- (560) Gao, H.; Xiao, F.; Ching, C. B.; Duan, H. *ACS Appl. Mater. Interfaces* **2012**, *4*, 7020–7026.
- (561) Wu, Z.-S.; Wang, D.-W.; Ren, W.; Zhao, J.; Zhou, G.; Li, F.; Cheng, H.-M. *Adv. Funct. Mater.* **2010**, *20*, 3595–3602.
- (562) Choi, B. G.; Huh, Y. S.; Hong, W. H.; Erickson, D.; Park, H. S. *Nanoscale* **2013**, *5*, 3976–3981.
- (563) Yan, J.; Wei, T.; Qiao, W.; Shao, B.; Zhao, Q.; Zhang, L.; Fan, Z. *Electrochim. Acta* **2010**, *55*, 6973–6978.
- (564) Wang, X.; Liu, S.; Wang, H.; Tu, F.; Fang, D.; Li, Y. *J. Solid State Electrochem.* **2012**, *16*, 3593–3602.
- (565) Sun, C.-Y.; Zhu, Y.-G.; Zhu, T.-J.; Xie, J.; Cao, G.-S.; Zhao, X.-B. *J. Solid State Electrochem.* **2013**, *17*, 1159–1165.
- (566) Wang, H.; Casalongue, H. S.; Liang, Y.; Dai, H. *J. Am. Chem. Soc.* **2010**, *132*, 7472–7477.
- (567) Lee, K. K.; Deng, S.; Fan, H. M.; Mhaisalkar, S.; Tan, H. R.; Tok, E. S.; Loh, K. P.; Chin, W. S.; Sow, C. H. *Nanoscale* **2012**, *4*, 2958–2961.
- (568) Qu, Q.; Yang, S.; Feng, X. *Adv. Mater.* **2011**, *23*, 5574–5580.
- (569) Shi, W.; Zhu, J.; Sim, D. H.; Tay, Y. Y.; Lu, Z.; Zhang, X.; Sharma, Y.; Srinivasan, M.; Zhang, H.; Hng, H. H.; Yan, Q. *J. Mater. Chem.* **2011**, *21*, 3422–3427.
- (570) Sun, X.; Xie, M.; Wang, G.; Sun, H.; Cavanagh, A. S.; Travis, J. J.; George, S. M.; Lian, J. J. *J. Electrochem. Soc.* **2012**, *159*, A364–A369.
- (571) Wang, J.; Gao, Z.; Li, Z.; Wang, B.; Yan, Y.; Liu, Q.; Mann, T.; Zhang, M.; Jiang, Z. *J. Solid State Chem.* **2011**, *184*, 1421–1427.
- (572) Cheng, Q.; Tang, J.; Shinya, N.; Qin, L.-C. *J. Power Sources* **2013**, *241*, 423–428.
- (573) Jin, Y.; Chen, H.; Chen, M.; Liu, N.; Li, Q. *ACS Appl. Mater. Interfaces* **2013**, *5*, 3408–3416.
- (574) Wang, G.; Tang, Q.; Bao, H.; Li, X.; Wang, G. *J. Power Sources* **2013**, *241*, 231–238.
- (575) Chmiola, J.; Yushin, G.; Gogotsi, Y.; Portet, C.; Simon, P.; Taberna, P. L. *Science* **2006**, *313*, 1760–1763.
- (576) Simon, P.; Gogotsi, Y. *Nat. Mater.* **2008**, *7*, 845–854.
- (577) Eliad, L.; Pollak, E.; Levy, N.; Salitra, G.; Soffer, A.; Aurbach, D. *Appl. Phys. A-Mater. Sci. Process.* **2006**, *82*, 607–613.
- (578) Eliad, L.; Salitra, G.; Soffer, A.; Aurbach, D. *Langmuir* **2005**, *21*, 3198–3202.
- (579) Fischer, A. E.; Pettigrew, K. A.; Rolison, D. R.; Stroud, R. M.; Long, J. W. *Nano Lett.* **2007**, *7*, 281–286.
- (580) Futaba, D. N.; Hata, K.; Yamada, T.; Hiraoka, T.; Hayamizu, Y.; Kakudate, Y.; Tanaike, O.; Hatori, H.; Yumura, M.; Iijima, S. *Nat. Mater.* **2006**, *5*, 987–994.
- (581) Fagioli, E.; Rena, P.; Danel, V.; Andrieu, X.; Mallant, R.; Kahlen, H. *J. Power Sources* **1999**, *84*, 261–269.
- (582) Fernandez, J. A.; Morishita, T.; Toyoda, M.; Inagaki, M.; Stoeckli, F.; Centeno, T. A. *J. Power Sources* **2008**, *175*, 675–679.
- (583) Kodama, M.; Yamashita, J.; Soneda, Y.; Hatori, H.; Kamegawa, K.; Moriguchi, I. *Chem. Lett.* **2006**, *35*, 680–681.
- (584) Ren, T. Z.; Liu, L.; Zhang, Y. Y.; Yuan, Z. Y. *J. Solid State Electrochem.* **2013**, *17*, 2223–2233.
- (585) Wei, J.; Zhou, D. D.; Sun, Z. K.; Deng, Y. H.; Xia, Y. Y.; Zhao, D. Y. *Adv. Funct. Mater.* **2013**, *23*, 2322–2328.
- (586) Kim, Y. J.; Abe, Y.; Yanaglura, T.; Park, K. C.; Shimizu, M.; Iwazaki, T.; Nakagawa, S.; Endo, M.; Dresselhaus, M. S. *Carbon* **2007**, *45*, 2116–2125.
- (587) Yan, Y. F.; Cheng, Q. L.; Zhu, Z. J.; Pavlinek, V.; Saha, P.; Li, C. Z. *J. Power Sources* **2013**, *240*, 544–550.
- (588) Ren, J.; Li, L.; Chen, C.; Chen, X.; Cai, Z.; Qiu, L.; Wang, Y.; Zhu, X.; Peng, H. *Adv. Mater.* **2013**, *25*, 1155–1159.
- (589) Sun, H.; You, X.; Deng, J.; Chen, X.; Yang, Z.; Ren, J.; Peng, H. *Adv. Mater.* **2014**, *26*, 2868–2873.
- (590) Ren, J.; Bai, W.; Guan, G.; Zhang, Y.; Peng, H. *Adv. Mater.* **2013**, *25*, 5965–5970.
- (591) Chen, X.; Qiu, L.; Ren, J.; Guan, G.; Lin, H.; Zhang, Z.; Chen, P.; Wang, Y.; Peng, H. *Adv. Mater.* **2013**, *25*, 6436–6441.
- (592) Yang, Z.; Deng, J.; Chen, X.; Ren, J.; Peng, H. *Angew. Chem., Int. Ed. Engl.* **2013**, *52*, 13453–13457.
- (593) Cai, Z.; Li, L.; Ren, J.; Qiu, L.; Lin, H.; Peng, H. *J. Mater. Chem. A* **2013**, *1*, 258–261.
- (594) Wang, K.; Meng, Q.; Zhang, Y.; Wei, Z.; Miao, M. *Adv. Mater.* **2013**, *25*, 1494–1498.
- (595) Li, X.; Zhao, T.; Wang, K.; Yang, Y.; Wei, J.; Kang, F.; Wu, D.; Zhu, H. *Langmuir* **2011**, *27*, 12164–12171.
- (596) Li, X.; Zhao, T.; Chen, Q.; Li, P.; Wang, K.; Zhong, M.; Wei, J.; Wu, D.; Wei, B.; Zhu, H. *Phys. Chem. Chem. Phys.* **2013**, *15*, 17752–17757.
- (597) Huang, T.; Zheng, B.; Kou, L.; Gopalsamy, K.; Xu, Z.; Gao, C.; Meng, Y.; Wei, Z. *RSC Adv.* **2013**, *3*, 23957–23962.
- (598) Meng, Y.; Zhao, Y.; Hu, C.; Cheng, H.; Hu, Y.; Zhang, Z.; Shi, G.; Qu, L. *Adv. Mater.* **2013**, *25*, 2326–2331.
- (599) Kou, L.; Huang, T.; Zheng, B.; Han, Y.; Zhao, X.; Gopalsamy, K.; Sun, H.; Gao, C. *Nat. Commun.* **2014**, *5*, 3754.
- (600) Miyasaka, T.; Murakami, T. N. *Appl. Phys. Lett.* **2004**, *85*, 3932–3934.
- (601) Wee, G.; Salim, T.; Lam, Y. M.; Mhaisalkar, S. G.; Srinivasan, M. *Energy Environ. Sci.* **2011**, *4*, 413–416.
- (602) Yang, Z.; Li, L.; Luo, Y.; He, R.; Qiu, L.; Lin, H.; Peng, H. *J. Mater. Chem.* **2013**, *1*, 954–958.
- (603) Xu, J.; Wu, H.; Lu, L.; Leung, S. F.; Chen, D.; Chen, X.; Fan, Z.; Shen, G.; Li, D. *Adv. Funct. Mater.* **2014**, *24*, 1814–1814.
- (604) Bae, J.; Park, Y. J.; Lee, M.; Cha, S. N.; Choi, Y. J.; Lee, C. S.; Kim, J. M.; Wang, Z. L. *Adv. Mater.* **2011**, *23*, 3446–3449.
- (605) Fu, Y.; Wu, H.; Ye, S.; Cai, X.; Yu, X.; Hou, S.; Kafafy, H.; Zou, D. *Energy Environ. Sci.* **2013**, *6*, 805–812.
- (606) Yang, Z.; Deng, J.; Sun, H.; Ren, J.; Pan, S.; Peng, H. *Adv. Mater.* **2014**, *26*, 7038–7042.
- (607) (a) Qiu, L.; Jiang, Y.; Sun, X.; Liu, X.; Peng, H. *J. Mater. Chem. A* **2014**, *2*, 15132–15138. He, S.; Qiu, L.; Fang, X.; Guan, G.; Chen, P.; Zhang, Z.; Peng, H. *J. Mater. Chem. A* **2015**, *3*, 9406–9410. Zhang, Z.; Guo, K.; Li, Y.; Li, X.; Guan, G.; Li, H.; Luo, Y.; Zhao, F.; Zhang, Q.; Wei, B.; Pei, Q.; Peng, H. *Nat. Photon.* **2015**, *9*, 223–238. Jiang, Y.; Sun, H.; Peng, H. *Sci. China Mater.* **2015**, *58*, 289–293. Pan, S.; Deng, J.; Guan, G.; Zhang, Y.; Chen, P.; Ren, J.; Peng, H. *J. Mater. Chem. A* **2015**, *3*, 6286–6290. Sun, H.; Deng, J.; Qiu, L.; Fang, X.; Peng, H. *Energy Environ. Sci.* **2015**, *8*, 1139–1159. Sun, X.; Zhang, J.; Lu, X.; Fang, X.; Peng, H. *Angew. Chem. Int. Ed.* **2015**, *54*, 3630–3634. Sun, X.; Lu, X.; Qiu, L.; Peng, H. *J. Mater. Chem. C* **2015**, *3*, 2642–2649. Weng, W.; Sun, Q.; Zhang, Y.; He, S.; Wu, Q.; Deng, J.; Fang, X;

Guan, G.; Ren, J.; Peng, H. *Adv. Mater.* **2015**, *27*, 1363–1369. Zhang, Y.; Bai, W.; Cheng, X.; Ren, J.; Weng, W.; Chen, P.; Fang, X.; Zhang, Z.; Peng, H. *Angew. Chem. Int. Ed.* **2014**, *53*, 14564–14568. Fang, X.; Peng, H. *Small* **2015**, *11*, 1488–1511. Pan, S.; Lin, H.; Deng, J.; Chen, P.; Chen, X.; Yang, Z.; Peng, H. *Adv. Energy Mater.* **2015**, *5*, 1401438. Sun, H.; Che, R.; You, X.; Jiang, Y.; Yang, Z.; Deng, J.; Qiu, L.; Peng, H. *Adv. Mater.* **2014**, *26*, 8120–8125. Lu, X.; Zhang, Z.; Li, H.; Sun, X.; Peng, H. *J. Mater. Chem. A* **2014**, *2*, 17272–17280. Zhang, Z.; Li, X.; Guan, G.; Pan, S.; Zhu, Z.; Ren, D.; Peng, H. *Angew. Chem. Int. Ed.* **2014**, *53*, 11571–11574. Zhang, Z.; Deng, J.; Li, X.; Yang, Z.; He, S.; Chen, X.; Guan, G.; Ren, J.; Peng, H. *Adv. Mater.* **2015**, *27*, 356–362. Chen, P.; Xu, Y.; He, S.; Sun, X.; Guo, W.; Zhang, Z.; Qiu, L.; Li, J.; Chen, D.; Peng, H. *Adv. Mater.* **2015**, *27*, 1042–1047.